The influence of the substrate on the structure and electronic properties of carbon-based 2D materials

Jessica Sforzini

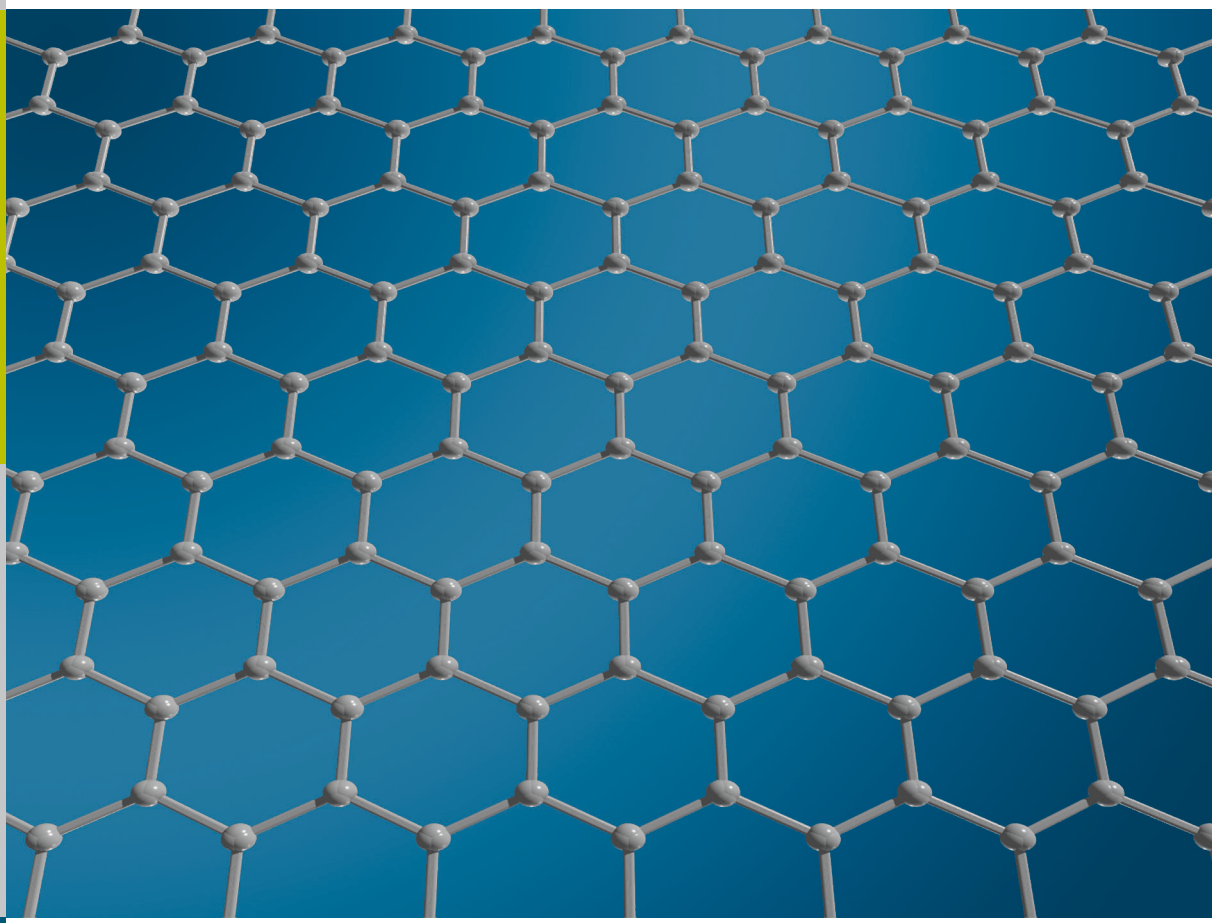

Schlüsseltechnologien / Key Technologies
Band / Volume 153
ISBN 978-3-95806-255-9

JÜLICH
FORSCHUNGSZENTRUM

Schriften des Forschungszentrums Jülich
Reihe Schlüsseltechnologien / Key Technologies Band / Volume 153

Forschungszentrum Jülich GmbH
Peter Grünberg Institut (PGI)
Functional Nanostructures at Surfaces (PGI-3)

The influence of the substrate on the structure and electronic properties of carbon-based 2D materials

Jessica Sforzini

Schriften des Forschungszentrums Jülich
Reihe Schlüsseltechnologien / Key Technologies Band / Volume 153

ISSN 1866-1807 ISBN 978-3-95806-255-9

Bibliographic information published by the Deutsche Nationalbibliothek.
The Deutsche Nationalbibliothek lists this publication in the Deutsche
Nationalbibliografie; detailed bibliographic data are available in the
Internet at http://dnb.d-nb.de.

Publisher and Distributor:	Forschungszentrum Jülich GmbH Zentralbibliothek 52425 Jülich Tel: +49 2461 61-5368 Fax: +49 2461 61-6103 Email: zb-publikation@fz-juelich.de www.fz-juelich.de/zb
Cover Design:	Grafische Medien, Forschungszentrum Jülich GmbH
Printer:	Grafische Medien, Forschungszentrum Jülich GmbH
Copyright:	Forschungszentrum Jülich 2017

Schriften des Forschungszentrums Jülich
Reihe Schlüsseltechnologien / Key Technologies, Band / Volume 153

D 82 (Diss. RWTH Aachen University, 2017)

ISSN 1866-1807
ISBN 978-3-95806-255-9

The complete volume is freely available on the Internet on the Jülicher Open Access Server (JuSER)
at www.fz-juelich.de/zb/openaccess.

Acknowledgements

I would like to acknowledge all the people who have supported me and contributed to the present work:

I would like to express my sincere gratitude to Prof. Dr. F. Stefan Tautz for giving me the opportunity to carry out my PhD in his group, for his continual support and encouragement and for his guidance over these past years.

I acknowledge Prof. Dr. Carsten Busse for taking his time to co-referee my thesis.

I am very thankful to Dr. Francois Bocquet, who has supervised me day by day, has helped me with all kind of questions in science that I faced during my work, for all his support and advice.

I thank Prof. Dr. Ultrike Starke and his group from the Max Planck Institute for Solid State Research in Stuttgart for providing the graphene samples.

I thank Dr. Lydia Nemec and her group from the Fritz Haber Institute of the Max Planck Society in Berlin for our fruitful collaboration.

I also thank Dr. Martin Švec and Mychola Telychko and their group from the Institute of Physics in Prague for the time spent in the Synchrotron beamlines and for our collaboration.

I acknowledge Prof. Dr. Peter Jakob for the discussion about the Fano-type analysis, and Prof. Dr. Harald Ibach for our work on the electron spectrometer.

I am grateful to all the staff of the I09 beamline (Diamond Light Source Synchrotron, Didcot, United Kingdom) and of the Material Science beamline (Elettra Synchrotron, Trieste, Italy) for their efficient technical and scientific support.

I thank our secretary team of the Peter Grünberg Institute-3 for dealing with bureaucratic formalities.

I also thank all my colleagues from the Peter Grünberg Institute-3 in the Forschungszentrum Jülich: especially my colleagues who shared the beamtimes; Martin Willenbockel, for his help with IT problems, together with Taner Estat and Aizhan Sabitova for the nice environment in the office; and Annemie Franken for her excellent technical support.

Special thanks go to all my friends I met during the past three years who have made Jülich an exciting place to live; to my dated Italian friends for being close despite the distance; to my parents, Stefano and Giuseppina, and to my sister and brother, Carlotta and Leonardo, for their pride and unlimited support; and to Stefano for being beside me also in this step.

Abstract

The exploration of two-dimensional (2D) materials, such as graphene, has become the hottest research of interest in recent years because they offer the possibility to create more efficient, smaller and cost-effective nano-devices. In order to realize potential applications of 2D materials in the areas of electronics and optoelectronics, there are many challenges associated with their electronic and structural behavior, which require the understanding of the interactions at 2D materials interfaces. With this in mind, the goal of this thesis was to assess interactions between various 2D layers and substrates, of interest for both fundamental studies and industrial applications, by studying the modification of the layer electronic and structural properties in relation to the supporting substrate using different surface science techniques.
In particular, interactions residing at graphene/6H-SiC(0001) interfaces were considered. At first, a new approach used to gauge the strength of these interactions was presented based on the determination of the graphene adsorption height with respect to the H-intercalated SiC substrate. By comparing this value with the graphene vertical distance of different graphene/substrate systems, we found H-intercalated graphene (H-QFMLG) free of interactions besides van der Waals, indicating that the effect of the underlying H-intercalated SiC on graphene was almost non existent.
The influence of this substrate on the structural and electronic properties of graphene was further investigated upon nitrogen doping in comparison to the carbon buffer layer terminated SiC in epitaxial graphene (EMLG). The outcome was that both graphene layers showed a similar n-type carrier increase but a dissimilar concentration and variety of dopants substituted into the graphene layers leading to the main conclusion that the effective doping of graphene was surprisingly dependent on the supporting material. In the case of H-QFMLG, the nitrogen dopants were found partially replacing the hydrogen intercalation at the interface, which in turn became N-doped contributing to the graphene doping ('proximity doping') but degrading the graphene layer in terms of buckling and interface interactions. On the contrary, the buffer layer in EMLG was found inert allowing a multicomponent substitution of the nitrogen dopants into graphene. However, this was not the case for

boron-doped EMLG, for which boron was found in one chemical configuration and in both buffer layer and graphene.
In the last part of the thesis, the focus was laid on the study of physical phenomena that occur at organic/metal interfaces. Specifically, the molecular symmetry reduction (from the D_{4h} symmetry group) via degeneracy lifting of the platinum- and palladium-phthalocyanine/Ag(111) complexes was investigated using vibrational spectroscopy. Because of the presence of an interfacial dynamical charge transfer, some vibrational peaks showed a Fano-type line shape. By their assignment to vibrational modes which were infrared active only in the C_{2v} symmetry group, we proved that a preferential charge transfer from the Ag surface into one of the originally doubly degenerate lowest unoccupied molecular orbitals took place, i.e. the electronic degeneracy was lifted and the molecule-surface complex acquired the twofold symmetry.

Zusammenfassung

Die Untersuchung zweidimensionaler (2D) Materialien wie Graphen ist in den letzte Jahren zu einem der heißesten Forschungsgebiete geworden, da solche Materialien neue Möglichkeiten zur kosteneffizienten Herstellung von effizienteren und kleineren nano-Bauteilen versprechen. Um potentielle Anwendungen von 2D-Materialien auf den Gebieten der Elektronik und Optoelektronik zu realisieren, müssen vielfache Herausforderungen in Bezug auf strukturelles und elektronisches Verhalten gemeistert werden. Dies Erfordert ein tiefgreifendes Verständnis der Wechselwirkungen an 2D-Material Grenzschichten. Vor diesem Hintergrund ist es das Ziel der vorliegenden Arbeit, einen Zugang zu den Wechselwirkungen verschiedener 2D-Schichten und Substrate, die sowohl in der Grundlagenforschung als auch in der Anwendung eine Rolle spielen, über die Untersuchung der Modifikation von strukturellen und elektronischen Eigenschaften der Schichten im Verhältnis zum Substrat, durch die Nutzung verschiedenster oberflächensensitiver Methoden, zu eröffnen.
Insbesondere wurden Wechselwirkungen an der Graphen/SiC(0001) Grenzschicht betrachtet. Zunächst wird ein neuer Ansatz vorgestellt, um die Stärke dieser Wechselwirkung anhand der Bestimmung der Graphen Adsorptionshöhe in Bezug auf das H-interkalierte SiC Substrat zu messen. Durch den Vergleich dieses Wertes mit den vertikalen Abständen verschiedener Graphen/Substrat Systeme ergab sich, dass H-interkaliertes Graphen (H-QFMLG), abgesehen von der van-der-Waals Wechselwirkung, wechselwirkungsfrei ist. Das zeigt, dass der Einfluss des darunter liegenden H-interkalierten SiC quasi nicht existent ist.
Der Einfluss dieses Substrats auf die strukturellen und elektronischen Eigenschaften von Graphen wurde weiterhin anhand von Stickstoff-Dotierung im Vergleich zum mit einer Kohlenstoff Pufferlage terminierten SiC im epitaktischen Graphen untersucht (EMLG). Im Ergebnis zeigen beide Graphen Schichten einen ähnlichen n-Typ Ladungsträger Zuwachs, aber eine unterschiedliche Konzentration und Verteilung der Fremdatome in den Schichten. Dies führt zu dem Schluss, dass eine effektive Graphen-Dotierung überraschend abhängig vom darunterliegenden Substrat ist. Im Fall von H-QFML stellt sich heraus, dass die Stickstoff Atome teilweise

die Wasserstoff Interkalation an der Grenzschicht ersetzen. Dadurch wurde diese n-dotiert und trug zur Graphen-Dotierung bei ('Proximity Doping') aber sorgte für eine Verschlechterung der Graphenschicht hinsichtlich Rauigkeit und Grenzschicht-Wechselwirkung. Dagegen war die Pufferlage im EMLG inert, was eine mehrfach-Komponenten Substitution der Stickstoff Atome im Graphen erlaubte. Dies war jedoch nicht der Fall für Bor-dotiertes EMLG, bei dem Bor in einer chemischen Konfiguration sowohl in der Pufferlage als auch im Graphen gefunden wurde.
Im letzten Teil der Arbeit wurde der Fokus auf die Untersuchung physikalischer Phänomene an Metall/Organischen Grenzflächen gelegt. Speziell wurde die Symmetrie-Reduktion (von der D_{4h}-Symmetrie Gruppe) durch die Aufhebung der Entartung an Platin- und Palladium-Phthalocyanin-Komplexen mit Hilfe von Vibrations-Spektroskopie untersucht. Wegen des Vorhandenseins eines dynamischen Ladungstransfers, zeigen einige Vibrations-Peaks eine Fano-artige Linienform. Durch deren Zuordnung Vibrationsmoden, die nur in der C_{2v} Symmetrie Infrarot-aktiv sind, können wir zeigen, dass ein bevorzugter Ladungstransfer von der Ag Oberfläche in eines der ursprünglich zweifach entarteten niedrigsten unbesetzten Molekülorbitale stattfindet, das bedeutet, dass die elektronische Entartung aufgehoben wurde und der Molekül-Oberflächen Komplex die zweizählige Symmetrie angenommen hat.

Publications

Papers included in this thesis:

Approaching Truly Freestanding Graphene: The Structure of Hydrogen-Intercalated Graphene on 6H-SiC(0001)

J. Sforzini, *L. Nemec, T. Denig, B. Stadtmüller, T.-L. Lee, C. Kumpf, S. Soubatch, U. Starke, P. Rinke, V. Blum, F. C. Bocquet and F. S. Tautz*

Physical Review Letters, ***114****, 106804 (2015)*

Structural and Electronic Properties of Nitrogen-Doped Graphene

J. Sforzini, *P. Hapala, G. van Straaten, M. Franke, A. Stöhr, S. Soubatch, P. Jelínek, T.-L. Lee, U. Starke, M. Švec, F. C. Bocquet and F. S. Tautz*

Physical Review Letters, ***116****, 126805 (2016)*

Transformation of metallic boron into substitutional dopants in graphene on 6H-SiC(0001)

J. Sforzini, *M. Telychko, O. Krejčí, M. Vondráček, M. Švec, F. C. Bocquet and F. S. Tautz*

Physical Review B Rapid Communication, ***93****, 041302 (2016)*

Adsorption-induced symmetry reduction of metal-phthalocyanine studied by vibrational spectroscopy

J. Sforzini, *F. C. Bocquet and F. S. Tautz*

Physical Review B, ***96****, 165410 (2017)*

Papers not included in this thesis:

Electronic and Chemical Properties of Donor, Acceptor Centers in Graphene

M. Telychko, P. Mutombo, P. Merino, P. Hapala, M. Ondráček, F. C. Bocquet, ***J. Sforzini****, O. Stetsovych, M. Vondráček, P. Jelínek and M. Švec*

ACS Nano, ***9****, 9180 (2015)*

Electron energy loss spectroscopy with parallel readout of energy and momentum

H. Ibach, F. C. Bocquet, ***J. Sforzini****, S. Soubatch and F. S. Tautz*

Review of Scientific Instruments, ***88****, 033903 (2017)*

List of Acronyms

2D	Two-Dimensional
ARPES	Angle-Resolved Photoemission Spectroscopy
BL	Buffer Layer
EMLG	Epitaxial Monolayer Graphene
H-QFMLG	Hydrogen-intercalated Quasifreestanding Monolayer Graphene
NIXSW	Normal Incidence X-ray Standing Waves
DFT	Density Functional Theory
Ge-QFMLG	Germanium-intercalated Quasifreestanding Monolayer Graphene
XPS	X-ray Photoelectron Spectroscopy
NEXAFS	Near-Edge X-ray Adsorption Fine Structure
PtPc	Platinum-Phthalocyanine
PdPc	Palladium-Phthalocyanine
HREELS	High-Resolution Electron Energy Loss Spectroscopy
E_{kin}	Kinetic Energy
BE	Binding Energy
E_F	Fermi Energy
I_{XSW}	Intensity of XSW field
P^H	Coherent Position
F^H	Coherent Fraction
EY	Electron Yield
IR	Infrared

Pc	Phthalocyanine
$\boldsymbol{E_D}$	Dirac point Energy
UHV	Ultra-High Vacuum
HOMO	Highest Occupied Molecular Orbital
LUMO	Lowest Unoccupied Molecular Orbital
HAS	Helium Atomic Scattering
LEED	Low Energy Electron Diffraction
QMS	Quadrupole Mass Spectrometer
UV	Ultraviolet
L	Langmuir
STM	Scanning Tunneling Microscopy
TPD	Temperature Programmed Desorption

Contents

1 Motivation and Outline

Since the isolation of a single layer graphene in 2004 [1], there has been a huge boost in the investigation of carbon-based Two-Dimensional (2D) materials during the past years. The interest in these type of materials is from both a scientific and technological aspect [2–4]. From a scientific point of view, the novel extraordinary properties, rising from the 2D confinement, discovered almost on a daily basis has opened a completely new chapter in condensed matter physics, attracting growing attention from the global scientific community. From a technological point of view, the interest clearly lies in harnessing such novel properties in the fabrication of smaller and more accessible nano-electronic devices, which offer many benefits for further miniaturization following Moore's Law and as a high-mobility option in the rising field of large-area and low-cost electronics [5].

Because a 2D material comprises only a single layer, a supporting substrate is commonly required in order to produce and use the layer for practical and industrial applications. Ideally, the substrate material should not influence the layer properties; in reality, however, it may strongly affect the layer in terms of ripple, surface roughness and doping (interfacial charge transfer) effects [6, 7]. These effects can be unwanted or can conversely be used to modify the layer properties in a desirable way. Interactions with the underlying substrate can significantly deteriorate the structure of the layer and/or result in the modification of its electronic behavior, affecting the ultimate performance of 2D materials-based devices. Motivated by the necessity of understanding the physical phenomena associated with interactions residing at a 2D material surface, the present thesis investigates different interfaces, considered of importance for both fundamentals studies and devices applications, and has the ambitious goal, in specific cases, to address the influence of the substrate on the layer properties.

As graphene, pioneer of 2D materials, possesses many unique and special properties making it a good candidate for theoretical and experimental studies as well as for potential electronic applications including radio-frequency modules and field effect

transistors, the first part of this dissertation is focused on the study of different graphene/SiC interfaces [8]. Among various preparation methods, graphene epitaxially grown on 6H-SiC(0001) is worthy of consideration because it probably offers the only viable route towards the introduction of graphene into the semiconductor industry since SiC is a wide band-gap semiconductor [9]. Although the research on graphene in general and on graphene/SiC in particular has been very intense during the last years, the strength of its interaction with a substrate (and interface) still remains an issue. With this class of supporting materials, i.e. intercalated SiC, a graphene layer is commonly considered 'interaction-free' (freestanding), making it difficult to study in terms of substrate effect with traditional techniques such as Angle-Resolved Photoemission Spectroscopy (ARPES). In Chap. 4, a new approach is presented which provides a direct insight into the interaction at the interface. The effect of the carbon Buffer Layer (BL) in Epitaxial Monolayer Graphene (EMLG) and hydrogen intercalation in Hydrogen-intercalated Quasifreestanding Monolayer Graphene (H-QFMLG), both on 6H-SiC(0001), on the graphene properties is investigated by means of the Normal Incidence X-ray Standing Wave (NIXSW) technique and Density Functional Theory (DFT). The research is then extended to other graphene/metal systems for comparison.

In this context, Germanium-intercalated Quasifreestanding Monolayer Graphene (Ge-QFMLG) appears a valuable system to further explore the interaction at the interface and to extend the previous study since, depending on the amount of germanium at the intercalation, the graphene layer shows ambipolar doping [10]. From a technological prospective, Ge-QFMLG may be largely applied in the fabrication of nano-junctions. However, a great concern exists about the dependence of the graphene doping level on the interface structure. In this regard, the investigation of this system using the NIXSW technique presented in Chap. 5 not only contributes to the understanding of the interaction at the interface, but also provides experimental invaluable data regarding the vertical structure of the germanium intercalation, relevant parameter for theoretical calculations.

Although graphene is a remarkable material with superlative electronic and thermal properties, its lack of a band gap and its chemical inertness present severe obstacles to its incorporation into the semiconductor industry. For versatile use of graphene in electronic applications, additional external doping process is considered an efficient route for tuning the carrier types and Fermi levels [11, 12]. Other than doping level tuning, motivation for substitutional doping of graphene includes opening an electronic band gap. To date, nitrogen is the most studied dopant of graphene as demonstrated by the increasingly high number of publications related to nitrogen-doped

graphene within the graphene community [11]. However, the role of the supporting material during the doping process has seldom been taken into consideration. Because any substrate (and interface) has a significant effect on the structure and electronic band of pristine graphene, it is of importance to investigate whether this effect is altered by doping, more generally whether the effectiveness of the graphene doping process is influenced by the environment. Having previously investigated pristine H-QFMLG and EMLG on 6H-SiC(0001) in terms of layer-substrate interaction, in Chap. 6 we go one step further and compare the two systems upon nitrogen doping. Combining ARPES and NIXSW allows to simultaneously quantify the increased n-type carrier concentration of graphene and vertically locate the dopants according to their chemical nature within the samples.

From the electronic point of view, boron represents the opposite charge carrier with respect to nitrogen, since it is less electronegative than carbon, and induces p-type conductivity in graphene. Although the most widely investigated dopant heteroatom is nitrogen, boron is also relevant and can induce novel and complementary properties leading to specific implementation in alternative electronic devices and technologies [13]. The research on boron-doped graphene has been less extensive than on nitrogen-doped graphene, and basic investigations on the chemical nature of the boron dopants are still lacking. In Chap. 7, we take advantage of the chemical sensitivity of X-ray Photoelectron Spectroscopy (XPS) and Near-Edge X-ray Absorption Fine Structure (NEXAFS) to study the mechanism of incorporation of the boron dopants into the graphene layer of EMLG/6H-SiC(0001) and to investigate whether they are also present in the substrate (and interface).

In addition to graphene-based materials, this thesis encompasses the study of 2D layers made of organic electronic materials, specifically metal-phthalocyanine compounds. Interest in this class of materials originates from their suitability in e.g. organic light emitted diodes and organic field-effect transistors allowing the fabrication of low-cost and low-energy nanoscale electronic devices [14, 15]. In this account, the organic layer is in contact with a metallic surface resulting in a strict dependence of the device performance on the organic/metal interface properties. The adsorption of phthalocyanine molecules on nobel metals has been an active research field during the past years such that only a few aspects of their interaction remain unresolved [16]. One of these is the symmetry of the molecules when adsorbed on the (111) orientation in relation to the charge transfer. In this context, Chap. 8 presents an approach to study the symmetry reduction via degeneracy lifting of Platinum-Phthalocyanine (PtPc) and Palladium-Pthalocyanine (PdPc) adsorbed on Ag(111) by High-Resolution Electron Energy Loss Spectroscopy

(HREELS).

2 Methods

This chapter presents the basics of the methods employed in this work. The first section will introduce photoemission spectroscopy, which refers to energy measurements of electrons emitted from solids by the photoelectric effect, as an introductory concept for the advanced x-ray standing wave technique. The latter is used as a main tool in Chap. 4, 5 and 6 to determine the adsorption height of graphene. Complementary to photoemission spectroscopy, the absorption spectroscopy is employed in Chap. 7 to probe the unoccupied states. Finally, the fundamentals of electron energy loss spectroscopy will be given to prepare the reader for the results presented in Chap. 8 and 9.

2.1 Photoelectron Spectroscopy (XPS and ARPES)

Photoelectron spectroscopy is based on the photoelectric effect, which was first fully explained by Einstein [17]. A schematic representation of it is shown in Fig. 2.1. As a result of the light-matter interaction, the absorption of the light in the solid takes place. If the photon energy $h\nu$ is larger than the work function of the sample, photo-excited electrons, called photoelectrons, can escape into vacuum (Fig. 2.1(b)). The work function corresponds to the minimum energy necessary to remove an electron from the solid into vacuum.

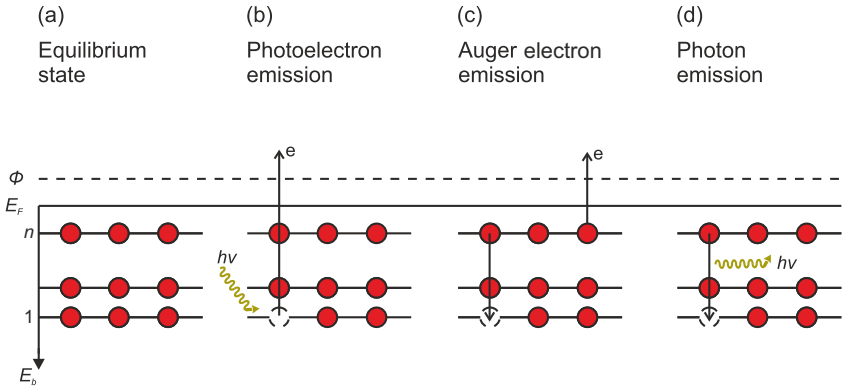

Figure 2.1: The schematic diagram of the photoemission process is shown. (a) The system is in the equilibrium state with n occupied energy levels. (b) After the light-matter interaction, one photoelectron is emitted from the core level generating a hole. (c) The system relaxes to the equilibrium by emission of an Auger electron or (d) by emission of a fluorescent photon.

Before interacting with light, the initial N-electron system is represented by the initial state wavefunction Ψ_i^N. After the photoemission process, the system is in one of the possible final states represented by the wavefunction Ψ_f^N. The probability (P_{if}) of the optical excitation from initial into final state in the solid is described by Fermi's 'Golden Rule' [18–20]

$$P_{if} = \frac{2\pi}{\hbar} \left| \left\langle \Psi_f^N \right| \widehat{V} \left| \Psi_i^N \right\rangle \right|^2 \delta(E_f - E_i - h\nu), \tag{2.1}$$

where $\widehat{V}$ is the Hamiltonian of the interaction between the electron and the vector potential $\mathbf{A}$ of the electromagnetic field, and $\hbar$ is the reduced Planck constant. The δ Dirac function represents the energy conservation law and contains the energies E_f and E_i of the final and initial state, respectively. Considering as a common choice the Coulomb gauge, the Hamiltonian $\widehat{V}$ can be written as

$$\widehat{V} = \frac{e}{mc} \mathbf{A} \cdot \mathbf{p}, \tag{2.2}$$

where $\mathbf{p}$ is the momentum of the photoelectron, m the electron mass, e the electron charge and c the speed of light. In the dipole approximation, only the first term ($\mathbf{A}_0$) of the periodic expansion in space of the vector potential ($\mathbf{A}$) is taken into account ($\mathbf{A} = \mathbf{A}_0$). In the Hartree-Fock formalism, the N-particle wavefunction of the initial state Ψ_i^N can be factorized as a product of the one electron orbital Φ_i^k,

from which the excitation occurs, and the remaining $(N-1)$-particle term such as

$$\Psi_i^N = \mathrm{A}\Phi_i^k\Psi_i^{N-1}, \tag{2.3}$$

where A is the antisymmetrizing operator necessary for satisfying the Pauli exclusion principle. A similar expression for the final state is only possible in the frozen approximation which assumes that the photoemission is an instantaneous process. Thus, the interactions with the $(N-1)$-particle system as well as relaxations of the system during the photoemission process are neglected. Within this assumption, the final wavefunction can be written as well as

$$\Psi_f^N = \mathrm{A}\Phi_f^k\Psi_f^{N-1}. \tag{2.4}$$

Hence, the transition matrix element in Eq. 2.1 becomes

$$\left\langle \Psi_f^N \right| \widehat{V} \left| \Psi_i^N \right\rangle = \left\langle \Psi_f^{N-1} | \Psi_i^{N-1} \right\rangle \left\langle \Phi_f^k \right| \widehat{V} \left| \Phi_i^k \right\rangle \tag{2.5}$$

where the first term is the $(N-1)$ overlap integral. If no rearrangement of the orbitals takes place during the photo excitation process (frozen orbital approximation, $\Psi_f^{N-1} = \Psi_i^{N-1}$), the overlap integral is equal to the Delta function $\delta_{i,f}$. The probability of the excitation in Eq. 2.1 can be written as

$$P_{if} = \frac{2\pi e}{mc\hbar} \left| \left\langle \Phi_f^k \right| \mathbf{A} \cdot \mathbf{p} \left| \Phi_i^k \right\rangle \right|^2 \delta(E_f^N + E_i^N - h\nu) \tag{2.6}$$

and depends on both the initial and final state. In reality, electron-electron correlations in the system cannot be neglected, and the probability that an excited state exists after the photoelectron removal needs to be integrated into the calculation of P_{if}. Energies calculated from Eq. 2.6 will be wrong, and corrections on the orbital energies are then necessary, which is beyond the scope of this work.

The XPS technique uses an x-ray beam as a photon source (200-2000 eV). An XPS spectrum is an energy distribution curve of the number of photoelectrons emitted under a certain angle for a fixed photon energy. The limited escape depth of electrons makes XPS a very surface sensitive method. Since the energy of the incident light

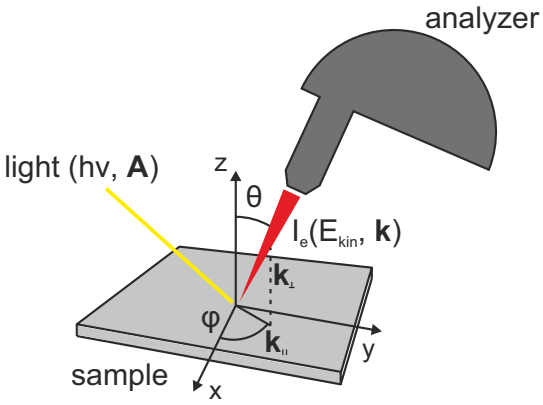

Figure 2.2: Sketch of the measurement geometry used in ARPES.

is high, atomic core level photoelectrons can be detected. The kinetic energy (E_{kin}) of the photoelectron is given by

$$E_{\text{kin}} = h\nu - E_b - \phi, \tag{2.7}$$

where E_b is the Binding Energy (BE) of the electron with respect to the Fermi Energy (E_F) and ϕ is the work function of the analyzer. Typically, the work function is of the order of few eV [21]. As the core levels of different chemical elements as well as a chemical element in different environments will have different BE, XPS spectra can provide a chemical fingerprint of the sample surface. Examples of that can be found in Chap. 6 and 7, in which the chemical nature of the dopants substituted into the graphene lattice is investigated.

When the energy of the incident photons is low enough (10-100 eV), only photoelectrons that originate from the valence levels are excited. In an ARPES experiment, the photoelectrons are detected as a function of their E_{kin} and emission angles, θ and ϕ, as shown in Fig. 2.2. This provides direct momentum resolved images of band dispersions. Within this work, ARPES experiments are used to measure the valence band of graphene in Chap. 4.3, 5 and 6. The wave vector of the photoelectrons in vacuum ($\mathbf{K}$) is related to E_{kin} according to:

$$|\mathbf{K}| = \frac{\sqrt{2mE_{\text{kin}}}}{\hbar}. \tag{2.8}$$

It can be divided into parallel and perpendicular components such as

$$\mathbf{K} = (\mathbf{K}_{||}) + (\mathbf{K}_{\perp}), \tag{2.9}$$

and each component can be expressed in terms of angles according to Fig. 2.2. The last equations refer to the momentum of the electron in vacuum. However, we are interested in the energy momentum inside the sample ($\mathbf{k}$). Because of the translational symmetry in the xy-plane and the absence of a potential in this plane, the parallel component of the momentum is conserved while the electron is refracted between the solid and the vacuum, and thus

$$|\mathbf{K}_{||}| = |\mathbf{k}_{||}| = \sqrt{\frac{2m}{\hbar^2}\mathrm{E}_{\mathrm{kin}}}\sin(\theta). \tag{2.10}$$

The treatment for $\mathbf{k}_{\perp}$ is more elaborated as the momentum is not conserved due to the presence of a potential step along the z-direction.

2.2 Normal Incidence X-ray Standing Waves (NIXSW)

The NIXSW technique uses XPS to detect core-level signals of species at the surface. The photon energy is varied around the Bragg condition of the crystal on which these species are adsorbed on. The development of Synchrotron beamlines has driven the technique to be applied in a wide range of fields in surface science. In Chap. 4, 5 and 6, it is mainly used to study the vertical distances between graphene and supporting substrates with high spatial resolution and chemical selectivity. Specifically, the graphene vertical distance with respect to the top Si atoms of the 6H-SiC(0001) substrate is determined. In the following, a brief introduction of the technique will be given based on the work of Woodruff [22].

In the situation of a Bragg reflection from a crystal, an incident wave (perpendicular to the Bragg planes) and a diffracted wave interfere to create a standing wave field characterized by a phase, related to the position of the atoms in the crystal, and by a wavelength that reflects the periodicity of the crystal. In the situation of multiple scattering, the reflectivity curve, known as Darwin curve, will have a finite width

around the Bragg condition either in terms of wavelenghts or scattering angles, because of the presence of out-of-phase scattered waves. The incident and diffracted x-ray waves are expressed by $\mathscr{E}_i = E_i e^{-2\pi i(\nu_i t - \mathbf{k}_i \mathbf{r})}$ and $\mathscr{E}_h = E_h e^{-2\pi i(\nu_h t - \mathbf{k}_h \mathbf{r})}$ respectively, where E_i and E_h are the complex amplitude and $\mathbf{k}_i$ and $\mathbf{k}_h$ are the x-ray propagation vectors related by $\mathbf{k}_h = \mathbf{k}_i + \mathbf{h}$. $\mathbf{h}$ represents the reciprocal lattice vector associated with the Bragg reflection from the (hkl) plane. Since the two waves are coherent, their frequencies are identical such that

$$\nu_i = \nu_h = \nu, \tag{2.11}$$

and thus the incident and diffracted waves are related by the reflectivity R and phase ϕ, both of which depend on the photon energy

$$\frac{E_h}{E_i} = \sqrt{R} e^{i\phi}, \tag{2.12}$$

with

$$R = \frac{|E_h|^2}{|E_i|^2}. \tag{2.13}$$

The total XSW field is calculated by the superposition of the two waves such that

$$\mathscr{E} = \mathscr{E}_i + \mathscr{E}_h = E_i e^{-2\pi i(\nu t - \mathbf{k}_i \mathbf{r})} + E_h e^{-2\pi i(\nu t - \mathbf{k}_h \mathbf{r})}, \tag{2.14}$$

and considering the relation in Eq. 2.12, it can be written as

$$\mathscr{E} = E_i e^{-2\pi i(\nu t - \mathbf{k}_i \mathbf{r})} + \sqrt{R} E_i e^{i\phi} e^{-2\pi i(\nu t - \mathbf{k}_h \mathbf{r})} = E_i e^{-2\pi i(\nu t - \mathbf{k}_i \mathbf{r})} (1 + \sqrt{R} e^{i(\phi - 2\pi \mathbf{h}\mathbf{r})}). \tag{2.15}$$

The normalized intensity (I_{XSW}) associated with the XSW field is equal to $\mathscr{E} \cdot \mathscr{E}^* / E_i^2$, and thus

$$I_{XSW} = |1 + \sqrt{R} e^{i(\phi - 2\pi \mathbf{h}\mathbf{r})}|^2 = 1 + R + 2\sqrt{R} \cos(\phi - 2\pi \mathbf{h}\mathbf{r}). \tag{2.16}$$

The scalar product **hr** describes the spatial modulation of the XSW field. In the direction normal to **h** its intensity is constant. When **r** is parallel to **h**, the XSW field is periodically modulated with spacing d_{hkl}, being d_{hkl} the distance between two consecutive Bragg planes. It results that $\mathbf{hr} = \frac{z}{d_{hkl}}$, with z the atomic position.

In the simplest case, one absorber atom has a finite position z. However, thermal vibrations and possible disorder at the surface lead to a distribution of $f(z)$ with $\int_0^{d_{hkl}} f(z)dz = 1$. Accordingly, I_{XSW} transforms into

$$I_{XSW} = 1 + R + 2\sqrt{R}\int_0^{d_{hkl}} f(z)\cos(\phi - 2\pi\frac{z}{d_{hkl}})dz. \tag{2.17}$$

This can also be written as

$$I_{XSW} = 1 + R + 2F^H\sqrt{R}\cos(\phi - 2\pi P^H), \tag{2.18}$$

defining two important parameters, the Coherent Position P^H and the Coherent Fraction F^H. These parameters are related to the Fourier transform $\widetilde{f}(\mathbf{h})$ of $f(z)$, $\widetilde{f}(\mathbf{h}) = \int_0^{d_{hkl}} f(z)e^{-2\pi i\frac{z}{d_{hkl}}dz}$. Both of them, by definition, have values between 0 and 1. F^H indicates the vertical spread of an atom having a certain P^H. $P^H = \frac{z}{d_{hkl}}$ indicates the average position of the absorber with respect to the nearest Bragg plane below. The vertical distance z of the absorber is then calculated by

$$z = (P^H + n)d_{hkl}, \tag{2.19}$$

where n is any integer number. Note that the values of $(P^H + n)$ and P^H are not distinguishable since P^H is the argument of a cosine function (Eq. 2.18). As a consequence, the absolute position of the absorber from the surface is not determined, but only its vertical position with respect to the extended Bragg plane underneath. Usually, this is not a problem as only one physically meaningful result is possible. The reader can find an example of it in the determination of the vertical distances of the graphene layer and Ge intercalation with respect to the top Si atoms of SiC in Chap. 5.

In the experiments reported in this thesis, the scattering channel for the XSW technique is the photoemission (photoelectron scattering). In the previous Sec. 2.1, we

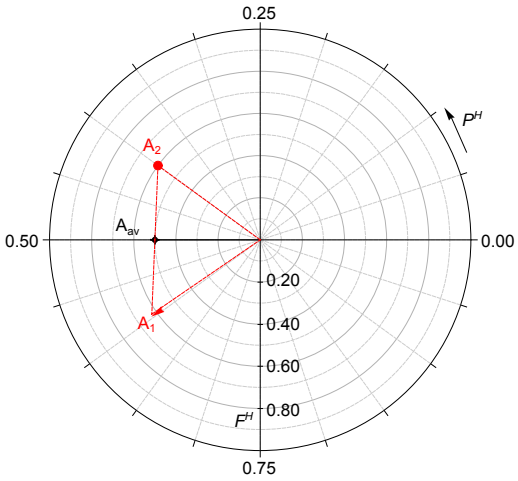

Figure 2.3: Example of the Argand diagram in which the average of P^H_{sum}=0.5 and of F^H_{sum}=0.5 of the species A is represented by the black dot (A_{av}). The last is split in two components: A_1 and A_2.

demonstrated that the transition probability from initial to final state is proportional to the transition matrix element $\langle \Phi_f^k | \mathbf{A} \cdot \mathbf{p} | \Phi_i^k \rangle$. In the electric dipole approximation, only the first (constant) term ($\mathbf{A}_0$) of the Taylor expansion of $\mathbf{A}$ is considered and thus $\mathbf{A} = \mathbf{A}_0$ is no longer a function of the position on the length scale of the initial state orbital of the photoexcited electron. This amounts to neglecting the spatial distribution of the electron in its initial state orbital. As a consequence, the photoelectron yield becomes proportional to the intensity of the standing wave as given by Eq. 2.18 at the position of the scatterer. Accordingly, for each species the integrated photoelectron signal (photoelectron yield (EY)) is taken as a measure of the XSW intensity (I_{XSW}). In practice, P^H and F^H of a species are determined by fitting the corresponding EY curve using Eq. 2.18. The influence of higher order multipole terms (electric quadrupole and magnetic dipole transitions) on the total EY remains usually small. However, in the situation of wavelenghts of the same order of magnitude as initial state orbital, the electric quadrupole term becomes important and the vector potential $\mathbf{A}$ cannot be treated as constant. As a consequence, the emitted photoelectron has a different angular distribution for the incoming and reflected beam. Vartanyants *et al.* derived the general form of the EY $\approx I_{XSW}$ considering multipole terms in the expansion of the vector potential $\mathbf{A}$ [23]. They introduced the forward/backscattered asymmetry parameter Q defined

as

$$Q = \frac{\gamma}{3}\cos(\theta) \tag{2.20}$$

where γ is the angular distribution parameter calculated in the quadrupole approximation [24, 25], and θ is the angle between the photoemitted electrons and the wave vector $\mathbf{k}_h$. When taking into account non-dipolar corrections, Eq. 2.18 transforms into

$$I_{XSW} = 1 + S_R R + 2|S_I|F^H\sqrt{R}\cos(\phi - 2\pi P^H + \psi), \tag{2.21}$$

with S_R, $|S_I|$ and ψ being dependent on Q

$$S_R = \frac{1+Q}{1-Q}, |S_I| = \frac{\sqrt{1+Q^2\tan(\Delta)}}{1-Q}, \psi = \arctan(Q\tan^2(\Delta)). \tag{2.22}$$

The Δ term represents the difference between the partial scattering wave shifts obtained asymptotically for $p-$ and $d-$ waves available from calculations [26]. Artificial values of P^H and F^H above the limit (> 1) are often found when non-dipolar corrections are not taken into account in situations where they should be taken into account, *i.e.* the EY curves are not fitted using Eq. 2.21. However, for a 90° geometry between the x-ray beam and the analyzer non-dipolar corrections vanish [23, 27]. In this work, this geometry set-up is employed, but vales of F^H above 1 are still detected due to the large acceptance angle of the analyzer. The reader can find more information regarding this topic in Sec. 3.4.1.

For the interpretation of the results, it is useful to plot the P^H and F^H values in a polar plot called Argand diagram. F^H represents the radius while P^H represents the polar angle. In cases where a species is arranged in more than one position at the surface, the measured P^H and F^H stand for the vector sum which we call P^H_{sum} and F^H_{sum}. The last two terms are interpreted as the sum of all P^H_k and F^H_k of the species in the k positions. One way to derive the absolute P^H_k and F^H_k values of each k position is to develop a structural model consisting of k components which satisfy the sum (for k=2)

$$F^H_{\text{sum}}e^{-2\pi i P^H_{\text{sum}}} = (a_1 F^H_1 e^{-2\pi i P^H_1} + a_2 F^H_2 e^{-2\pi i P^H_2}), \tag{2.23}$$

where a_1 and a_2 represent the quantity of the species in the $k = 1$ and $k = 2$ positions. The quantities a_1 and a_2 are normalized such that $\sum_{k=1}^{2} a_k = 1$. This method can well be visualized in the Argand diagram shown in Fig. 2.3. The black point is represented by P^H_{sum}=0.5 and F^H_{sum}=0.5 of the $\mathrm{A_{sum}}$ species which can be split in two components, $\mathrm{A_1}$ and $\mathrm{A_2}$. For simplicity, the abundance of the species A in the two layers is considered equal ($a_1 = a_2 = 0.5$). This method is applied in Chap. 5 to analyze XSW data regarding Ge-QFMLG on 6H-SiC(0001).

2.3 Near Edge X-ray Absorption Fine Structure (NEXAFS)

A complementary technique to photoelectron spectroscopy is x-ray absorption fine structure spectroscopy. Whereas the photoemission measurements probe the occupied states of the material, the absorption measurements provide an energy-resolved picture of the unoccupied density of states. The NEXAFS technique was developed in the 1980s with the goal of elucidating the structure of molecules bonded to surfaces, in particular low-Z molecules. This method requires a tunable monochromatic light source as well as high intensity and energy resolution. Synchrotron radiation sources are well suited for NEXAFS spectroscopy.

In contrast to XPS, the x-ray photon energy is scanned over a core-level absorption near edge (50-100 eV above the core level ionization) in order to investigate fine structures associated with resonant transitions from core levels into excited states of the material. After the emission of the photoelectron (Fig. 2.1(b)), the system relaxes back to the equilibrium state. The photo-generated hole is filled by an electron from a higher shell either radiatively by emission of a fluorescent photon, or non-radiatively by emission of an Auger electron (Fig. 2.1(c,d)). In the limit of small adsorbate concentrations, the number of photons absorbed in the layer is defined as

$$N_{abs} = IA(1 - e^{-\sigma(h\nu)\rho}) \approx IA\sigma\rho, \tag{2.24}$$

where I in the incident photon flux density, A is the area exposed to the beam depending on the x-ray incident angle, ρ is the atomic area density and σ is the

x-ray absorption cross section [28]. An in-depth derivation of the absorption cross section was presented by Stöhr, and we refer the reader to his work for further information [29]. By definition, the absorption cross section can be written in general as

$$\sigma = \frac{P_{if}}{F}, \tag{2.25}$$

where F is the photon flux given by the energy flux of the electromagnetic field divided by the photon energy, and P_{if} is the transition probability per unit time from the initial state Ψ_i^N to the final state Ψ_f^N. The mathematical treatment of P_{if} can already be found in Sec. 2.1. With this result, the cross section can be written as

$$\sigma = \frac{A^2 c}{8\pi\hbar\nu}\frac{2\pi e}{mc\hbar}\left|\left\langle\Phi_f^k\right|\mathbf{A}\cdot\mathbf{p}\left|\Phi_i^k\right\rangle\right|^2\delta(E_f + E_i - h\nu) \tag{2.26}$$

where A is the magnitude of the vector potential $\mathbf{A}$.

The understanding of the resonances which dominate an x-ray absorption spectrum of π conjugated systems requires basic knowledge of molecular orbital theory. Although the calculation of the detailed resonance positions and intensities necessitates the initial and final wavefunctions, there are some simple symmetry considerations that can be made to facilitate the interpretation of the spectra. For K-shell excitations (of interest here) the initial 1s state is always of σ symmetry while the final state allowed by the dipole selection rule has to contain a p-orbital component and may be of σ or π symmetry. An orbital is of π symmetry (σ symmetry) when its rotation with respect to the molecular axis does (does not) result in a phase shift. There exist σ^* resonances when the electron is excited from the 1s core level to a σ antibonding orbital, and π^* resonances when the electron is excited from the 1s core level to a π antibonding orbital. Since NEXAFS transitions are governed by the dipole selection rule, the absorption cross-section shows a polarization dependent angular anisotropy. By rotating the sample, it is therefore possible to vary the direction of the incident light with respect to the sample normal, and thus to determine the orientation of molecular adsorbates.

In the case of polarized incident light, i.e. synchrotron radiation, the vector potential $\mathbf{A}$ in Eq. 2.26 can be written as a time-dependent electromagnetic wave of wave

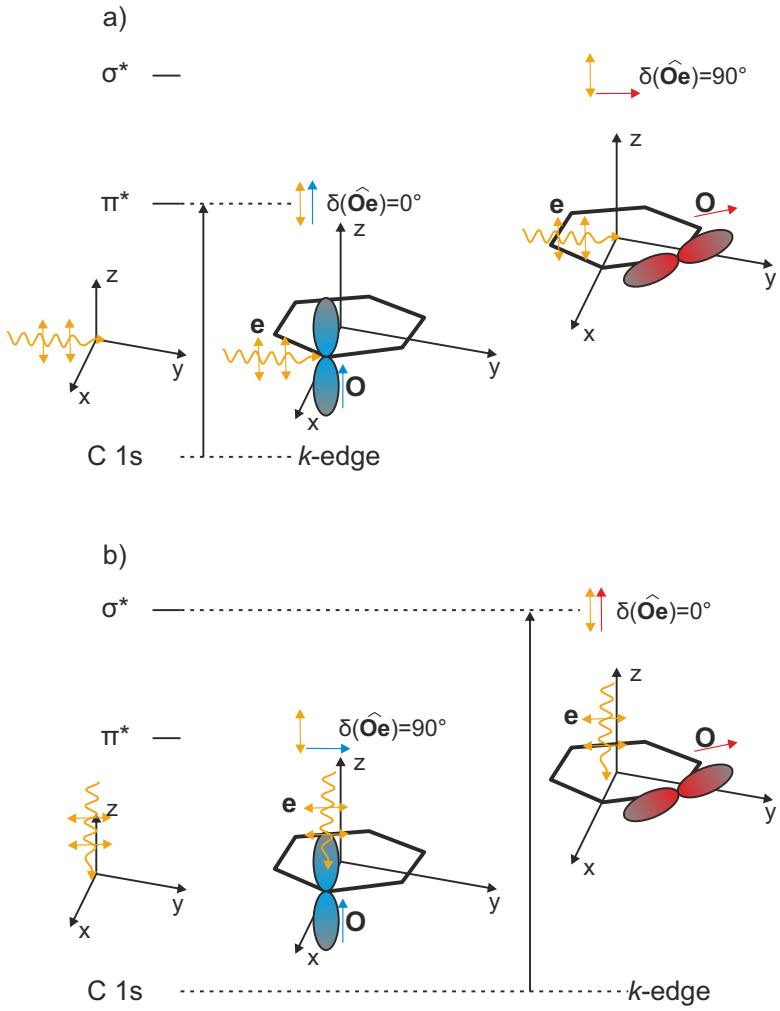

Figure 2.4: The representation of the π^* and σ^* resonances of graphene are shown. The incident light is characterized by the electric field vector **e** while the direction of the final state orbital is indicated with **O**. The angle between them is δ. In a) the incident light is in the xy-plane. As the orbital component **O** of π symmetry is parallel to **e**, a transition from the C 1s core levels to the unoccupied π^* orbitals occurs ($\delta(\hat{\mathbf{Oe}}) = 0°$). In b) the incident light is directed on the z-direction. As the orbital component **O** of σ symmetry is parallel to **e**, a transition from the C 1s core levels to the unoccupied σ^* orbitals occurs ($\delta(\hat{\mathbf{Oe}}) = 0°$).

vector $\mathbf{k}$, unit vector $\mathbf{e}$ and frequency ω such that $\mathbf{A} = \mathbf{e}A\cos(\mathbf{kx} - \omega t)$. Hence, the cross section can be approximated as

$$\sigma \simeq |\left\langle \Phi_f^N | \mathbf{A} \cdot \mathbf{p} | \Phi_i^N \right\rangle|^2 \simeq |\mathbf{e}\left\langle \Phi_f^N | \mathbf{p} | \Phi_i^N \right\rangle|^2 \approx |\mathbf{e} \cdot \mathbf{O}|^2 \approx \cos^2(\delta), \tag{2.27}$$

with δ being the angle between the electric field vector $\mathbf{e}$ and $\mathbf{O} = \left\langle \Phi_f^N | \mathbf{p} | \Phi_i^N \right\rangle$, a vector which, for a non-directional 1s initial state orbital Φ_i^N, specifies the directionality of the final state orbital Φ_f^N. As in common case the direction of $\mathbf{O}$ is described through a polar and azimuthal angle, at least two NEXAFS spectra acquired at different azimuthal angles are necessary in order to determine the orientation of molecular adsorbates. However, for three-fold or higher molecular symmetry, of interest here, the intensity of the resonance is considered constant in the azimuthal direction due to formation of surface-induced equivalent in-plane geometries, and thus only the polar angle is varied during the experiments. In Chap. 7, an example of strong angular dependent resonances is provided by a monolayer of graphene oriented parallel on a surface. For the sake of simplicity only an isolated carbon ring is shown in Fig. 2.4. The σ^* orbitals have a maximum orbital amplitude along the bond axis (xy-plane) while the π^* orbitals have maximum amplitude normal to the bond direction (z-direction). The π^* resonance intensity is largest when the electric field vector lies along the z-direction of the π final state molecular orbital ($\sigma \approx \cos^2(\delta = 0°) \approx 1$) and vanishes when $\mathbf{e}$ is perpendicular to $\mathbf{O}$. The same applies to the σ^* resonance intensity. As the electric field vector lies in the xy-plane, the σ^* resonance will have an intensity maximum.

2.4 High-Resolution Electron Energy Loss Spectroscopy (HREELS)

The HREELS technique is a powerful tool in the field of vibrational spectroscopy applied to chemical analysis. The technique is based on the detection of electron energy losses when electrons are inelastically scattered on matter. In 1967, the first reported application to a solid surface demonstrated the possibility to measure vibrations of molecules with high sensitivity but relatively poor resolution ($\approx$ 100 cm^{-1}) [30]. The achievement of high resolution, due to the improvements of the instrument design, led to rapidly growing interest in HREELS as a surface science technique [31, 32].

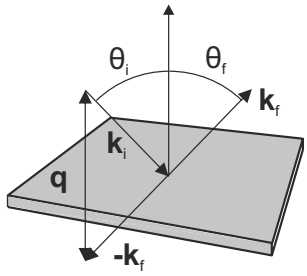

Figure 2.5: Scattering geometry of an electron (incoming and outgoing wave vector $\mathbf{k}_i$ and $\mathbf{k}_f$ respectively) from a surface excitation (wave vector $\mathbf{q}$). The incident and scattering angles are θ_i and and θ_f, respectively.

When an electron approaches a surface, it interacts inelastically with the atomic electron distribution via short range interactions. However, in the presence of fluctuating charges at the surface, such as vibrating dipoles, the electron also experiences their electric field outside the crystal via long range Coulomb interactions. The potential of the excitation can be approximated by

$$\phi \approx \mathrm{e}^{-\mathbf{q}_{||}|z|}, \tag{2.28}$$

with $\mathbf{q}_{||}$ being the parallel component of the excitation wave vector $\mathbf{q}$ (see Fig. 2.4). Hence, the z range of the potential is determined by the inverse of the wave vector of the excitation ($z \approx \mathbf{q}_{||}^{-1}$). In the situation of scattering angles close to the specular reflection direction, the z range of the potential is of the order of few hundred Å. This indicates that the electron spends a much smaller fraction of its time in the vicinity of the surface than within the region outside, where the fluctuating field is large, and therefore it interacts mainly via the long range interaction. Consequently, dipoles which extend out of the surface contribute more to the scattering process than dipoles parallel to the surface. As the moving electron interacts with the dipole field in the dipole scattering mechanism, the HREELS spectrum is governed by the dipole selection rule; thus, only Infrared (IR) active modes, which produce a dynamic dipole moment $\boldsymbol{\mu}$, will be excited.

Several theoretical formulations have been made to describe the interaction in the dipole scattering regime. As the semi-classical theory developed by Lucas *et al.* received remarkable confirmation, here we will briefly discuss the main points, referring the reader to the original articles for more detailed information [33, 34]. Considering the electron as a particle moving in a classical trajectory, the probability ($P(\omega)$) that an electron loses the energy $\hbar\omega$ ($\hbar\omega <$ impact energy) by creation

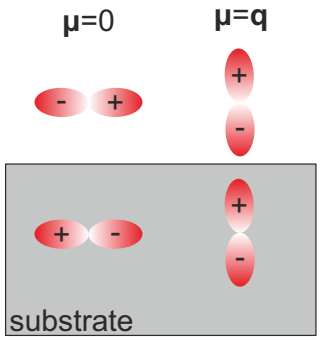

Figure 2.6: Representation of the surface selection rule. The dynamic dipole moment $\boldsymbol{\mu}$ is expressed as partial charges (+/-).

of one surface excitation at 0 K is expressed by

$$P(\omega) = \frac{4e^2}{\hbar\pi^2} \int_D d^2q_{||} \frac{q_{||}v_\perp^2}{[(\omega - \mathbf{q}_{||}\mathbf{v}_{||})^2 + q_{||}^2 v_\perp^2]^2} \times \mathrm{Im}\frac{-1}{\varepsilon(\mathbf{q}_{||},\omega)+1}. \tag{2.29}$$

The first part of the expression of $P(\omega)$ depends on $\mathbf{q}_{||}$ and on the electron velocity $(\mathbf{v}_{||}, v_\perp)$. The integration D selects the portion of the dipolar lobe close to the specular reflection trajectory that intersects the detector. The second factor of the integrand defines the spectral shape of the HREELS spectrum and contains the effective dielectric function $\varepsilon(\mathbf{q}_{||},\omega)$. As in this work we are interested in studying vibrations of adsorbed layers on crystals, the latter quantity can be divided into two components $\varepsilon(\mathbf{q}_{||},\omega) = \varepsilon_1(\mathbf{q}_{||},\omega) + \varepsilon_2(\mathbf{q}_{||},\omega)$. $\varepsilon_1(\mathbf{q}_{||},\omega)$ contains ε_{bulk} and describes the interaction outside the crystal between the electric field produced by the atoms in the bulk crystal and the electrons. $\varepsilon_2(\mathbf{q}_{||},\omega)$ contains both ε_{bulk} and ε_{layer} and describes the electron scattering by the field produced by the dipoles in the absorbed layer and by their images in the substrate. As a consequence, the total oscillating dipole moment $\boldsymbol{\mu}$ parallel to the surface of the molecule/substrate system vanishes in the dipole regime because the image dipoles produced in the substrate are anti-parallel to the real ones. Therefore, in the dipole scattering regime, only those vibrations that give rise to dipole changes perpendicular to the surface will be observed in HREELS. A schematic representation of the principle of the surface selection rule is shown in Fig. 2.6.

If HREELS was restricted to the dipole scattering regime, its application in surface science would be limited. In a famous paper, Ho *et al.* reported the observation in the HREELS spectrum of vibrations parallel to the surface when electrons were detected at angles far away from the specular direction [35]. According to the surface selection rule, such modes are dipolar forbidden, so that another mechanism must

exists. This mechanism is called impact scattering. Considering larger scattering angles, the distance $z \approx \mathbf{q}_{||}^{-1}$, at which the electron interacts, becomes only few Å from the surface. Hence, the scattering process is due essentially to short range interactions involving large momentum transfers (short wavelength surface excitations). One immediate consequence is related to the image dipole: the scattering electron is so close to the surface that it does not 'see' the image dipole anymore, and interacts also with dipoles parallel to the surface. In principle, all modes are allowed. However, there exist impact scattering selection rules, for which further information can be found in Ref. [31, 32]. From the theoretical point of view, impact scattering requires to introduce a precise physical description of a crystal surface as well as a description of multiple scattering. Classical and/or semi-classical approaches fail, and a more complex quantum-mechanical theory must be considered. However, within this work, e.g., Chap. 8, spectra from impact scattering regime were only used in comparison with those acquired in the dipole scattering regime to study the symmetry of the Phthalocyanine (Pc) molecules/substrate complexes. Therefore, we omit the derivation of the selection rules for the impact scattering regime, and we refer the reader to the work of Mills [36].

3 Sample Details and Experimental Set-Ups

3.1 Graphene

Within this thesis, graphene-based materials are the central topic in Chap. 4, 5, 6 and 7. The modification of the graphene structural and electronic properties upon contact with a substrate and upon substitutional doping have been investigated. The basic structure, properties and applications of graphene, with specific focus on epitaxial graphene on SiC, will be introduced in the following to prepare the ground for the reader.

3.1.1 Literature

Since the isolation of graphene −a two-dimensional sheet of sp^2-bonded carbon− in 2004, intense scientific attention has focused on graphene [1]. In their paper Novoselov, Geim and co-workers were able to demonstrate some of its extraordinary electrical properties in addition to the possibility of obtaining a single honeycomb lattice layer by mechanical exfoliation of a graphite crystal. Strong ambipolar electric field effect, large carrier mobility and precise tunability of charge carrier concentrations were some of the reported peculiar properties. Since then, other interesting features have been discovered, e.g., room temperature quantum Hall effect and ballistic charge transport [37, 38]. Because of all these characteristics, graphene has potential applications in high frequency field effect transistors, nanoscale electrical interconnections, optoelectronics and radio frequency devices [39, 40].

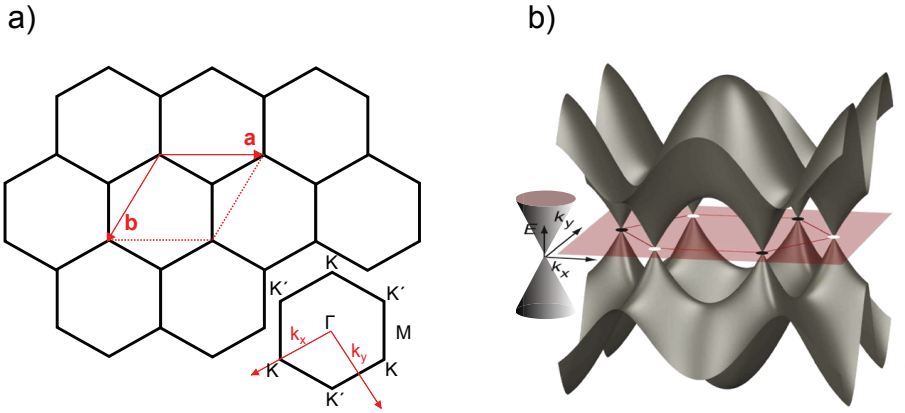

Figure 3.1: (a) The graphene primitive unit cell is defined by the vectors **a** and **b**. The angle between them is 120°. The Brillouin zone of graphene is highlighted at the bottom. (b) The image shows the graphene full energy dispersion. The linear dispersion of the electron energy vs momentum at the K point is illustrated in the inset. The Fig.(b) is adapted with permission from Ref. [41] Copyright 2008 by American Physical Society.

3.1.2 Electronic Properties

The origin of the above mentioned properties is attributed to the unique graphene electronic and crystallographic structure. In Fig. 3.1(a), the two-dimensional hexagonal carbon lattice is shown. Each carbon atom assumes an sp^2 configuration and is bonded to three nearest carbon atoms through three σ bonds. The remaining electron, located in the $2p_z$ orbital, produces an out-of-plane π bond. The primitive unit cell is formed by the vectors **a** (along the [100] direction) and **b** (along the [010] direction), forming an angle of 120° between them and contains two chemically equivalent but symmetrically inequivalent atoms. The Brillouin zone of graphene is highlighted at the bottom of Fig. 3.1(a) showing the Γ, M and K (K') points. The dispersion relation, produced using the tight-binding model, between the electron energy and the momentum **k** in graphene is represented by the equation

$$E(\mathbf{k}) = \pm t\sqrt{1 + \cos^2(\frac{\mathbf{k_y}a}{2}) + 4\cos(\frac{\mathbf{k_x}a\sqrt{3}}{2})\cos(\frac{\mathbf{k_y}a}{2})}, \tag{3.1}$$

where $t \approx 2.8$ eV is the nearest neighbor hopping energy, and $a \approx 2.46$ Å is the

lattice constant. The valence (π) and conduction (π^*) bands have opposite sign of E. In the vicinity of the K and K' points, the dispersion equation is reduced to

$$E(\mathbf{k}) = \pm v_F \hbar \sqrt{\Delta \mathbf{k_y}^2 + \Delta \mathbf{k_x}^2} \tag{3.2}$$

where $v_F \approx 10^6$ m/s is the Fermi velocity. The last equation shows the linear conical dependence of the energy on the momentum, which is responsible for the peculiar electronic properties of graphene (Fig. 3.1(b)). As the same behavior is observed for the chiral massless Dirac particles, the K and K' points are called Dirac points. Ideally, the Dirac point energy (E_D), measured at the K point, is at E_F. However, due to the interaction with a substrate, E_D of the graphene layer may show a shift. The graphene layer becomes n-type doped when E_D is downshifted with respect to E_F and is p-type doped when E_D is above E_F. This can be well visualized in ARPES experiments, and throughout the thesis the reader will encounter numerous examples (Chap. 4.3, 5 and 6).

3.1.3 Synthesis

Regarding the production of a graphene monolayer, nowadays it can be obtained via different preparation techniques. More than ten years ago, it was first isolated by using scotch tape to mechanically exfoliate graphite [1]. This method produces high quality layers of graphene, but it is limited to a research level customers. On the other hand, graphene produced by liquid phase exfoliation can be adapted to large scale fabrication, but the layer quality is not high enough for electronics applications [42]. Another possibility consists in the production of the layer via chemical vapor deposition [39]. This technique allows the creation of graphene on different metallic substrates with consequent alteration of its electronic properties. For example, the ARPES measurements of the graphene layer grown on Co(001) shows an n-type doping [43], while graphene on Au/Ru(001) shows a p-type doping [44]. Although chemical vapor deposition allows to grow a graphene layer on many and different substrates, it might introduce some contamination in the layer during the synthesis due to the use of precursors.

3.1.4 Epitaxial Growth on SiC

An intermediate solution between large scale production and layer quality is the epitaxial growth of a graphene layer on the 6H-SiC(0001) substrate, used in this work. In the following, a description of this preparation method is provided based on Ref. [45]. The graphene layer is obtained by thermal decomposition via sublimation of the Si atoms of SiC. Consequently, the carbon atoms at the surface arrange in a honeycomb-like structure. The first produced carbon layer cannot properly be called graphene, because it does not show the linear dispersion around E_F. In fact, this layer, called BL, is the known C-rich $(6\sqrt{3}\times 6\sqrt{3})R30°$ reconstruction of SiC in which part of the carbon atoms is covalently bonded to the silicon atoms at the surface, and thus, shows an sp^3-hybridization [46]. As more silicon atoms sublimate, a second buffer layer grows underneath and allows the decoupling of the previous one from the surface, hence the graphene formation. When the sample is grown in Ar atmosphere, the layer shows a high degree of uniformity. In contrast, as the sublimation of the Si atoms in Ultra-High Vacuum (UHV) is more difficult to control, the corresponding layer quality is reduced. A sample in which the graphene layer is decoupled from SiC by the BL is known as EMLG. Due to the presence of this carbon structure at the interface, the layer shows an n-type doping. Its structural and electronic properties are investigated in Chap. 4 and 6.

Another way to obtain a graphene layer on 6H-SiC(0001) consists in intercalating atomic species underneath the BL. For example, hydrogen or germanium atoms can saturate the silicon dangling bonds at the surface, lifting the buffer layer which becomes a proper graphene layer. The decoupling of the graphene layer from SiC by intercalation is more efficient compared to EMLG, and the graphene layer shows properties close to the freestanding situation. Structures and electronic properties of both H-QFMLG and Ge-QFMLG are presented in Chap. 4, 5 and 6.

3.2 Phthalocyanine

Within this work, we have chosen PdPc and PtPc molecules to study the properties of organic-metal interfaces. As their vibrational and structural properties are investigated in Chap. 8, in the following the past literature of metal-Pc adsorbed on metallic surfaces will be reviewed as well as details regarding their theoretical vibrational frequencies will be provided.

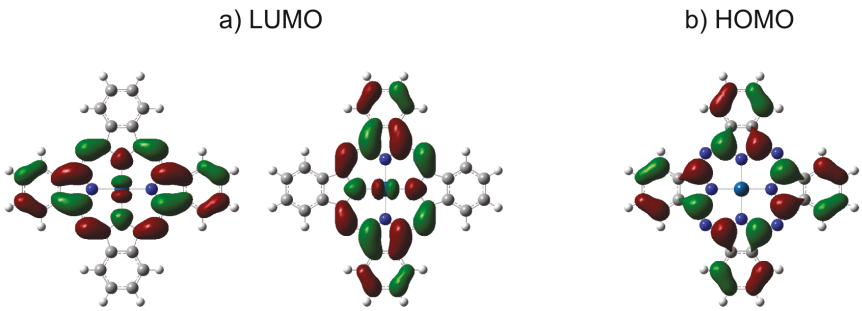

Figure 3.2: (a) The LUMO and (b) HOMO orbitals of the Pc molecule calculated using the LanL2DZ basis set and the B3LYP functional.

3.2.1 Structure

A Pc molecule consists of four pyrrolic groups, bonded through nitrogen atoms, at which four phenyl groups are attached. The inner cavity can be filled by coordination of metals. The chemistry of phthalocyanine is a field which received great interest during the past decades because of the versatility of these molecules. Complexes are formed with most of the elements of the periodic table, and depending on the nature of the central metal as well as of the possible ligands, the reactivity, electronic and structural properties vary, allowing the molecules to be suitable in many applications [15, 47].

3.2.2 Two-Dimensional Ordering

A major research field is focused on the supramolecular ordering of Pc molecules when adsorbed on substrates and related properties. Gottfried reviewed the past literature of Pc molecules, and a brief introduction, based on his work, will be provided [16]. All metal-Pc molecules are able to form long range ordered two- and three-dimensional structures on surfaces. Since the first structural study of Pc layers on the copper substrate appeared in the literature [48], a large variety of molecules on different substrates have been investigated. In general, they adsorb with the molecular plane parallel to the surface and assemble according to the nature of the substrate. On weakly interacting substrates, such as oxides, the growth of the second layer may occur before the full monolayer is formed [49–51]. On metallic surfaces, the structural behavior depends on the balance between van der Waals

forces and repulsive interaction. In the submonolayer range, gas-phase like structures are observed due to molecular repulsive interactions, while at higher coverages a continuous shrinking of the unit cell is detected by increasing the coverage [52, 53].

3.2.3 Vibrational Properties

Also the vibrational properties of Pc layers on metals depend on the interaction at the interface. For example, HREELS measurements of FePc on Ag(111) report a considerable red shift of vibrational energies compared to calculations suggesting a strong layer/substrate interaction due to the presence of a covalent bond between the metal and the crystal [54]. Strong interaction at the interface is also found for ZnPc on Ag(110) and Ag(100), as suggested by the presence of raman modes in the HREELS spectrum of a monolayer [55, 56]. In contrast, the absence of frequency shift of vibrational peaks in, for example, CuPc on Au(100) shows that the interface is free of chemical interaction [57].

3.2.4 PdPc and PtPc

Since in this work we are interested in the vibrational properties of PdPt and PtPc on Ag(111), DFT calculations of the isolated PdPc and PtPc molecules were performed using GAUSSIAN [58] in order to calculate the molecular orbitals and the vibrational eigenfrequencies. The calculations were performed using the LanL2DZ basis set and the B3LYP functional. This basis set is chosen as it applies to transition elements (Pd and Pt), while the functional performs satisfactorily for organic molecules as reported in the literature [59]. The oxidation state of the central atom in metal-Pc is +2. Most of the metals with d orbitals have radii which match the available space between the coordinating nitrogen atoms, and thus, the molecule is planar. PdPc and PtPc are planar and belong to the D_{4h} symmetry group. Under this symmetry group, the d orbitals of the central metal transform into three non-degenerate (d_{xy}, d_{z^2}, $d_{x^2-y^2}$) and one degenerate energy levels (d_{xz}, d_{yz}). The orbitals with the lowest (d_{xy}) and highest ($d_{x^2-y^2}$) energies are confined in the molecular plane, while the other three are projected perpendicular to the molecule. Normally, the interaction between the molecules and the metal substrate, on which they are absorbed, decreases as the d orbitals fill [16]. Pd ($[Kr]4d^{10}$) and Pt ($[Xe]4f^{14}5d^{9}6s^{1}$) have fully (or almost) occupied d orbitals, and hence, we expect weak interaction

with the substrate. These metal orbitals mix to a different degree with the 2p states of C and N forming the molecular orbitals. The Highest Occupied Molecular Orbital (HOMO) and Lowest Unoccupied Molecular Orbital (LUMO) of the Pc molecules of interested here (Fig. 3.2) are represented by the A_{1u} and $2E_g$ delocalized orbitals with marginal contribution of the metal states. The LUMO is doubly degenerate.

Regarding the vibrational properties, PdPc and PtPc possess 165 vibrational modes classified according to their vibrational representation $\Gamma_{vibr} = 14A_{1g} + 13A_{2g} + 14B_{1g} + 14B_{2g} + 26E_g + 56E_u + 8A_{2u} + 6A_{1u} + 7B_{1u} + 7B_{2u}$. The A_{2u} and E_u modes, producing a dynamic dipole moment $\boldsymbol{\mu}$, are IR active modes. According to the surface selection rule explained in Sec. 2.4 and considering a flat adsorption geometry, the A_{2u} modes are excited by both dipole scattering and impact scattering because of the dipole along the z-direction (perpendicular to the surface). The E_u modes, producing a dipole in the xy-plane, are excited only by impact scattering. The rest of the modes are either non-active or produce only a change of the polarizability. The calculated vibrational frequencies of the isolated PtPc and PdPc accompanied by their corresponding assignments and symmetries are listed in Appendix A 11, while the experimental vibrational properties are investigated in Chap. 8.

3.3 Surface Phonons of Cu(111)

We have developed an own HREELS spectrometer coupled with a hemispherical analyzer with two-dimensional detector in order to reduce the experiment's acquisition time, and simultaneously to detect electrons with energy and angular resolution. Details about the spectrometer design and testing can be found in Chap. 9. In order to illustrate the features of this new design, the energy dispersion curves of Cu(111) are chosen as a test system. As they have already been extensively investigated, in the following a brief review of the past experiments will be examined.

3.3.1 Past Literature

The field of surface lattice dynamics has attracted great interest during the 1980s when it became possible to measure surface vibrations in a wide energy range as a

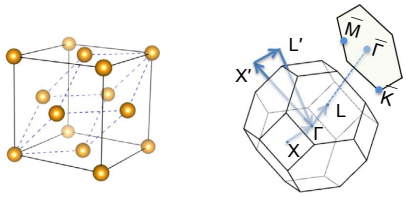

Figure 3.3: On the left side the face centered cubic lattice structure is shown. The first Brillouin zone of the bulk and of the surface projected onto the (111) surface is shown on the right side. The Fig. is adapted from Ref. [61] Copyright 2015, Rights Managed by Nature Publishing Group.

function of the wave vectors in the two-dimensional Brillouin zone. The nature of the surface vibrations depends strictly on the crystal symmetry and structure. The face centered cubic cell of the metal and the corresponding Brillouin zone projected onto the (111) direction together with the important points are shown in Fig. 3.3. The surface phonons differ from the bulk phonons as they are generated from the surface termination of the crystal structure, therefore giving information on the surface relaxation and presence of defects and adsorbates. Two complementary experimental methods for measuring the dispersion relations of surface phonons and surface resonances of clean and covered surfaces are Helium Atomic Scattering (HAS) and HREELS. While in HAS the resolution is higher and multiple scattering processes are absent, the HREELS technique allows to measure losses in a wider energy range [60].

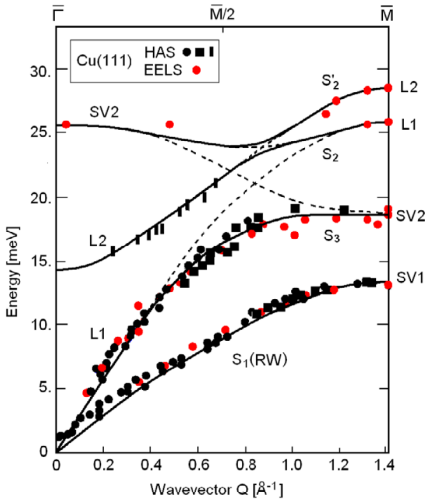

Figure 3.4: The calculated surface phonon density of states (full lines) of Cu(111) in comparison with the HAS (black symbols) and HREELS (red dots) data. The Fig. is adapted from Ref. [62], © IOP Publishing. Reproduced with permission. All rights reserved.

The first measurements of surface phonon dispersions date back to 1985 when Harten and co-workers raised excitement in the surface science community with their surprising results related to the (111) surfaces of Cu, Ag and Au [63, 64]. Using the HAS technique, a new bulk resonance (L_1) was detected in addition to the Rayleigh mode S_1(SW) (Fig. 3.4). Bortolani and co-workers thought that the only mechanism available to explain this unexpected perturbation was a modification of the bulk force constant. In fact, as a pseudo-mode embedded in the bulk continuum, this mode arises from substrate shear vibrations [65]. By reducing the lateral interactions by about 50% in the uppermost layer, they could reproduce this unexpected acoustic longitudinal mode L_1 [66]. Subsequent theoretical analysis explained this mode in Au and Cu as well as a weakening of the lateral forces of about 70%. The origin of this effect has been the subject of considerable speculation because of the absence of surface relaxation in the (111) surfaces of Ag and Cu. Bortolani attributed the surface force constant softening to a weakening of the s-d hybridization. However, those explanations appeared surprising for Mohamed and Hall, and a couple of years later, they performed off-specular HREELS measurements together with *ab initio* theoretical calculations of Cu(111) [64, 67]. Their HREELS phonon data were extended along the $\overline{\Gamma}\overline{\mathrm{M}}$ direction. The HREELS and HAS data at the $\overline{\mathrm{M}}$ point are in agreement on the acoustic longitudinal mode L_1 and on the Rayleigh mode S_1(SW). However, HREELS also reported the first experimental data of the band gap mode (S_2) found at around 26 meV at the $\overline{\mathrm{M}}$ point. As the frequency of this band gap mode can theoretically be reproduced only considering a lateral interaction reduction of less than 15%, the new HREELS data demonstrated that the lattice dynamics in the surface and bulk Cu(111) are very similar. Thus, the appearance of the anomalous bulk resonance is not related to a weakening of the lateral interaction, as suggested by Bortolani and followers, but is due to its hybridization with the optical surface mode S_3. Within this work, we are interested in measuring again the surface phonons of Cu(111) using HREELS, but with two-dimensional energy and momentum mapping as they are well-studied and show high intensity.

3.4 Experimental Details and Set-Ups

All the experiments of the graphene samples, investigated in this work, were performed in Synchrotron facilities. Specifically, the data presented in Chap. 4, 5 and 6 were acquired at the I09 Surface and Interface beamline of Diamond Light

Source (Didcot, United Kingdom). The experiments presented in Chap. 7 were carried out at the Material science beamline of Elettra Synchrotron (Trieste, Italy). The experimental data on the organic layers, presented in Chap. 8, were carried out in the HREELS laboratory (Forschungszentrum Jülich, Germany) while the 2D phonon dispersion curves of Cu(111) were measured in the ESCA laboratory (Forschungszentrum Jülich, Germany) (Chap. 9).

3.4.1 Surface and Interface Beamline

The ARPES and NIXSW experiments of BL, EMLG, H-QFMLG and Ge-QFMLG on 6H-SiC(0001) (Chap. 4, 5, 6) were carried out at room temperature and under UHV conditions at the I09 beamline, Diamond Light Source Synchrotron, Didcot, United Kingdom. The samples were prepared at the Max Planck Institute for Solid State Research in the group of U. Starke [45]. The beamline end-station is composed of two preparation chambers and one analysis chamber, as depicted in Fig. 3.5. The preparation chambers are equipped with Low Electron Energy Diffraction (LEED), a load lock, a Quadrupole Mass Spectrometer (QMS), ion sputter guns. The preparation chambers were used to outgass the samples and to dope (with nitrogen) the graphene layers.

The samples are transferred between the preparation chamber 1 and the analysis chamber with the use of a 5-axes manipulator. The analysis chamber is equipped with a VG scienta EW 4000 hemispherical electron analyzer with a 70 frame/sec CCD camera and having an acceptance angle of 60°. The angle between the analyzer optical axes with the x-ray beam is 90°. In the soft x-ray experiments, the beam provides a photon energy in the range of 100-500 eV and it is focused on the sample with an area of 40×20 μm^2. In the hard x-ray experiments, the beam provides a photon energy around 2400 eV and it is defocused on the sample surface with a size of 300×300 μm^2. By rotating the sample, the angles of the sample surface with the analyzer optical axes and x-ray beam can be varied during XPS. In the NIXSW experiments, the beam is directed on the sample surface in nearly normal incidence (about 88° with respect to the sample surface), allowing the simultaneous acquisition of the reflectivity and photoelectrons, as shown in the inset of Fig 3.5. The analysis chamber is also equipped with a monochromatized Ultraviolet (UV) lamp to perform ARPES measurements using the Helium Iα radiation (21.2 eV). The angle between the light and the analyzer optical axes is 45°.

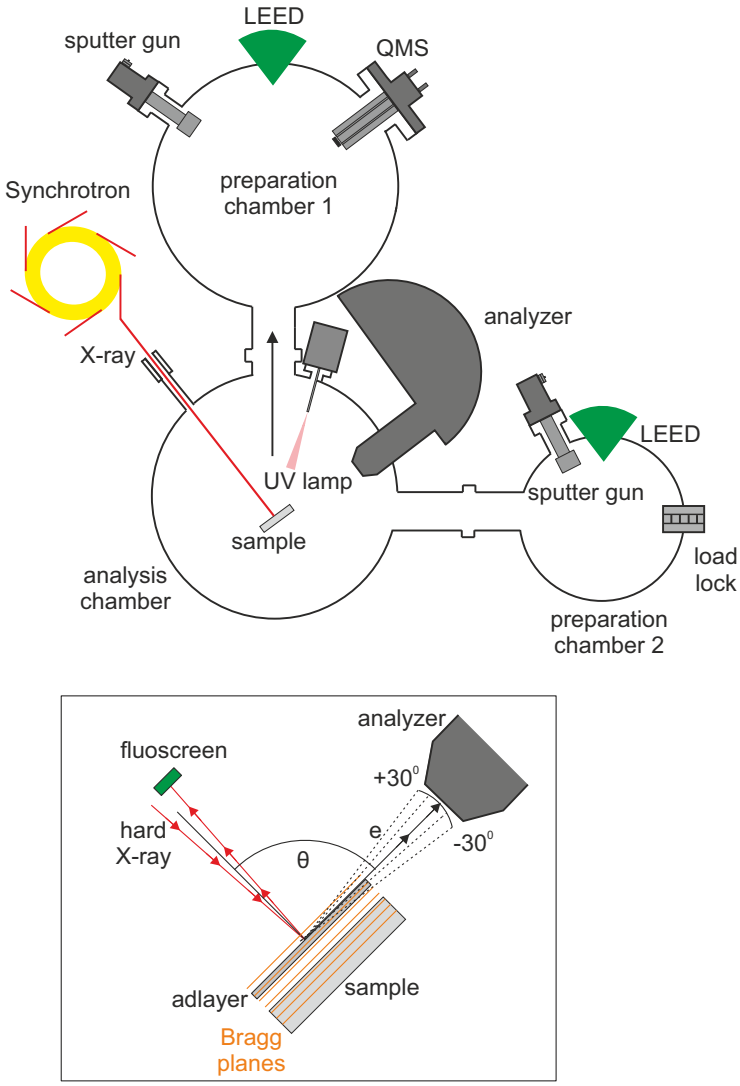

Figure 3.5: Schematic drawing of the UHV system present at the I09 beamline, Diamond Light Source, Didcot, United Kingdom. The preparation chambers are equipped with LEED, sputter guns and QMS. The analysis chamber is equipped with an EW 4000 hemispherical analyzer and a UV lamp. After the ondulators, the soft and hard x-ray beams pass through a grating plane and a Si(111) double crystal monochromator, and then are focused by a series of mirrors on the sample. The inset shows the geometry used for the NIXSW experiments. The angle between the x-ray beam and the analyzer optical axes is 90°. The analyzer collects the photoelectrons with an acceptance angle of 60°.

Regarding the analysis of the ARPES data, the 3D plot (Intensity, E_{kin}, θ) was transformed in **k** space according to Eq. 2.10 using a script developed in python. In the NIXSW experiments, the photon energy of the incoming x-ray beam is varied around the (*hkil*) reflection of the crystal. As the first useful reflection of 6H-SiC(0001) is the (0006) reflection (see Appendix B 12), the experimental reflectivity curve was obtained in a range of ± 2.5 eV around 2463 eV corresponding to the (0006) Bragg energy with $d_{0006} = 2.517$ Å, and was fitted in Torricelli software [68, 69]. Details about the calculation of the theoretical reflectivity of SiC are given in the Appendix B 12. At each photon energy, XPS spectra (C 1s, Si 2d, Ge 3d and N 1s) were acquired. The XPS spectra were fitted using CasaXPS software to extract EY [70]. The EY profiles were then fitted according to Eq. 2.18 using Torricelli software. Although a 90° geometry between the x-ray beam and the analyzer is employed, non-dipolar corrections must be taken into account to fit the EY curves due to the large acceptance angle of the analyzer (see Sec. 2.2). According to Eq. 2.20, $Q = \frac{\gamma}{3}\cos(\theta = 90 \pm 30°) \neq 0$, thus the EY profiles must be fitted using the general form of I_{XSW} (Eq. 2.21). One way to determine the asymmetric parameter Q is to prepare an incoherent layer for which $F^H = 0$ such that Eq. 2.21 is reduced to

$$I_{XSW} = 1 + \frac{1+Q}{1-Q}R. \tag{3.3}$$

Thus, by fitting the EY curves of the incoherent layer it is possible, in principle, to retrieve the parameter Q as a function of θ (R is known). Such studies have recently been performed in our group for several elements, including C 1s and N 1s. However, as this study is still in progress, non-dipolar corrections were not used in this work. As a consequence, the F^H values may be affected while the P^H values are barely influenced.

3.4.2 Material Science Beamline

The NEXAFS experiments of boron-doped EMLG on 6H-SiC(0001) (Chap. 7) were carried out under UHV conditions at the Material Science beamline, Elettra Synchrotron, Trieste, Italy. The beamline end-station (Fig. 3.6) is composed of a small preparation chamber, used only to insert the samples through the load lock, and of a main chamber equipped with LEED, an ion sputter gun, a boron e-beam evaporator, a Si-evaporator and a Specs Phoibos 150 hemispherical electron energy analyzer. The boron evaporator is a commercial e-beam (EFM3 from FOCUS GmbH) with a copper shroud cooled by water. Boron crystallites (<40 μm) of 90 % purity were

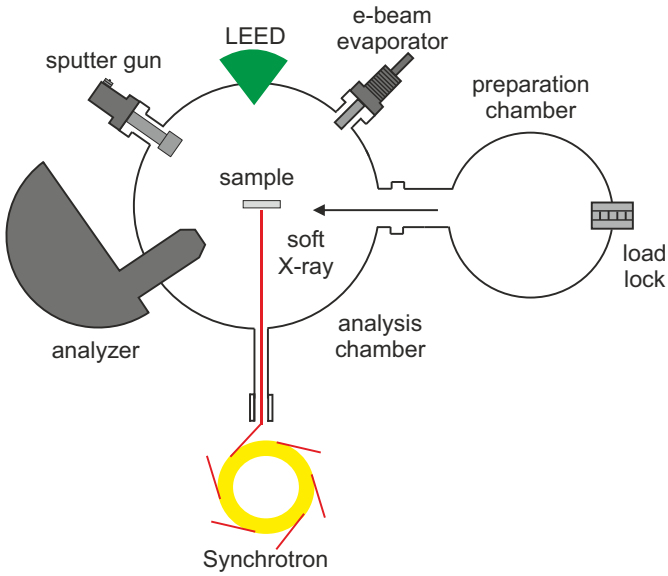

Figure 3.6: Schematic drawing of the UHV system present at the Material Science beamline, Elettra Synchrotron, Trieste, Italy. The analysis chamber is equipped with a Specs phoibos 150 hemispherical analyzer. The x-ray beam passes through a grating plane monochromator, which modulates its energy, and is focused on the sample by a series of mirrors.

evaporated from a graphite crucible heated at 1 kV corresponding to an emission current of 80 mA. The B-doped EMLG was prepared in the main chamber and in UHV atmosphere by thermal decomposition of SiC. Boron atoms were prior deposited on the Si-rich (3×3) reconstruction [71]. The detailed description of the preparation can be found in Chap. 7. The analyzer is mounted under an angle of 60° with respect to the x-ray beam. The NEXAFS (C K-edge and B K-edge) and XPS (C 1s, Si 2p and B 1s) spectra were recorded using an incident photon energy in the range of 150-400 eV. The measurements were performed in grazing incidence, in which the angle between the incident x-ray and the sample surface normal is 60° for XPS and 80° for NEXAFS, and in normal incidence geometry for NEXAFS only. Both XPS and NEXAFS spectra were analyzed using KolXPD software [72]. The energy was calibrated according to the Fermi edge. The NEXAFS spectra were divided by the mesh current (only B K-edge), and normalized by the curves measured for the clean sample.

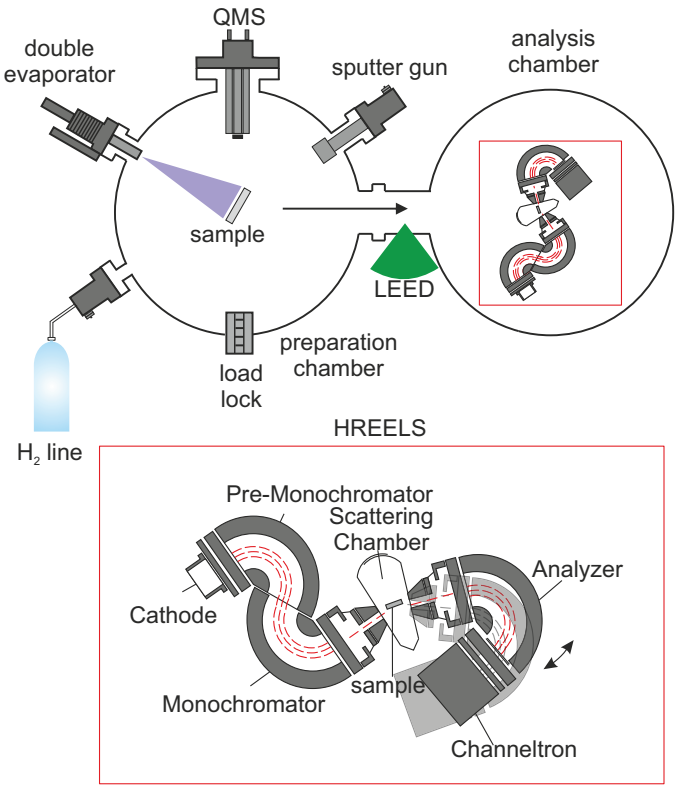

Figure 3.7: Schematic drawing of the UHV system present in the HREELS laboratory, Forschungszentrum Jülich, Germany. The preparation chamber is equipped with a sputter gun, a QMS, a double evaporator and a leak valve through which the H_2 gas flows. In the analysis chamber LEED and HREELS are present. At the bottom, a schematic representation of the Ibach-type HREELS spectrometer is provided.

3.4.3 HREELS Laboratory

The UHV system set-up shown in Fig. 3.7 was used to prepare and measure organic layers of PtPc and PdPc molecules on the Ag(111) crystal (Chap. 8). It is composed of a preparation chamber with a base pressure of 4×10^{-9} mbar, and an analysis chamber with a base pressure of 4×10^{-10} mbar, separated by a gate valve through which, without vacuum breaking, the Ag crystal is transferred. The preparation chamber is equipped with a load lock, a double evaporator containing the organic molecules, a QMS, an ion sputter gun and a leak valve connected to an H_2 line.

The PdPc and PtPc layers on Ag(111) were prepared in the preparation chamber

via thermal evaporation of molecules. The Ag crystal surface was prepared by cycles of Ar^+ ion sputtering at 1 keV, and subsequent annealing to 730 K. PdPc and PtPc powders were sublimated from a Knudsen cell evaporator equipped with a shutter, which enhances the control of the deposited material. The sublimation process was followed by monitoring the fragment 125 a.m.u. with the QMS. During the vaporization, the pressure in the chamber did not exceed 1×10^{-8} mbar. After reaching the respective temperatures for the various investigated molecules (770 K and 620 K for PdPc and PtPc respectively), a calibrated amount of molecules was deposited on the surface. The calibration was done based on the integrated area of the QMS signal over time. The H_2 exposure of the layers was performed by flowing the gas into the preparation chamber until the pressure reached 5×10^{-6} mbar. The exposures are measured in Langmuir (L) (the exposure for 1 s at the pressure of 10^{-6} mbar corresponds to 1 L).

The analysis chamber is equipped with LEED and HREELS. The LEED measurements were performed using an MCP-LEED and using a beam energy between 10 and 40 eV. A schematic drawing of the Ibach-type spectrometer used in this work is shown at the bottom of Fig. 3.7. The spectrometer consists of a cathode lens system, a double stage monochromator, a single stage energy analyzer and a channeltron electron multiplier detector. The electrons are first emitted from an LaB_6 cathod source which is encapsulated by a negatively charged, so called repeller, that prevents stray electrons from coming into the detector unit. The purpose of this system is to focus the beam on the entrance slit of the pre-monochromator unit and to get a high initial electron flux. The monochromators are done with cylindrical deflection analyzers to afford high resolution and serve to narrow the energy spread and to generate a highly monoenergetic beam of low-energy electrons. The beam then passes through accelerating and decelerating lenses for focusing the monochromated beam onto the sample and for focusing the reflected beam onto the entrance of the energy analyzer. The electron beam is sorted out by the single-stage energy analyzer into the detector. The analyzer is designed to be rotatable against the monochromator section around the scattering chamber, allowing different experimental geometries (for off-specular measurements).

The HREELS spectra were acquired with a primary beam energy of 6.3 eV and in the energy loss range of $-400 - 4500$ cm^{-1}. The incoming beam is directed to the sample with an angle of 45° with respect to the surface normal. In the specular (off-specular) geometry the outgoing beam is detected with an angle of 45° (60°) with respect to the surface normal. The spectra were analyzed using IGOR PRO software [73].

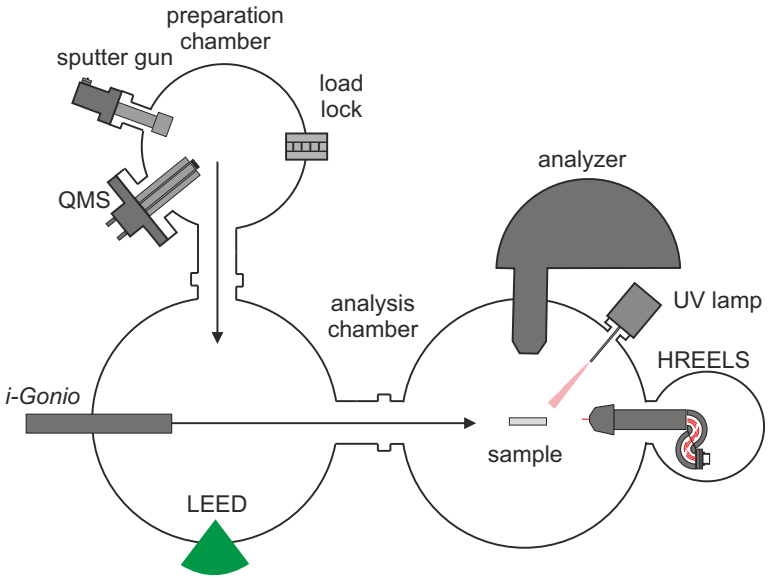

Figure 3.8: Schematic drawing of the UHV system present in the ESCA laboratory, Forschungszentrum Jülich, Germany. The preparation chamber is equipped with a load lock, a QMS and a sputter gun. The analysis chamber is equipped with an R 4000 hemispherical analyzer, a UV lamp and an HREELS monochromator.

3.4.4 ESCA Laboratory

The UHV system set-up shown in Fig. 3.8 was used to measure phonons of the Cu(111) surface, a reference system chosen to test the electron gun coupled with a hemispherical analyzer (Chap. 9). The system is composed of a preparation chamber with a base pressure of 1×10^{-9} mbar and of two analysis chambers with a base pressure of 1×10^{-10} mbar. The preparation chamber is composed of a load lock (for the sample loading), a QMS and a sputter gun. The Cu(111) surface was prepared in this chamber by cycles of Ar^+ sputtering at 800 eV and consequent annealing to 700 K. The analysis chambers are equipped with an MCP LEED and a VG Scienta R 4000 hemispherical electron analyzer having an acceptance angle of 30° and a FireWire CCD camera. The sample is transferred between the analysis chambers with the use of the 6-axes *i-Gonio* manipulator. At 45° with respect to the analyzer optical axis a UV lamp is installed for ARPES measurements. The special feature of this machine lies in the electron monochromator mounted at 90° with respect to the optical axis of the analyzer entrance. The detailed description and operation of the gun will be given in Chap. 9.

4 Hydrogen-Intercalated Graphene

4.1 Introduction

Since its isolation in 2004, graphene has been extensively investigated due to its outstanding electronic and structural properties which make it suitable for numerous electronic applications [74–76]. Of the current preparation techniques, epitaxial graphene grown on the 6H-SiC(0001) substrate is envisioned as a large-scale production because of the semiconductor nature of SiC which, for example, eliminates the need for a graphene layer transfer. However, as outlined in Sec. 3.1.4, the epitaxial growth of a graphene layer on SiC (in Epitaxial Monolyare Graphene (EMLG)) is accompanied by the formation of the BL (a carbon honeycomb lattice in which part of the atoms are covalently bonded to the top Si atoms at the surface), which affects the graphene layer in terms of doping, layer corrugation and electron mobility.

Recently, Riedl *et al.* made progress regarding the modification of the interface between the SiC substrate and the graphene layer [77]. The intercalation of atomic hydrogen between the BL and SiC yields the formation of H-intercalated Quasi Freestanding Monolayer Graphene (QFMLG) in which the resulting graphene layer shows properties close to the freestanding situation. Specifically, the n-type doping of the graphene layer present in EMLG vanishes and neutrality, $E_D \approx E_F$, is recovered.

Although the decoupling of the graphene layer from SiC by intercalation has been proved by photoemission, ARPES experiments are not sufficient to gauge the strength of this weak interaction at the interface since many graphene/substrate systems show quasifreestanding properties. In order to evaluate which system preserves best the graphene properties, we introduce a new parameter to assess the graphene/substrate interaction. The findings are published in: *Approaching Truly Freestanding Graphene:*

The structure of hydrogen-Intercalated Graphene on 6H-SiC(0001) and summarized in the following.

The vertical distance of the graphene layer with respect to the first Si atoms of the 6H-SiC(0001) substrate in H-QFMLG is experimentally measured using the NIXSW technique. The value is in agreement with DFT simulations which include van der Waals corrections. In terms of residual interactions at the interface, H-QFMLG shows the highest freestanding character of any graphene layer in comparison with other graphene/substrate systems reported in the literature for which the graphene adsorption height has been measured and/or calculated. These results show that the hydrogen passivated SiC substrate is the least interacting support for graphene.

4.2 Reprint of Physical Review Letters 114, 106804 (2015)

The following paper with the title *Approaching Truly Freestanding Graphene: The structure of hydrogen-Intercalated Graphene on 6H-SiC(0001)* [78] Copyright 2015 by the American Physical Society contains the following contributions from the authors:

The research has been conceived and designed by J. Sforzini, F. C. Bocquet, and F. S. Tautz.

The sample, H-QFMLG on 6H-SiC(0001), has been prepared by T. Denig and U. Starke.

The DFT calculations of H-QFMLG and of EMLG have been performed by L. Nemec, P. Rinke and V. Blum.

The experiments have been carried out at the Science and Interface beamline (Diamond Light Source) by J. Sforzini, and F. C. Bocquet with the support of B. Stadtmüller, S. Soubatch, C. Kumpf, and T-L. Lee, who has also set up the beamline.

The experimental data have been analyzed by J. Sforzini with the support of F. C. Bocquet and F. S. Tautz.

The interpretation of the results has been developed in discussion between J. Sforzini, L. Nemec, F. C. Bocquet and F. S. Tautz.

The paper has been written by J. Sforzini, F. C. Bocquet and F. S. Tautz.

PRL 114, 106804 (2015) PHYSICAL REVIEW LETTERS week ending 13 MARCH 2015

Approaching Truly Freestanding Graphene: The Structure of Hydrogen-Intercalated Graphene on 6*H*-SiC(0001)

J. Sforzini,[1,2] L. Nemec,[3] T. Denig,[4] B. Stadtmüller,[1,2,*] T.-L. Lee,[5] C. Kumpf,[1,2] S. Soubatch,[1,2] U. Starke,[4] P. Rinke,[3,6] V. Blum,[3,7] F. C. Bocquet,[1,2,†] and F. S. Tautz[1,2]

[1]*Peter Grünberg Institut (PGI-3), Forschungszentrum Jülich, 52425 Jülich, Germany*
[2]*Jülich Aachen Research Alliance (JARA), Fundamentals of Future Information Technology, 52425 Jülich, Germany*
[3]*Fritz-Haber-Institut der Max-Planck-Gesellschaft, 14195 Berlin, Germany*
[4]*Max Planck Institute for Solid State Research, Heisenbergstraße, 70569 Stuttgart, Germany*
[5]*Diamond Light Source Ltd, Didcot, OX110DE Oxfordshire, United Kingdom*
[6]*COMP/Department of Applied Physics, Aalto University, P.O. Box 11100, Aalto FI-00076, Finland*
[7]*Department of Mechanical Engineering and Material Science, Duke University, Durham, North Carolina 27708, USA*

(Received 13 November 2014; published 10 March 2015)

We measure the adsorption height of hydrogen-intercalated quasifreestanding monolayer graphene on the (0001) face of 6*H* silicon carbide by the normal incidence x-ray standing wave technique. A density functional calculation for the full $(6\sqrt{3} \times 6\sqrt{3})$-*R*30° unit cell, based on a van der Waals corrected exchange correlation functional, finds a purely physisorptive adsorption height in excellent agreement with experiments, a very low buckling of the graphene layer, a very homogeneous electron density at the interface, and the lowest known adsorption energy per atom for graphene on any substrate. A structural comparison to other graphenes suggests that hydrogen-intercalated graphene on 6*H*-SiC(0001) approaches ideal graphene.

DOI: 10.1103/PhysRevLett.114.106804 PACS numbers: 73.20.Hb, 61.48.Gh, 68.49.Uv, 71.15.Mb

During the past decade, graphene attracted broad interest for its structural and electronic properties [1,2], which makes it a promising material for a wide range of applications, e.g., transistors in nanoscale devices [3] and energy storage [4]. The exact material properties of graphene depend on the growth conditions on a given substrate and its interaction with the substrate. In order to maintain its unique electronic properties, it is important to understand the coupling between the graphene layer and the substrate, in terms of covalent and noncovalent bonding, residual corrugation, and doping.

Large-scale ordered epitaxial graphene can be grown on various metal substrates. However, the metallic contact to the graphene layer determines its transport properties through, for instance, buckling or doping of the graphene layer [5,6]. It is therefore paramount to find a substrate for which the interactions are minimized in order to preserve the extraordinary properties of a single graphene layer. In addition, the use of a nonmetallic substrate is necessary to be able to use graphene, for instance, in electronic devices.

In this context, graphene growth on various faces of the wide band gap semiconductor silicon carbide (SiC) appears appealing. Riedl *et al.* [7] demonstrated the possibility to decouple graphene from SiC by intercalation of hydrogen atoms [quasifreestanding monolayer graphene (QFMLG)]. It is known from the band structure, core levels, and Raman spectroscopy of graphene [8,9] that the intercalation process reduces the interaction with the substrate substantially (removal of covalent bonds, less doping and strain). However, these measurements are indirect and, moreover, for weakly interacting graphenes the sensitivity of angle-resolved photoelectron spectroscopy (ARPES) becomes insufficient to assess the interaction with the substrate [10].

An alternative criterion to gauge the interaction strength of graphene with a substrate is its adsorption height. However, for hydrogen-intercalated graphene, the adsorption height is not known experimentally. Moreover, it is not clear whether for such a weakly interacting system this height can be calculated reliably as it is entirely determined by the van der Waals (vdW) interaction, which is difficult to treat. In this Letter, we present a density functional theory (DFT) calculation of QFMLG using the full unit cell and a vdW correction to the exchange correlation potential in which the dispersion coefficients are derived from the self-consistent electron density [11]. The calculation yields an adsorption height that is indicative of a purely vdW interaction. We validate this calculation with an accurate experimental height determination by normal incidence x-ray standing wave (NIXSW) and find an excellent agreement. By comparing our results to the adsorption height of graphene on various substrates taken from the literature, we demonstrate that QFMLG on SiC has the least graphene-substrate interaction among all studied systems. This is confirmed in our DFT calculations by a very low buckling of the graphene layer, a very

homogeneous electron density at the interface, and the lowest known adsorption energy per atom for graphene on any substrates.

Experiments and calculations were carried out for graphene on 6*H*-SiC(0001). Because of its smoothness and homogeneity, the Si-terminated surface of the 6*H*-SiC is widely used to achieve a controlled formation of high quality epitaxial graphene monolayers [12–15]. However, the first honeycomb carbon layer formed on the SiC(0001) surface consists of sp^2 and sp^3 hybridized orbitals leading to the formation of the so-called zero-layer graphene (ZLG) [16,17]. Since some of its atoms are covalently bonded to the Si atoms of the SiC surface, the ZLG does not show the typical Dirac cone in its band structure [8]. To recover the typical electronic properties of graphene, namely linear dispersion of the π and π^* bands at the K point of the hexagonal Brillouin zone, the formation of an additional graphene layer on top of the ZLG is required, generating epitaxial monolayer graphene (EMLG). Although the ZLG decouples the EMLG from the substrate, it is still considered to be a main obstacle for the development of graphene-based electronic devices because of the residual interactions. In fact, the Si dangling bonds in the top layer induce a significant doping in the EMLG even through the ZLG [18]. Replacing the carbon ZLG by a more passivating layer is therefore necessary to produce freestandinglike graphene on the SiC substrate. This can be achieved by hydrogen intercalation. The hydrogen atoms passivate the Si atoms in the top SiC bilayer. In this process the bonds between the ZLG and Si atoms are broken, the sp^3 atoms in the ZLG rehybridize, and the ZLG is lifted above the hydrogen atoms at the interface, forming QFMLG. Thus, hydrogen takes over the decoupling role of the ZLG layer in the EMLG.

The NIXSW experiments were performed in an ultrahigh vacuum end station at the I09 beam line at Diamond Light Source (Didcot, United Kingdom) equipped with a VG Scienta EW4000 hemispherical electron analyzer (acceptance angle of 60°) perpendicular to the incident beam direction. All data sets were recorded at room temperature and in a normal incidence geometry. A photon energy of approximately 2463 eV was used to excite the 6*H*-SiC(0006) reflection, which has a Bragg plane spacing of 2.517 Å. The NIXSW method, combining dynamical x-ray diffraction and photoelectron spectroscopy, is a powerful tool for determining the vertical adsorption distances at surfaces with sub-Å accuracy and high chemical sensitivity. The samples were prepared by thermal decomposition of SiC to produce the ZLG and then by annealing up to 700 °C in molecular hydrogen at atmospheric pressure to produce the QFMLG. After being transported in air to the beam line, the samples were outgassed in the end station before the x-ray measurements. ARPES using monochromatized He Iα radiation and low energy electron diffraction, shown in Ref. [19], were used to check the electronic and structural properties. The x-ray results were obtained from two samples at different spots and showed no sample and position dependence.

The surface SiC (C^{SiC}_{surf}) and graphene components of the C 1*s* spectrum are found at binding energies of 283.1 and 284.7 eV, respectively [Fig. 1(a)], and the Si 2*s* is found at 152.2 eV [Fig. 1(b)] for the surface SiC (Si^{SiC}_{surf}). The photoelectron yield of each chemical species is deduced from the peak area determined by a line-shape analysis of the core-level spectrum. This is repeated for all photon energy steps over a 2 eV range around the Bragg energy (E_{Bragg}) for all three species. Following a well-established procedure [19], we fit the final reflectivity and photoelectron yield curves with dynamical diffraction theory to determine the heights of the three different species with respect to the bulk-extrapolated SiC(0006) atomic plane. The C^{SiC}_{surf} atoms are located at 0.61 ± 0.04 Å below the bulk-extrapolated silicon plane and the Si^{SiC}_{surf} 0.05 ± 0.04 Å above. Thus, we obtain an experimental Si-C distance of 0.66 ± 0.06 Å, in agreement with the SiC crystalline structure [20,21]. In the same way, we find the adsorption height of the graphene layer with respect to the topmost Si layer to be 4.22 ± 0.06 Å, as shown in Fig. 2(a). We note that this height is approximately equal to the sum of the vdW radii of carbon and hydrogen (plus the Si-H distance of approximately 1.50 Å), and thus indicates the absence of interactions besides vdW.

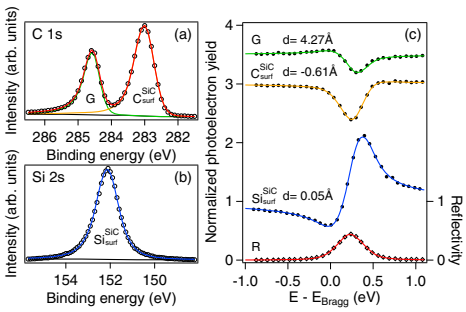

FIG. 1 (color online). NIXSW data measured for QFMLG on 6*H*-SiC(0001). (a) C 1*s* core level, fitted with two asymmetric Lorentzians. G and C^{SiC}_{surf} correspond to the graphene and the surface carbon atoms of SiC, respectively. (b) Si 2*p* core level fitted with a pseudo-Voigt function. Both were measured with a photon energy of 2494 eV. (c) Black dots show experimental photoelectron yield curves versus photon energy relative to the (0006) Bragg energy (2463 eV). The error bars, estimated according to Ref. [22], are smaller than the symbols. Fits to the yield curves for the surface atoms of SiC (Si^{SiC}_{surf}, C^{SiC}_{surf}) and graphene (G) are shown in blue, orange, and green, respectively [19,23–25]. The reflectivity R is plotted with black diamonds and its best fit in red. The absolute distances for each component are given with respect to the bulk-extrapolated silicon planes. The error bar for each value is ±0.04 Å.

PRL 114, 106804 (2015) PHYSICAL REVIEW LETTERS week ending 13 MARCH 2015

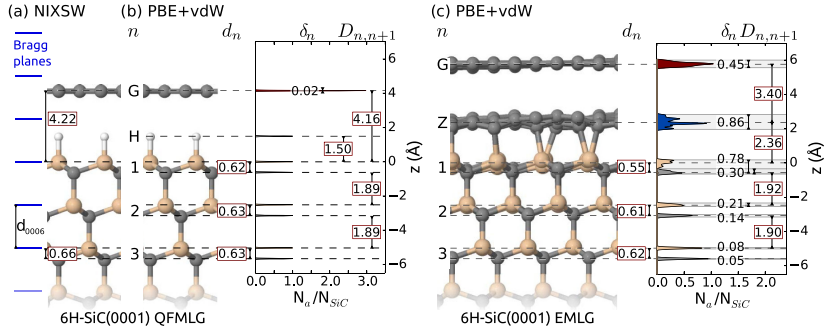

FIG. 2 (color online). (a) Vertical distances measured by NIXSW on QFMLG. The position of the Bragg planes around the surface are indicated by blue lines. PBE + vdW calculated geometry for (b) QFMLG and for (c) EMLG on 6*H*-SiC(0001) and histograms of the number of atoms N_a versus the atomic coordinates (z) relative to the topmost Si layer (Gaussian broadening: 0.02 Å). N_a is normalized by N_{SiC}, the number of SiC unit cells. $D_{n,n+1}$ is the distance between the layer n and $n+1$, d_n gives the Si-C distance within the SiC bilayer n, and δ_n is the corrugation of the layer n. All values are given in Å.

To test whether the structure of this predominantly vdW interacting interface can be predicted using DFT and to gain a detailed understanding of how hydrogen decouples the graphene layer from the substrate, we performed DFT calculations for the QFMLG and EMLG. The calculations were carried out using the all-electron, localized basis set code FHI-aims (tight settings) [26–29] and the Perdew-Burke-Ernzerhof (PBE) functional [30] with a correction for vdW effects (PBE + vdW). There are many different approaches to include long-range dispersion effects in DFT calculations [31]. We use the well-established Tkatchenko-Scheffler [11] method to efficiently include vdW effects in large-scale DFT calculations with thousands of atoms. It is a pairwise approach, where the effective C6 dispersion coefficients are derived from the self-consistent electron density. For the bulk lattice parameter of the 6*H*-SiC polytype, we find $a = 3.082$ Å and $c = 15.107$ Å. We stress that we investigate the QFMLG and EMLG reconstructions in the experimentally observed large commensurate $(6\sqrt{3} \times 6\sqrt{3})$-*R*30° supercell, almost strain-free (PBE + vdW: 0.1%) [32], consisting of 6 SiC bilayers under each surface reconstruction (1850 and 2080 atoms for the QFMLG and EMLG, respectively). We fully relaxed the top three SiC bilayers and all planes above (residual energy gradients $< 8 \times 10^{-3}$ eV/Å).

Figure 2 compares the measured structure of QFMLG [Fig. 2(a)] and the calculated structure of the QFMLG and EMLG [Figs. 2(b) and 2(c)] on 6*H*-SiC predicted at the PBE + vdW level. In addition, we include a histogram of the atomic z coordinates relative to the top Si layer normalized by the number of SiC unit cells. For illustration purposes, we broadened the histogram lines using a Gaussian with a width of 0.02 Å. For the QFMLG, we find a bulklike distance of 1.89 Å between the SiC bilayers. The Si-C distance within the top SiC bilayer (0.62 Å) and the remaining Si-C bilayer distances are practically bulk-like (0.63 Å), in good agreement with the experimental result (0.66 ± 0.06 Å). The distance between the top Si layer and the graphene layer is 4.16 Å for 6*H*-SiC, again in good agreement with the measured 4.22 ± 0.06 Å. The 0.02 Å corrugation of the graphene layer is very small. For the hydrogen layer and all layers underneath, the corrugation is $< 10^{-2}$ Å.

The situation is very different for the EMLG in Fig. 2(c). Here a significant buckling of the graphene layer is observed [33,34]. In the EMLG, the interface between bulk SiC and graphene is formed by the partially covalently bonded ZLG. This interface layer is corrugated by 0.86 Å, leading to a buckling of the graphene layer of 0.45 Å, as well as a strong corrugation of 0.78 Å in the top Si layer. The interlayer distance (1.92 Å) between the top substrate bilayers is increased in comparison with the bulk value, while the Si-C distance within the topmost SiC bilayer is substantially reduced; see Fig. 2(c). In summary, our calculations provide a valid description of the graphene SiC interface, as they reproduce quantitatively the NIXSW-measured Si-graphene distances for both QFMLG and EMLG [32,33].

Using a smaller approximated $(\sqrt{3} \times \sqrt{3})$-*R*30° cell (50 atoms for QFMLG), we tested the influence of the exchange correlation functional and the type of vdW correction on the geometries [19]. The Si-graphene distance for QFMLG calculated in the approximated cell using the same methodology as discussed above is 4.25 Å. When we applied the highest level of theory using the Heyd-Scuseria-Ernzerhof hybrid functional (HSE06) [35] with a vdW correction incorporating many-body effects (HSE06 + MBD) [36–38], the Si-graphene distance increased slightly to 4.26 Å. The difference of 0.01 Å between PBE + vdW and HSE06 + MBD is negligible.

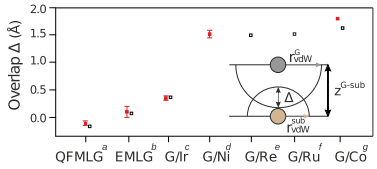

FIG. 3 (color online). Comparison of the overlap Δ for different epitaxial graphene systems. Δ is calculated by subtracting z^{G-sub} from the sum of graphene and substrate vdW radii. The empty and the filled squares correspond to DFT and measured values, respectively. (a) This work; (b) Refs. [32,33]; (c) Ref. [5]; (d) Ref. [6]; (e) Ref. [42]; (f) Ref. [43]; (g) Ref. [44].

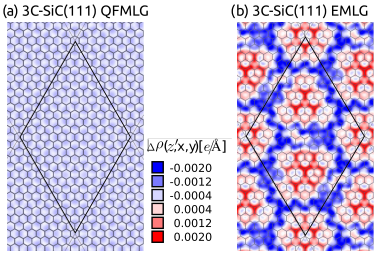

FIG. 4 (color online). Electron density differences $\Delta\rho(r) = \rho_{full}(r) - [\rho_G(r) + \rho_{sub}(r)]$ for (a) 3*C*-SiC QFMLG and (b) 3*C*-SiC EMLG, calculated in the *x*-*y* plane between the substrate and the graphene layer (at $z' = 1.08$ Å below the graphene layer). The $(6\sqrt{3} \times 6\sqrt{3})$-*R*30° supercell is shown in black and the graphene layer in gray.

We can thus conclude that changes in the predicted vertical structure of the $(6\sqrt{3} \times 6\sqrt{3})$-*R*30° supercell would also be small even if higher-level approximations to the exchange correlation functional were employed.

Comparing the buckling of QFMLG (0.02 Å) and of EMLG (0.45 Å), we can conclude that QFMLG is much more ideal for device applications than EMLG. This is confirmed by a qualitative analysis in terms of overlapping vdW radii [39,40] where the overlap is defined by $\Delta = r^{G}_{vdW} + r^{sub}_{vdW} - z^{G-sub}$ with r^{G}_{vdW}, r^{sub}_{vdW}, and z^{G-sub} being the vdW radii of graphene and of the atoms immediately below the graphene layer, and the measured distance between the graphene and the topmost atoms of the substrate, respectively. $\Delta > 0$ means that the vdW radii of the graphene and of the substrate overlap, indicating some degree of chemical interaction. On the other hand, for $\Delta \lesssim 0$, the graphene-substrate interaction is expected to be very weak. In Fig. 3, the overlap is plotted for QFMLG in comparison with other systems for which the adsorption heights have been measured or calculated. Epitaxial graphenes on SiC exhibit the lowest overlaps and QFMLG has by far the lowest value. This is also reflected in the low adsorption energy calculated for QFMLG, which is 59 meV/atom, significantly smaller than the corresponding values for EMLG (89.2 meV/atom) and graphite (81 meV/atom) [41].

Finally, we show that purely physisorptive adsorption with negligible buckling translates into a more decoupled electronic structure of the graphene. For this purpose, we calculate the change of electron density at the interface for QFMLG and EMLG. The calculations were performed with a 3*C*-SiC substrate as it allows us to use a smaller substrate thickness (4 layers instead of 6 for 6*H*-SiC) and renders the calculation more affordable. The SiC polytype (3*C* and 6*H*) is known not to influence the surface reconstructions [45,46]. We confirmed this by DFT for QFMLG and EMLG on both 6*H*-and 3*C*-SiC [19]. The electron density of the system is represented on an evenly distributed grid for the full system $\rho_{full}(r)$. Similarly, the graphene layer $\rho_G(r)$ and the substrate $\rho_{sub}(r)$, calculated in isolation from each other, include the hydrogen layer for QFMLG and the ZLG for EMLG. The electron density difference $\Delta\rho(r)$ is given by $\Delta\rho(r) = \rho_{full}(r) - [\rho_G(r) + \rho_{sub}(r)]$. Figure 4 shows $\Delta\rho(r)$ in the *x*-*y* plane at a given height between the substrate and the graphene layer. The resulting pattern is very similar for any chosen height [19]. In QFMLG, all Si atoms are saturated by hydrogen [47], resulting in negligible variations of the charge density within the *x*-*y* plane, as seen in Fig. 4(a). For EMLG, see Fig. 4(b), the electron density is modulated by the interplay of saturated and unsaturated Si bonds to the ZLG layer. The negligible $\Delta\rho(r)$ of QFMLG is an additional indication for the improved decoupling of the graphene layer from the substrate, thus preventing its buckling. This is in agreement with STM results [34] showing no corrugation within the experimental accuracy.

In conclusion, we have shown that DFT PBE + vdW calculations, for the large experimentally observed unit cell, accurately predict the adsorption height of QFMLG, in agreement with NIXSW measurements. QFMLG is the system having the largest adsorption distance among studied graphene-substrate systems; in particular, the overlap vanishes, suggesting a very effective decoupling of the graphene layer. Indeed, the calculations show that in comparison to EMLG, QFMLG is a very flat graphene layer with a very homogeneous electronic density at the interface. This significant difference translates into a dramatic improvement of transistors after hydrogen intercalation [48,49]. It suggests that the adsorption distance is a valid parameter to assess the ideality of graphene.

F. C. B. acknowledges financial support from the Initiative and Networking Fund of the Helmholtz Association, Postdoc Programme VH-PD-025. This research has been supported by the Academy of Finland through its Centres of Excellence Program (Project No. 251748). The authors would like to thank S. Schröder and C. Henneke for their support during the XSW beam-time, D. McCue for his excellent technical support at the I09 beam-line and B. Detlefs for helpful discussion.

*Present address: Department of Physics and Research Center OPTIMAS, University of Kaiserslautern, Erwin-Schrödinger-Strasse 46, 67663 Kaiserslautern, Germany.
†f.bocquet@fz-juelich.de

[1] Y. Zhang, Z. Jiang, J. P. Small, M. S. Purewal, Y.-W. Tan, M. Fazlollahi, J. D. Chudow, J. A. Jaszczak, H. L. Stormer, and P. Kim, Landau-Level Splitting in Graphene in High Magnetic Fields, Phys. Rev. Lett. **96**, 136806 (2006).
[2] M. I. Katsnelson, K. S. Novoselov, and A. K. Geim, Chiral tunnelling and the Klein paradox in graphene, Nat. Phys. **2**, 620 (2006).
[3] G. Fiori and G. Iannaccone, Multiscale modeling for graphene-based nanoscale transistors, Proc. IEEE **101**, 1653 (2013).
[4] D. Wang, R. Kou, D. Choi, Z. Yang, Z. Nie, J. Li, L. V. Saraf, D. Hu, J. Zhang, G. L. Graff, J. Liu, M. A. Pope, and I. A. Aksay, Ternary self-assembly of ordered metal oxide-graphene nanocomposites for electrochemical energy storage, ACS Nano **4**, 1587 (2010).
[5] C. Busse, P. Lazić, R. Djemour, J. Coraux, T. Gerber, N. Atodiresei, V. Caciuc, R. Brako, A. T. NDiaye, S. Blügel, J. Zegenhagen, and T. Michely, Graphene on Ir(111): Physisorption with Chemical Modulation, Phys. Rev. Lett. **107**, 036101 (2011).
[6] Y. Gamo, A. Nagashima, M. Wakabayashi, M. Terai, and C. Oshima, Atomic structure of monolayer graphite formed on Ni(111), Surf. Sci. **374**, 61 (1997).
[7] C. Riedl, C. Coletti, T. Iwasaki, A. A. Zakharov, and U. Starke, Quasi-Free-Standing Epitaxial Graphene on SiC Obtained by Hydrogen Intercalation, Phys. Rev. Lett. **103**, 246804 (2009).
[8] S. Forti and U. Starke, Epitaxial graphene on SiC: from carrier density engineering to quasi-free standing graphene by atomic intercalation, J. Phys. D **47**, 094013 (2014).
[9] F. Speck, J. Jobst, F. Fromm, M. Ostler, D. Waldmann, M. Hundhausen, H. B. Weber, and T. Seyller, The quasi-free-standing nature of graphene on H-saturated SiC(0001), Appl. Phys. Lett. **99**, 122106 (2011).
[10] J. C. Johannsen, S. Ulstrup, M. Bianchi, R. Hatch, D. Guan, F. Mazzola, L. Hornekr, F. Fromm, C. Raidel, T. Seyller, and P. Hofmann, Electron-phonon coupling in quasi-free-standing graphene, J. Phys. Condens. Matter **25**, 094001 (2013).
[11] A. Tkatchenko and M. Scheffler, Accurate Molecular Van Der Waals Interactions from Ground-State Electron Density and Free-Atom Reference Data, Phys. Rev. Lett. **102**, 073005 (2009).
[12] I. Forbeaux, J.-M. Themlin, and J.-M. Debever, Heteroepitaxial graphite on 6H—SiC(0001): Interface formation through conduction-band electronic structure, Phys. Rev. B **58**, 16396 (1998).
[13] K. V. Emtsev, A. Bostwick, K. Horn, J. Jobst, G. L. Kellogg, L. Ley, J. L. McChesney, T. Ohta, S. A. Reshanov, J. Röhrl, E. Rotenberg, A. K. Schmid, D. Waldmann, H. B. Weber, and T. Seyller, Towards wafer-size graphene layers by atmospheric pressure graphitization of silicon carbide, Nat. Mater. **8**, 203 (2009).
[14] U. Starke and C. Riedl, Epitaxial graphene on SiC(0001) and $SiC(000\bar{1})$: from surface reconstructions to carbon electronics, J. Phys. Condens. Matter **21**, 134016 (2009).
[15] C. Riedl, C. Coletti, and U. Starke, Structural and electronic properties of epitaxial graphene on SiC(0 0 0 1): a review of growth, characterization, transfer doping and hydrogen intercalation J. Phys. D **43**, 374009 (2010).
[16] F. Varchon, R. Feng, J. Hass, X. Li, B. N. Nguyen, C. Naud, P. Mallet, J.-Y. Veuillen, C. Berger, E. H. Conrad, and L. Magaud, Electronic Structure of Epitaxial Graphene Layers on SiC: Effect of the Substrate, Phys. Rev. Lett. **99**, 126805 (2007).
[17] K. V. Emtsev, F. Speck, T. Seyller, L. Ley, and J. D. Riley, Interaction, growth, and ordering of epitaxial graphene on $SiC\{0001\}$ surfaces: A comparative photoelectron spectroscopy study, Phys. Rev. B **77**, 155303 (2008).
[18] A. Bostwick, T. Ohta, J. L. McChesney, K. V. Emtsev, T. Seyller, K. Horn, and E. Rotenberg, Symmetry breaking in few layer graphene films, New J. Phys. **9**, 385 (2007).
[19] See Supplemental Material at http://link.aps.org/supplemental/10.1103/PhysRevLett.114.106804 for APRES and LEED data used to check the electronic and structural properties of the samples presented in this work. More details about the NIXSW technique are introduced. In addition, we include structural details calculated in the approximated $\sqrt{3} \times \sqrt{3}$-$R30°$ cell using different approximations to the exchange correlation functionals and van der Waals treatment.
[20] B. Lee, S. Han, and Y.-S. Kim, First-principles study of preferential sites of hydrogen incorporated in epitaxial graphene on 6H-SiC(0001), Phys. Rev. B **81**, 075432 (2010).
[21] J. Wang, L. Zhang, Q. Zeng, G. L. Vignoles, and L. Cheng, Surface relaxation and oxygen adsorption behavior of different SiC polytypes: a first-principles study, J. Phys. Condens. Matter **22**, 265003 (2010).
[22] G. Mercurio, O. Bauer, M. Willenbockel, N. Fairley, W. Reckien, C. H. Schmitz, B. Fiedler, S. Soubatch, T. Bredow, M. Sokolowski, and F. S. Tautz, Adsorption height determination of nonequivalent C and O species of PTCDA on Ag(110) using x-ray standing waves, Phys. Rev. B **87**, 045421 (2013).
[23] D. P. Woodruff, Normal incidence X-ray standing wave determination of adsorbate structures, Prog. Surf. Sci. **57**, 1 (1998).
[24] D. P. Woodruff, Surface structure determination using x-ray standing waves, Rep. Prog. Phys. **68**, 743 (2005).
[25] I. A. Vartanyants and M. V. Kovalchuk, Theory and applications of x-ray standing waves in real crystals, Rep. Prog. Phys. **64**, 1009 (2001).
[26] V. Blum, R. Gehrke, F. Hanke, P. Havu, V. Havu, X. Ren, K. Reuter, and M. Scheffler, Ab initio molecular simulations with numeric atom-centered orbitals, Comput. Phys. Commun. **180**, 2175 (2009).
[27] V. Havu, V. Blum, P. Havu, and M. Scheffler, Efficient O (N) integration for all-electron electronic structure calculation using numeric basis functions, J. Comput. Phys. **228**, 8367 (2009).
[28] T. Auckenthaler, V. Blum, H. Bungartz, T. Huckle, R. Johanni, L. Krämer, B. Lang, H. Lederer, and P. Willems, Parallel solution of partial symmetric eigenvalue problems from electronic structure calculations, Parallel Comput. **37**, 783 (2011).
[29] X. Ren, P. Rinke, V. Blum, J. Wieferink, A. Tkatchenko, A. Sanfilippo, K. Reuter, and M. Scheffler, Resolution-of-identity approach to Hartree-Fock, hybrid density functionals, RPA, MP2 and GW with numeric atom-centered orbital basis functions, New J. Phys. **14**, 053020 (2012).

[30] J. P. Perdew, K. Burke, and M. Ernzerhof, Generalized Gradient Approximation Made Simple (vol 77, Pg 3865, 1996), Phys. Rev. Lett. **78**, 1396 (1997).
[31] J. F. Dobson and T. Gould, Calculation of dispersion energies, J. Phys. Condens. Matter **24**, 073201 (2012).
[32] L. Nemec, V. Blum, P. Rinke, and M. Scheffler, Thermodynamic Equilibrium Conditions of Graphene Films on SiC, Phys. Rev. Lett. **111**, 065502 (2013).
[33] J. D. Emery, B. Detlefs, H. J. Karmel, L. O. Nyakiti, D. K. Gaskill, M. C. Hersam, J. Zegenhagen, and M. J. Bedzyk, Chemically Resolved Interface Structure of Epitaxial Graphene on SiC(0001), Phys. Rev. Lett. **111**, 215501 (2013).
[34] S. Goler, C. Coletti, V. Piazza, P. Pingue, F. Colangelo, V. Pellegrini, K. V. Emtsev, S. Forti, U. Starke, F. Beltram, and S. Heun, Revealing the atomic structure of the buffer layer between SiC(0001) and epitaxial graphene, Carbon **51**, 249 (2013).
[35] A. V. Krukau, O. A. Vydrov, A. F. Izmaylov, and G. E. Scuseria, Influence of the exchange screening parameter on the performance of screened hybrid functionals, J. Chem. Phys. **125**, 224106 (2006).
[36] A. Ambrosetti, A. M. Reilly, R. A. DiStasio, and A. Tkatchenko, Long-range correlation energy calculated from coupled atomic response functions, J. Chem. Phys. **140**, 18A508 (2014).
[37] A. Tkatchenko, A. Ambrosetti, and R. A. DiStasio, Interatomic methods for the dispersion energy derived from the adiabatic connection fluctuation-dissipation theorem, J. Chem. Phys. **138**, 074106 (2013).
[38] A. Tkatchenko, R. A. DiStasio, R. Car, and M. Scheffler, Accurate and Efficient Method for Many-Body van der Waals Interactions, Phys. Rev. Lett. **108**, 236402 (2012).
[39] A. Bondi, van der Waals volumes and radii, J. Phys. Chem. **68**, 441 (1964).
[40] S. Batsanov, Van der Waals radii of elements, Inorg. Mater. (USSR) **37**, 871 (2001).
[41] In Ref [5], a value of 50 meV/atom has been found for graphene on Ir(111). However, this value is an average over a chemically modulated physisorbed graphene layer. Hence, parts of the layer have a much larger adsorption energy.
[42] E. Miniussi, M. Pozzo, A. Baraldi, E. Vesselli, R. R. Zhan, G. Comelli, T. O. Mentes, M. A. Niño, A. Locatelli, S. Lizzit, and D. Alfè, Thermal Stability of Corrugated Epitaxial Graphene Grown on Re(0001), Phys. Rev. Lett. **106**, 216101 (2011).
[43] B. Wang, S. Günther, J. Wintterlin, and M.-L. Bocquet, Periodicity, work function and reactivity of graphene on Ru(0001) from first principles, New J. Phys. **12**, 043041 (2010).
[44] D. Eom, D. Prezzi, K. T. Rim, H. Zhou, M. Lefenfeld, S. Xiao, C. Nuckolls, M. S. Hybertsen, T. F. Heinz, and G. W. Flynn, Structure and electronic properties of graphene nanoislands on Co(0001), Nano Lett. **9**, 2844 (2009).
[45] J. Schardt, J. Bernhardt, U. Starke, and K. Heinz, Crystallography of the (3×3) surface reconstruction of 3C-SiC (111), 4H-SiC(0001), and 6H-SiC(0001) surfaces retrieved by low-energy electron diffraction, Phys. Rev. B **62**, 10335 (2000).
[46] O. Pankratov, S. Hensel, P. Götzfried, and M. Bockstedte, Graphene on cubic and hexagonal SiC: A comparative theoretical study, Phys. Rev. B **86**, 155432 (2012).
[47] F. C. Bocquet, R. Bisson, J.-M. Themlin, J.-M. Layet, and T. Angot, Reversible hydrogenation of deuterium-intercalated quasi-free-standing graphene on SiC(0001), Phys. Rev. B **85**, 201401 (2012).
[48] S. Hertel, D. Waldmann, J. Jobst, A. Albert, M. Albrecht, S. Reshanov, A. Schöner, M. Krieger, and H. B. Weber, Tailoring the graphene/silicon carbide interface for monolithic wafer-scale electronics, Nat. Commun. **3**, 957 (2012).
[49] F.-H. Liu, S.-T. Lo, C. Chuang, T.-P. Woo, H.-Y. Lee, C.-W. Liu, C.-I. Liu, L.-I. Huang, C.-H. Liu, Y. Yang, C.-Y. S. Chang, L.-J. Li, P. C. Mende, R. M. Feenstra, R. E. Elmquist, and C.-T. Liang, Hot carriers in epitaxial graphene sheets with and without hydrogen intercalation: role of substrate coupling, Nanoscale **6**, 10562 (2014).

– Supplemental material –
Approaching Truly Freestanding Graphene: The Structure of Hydrogen-Intercalated Graphene on 6*H*-SiC(0001)

J. Sforzini,[1,2] L. Nemec,[3] T. Denig,[4] B. Stadtmüller,[1,2] T-L. Lee,[5] C. Kumpf,[1,2] S. Subach,[1,2] U. Starke,[4] P. Rinke,[6,3] V. Blum,[7,3] F.C. Bocquet,[1,2,*] and F.S. Tautz[1,2]

[1]*Peter Grünberg Institut (PGI-3), Forschungszentrum Jülich, 52425 Jülich, Germany*
[2]*Jülich Aachen Research Alliance (JARA), Fundamentals of Future Information Technology, 52425 Jülich, Germany*
[3]*Fritz-Haber-Institut der Max-Planck-Gesellschaft, 14195 Berlin, Germany*
[4]*Max Planck Institute for Solid State Research, Heisenbergstraße, 70569 Stuttgart, Germany*
[5]*Diamond Light Source Ltd, Didcot, OX11ODE, Oxfordshire, United Kingdom*
[6]*COMP/Department of Applied Physics, Aalto University, P.O. Box 11100, Aalto FI-00076, Finland*
[7]*Department of Mechanical Engineering and Material Science, Duke University, Durham, NC 27708 USA*

(Dated: February 17, 2015)

In the following, we discuss our measurements and calculations in more detail. In particular:

- Details on sample quality
- NIXSW details
- Influence of the DFT functional
- Bulk stacking order
- Influence of the polytype
- The electron density maps

DETAILS ON SAMPLE QUALITY

In order to check the quality of the quasifreestanding monolayer graphene (QFMLG) samples, we applied two different techniques. We first measured a low energy electron diffraction (LEED) pattern, a fast method to check the presence of long range order at the surface. A characteristic pattern is shown in Fig. 1. In addition, we performed angle resolved photoelectron spectroscopy, revealing the band structure of the surface. As shown in Fig. 2, the typical linear band dispersion expected for graphene is measured around the K-point of its surface Brillouin zone.

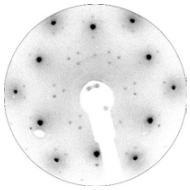

FIG. 1: LEED image taken with an incidence energy of 126 eV on QFMLG.

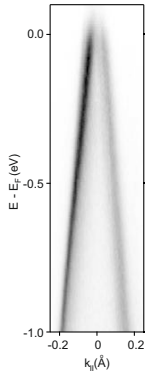

FIG. 2: ARPES spectrum of QFMLG performed in the ΓK direction and taken around K point (here at $k_{\parallel} = 0$) with the HeIα.

NIXSW DETAILS

The normal incidence x-ray standing wave technique gives access to adsorption heights of surface elements with respect to the lattice plane of a crystalline substrate. More details can be found in [1–3]. By tuning the incident photon energy (E) around the Bragg energy of the $H = (hkl)$ reflection, the spacial position of the x-ray standing wave field created in the vicinity of the surface shifts with respect to the lattice planes of the substrate. As a consequence, the photoelectron yield (Y) of a given adsorbed species varies. The resulting quantity, $Y(E)$, can be calculated with the following equation:

$$\begin{aligned} Y(E) =& 1 + S_R R \\ &+ 2F^H\sqrt{R}|S_I|\cos(\phi - 2\pi P^H + \Psi). \end{aligned} \quad (1)$$

By fitting the experimental data with eq. 1, two important independent parameters are extracted, for each

	P^H	F^H	d (Å)
Si_{Bulk}	0.019	1.23	0.048
C_{Bulk}	0.759	1.043	−0.607
$C_{Graphene}$	0.697	0.746	4.272

TABLE I: Averaged NIXSW measured values P^H and F^H for each component. The last column corresponds to the converted absolute positions with respect to the Bragg plane closest to the topmost Si atoms.

chemically differentiated species: the coherent position P^H and the coherent fraction F^H. P^H represents the average atomic positions and F^H can be understood as an order indicator of a given P^H. R and ϕ are the theoretical reflectivity and phase of the sample, respectively. The so-called non dipolar parameters, S_R, S_I and Ψ, were not used (that is to say set to 1, 1 and 0, respectively). The reason for this is that no reliable values are so far available for this geometry in the literature. All P^H and F^H values, averaged over all data sets, are shown in Tab. I. The value of both parameters should lie between 0 and 1. However non-dipolar effects [4] can influence the F^H values. This is clearly visible in the coherent fraction of silicon (1.23) for which a value very close to 1 is expected as it is a bulk species.

It is known that the graphene layer covers the steps of SiC(0001) [5], which as a consequence reduces the measured averaged coherent fraction (0.75), when compared to the perfectly flat C^{SiC}_{surf} (1.04). It is worth noting that for samples having a graphene coverage close but above one (not shown), the coherent fraction is dramatically reduced (0.48) in comparison to samples of coverage close but lower than one monolayer, measured on the same set-up (0.75).

Error bars estimation

Fitting the components of each core level is rather simple as it requires a very simple fitting model and the peaks are well defined, Fig. 1(a,b) of the main article. The error bar of each component's area is determined by a Monte Carlo analysis and is much smaller than the symbols used in Fig. 1(c) of the main article. When fitting the electron yield, the P^H and F^H parameters of a given data set have a negligible error bar. However, when comparing data obtained from several spots on two different QFMLG samples, we observe small variations. We attribute this to possible sample inhomogeneities, or small beamline, manipulator and analyzer instabilities.

The values given in Tab. I are averaged over 7 C 1*s* and 2 Si2*s* data sets, as shown in Tab. II. For all species, the P^H varies by 0.022 at maximum. This corresponds to an error bar smaller than ±0.04 Å for absolute positions. For distances, the error is then ±0.06 Å.

Sample	Position	Species	P^H	F^H
A	1	Si_{Bulk}	0.020	1.229
A	2	Si_{Bulk}	0.018	1.230
A	3	C_{Bulk}	0.760	1.035
		$C_{Graphene}$	0.702	0.699
A	3	C_{Bulk}	0.760	1.041
		$C_{Graphene}$	0.698	0.788
A	1	C_{Bulk}	0.760	1.043
		$C_{Graphene}$	0.696	0.798
A	4	C_{Bulk}	0.760	1.041
		$C_{Graphene}$	0.707	0.580
A	5	C_{Bulk}	0.760	1.051
		$C_{Graphene}$	0.704	0.623
B	6	C_{Bulk}	0.758	1.048
		$C_{Graphene}$	0.688	0.864
B	7	C_{Bulk}	0.755	1.039
		$C_{Graphene}$	0.685	0.872

TABLE II: Coherent positions and fractions for each data set obtained on QFMLG.

INFLUENCE OF THE DFT FUNCTIONAL

The supplemental material of a previous work by some of the authors [6] included details on the numerical convergence of calculations for similar structures with respect to the number of basis functions and the grid density in real and reciprocal space. For the $(6\sqrt{3} \times 6\sqrt{3})$ interfaces we chose the Γ-point for accurate integrations in reciprocal space. The FHI-aims code employs numeric atom-centered basis sets. Basic descriptions of their mathematical form and properties are published in [7]. The basis set and numerical real space grids are of high quality as defined by the *tight* settings including a *tier*1+dg basis set for Si and a *tier*2 basis set for C [7].

To test the influence of the exchange correlation functional on the geometry we used three different exchange correlation functionals, the local density approximation (LDA) [8], the Perdew-Burke-Enzerhof generalized gradient approximation (PBE) [9] and the Heyd-Scuseria-Ernzerhof hybrid functional (HSE06)[10]. In HSE06 the amount of exact exchange is set to $\alpha = 0.25$ and a range-separation parameter $\omega = 0.2\text{Å}^{-1}$ is used.

For an accurate description of the different surface phases, in particular hydrogen-graphene bonding in the QFMLG phase, we include long range electron correlations, so-called van der Waals (vdW) effects. Here, we compare the results of two different schemes. The first scheme used in this work is the well established Tkatchenko-Scheffler (TS) [11] method. It is a pairwise approach, where the effective C6 dispersion coefficients are derived from the self-consistent electron density. The second approach is a more recent refinement to the TS scheme incorporating many-body effects [12–14]. In this scheme, the atoms are modelled as spherical quantum harmonic oscillators, which are coupled through dipole-dipole interactions. The cor-

6H-SiC ZLG																		
	PBE+vdW			PBE+MBD			LDA			HSE06+vdW			HSE06+MBD					
n	$D_{n,n+1}$	d_n	δ_n Si/C	$D_{n,n+1}$	d_n	δ_n Si/C	$D_{n,n+1}$	d_n	δ_n Si/C	$D_{n,n+1}$	d_n	δ_n Si/C	$D_{n,n+1}$	d_n	δ_n
Z	2.37	—	—/ 0.30	2.35	—	—/ 0.29	2.30	—	—/ 0.37	2.38	—	—/ 0.30	2.37	—	—/ 0.30
1	1.92	0.48	$0.42/<10^{-2}$	1.92	0.51	$0.40/<10^{-2}$	1.91	0.53	$0.31/<10^{-2}$	1.92	0.48	$0.48/<10^{-2}$	1.92	0.48	$0.47/<10^{-2}$
2	1.88	$0.61<10^{-2}$	$/<10^{-2}$	1.89	$0.61<10^{-2}$	$/<10^{-2}$	1.88	$0.60<10^{-2}$	$/<10^{-2}$	1.88	$0.61<10^{-2}$	$/<10^{-2}$	1.88	$0.61<10^{-2}$	$/<10^{-2}$
3	1.89	$0.62<10^{-2}$	$/<10^{-2}$	1.90	$0.63<10^{-2}$	$/<10^{-2}$	1.88	$0.62<10^{-2}$	$/<10^{-2}$	1.88	$0.62<10^{-2}$	$/<10^{-2}$	1.89	$0.62<10^{-2}$	$/<10^{-2}$

6H-SiC QFMLG															
	PBE+vdW			PBE+MBD			LDA			HSE06+vdW			HSE06+MBD		
n	$D_{n,n+1}$	d_n	δ_n Si/C	$D_{n,n+1}$	d_n	δ_n Si/C	$D_{n,n+1}$	d_n	δ_n Si/C	$D_{n,n+1}$	d_n	δ_n Si/C	$D_{n,n+1}$	d_n	δ_n
G	2.75	—	$-/<10^{-2}$	2.76	—	$-/<10^{-2}$	2.71	—	$-/<10^{-2}$	2.71	—	$-/<10^{-2}$	2.77	—	$-/<10^{-2}$
H	1.50	—	— / —	1.50	—	— / —	1.51	—	— / —	1.49	—	— / —	1.49	—	— / —
1	1.89	$0.62<10^{-2}$	$/<10^{-2}$	1.89	$0.62<10^{-2}$	$/<10^{-2}$	1.88	$0.61<10^{-2}$	$/<10^{-2}$	1.88	$0.62<10^{-2}$	$/<10^{-2}$	1.88	$0.61<10^{-2}$	$/<10^{-2}$
2	1.89	$0.63<10^{-2}$	$/<10^{-2}$	1.89	$0.63<10^{-2}$	$/<10^{-2}$	1.88	$0.63<10^{-2}$	$/<10^{-2}$	1.88	$0.63<10^{-2}$	$/<10^{-2}$	1.88	$0.63<10^{-2}$	$/<10^{-2}$
3	1.89	$0.63<10^{-2}$	$/<10^{-2}$	1.89	$0.63<10^{-2}$	$/<10^{-2}$	1.88	$0.62<10^{-2}$	$/<10^{-2}$	1.88	$0.62<10^{-2}$	$/<10^{-2}$	1.88	$0.63<10^{-2}$	$/<10^{-2}$

TABLE III: Influence of the functional on the interface structure of 6H-SiC ($\sqrt{3}$-SiC model cell). $D_{n,n+1}$ is the distance between layer n and $n+1$, d_n gives the distance within SiC bilayer n, and δ_n the corrugation of layer n. All distances are given in Å.

responding many-body Hamiltonian is diagonalized to calculate the many-body vdW energies. As a result, this approach accounts for long-range many-body dispersion (MBD) effects employing a range-separated (rs) self-consistent screening (SCS) of polarizabilities and is therefore called MBD@rsSCS (for details see Ref. [14]). To include the long-range tail of dispersion interaction we couple each functional with either the pairwise TS scheme, here refered to as PBE+vdW (HSE06+vdW), or the MBD@rsSCS scheme in this work abbreviated as PBE+MBD (HSE06+MBD).

In Table III we list the layer distance ($D_{n,n+1}$), the Si-C distance within a SiC bilayer (d_n) and the layer corrugation (δ_n), the difference between the highest and lowest atom in the layer, for QFMLG and EMLG on 6H-SiC(0001) calculated with different exchange correlation functionals and vdW corrections. We conclude that PBE+vdW, PBE+MBD, HSE06+vdW and HSE06+MBD yield the same results for both phases.

BULK STACKING ORDER

For 3C-SiC(111), the stacking order close to the surface is independent of where the surface is cut. However, for the 6H-SiC(0001) this is different as the SiC bilayers are rotated every third layer by 30 degree in the unit cell. The position of the rotation is indicated in Fig. 3 by a kink in the grey line. We tested the influence of the stacking order for 6H-SiC using an approximated $\sqrt{3}\times\sqrt{3}$-R30° unit cell. The surface energies calculated using PBE+vdW of the 6H-SiC ZLG and the atomic structure are shown in Fig. 3. We find the lowest surface energy for ABCACB and ACBABC stacked SiC. We therefore use a ABCACB stacked 6H-SiC substrate.

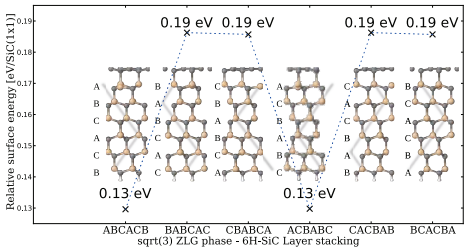

FIG. 3: The zero-layer graphene (ZLG) of the hexagonal SiC polytype (6H-SiC) using an approximated $\sqrt{3}\times\sqrt{3}$-R30° unit cell and their surface energies are shown for different SiC-bilayer stacking order calculated using PBE+vdW.

INFLUENCE OF THE POLYTYPE

To evaluate the influence of the SiC polytype on the geometry, we list the key geometry parameters in Tab. IV for the QFMLG and EMLG phase for two different polytypes, the 3C-SiC and 6H-SiC. For the QFMLG phase the interface geometries are practically identical. Likewise the interface of the EMLG phase shows polytype induced changes that are smaller than 0.04 Å. Therefore, 3C and 6H polytypes can be exchanged without qualitatively changing the result of the calculation. It should be noted that the advantage of 3C is that the number of bilayers one uses in the slab can be smaller than six.

THE ELECTRON DENSITY MAPS

We calculate the change of the electron density at the interface for the QFMLG and the EMLG phase for the 3C-SiC polytype. As shown in Tab. IV, the interface geometry hardly changes with polytype, and the same qualitative difference between the QFMLG and EMLG

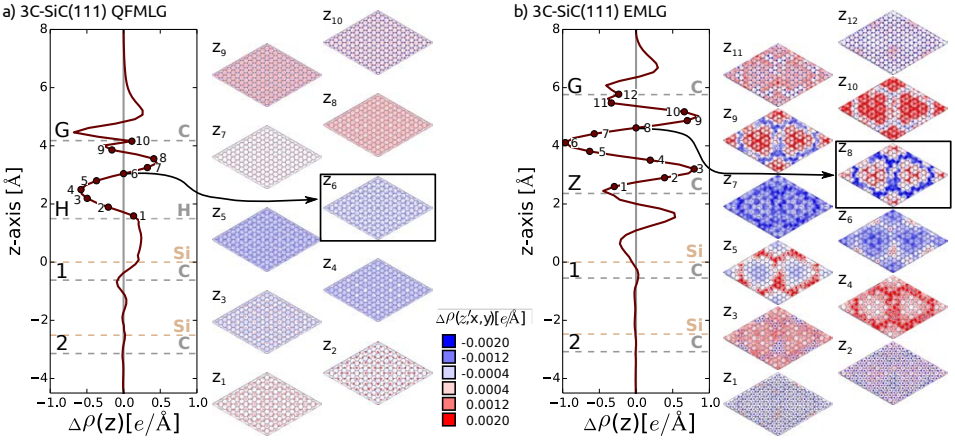

FIG. 4: The difference in the electron density ($\Delta\rho(r) = \rho_{\rm full}(r) - (\rho_{\rm G}(r) + \rho_{\rm sub}(r))$) is shown for (a) the $3C$-SiC QFMLG and (b) the $3C$-SiC EMLG phase. We integrated $\Delta\rho$ in the x-y-plane and plotted it along z. The position of the Si, C, H, and graphene-layer are indicated by dashed lines. We show $\Delta\rho(z_i)$ in the x-y-plane at equidistant z_i heights between the graphene layer and the substrate. In the main paper we include the electron density map at the inflection point of $\Delta\rho(z)$: z_6 for QFMLG and z_8 for EMLG.

QFMLG							
	$6H$-SiC				$3C$-SiC		
n	$D_{n,n+1}$	d_n	δ_n	Si/C	$D_{n,n+1}$	d_n	δ_n Si/C
G	2.66	—	0.02		2.68	—	0.01
H	1.50	—	0.00/0.00		1.50	—	0.00/0.00
1	1.89	0.62	0.00/0.00		1.89	0.62	0.00/0.00
2	1.89	0.63	0.00/0.00		1.89	0.63	0.00/0.00
3	1.89	0.63	0.00/0.00		1.89	0.63	0.00/0.00
EMLG							
	$6H$-SiC				$3C$-SiC[6]		
n	$D_{n,n+1}$	d_n	δ_n	Si/C	$D_{n,n+1}$	d_n	δ_n Si/C
G	3.40	—	0.45		3.40	—	0.41
Z	2.36	—	0.86		2.36	—	0.82
1	1.92	0.55	0.78/0.30		1.93	0.55	0.74/0.31
2	1.90	0.61	0.21/0.14		1.90	0.61	0.21/0.13
3	1.89	0.62	0.08/0.05		1.89	0.62	0.08/0.05

TABLE IV: Geometry comparison of the layer distance ($D_{n,n+1}$), the Si-C distance within a SiC bilayer (d_n) and the layer corrugation, the difference between the highest and lowest atom in the layer, (δ_n) for two different SiC polytypes, $6H$-SiC(0001) and $3C$-SiC(111), including both phases the QFMLG and EMLG calculated with PBE+vdW. The data for the $3C$-SiC EMLG phase was taken from [6].

phases can be observed for the $6H$-SiC polytype. The electron density ($\rho(r)$) of a 4-bilayer $3C$-SiC slab is represented on an evenly distributed grid ($260 \times 260 \times 350$) for the full system $\rho_{\rm full}(r)$, the graphene layer alone $\rho_{\rm G}(r)$ and the substrate alone $\rho_{\rm sub}(r)$ including the H layer for the QFMLG phase and the ZLG for the EMLG phase. The electron density difference $\Delta\rho(r)$ is given by $\Delta\rho(r) = \rho_{\rm full}(r) - (\rho_{\rm G}(r) + \rho_{\rm sub}(r))$. The change in the electron density along the z-axis $\Delta\rho(z) = \int dx\, dy\, \Delta\rho(r)$ is shown in Fig. 4 (a) for the QFMLG and Fig. 4 (b) for the EMLG. Figure 4 shows $\Delta\rho(r)$ in the x-y-plane at equidistant heights of 0.3 Å at the interface region. In the main paper we include the electron density map $\Delta\rho(z_{(6,8)}, x, y)$ at the inflection point $z = z_{(6,8)}$ of $\Delta\rho(z)$. In the QFMLG all Si atoms are saturated by hydrogen resulting in small variation of the charge density within the x-y-plane (Fig. 4 (a)) independent of the chosen height. In the EMLG phase the in-plane electron density is influenced by the interplay of saturated and unsaturated Si bonds in the ZLG layer. The modulations in the charge distribution Fig. 4 (b) are visible at any chosen position z_i in the interface region.

* Electronic address: f.bocquet@fz-juelich.de

[1] D. P. Woodruff, Prog. Surf. Sci. **57**, 1 (1998).
[2] I. A. Vartanyants and M. V. Kovalchuk, Rep. Prog. Phys. **64**, 1009 (2001).
[3] D. P. Woodruff, Rep. Prog. Phys. **68**, 743 (2005).
[4] G. J. Jackson, B. C. C. Cowie, D. P. Woodruff, R. G. Jones, M. S. Kariapper, C. Fisher, A. S. Y. Chan, and M. Butterfield, Phys. Rev. Lett. **84**, 2346 (2000).
[5] P. Lauffer, K. V. Emtsev, R. Graupner, T. Seyller,

L. Ley, S. A. Reshanov, and H. B. Weber, Phys. Rev. B **77**, 155426 (2008), URL http://link.aps.org/doi/10.1103/PhysRevB.77.155426.

[6] L. Nemec, V. Blum, P. Rinke, and M. Scheffler, Phys. Rev. Lett. **111**, 065502 (2013).

[7] V. Blum, R. Gehrke, F. Hanke, P. Havu, V. Havu, X. Ren, K. Reuter, and M. Scheffler, Comp. Phys. Comm. **180**, 2175 (2009).

[8] J. P. Perdew and Y. Wang, Phys. Rev. B **45**, 13244 (1992).

[9] J. P. Perdew, K. Burke, and M. Ernzerhof, Phys. Rev. Lett. **78**, 1396 (1997).

[10] A. V. Krukau, O. A. Vydrov, A. F. Izmaylov, and G. E. Scuseria, J. Chem. Phys. **125**, 224106 (2006).

[11] A. Tkatchenko and M. Scheffler, Phys. Rev. Lett. **102**, 073005 (2009).

[12] A. Tkatchenko, R. A. DiStasio, R. Car, and M. Scheffler, Phys. Rev. Lett. **108**, 236402 (2012).

[13] A. Tkatchenko, A. Ambrosetti, and R. A. DiStasio, J. Chem. Phys. **138**, 074106 (2013).

[14] A. Ambrosetti, A. M. Reilly, R. A. DiStasio, and A. Tkatchenko, J. Chem. Phys. **140**, 18A508 (2014).

5 Germanium-Intercalated Graphene

5.1 Introduction

As outlined in the previous chapter, the structural properties of epitaxial graphene are influenced in a disadvantageous way by the coupling with the SiC substrate, and a postprocessing intercalation with, e.g., hydrogen, can provide a complete detachment of the graphene layer from the substrate [78]. The chemical functionalization of the graphene/substrate interface not only changes the structural properties of graphene, but modifies the electronic band gap as well as the electronic charge transfer.

In this context, the intercalation of germanium between graphene and the SiC substrate appears the most interesting, because it provides ambipolar doping in graphene [10, 79]. Unlike H-QFMLG, the Ge-induced decoupling of the C-rich $(6\sqrt{3} \times 6\sqrt{3})R30°$ reconstruction from the SiC substrate takes place in different ways. According to Ref. [10], the graphene layer shows n-type doping when there is about one Ge layer intercalated while a p-type graphene layer is achieved doubling the amount of Ge present at the intercalation. In principle, a lateral p-n junction can be generated as the two phases coexist in a narrow annealing temperature range.

While the p-type and n-type nature of the graphene layer have been verified by ARPES measurements [10], the origin of the difference in electron charge transfer as a function of the Ge concentration remains unknown. There are a few theoretical attempts to explain the dependence of the graphene doping type on the Ge structure, but they do not reproduce the experimental evidence of a p-doped phase, mostly due to the use of poor modeling schemes involving too small unit cells [80–82].

In this chapter, the NIXSW technique is employed to determine with high accuracy the vertical distances of the species (Ge and graphene) above the (0006) Bragg plane of the 6H-SiC(0001) crystal for both p-type Ge-QFMLG and n-type Ge-QFMLG. We confirm that the Ge atoms in the n-phase arrange at the interface in one ordered layer at 2.419 ± 0.012 Å from the top Si atoms. The graphene adsorption height in this phase is 5.972 ± 0.010 Å, but the interface still presents residual interactions. In p-type Ge-QFMLG, the graphene adsorption height is larger by about 1.5 Å than in the n-type phase. As the intercalation is composed of more than one layer and the Ge species from the layers cannot be distinguished in XPS, the absolute vertical distances of the Ge atoms in the two layers cannot be resolved and only inferred models are discussed.

5.2 Experimental Details

The experiments were performed at the beamline I09 of the Diamond Light Source Synchrotron, Didcot, United Kingdom. The description of the end-station is given in Sec. 3.4.1. The Ge-QFMLG sample was prepared in the group of U. Starke by depositing about 5 layers of Ge on the C-rich $(6\sqrt{3} \times 6\sqrt{3})R30°$ reconstruction of the 6H-SiC(0001) crystal [10]. After annealing to 720° C, the p-type phase of Ge-QFMLG is achieved. The cleanness and quality of the p-type sample was checked by LEED, XPS and ARPES. Prior to NIXSW measurements, the sample was outgassed to remove any air contamination. The (0006) Bragg reflection of the 6H-SiC(0001) crystal is found at about 2463 eV, and the lattice spacing is 2.517 Å. The Si 2p, C 1s and Ge 3d core level spectra were measured in a 2 eV range around the Bragg energy. The experimental EY curves are then fitted using TORRICELLI software [69]. Finally, the sample has been annealed up to 920°C to obtain the n-type phase, and the experiments were repeated as for the p-type phase.

5.3 Electronic Properties

In order to check the quality and homogeneity of the sample as well as to identify the phase, ARPES measurements of the electronic band structure around the $\overline{\mathrm{K}}$ point of the graphene Brillouin zone were performed. After depositing the Ge atoms on the C-rich $(6\sqrt{3} \times 6\sqrt{3})R30°$ reconstruction of the 6H-SiC(0001) crystal and annealing up to 720° C, the graphene π band appears as shown in Fig. 5.1(a). At this annealing

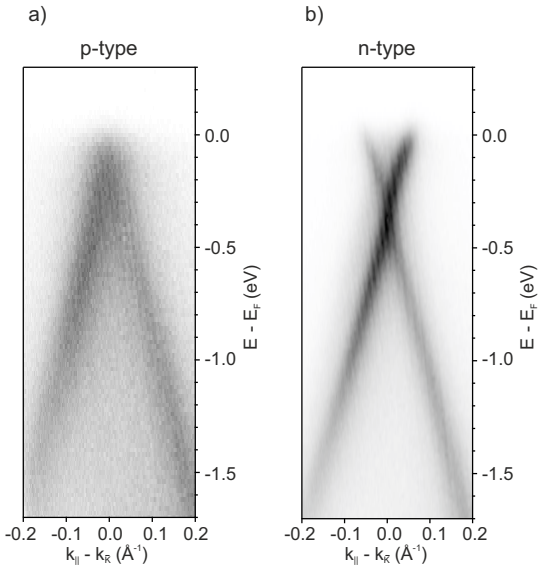

Figure 5.1: ARPES spectra measured in the $\overline{\Gamma K}$ direction and around the $\overline{K}$ point of the graphene Brillouin zone with a HeI$_\alpha$ radiation of (a) p-type Ge-QFMLG and (b) n-type Ge-QFMLG.

temperature, the graphene layer is of p-type with E_D situated slightly above E_F. By annealing up to 920° C, the Ge atoms at the interface partially sublimate, leading to an n-type graphene layer. Fig. 5.1(b) shows the ARPES spectrum obtained after annealing to this temperature. As expected, E_D is shifted downward by about 0.35 eV with respect to E_F [10].

5.4 Structural Properties

Turning to the results, we first present the XPS fit models which are used to evaluate the NIXSW data sets. A doublet symmetric line shape is used to fit the Si 2p signal of both phases at around 100.5 eV. Due to the spin-orbit splitting ($p_{1/2}$ and $p_{3/2}$), two components with an area ratio 1:2 and ΔE=0.60 eV are used as shown in Fig. 5.2(a) and (j) for p-type Ge-QFMLG and n-type Ge-QFMLG, respectively. The C 1s signal of both phases (Fig. 5.2(d) and (m)) is very similar to the one obtained for H-QFMLG, and therefore, the same fit model is employed (see Ref. [78]). The spectra are composed of a peak C_{SiC} (BE of 283 eV) which corresponds to the signal of the carbon atoms in the SiC bulk, and of a peak C_{Gr} (BE of 284.7 eV)

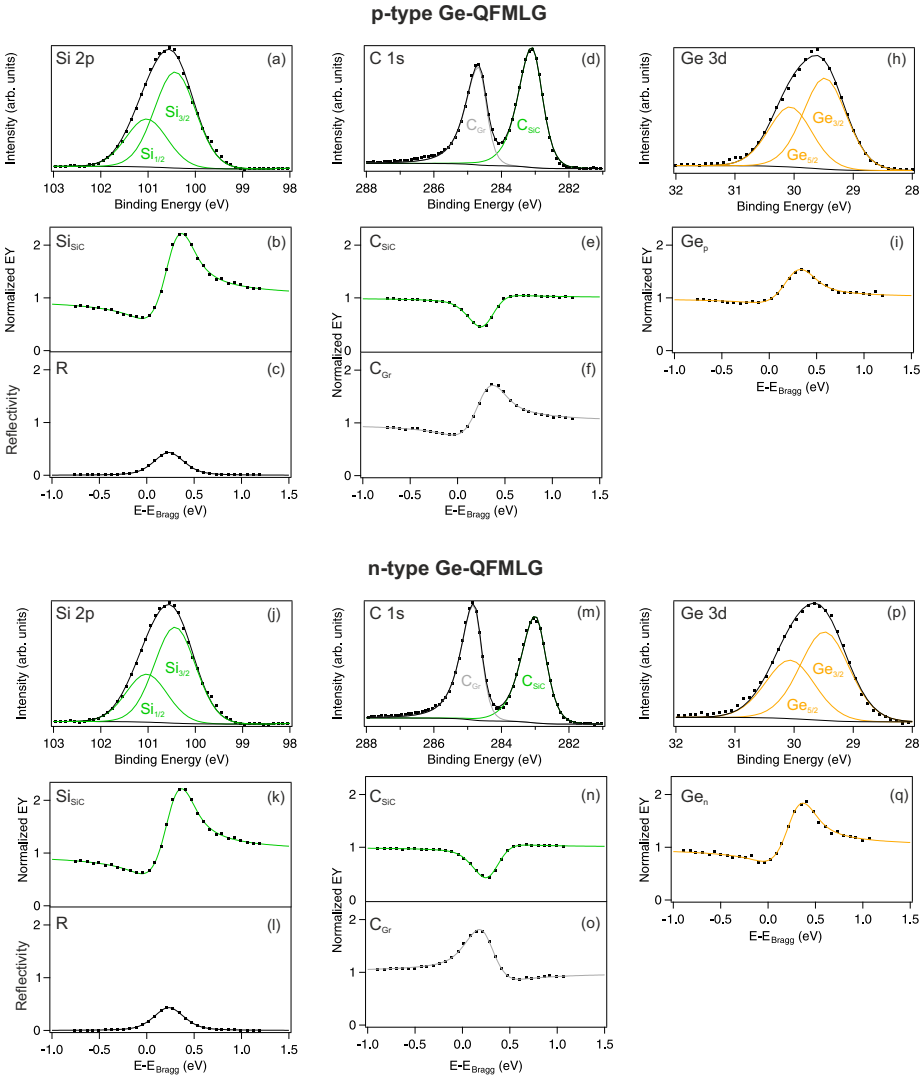

Figure 5.2: NIXSW results of p-type Ge-QFMLG (top) and of n-type Ge-QFMLG (bottom). (a) and (j) Si 2p core level fitted using two symmetric components, according to the spin-orbit splitting, related to the Si_{SiC} species which corresponds to the Si atoms in the SiC bulk. (b) and (k) Fit (green line) of the experimental EY (black dots) of Si_{SiC}. (c) and (l) The reflectivity R (black dots) of the SiC crystal with its best fit (black line). (d) and (m) C 1s core level fitted using two Lorenztian asymmetric components, C_{SiC} (green line) which corresponds to the C atoms in the SiC bulk, and C_{Gr} (grey line) which corresponds to the C atoms in the graphene. (e) and (n) Fit (green line) of the experimental EY (black dots) of C_{SiC}. (f) and (o) Fit (grey line) of the experimental EY (black dots) of C_{Gr}. (h) and (p) Ge 3d core level fitted using two symmetric components, according to the spin-orbit splitting, related to the Ge atoms at the interface. (i) and (q) Fit (orange line) of the experimental EY (black dots) of Ge. The core levels are acquired with a photon energy of 2461 eV. The error bars of the experimental EY data are smaller than the symbols.

which corresponds to the signal of the carbon atoms in the graphene layer. Finally, two symmetric lines, related to the spin-orbit splitting ($d_{3/2}$ and $d_{5/2}$), with an area ratio 3:2 and ΔE=0.57 eV, are used to fit the Ge 3d single peak (BE of 29.5 eV) as shown in Fig. 5.2(h) and (p) for the p-type phase and n-type phase, respectively.

The XPS models developed above are used to analyze the Si 2p, C 1s and Ge 3d NIXSW data sets in order to obtain the EY curves. The fit of the EY curves gives the P^H of each species with respect to the (0006) Bragg plane of the 6H-SiC(0001) crystal and the corresponding F^H. The P^H, F^H and their corresponding z values are summarized in Table 5.1. Regarding the bulk species, the Si atoms (Si_{SiC}) and the C atoms (C_{SiC}) of the SiC crystal have the same vertical distances for both the n-type and p-type phases. The EY curve of the Si_{SiC} species is shown in Fig. 5.2(b) and (k). Its P^H is found to be 0.040 ± 0.003, and according to Eq. 2.19, corresponds to a distance z of 0.101 ± 0.005 Å for $n = 0$. The fit of the EY curve of the C_{SiC} species in Fig. 5.2(e) and (n) gives a P^H of 0.765 ± 0.001 corresponding to z of -0.591 ± 0.003 Å. Combining the vertical distances of C_{SiC} and Si_{SiC}, we find a vertical distance along the Si-C bond (d_{Si-C}) of 1.825 ± 0.008 Å in good agreement with previous experimental and theoretical studies (see Ref. [78] and therein).

p-type	Si_{SiC}	C_{SiC}	C_{Gr}	Ge_p
P^H	0.040 ± 0.003	0.765 ± 0.001	0.005 ± 0.004	0.001 ± 0.011
F^H	1.276 ± 0.023	0.990 ± 0.001	0.717 ± 0.014	0.366 ± 0.023
z (Å)	0.101 ± 0.005	-0.591 ± 0.003	7.563 ± 0.006	2.520 ± 0.013
n	0	-1	3	1
n-type	Si	C_{SiC}	C_{Gr}	Ge_n
P^H	0.040 ± 0.003	0.761 ± 0.001	0.413 ± 0.003	0.001 ± 0.005
F^H	1.276 ± 0.023	1.009 ± 0.008	0.553 ± 0.012	0.835 ± 0.023
z (Å)	0.101 ± 0.005	-0.601 ± 0.003	6.073 ± 0.005	2.520 ± 0.007
n	0	-1	2	1

Table 5.1: The coherent position P^H, coherent fraction F^H and the vertical height z of the species present in p-type Ge-QFMLG (top) and in n-type Ge-QFMLG (bottom) are summarized. The z values are calculated according to Eq. 2.19 where n indicates the number of Bragg planes.

Regarding the graphene layer (C_{Gr}) and intercalated germanium (Ge) species, the situation is different between n-type and p-type Ge-QFMLG. Since the n-type phase contains less Ge in the intercalation layer, we first discuss the experimental results of this phase. The EY curve fit in Fig. 5.2(q) gives a P^H and F^H, related to the Ge_n species, of 0.001 ± 0.005 and 0.835 ± 0.023, respectively (see Table 5.1). In terms of

vertical distance z, Ge_n is found at 2.520 ± 0.007 Å, if n=1 is imposed in Eq. 2.19. Its high F^H suggests that the Ge atoms form a well-ordered layer. The fit of the EY curve of the C_{Gr} species in Fig. 5.2(o) gives a P^H of 0.413 ± 0.003. If n=1 was imposed, the vertical distance z of the graphene layer would result 3.557 ± 0.005 Å, and thus, the distance between the Ge atoms and the graphene layer would be approximately only 1 Å, which is very unlikely. Therefore, an additional Bragg distance needs to be taken into account in the calculation resulting to a vertical distance z of the graphene layer equal to 6.073 ± 0.005 Å, with n=2.

Fig 5.3 shows the proposed structural model for n-type Ge-QFMLG according to the z values defined previously. The Ge atoms, with a small vertical spread, are located 2.419 ± 0.012 Å above the Si atoms. d_{Si-Ge} experimentally found in this work agrees with the Si-Ge bond distance measured in a SiGe crystal (2.420 Å) [83]. As expected, the Ge atoms in the intercalation layer show a larger vertical distance with respect to Si compared to the H intercalation layer in H-QFMLG, and hence, the graphene absorption height in n-type Ge-QFMLG is larger as well. d_{Ge-Gr} is 3.553 ± 0.012 Å and thus d_{Si-Gr} amounts to 5.972 ± 0.010 Å. In terms of residual interaction, the Van der Waals overlap, defined in Chap. 4, is +0.32 Å, indicating that the interface between the intercalation and the graphene layer still presents some degree of interaction. The detected lower F^H (0.553 ± 0.012) of the graphene layer in n-type Ge-QFMLG compared to the one observed in H-QFMLG (0.746) also suggests a stronger buckling of the graphene layer. A possible explanation of it is discussed later.

In light of the above considerations, the interpretation of the results for p-type Ge-QFMLG are presented in comparison with the n-type phase structural model. The Ge 3d and C 1s core levels do not present any difference between the n- and p-type phase, but the EY curves do present distinct (P^H) F^H values. Fig. 5.2(i) shows the EY curve of the Ge_p species of p-type Ge-QFMLG. Its fit gives a P^H and F^H of 0.001 ± 0.011 and 0.366 ± 0.023, respectively (see Table 5.1). In terms of vertical distances, the Ge intercalation would appear at the same height as in the n-type phase (P^H of Ge_n and Ge_p are both 0.001). In fact, with n=1 in Eq. 2.19, z of Ge_p corresponds to 2.520 ± 0.013 Å. Note that F^H of Ge_p decreases dramatically from the n-type phase to the p-type phase (from 0.835 to 0.366) and the origin will be discussed later. A P^H and a F^H of 0.005 ± 0.004 and 0.717 ± 0.014 are obtained by fitting the EY curve of C_{Gr} in Fig. 5.2(o). In terms of vertical distances, we exclude a possibility where n=1 in Eq. 2.19 because the graphene layer would have the same adsorption height as the Ge intercalation, as shown in Fig. 5.4(a). If n=2 was imposed, the graphene layer would be located on the next Bragg plane, and

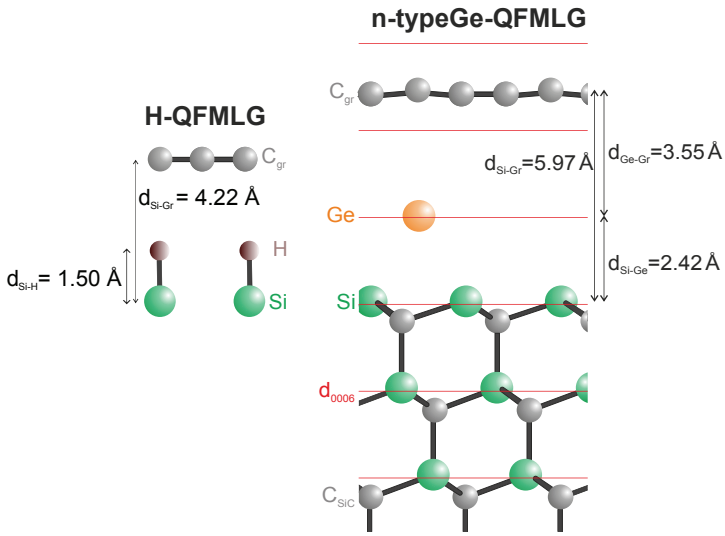

Figure 5.3: Summary of the vertical distances measured by NIXSW of n-type Ge-QFMLG. The Bragg planes are indicated by red lines as d_{0006}. The corresponding P^H, F^H and z values of Si, C_{SiC}, C_{Gr} and Ge_n are listed in Table 5.1. On the left side, the vertical distances measured and calculated of H-QFMLG are reported for comparison (see Chap.4).

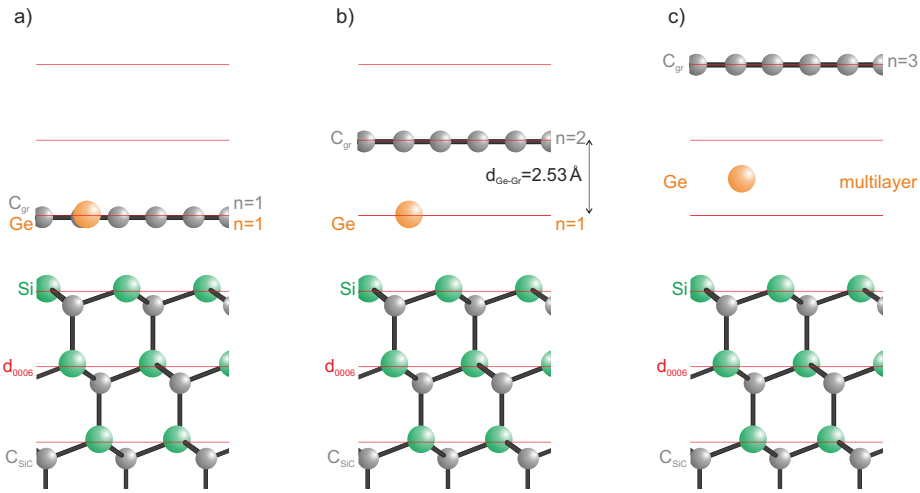

Figure 5.4: Graphical representation of the possible vertical distances of the C_{Gr} and Ge_p species in p-type Ge-QFMLG as a function of n in Eq. 2.19.

d_{Ge-Gr} would result 2.527 ± 0.019 Å(Fig. 5.4(b)), which is more than 1 Å smaller compared to the one detected in the n-type Ge-QFMLG sample. According to Scanning Tunneling Microscopy (STM) experiments [79], the graphene height in the p-type phase is about 2 Å larger than in the n-type phase. Converting P^H of C_{Gr} for the p-type phase using n=3, we obtain a graphene z of 7.563 ± 0.006 Å which is indeed larger than the measured 6.073 Å for the n-type phase in agreement with Ref. [79]. As a consequence, the intercalation in the p-type phase must be composed of more layers with different heights, explaining the low F^H (0.366 ± 0.023) of the Ge_p species (Fig. 5.4(c)). However, the chemical shift of the Ge 3d core level when bound to Ge or to Si is beyond the resolution of the instrument, and therefore, it is not possible to distinguish two or more components, but only extract the sum of P^H and F^H (Ge_p).

In order to define a structural representation of p-type Ge-QFMLG, we attempt to develop a model containing two components, Ge_1 and Ge_2, of which the sum of their P^H and F^H satisfies 0.001 and 0.366, respectively. According to Eq. 2.23, the two components are related such that

$$F^H_{\text{sum}} e^{-2\pi i P^H_{\text{sum}}} = (0.366) e^{-2\pi i (0.001)} = (a_1 F^H_1 e^{-2\pi i P^H_1} + a_2 F^H_2 e^{-2\pi i P^H_2}). \tag{5.1}$$

In Fig. 5.5 a first model is presented. This model is based on the assumption that the intercalation is composed of a first Ge layer having the same d_{Si-Ge} and the same Ge vertical spread as that in the n-type phase. Hence, we impose P^H_1 and F^H_1 of Ge_1 equal to 0.001 and 0.835, respectively. We also consider the abundance of the Ge atoms in the two layers equal ($a_1 = a_2 = 0.5$). Consequently, P^H_2 and F^H_2 of Ge_2 must be 0.501 and 0.103, as visualized in the Argand Diagram. In this situation, the interface is formed by a first ordered layer of Ge (Ge_1) at 2.419 Å with respect to the top Si atoms, and by a second layer of Ge (Ge_2) with a vertical distance of 1.258 Å from Ge_1 ($d_{Ge_1-Ge_2}$). However, its F^H_2 is very low, which is very unlikely since it indicates the presence of an incoherent layer, and therefore, this model is excluded.

Ge_2	$a_2 = 0.50$	$a_2 = 0.45$	$a_2 = 0.40$	$a_2 = 0.35$	$a_2 = 0.30$
P^H_2	0.501	0.501	0.501	0.501	0.501
F^H_2	0.103	0.207	0.338	0.505	0.728

Table 5.2: The coherent fraction F^H_2 of Ge_2 as a function of the abundance a_2 for p-type Ge-QFMLG.

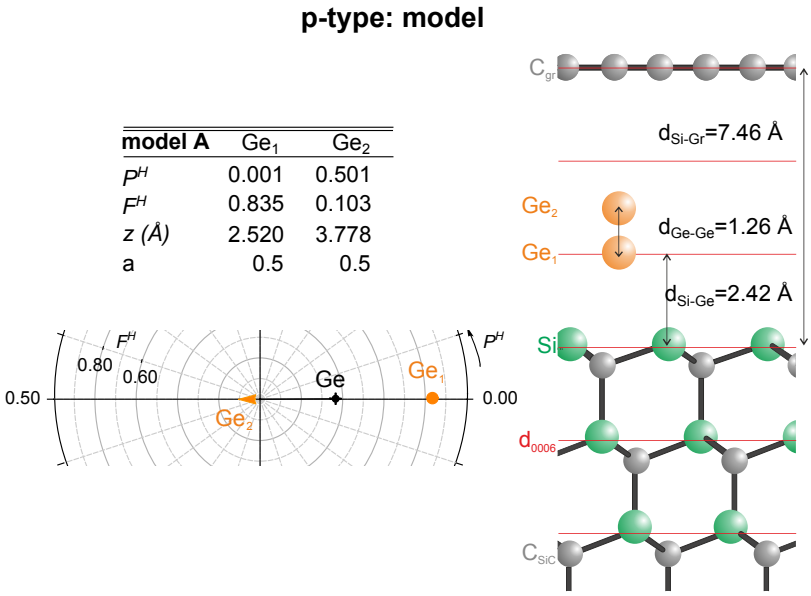

Figure 5.5: The model A for p-type Ge-QFMLG is presented. On the left side of the panel the Argand diagram of Ge (black cross) is depicted considering P^H and F^H (orange point and arrow) of Ge_1 and Ge_2 shown in the tables. The vertical distances are summarized in the sketch on the right side.

Further models are developed based again on the assumption that P_1^H and F_1^H of Ge_1 are essentially equal to the values obtained for the n-type phase. However, in contrast to the previous model the quantity of Ge atoms in the two layers is different ($a_1 \neq a_2$). If we consider that the Ge atoms in n-type Ge-QFMLG partially sublimate upon annealing, the intercalation is incomplete. As a consequence, the interaction between the graphene layer and the Ge layer is not homogenous, yielding a buckling of the graphene layer as indeed indicated by the detected low F^H (0.553). From Ref. [10], it is known that the amount of Ge in the p-type phase is approximately doubled than that in the n-type phase. In this context, we assume that this abundance difference is distributed such that a part of Ge is located in the first layer (Ge_1) until saturation is reached, and the remaining Ge arranges in a second layer (Ge_2) on top of the previous one. According to Eq. 5.1, when changing the values of a_1 and a_2, only F_2^H of Ge_2 will be affected, while P_2^H remains stable since Ge_1 and Ge_p show the same phase (equal $P^H = 0.001$). Tab. 5.2 shows the possible F_2^H values obtained in the $0.30 < a_2 < 0.50$ range. For $a_2 < 0.30$, the resulting F_2^H has no physical meaning (above 1). We find that the vertical spread of Ge_2 is proportional to its abundance. Within this model, the intercalation is composed of

a complete layer Ge_1 at 2.419 Å with respect to the top Si atoms, and of a partially incomplete second layer Ge_2 at 1.258 Å with respect to Ge_1 (right side Fig. 5.5). However, the F_2^H value remains unknown. d_{Gr-Ge_2} is 3.785 Å, which is larger than that measured for the n-type phase. Consequently in terms of residual interaction, the Van der Waals overlap Δ decreases from +0.32 to +0.03 Å from n-type Ge-QFMLG to p-type Ge-QFMLG, indicating that the graphene layer is less affected by the interface, as also suggested by the larger F^H of the graphene layer detected in p-type Ge-QFMLG (0.717) compared to the one detected in n-type Ge-QFMLG (0.556).

5.5 Summary and Conclusion

In conclusion, we have investigated Ge-QFMLG on 6H-SiC(0001) using the NIXSW technique. By annealing up to 920° C, the n-type phase is achieved in which the intercalation is formed by a well-ordered layer of Ge atoms at a vertical distance of 2.419 ± 0.012 Å with respect to the top Si atoms of the SiC crystal. On the other hand, in the p-type phase the larger graphene adsorption height indicates that the Ge atoms arrange in more than one layer at the interface. However, since no chemical shift is detectable in the Ge 3d core level spectra, the vertical distances of Ge in the layers cannot be resolved. In terms of residual interaction, the van der Waals overlap of +0.32 Å together with a considerable buckling of the graphene layer suggest that the graphene layer in the n-type phase is not completely decoupled from the substrate and thus some interactions are still present at the interface. In contrast, according to our structural models, the van der Waals overlap in p-type Ge-QFMLG is approximately equal to the graphene adsorption height, indicating that the graphene layer is better decoupled. However, in order to fully reveal the multilayered structure of the Ge intercalation, additional NIXSW data considering, for example, the (00012) reflection of 6H-SiC(0001), and/or reflectivity experiments are needed to draw definitive conclusion.

6 Nitrogen Doping of Graphene

6.1 Introduction

After a decade of intense research, the lack of a band gap in pristine graphene still prevents its full application in the semiconductor industry. For example, graphene-based materials do not show the excellent switching capability which is a necessary prerequisite for their integration in electronic devices. Therefore, opening a sizeable and well-tuned bandgap in graphene is a significant challenge for graphene-based electronic devices. One way to achieve this is by substitution of heteroatoms into the graphene lattice.

Because carbon and nitrogen are neighbours in the preiodic table, doping graphene with nitrogen has been intensively investigated [11, 84–86]. Several studies focus on the methods to produce N-doped graphene and its characterization. For example, an STM-based study shows that the nitrogen dopants are indeed present in the graphene layer and that they assume different configurations [86]. XPS measurements confirm the presence of several chemical states in the nitrogen core-level [11]. However, the influence of nitrogen doping on the structural properties of graphene has not been explored yet. Furthermore, the precise identification of these nitrogen species, i.e. are they located in the graphene honeycomb lattice, in the interface or in the near-surface bulk of the substrate, are of importance when using graphene for electronic applications. A comparative study of the doping process on different graphene systems is published in: *Structural and Electronic Properties of Nitrogen-Doped Graphene* and summarized in the following in order to investigate these key factors.

By means of the NIXSW technique, we are able to correlate each chemical state, detected in the N core-level spectra, with its vertical distance, demonstrating that the nitrogen dopants are indeed in the graphene plane. However, a substantial part of the nitrogen atoms also affects the environment. In order to evaluate the role

of the interface and the substrate, we compare N-doped H-QFMLG and N-doped EMLG both on 6H-SiC(0001). The effectiveness of the doping is confirmed by ARPES measurements. Although both systems are quantitatively equally doped, the doping mechanisms differ. As the BL is inert against the doping, EMLG is only doped by the substituted nitrogen atoms in the graphene layer. In contrast, the nitrogen in H-QFMLG, partially replacing the hydrogen at the intercalation, injects charge carriers ('proximity doping') and degrades the graphene layer in terms of an increased layer corrugation. These surprising results show that the type of interface affects the doping process as well as that the substrate has a strong influence on the doping effectiveness.

6.2 Reprint of Physical Review Letters 116, 126805 (2016)

The following paper with the title *Structural and Electronic Properties of Nitrogen-Doped Graphene* [87] Copyright 2016 by the American Physical Society contains the following contributions from the authors:

The research has been conceived and designed by J. Sforzini, F. C. Bocquet, and F. S. Tautz.

The samples, H-QFMLG and EMLG on 6H-SiC(0001), have been prepared by A. Stör, S. Link and U. Starke.

The DFT calculations of the graphene bands have been performed by P. Hapala and P. Jelínek.

The experiments have been carried out at the Science and Interface beamline (Diamond Light Source) by J. Sforzini, and F. C. Bocquet with the support of M. Švec, S. Soubatch, M. Franke, G. van Straaten and T-L. Lee, who has also set up the beamline.

The experimental data have been analyzed by J. Sforzini with the support of F. C. Bocquet and F. S. Tautz.

The interpretation of the results has been developed in discussion between J. Sforzini, F. C. Bocquet, M. Švec and F. S. Tautz.

The paper has been written by J. Sforzini, F. C. Bocquet and F. S. Tautz.

PRL **116,** 126805 (2016) PHYSICAL REVIEW LETTERS week ending 25 MARCH 2016

Structural and Electronic Properties of Nitrogen-Doped Graphene

J. Sforzini,[1,2] P. Hapala,[3] M. Franke,[1,2] G. van Straaten,[1,2] A. Stöhr,[4] S. Link,[4] S. Soubatch,[1,2] P. Jelínek,[3] T.-L. Lee,[5] U. Starke,[4] M. Švec,[3] F. C. Bocquet,[1,2,*] and F. S. Tautz[1,2]

[1]*Peter Grünberg Institut (PGI-3), Forschungszentrum Jülich, 52425 Jülich, Germany*
[2]*Jülich Aachen Research Alliance (JARA), Fundamentals of Future Information Technology, 52425 Jülich, Germany*
[3]*Institute of Physics of the Czech Academy of Sciences, Cukrovarnická 10, 16200 Prague, Czech Republic*
[4]*Max Planck Institute for Solid State Research, Heisenbergstraße, 70569 Stuttgart, Germany*
[5]*Diamond Light Source Ltd, Didcot OX110DE, Oxfordshire, United Kingdom*

(Received 17 July 2015; revised manuscript received 22 January 2016; published 24 March 2016)

We investigate the structural and electronic properties of nitrogen-doped epitaxial monolayer graphene and quasifreestanding monolayer graphene on 6*H*-SiC(0001) by the normal incidence x-ray standing wave technique and by angle-resolved photoelectron spectroscopy supported by density functional theory simulations. With the location of various nitrogen species uniquely identified, we observe that for the same doping procedure, the graphene support, consisting of substrate and interface, strongly influences the structural as well as the electronic properties of the resulting doped graphene layer. Compared to epitaxial graphene, quasifreestanding graphene is found to contain fewer nitrogen dopants. However, this lack of dopants is compensated by the proximity of nitrogen atoms at the interface that yield a similar number of charge carriers in graphene.

DOI: 10.1103/PhysRevLett.116.126805

The discovery of graphene and its exceptional properties has triggered very active research on this material [1,2]. One strong focus has been aiming at modifying graphene's electronic properties for device applications [3]. Substituting the carbon atoms (C) by other elements is one way to dope the layer. To date, nitrogen (N) belongs to the most studied dopants for graphene [4–6]. This is demonstrated by the remarkable performance improvements resulting from the use of N-doped graphene-based components in, e.g., lithium-ion batteries [7], ultracapacitors [8,9], fuel cells [10], and field-effect transistors [11,12]. However, our understanding of the doping process at the atomic level is still in its infancy. It is suspected that N incorporation alters the structure of graphene and degrades its quality [13,14], while other factors, such as the effects of the underlying support (i.e., the substrate and possibly an interface layer) on the doping, remain largely unexplored.

In this Letter, we study the effects of N doping on the structural and electronic properties of graphene, with particular emphasis on the influence of the support on the doping. To this end, N-doped epitaxial monolayer graphene (EMLG) and H-intercalated quasifreestanding monolayer graphene (QFMLG), both grown on 6*H*-SiC(0001), are investigated by the normal incidence x-ray standing wave (NIXSW) technique, which determines the vertical positions of the individual chemical species in the near surface region. The effects of the structural changes on the electronic bands are checked by angle-resolved photoelectron spectroscopy (ARPES) and density functional theory (DFT). We find that the support dramatically influences how much N, as well as how N, incorporates in graphene, which in turn affects the dopant-induced band broadening. In the case of EMLG, the support itself remains structurally intact after the doping. In contrast, the QFMLG/SiC interface becomes N doped, and consequently graphene is pushed locally by the N atoms away from the H terminated SiC substrate and buckles. Furthermore, the interaction with the thus doped interface provides additional charge carriers to graphene in QFMLG.

The samples were prepared following the procedure described in Ref. [15]. The *in situ* N doping and the x-ray measurements were performed at the I09 beam line, Diamond Light Source [16]. Before doping, the absence of N from the sample surfaces was confirmed by x-ray photoelectron spectroscopy (XPS). The EMLG and QFMLG were doped by exposing the samples (at room temperature) to 100 eV N^+ ions for 4 min and annealing at 1200 and 1000 K, respectively. The N_2 pressure during the ion implantation did not exceed 6×10^{-7} mbar. The absence of point defects induced by this implantation method has been checked by scanning tunneling microscopy (STM) for annealing temperatures as low as 1000 K. Furthermore, we confirmed the stability of the H intercalation layer at 1000 K in QFMLG using ARPES. Higher doping levels were achieved for EMLG and QFMLG by repeating this procedure. A sample with only a buffer layer (BL) was also studied as a reference.

PRL 116, 126805 (2016) PHYSICAL REVIEW LETTERS week ending 25 MARCH 2016

We first present the structures of N-doped graphene as determined by the NIXSW technique. We measured a set of XPS spectra (C 1s, Si 2p, N 1s) over a photon energy range of 2 eV around the (0006) Bragg energy (2462 eV) of 6H-SiC. Fitting the photoelectron yield (EY) as a function of the photon energy with theory [17] determines two parameters for each chemical component of a core level: the coherent position P^H and the coherent fraction F^H, which represent the position of the emitter between two Bragg planes and its spread perpendicular to the planes, respectively. Knowing the Bragg plane spacing of the $H = (0006)$ reflection of the 6H-SiC crystal ($d_H = 2.517$ Å), the possible vertical positions z_X of each component X with respect to the topmost Si layer can be calculated by $z_X = (n + P^H_X - P^H_{\mathrm{Si}}) \times d_H$, where n is an integer, P^H_X and P^H_{Si} are the coherent positions of the component X and of the top few Si layers, respectively. The results for Si 2p and C 1s of the undoped samples, neglecting nondipolar effects [18] and summarized in Table I, are in excellent agreement with the literature [19].

In Figs. 1(a)–1(c), N 1s spectra are shown for the BL, EMLG, and QFMLG samples after 4 min of doping. The spectra of the three samples present different sets of components, revealing the distinct chemical states of N. The EY curves of the different N 1s components together with their best fits are displayed in Figs. 1(d)–1(f). Using the vertical positions derived from the NIXSW technique, summarized in Table I, we will show below that these chemical components can be associated with N incorporation into the different constituents of the samples.

Before considering the results for EMLG and QFMLG, it is worth studying the effect of N doping on the BL sample, because the buffer layer on SiC is also the support for graphene in EMLG. The N 1s spectrum of the BL [Fig. 1(a)] exhibits a main component at 397.5 eV and a shoulder at 399.7 eV. The main component is also present for the EMLG and QFMLG samples [Figs. 1(b) and 1(c)]. The NIXSW analysis of this component for the three doped samples renders a common coherent position $P^H_{\mathrm{N_{SiC}}}$ of 0.66 ± 0.01 [Figs. 1(d)–1(f)], which does not match the vertical positions of any of the C or intercalation layers. As only the SiC substrate is common to all three samples, and since the binding energy of 397.5 eV agrees with the previous measurements on N-doped bulk SiC [22], we assign this N 1s component to N atoms that have diffused into the substrate during annealing, or that were directly implanted into the bulk during sputtering, designated as $\mathrm{N_{SiC}}$ in the following. $\mathrm{N_{SiC}}$ is found to be 0.21 ± 0.09Å below the C planes in the bulk ($\mathrm{C_{SiC}}$). A further interpretation of its exact position is beyond the scope of this Letter. Besides the common component $\mathrm{N_{SiC}}$, the spectrum of the doped BL sample exhibits a shoulder at a binding energy of 399.7 eV [Fig. 1(a)], which has also been observed in heavily doped SiC [22]. Moreover, it is found that the BL vertical position ($z_{\mathrm{C_{BL}}} = 2.30 \pm 0.02$ Å before and 2.28 ± 0.02 Å after doping) and its buckling ($F^H_{\mathrm{C_{BL}}} = 0.77 \pm 0.04$ to 0.74 ± 0.04) are hardly affected by the doping. This suggests that N dopants are unstable in the BL and tend to diffuse into the SiC substrate upon annealing, leaving the BL intact.

The N 1s spectra for both EMLG and QFMLG [Figs. 1(b) and 1(c)] show features at binding energies between 3 and 5.5 eV above $\mathrm{N_{SiC}}$. A closer look at Fig. 1(b) for EMLG reveals that more than one component is necessary to fit this peak. We present a fit result with three components at 400.7, 401.8, and 403.1 eV. Although their chemical states are different, the three N species share the same vertical position $P^H_{\mathrm{N_{gr}}} = 0.31$ (also when assuming a two-component model) and a high degree of ordering along the vertical direction, $F^H_{\mathrm{N_{gr}}} = 0.76 \pm 0.17$ (Table I). The sum of the three components is represented by the bottom EY curve in Fig. 1(e). Converting $P^H_{\mathrm{N_{gr}}}$ to

TABLE I. Summary of NIXSW results before and after 4 min of doping. For $\mathrm{C_{SiC}}$ and $\mathrm{N_{SiC}}$, the z value is given for $n = -1$. The error bar on F^H is 0.04, and 0.17 for C 1s, and N 1s components.

Pristine	BL			EMLG			QFMLG			
	P^H	F^H	z(Å)	P^H	F^H	z(Å)	P^H	F^H	z(Å)	Error (Å)
Si	0.03	1.31	0	0.04	1.33	0	0.03	1.31	0	
$\mathrm{C_{SiC}}$	0.75	1.10	−0.70	0.76	1.04	−0.68	0.75	0.99	−0.71	±0.01
$\mathrm{C_{BL}}$	0.94	0.77	2.30	0.97	0.53	2.37				±0.02
$\mathrm{C_{gr}}$				0.29	1.01	5.67	0.73	0.68	4.28	±0.01
Doped	**BL**			**EMLG**			**QFMLG**			
Si	0.04	1.33	0	0.03	1.31	0	0.03	1.31	0	
$\mathrm{C_{SiC}}$	0.76	1.07	−0.70	0.76	1.03	−0.69	0.76	1.01	−0.70	±0.01
$\mathrm{C_{BL}}$	0.94	0.74	2.28	0.98	0.41	2.37				±0.02
$\mathrm{C_{gr}}$				0.28	1.13	5.65	0.84	0.52	4.56	±0.01
$\mathrm{N_{SiC}}$	0.67	0.97	−0.91	0.66	0.79	−0.94	0.65	0.29	−0.96	±0.09
$\mathrm{N_{gr}}$				0.31	0.76	5.72	0.82	0.75	4.49	±0.05
$\mathrm{N_{int}}$							0.11	0.98	2.71	±0.04

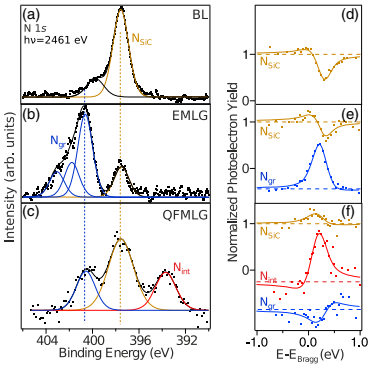

FIG. 1. N-doped samples after 4 min of N ion bombardment and annealing. N 1*s* XPS spectra for (a) the BL, (b) the EMLG, and (c) the QFMLG. The spectra were fitted using symmetrical Voigt line shapes. The experimental data points are shown as black dots, and the envelope as a black line. N_{SiC} is displayed in orange, N_{gr} in blue, and N_{int} in red. The corresponding EY curves are displayed in panels (d)–(f) with their best fits. The EY curves of N_{gr} and N_{int} are offset for clarity.

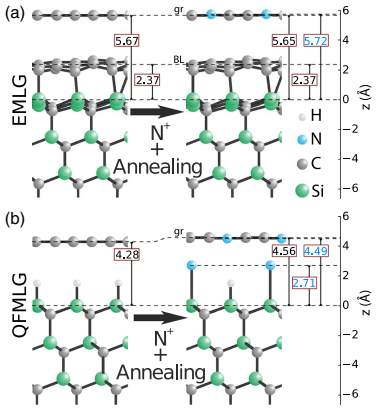

FIG. 2. Summary of the vertical positions (in Å) measured by the NIXSW technique for each atomic species in (a) EMLG and in (b) QFMLG, before and after N doping.

$z_{N_{gr}}$, we find that with $n = 2$ the height of the three species ($z_{N_{gr}} = 5.72 \pm 0.05$ Å) corresponds to the graphene vertical position [see Fig. 2(a)], which is not affected by the doping ($z_{C_{gr}} = 5.67 \pm 0.01$ Å before and 5.65 ± 0.01 Å after N doping). We therefore attribute the three N 1*s* components to N atoms incorporated into the graphene layer (N_{gr}) of EMLG. The NIXSW analysis of the BL in the EMLG sample shows that it remains unperturbed after N implantation [see Table I and Fig. 2(a)], as also observed above for the BL sample. Therefore, doping the EMLG with N does not affect the overlap of the van der Waals (vdW) radii or the interaction between the graphene layer and its support.

We note that a recent combined XPS and STM study [23] reported a nearly identical N 1*s* line shape as observed here for a N-doped mixture of mono- and bilayer graphene on 6*H*-SiC, where N_{gr} was modeled with two components associated with the graphene multilayer. This peak assignment is incompatible with the present NIXSW analysis, which shows that all N_{gr} components share the same vertical position. However, a key observation offering a plausible interpretation of the line shape of N_{gr} comes from the STM results in Ref. [23], which reveal a mixture of single N atoms and aggregates of two N atoms (mostly in a metaconfiguration) for the doping concentrations relevant to the present XPS and NIXSW experiments. We therefore assign the multiple N_{gr} components to single N atoms as well as to aggregates of two or more N atoms in graphene.

We now turn to QFMLG. In contrast to EMLG, after doping QFMLG, its graphene layer is pushed up significantly from $z_{C_{gr}} = 4.28 \pm 0.01$Å to 4.56 ± 0.01Å [see Table I and Fig. 2(b)]. The analysis of the EY curve for the N 1*s* component at 400.6 eV [Fig. 1(c)] yields a vertical position of $z_{N_{gr}} = 4.49 \pm 0.05$Å that is comparable to $z_{C_{gr}}$ of the doped graphene layer. One can therefore associate this component with the N implanted in graphene (N_{gr}). However, unlike doped EMLG, where multiple N_{gr} components are present [Fig. 1(b)], N_{gr} of doped QFMLG represents a single type of dopant, as evidenced by the well-defined N 1*s* component at 400.6 eV, which has the same binding energy as the main component of N_{gr} in EMLG (indicating that this dopant configuration is least dependent on the choice of support). Furthermore, by comparing the intensity of N_{gr}, normalized to the intensity of the graphene component in the C 1*s* core level, we find that there are twice less N atoms substituting C in the graphene honeycomb lattice of QFMLG than in that of EMLG, for the same N sputter conditions.

In addition to N_{SiC} and N_{gr}, doped QFMLG exhibits a third N 1*s* component at a binding energy of 393.7 eV [Fig. 1(c)]. Our NIXSW analysis shows that this component N_{int}, which yields a vertical position $z_{N_{int}} = 2.71 \pm 0.04$Å, can be best interpreted as N atoms replacing some of the H atoms within the intercalation layer. Because of its larger atomic size, N_{int} is situated at a higher position than that expected for H ($z_H = 1.5$Å) [24], leading to the above-mentioned elevation of graphene after the doping. Note, however, that graphene is lifted less (0.28 Å) than the H to N height difference (1.21 Å). This means that locally the vdW radii of the doped graphene layer and the intercalated N atoms must overlap. As we will see below, this has an important consequence for the electronic properties of N-doped QFMLG. Also note that the concomitant reduction of

PRL 116, 126805 (2016) PHYSICAL REVIEW LETTERS week ending 25 MARCH 2016

the graphene coherent fraction from $F^{H}_{C_{gr}} = 0.68 \pm 0.04$ to 0.52 ± 0.04 upon doping is an indication that the graphene is now buckled. Our result thus shows that, while pristine QFMLG exhibits the weakest coupling with the substrate [24], its structure is more affected by N doping than that of EMLG. We stress that considering the low concentration of N and the stability of the intercalated H at 1000 K, as proven by the presence of the Dirac cone after annealing [Figs. 3(e) and 3(f)], a scenario in which H is either fully desorbed or fully replaced by N can be excluded.

Having established the structural modifications of graphene under N doping, we now discuss the effects on its electronic properties. ARPES spectra measured around the $\bar{K}$ point of EMLG and QFMLG are shown in Fig. 3 for pristine graphene and for two doping steps. As expected, the Dirac point of the pristine EMLG is found about 0.4 eV below the Fermi edge [15]. The first doping step of 4 min shifts the Dirac cone towards higher binding energies by 0.2 eV, which corresponds to a carrier density increase of 1.4×10^{13} cm^{-2} [25]. It thus confirms that the N incorporation into the graphene sheet has led to *n*-type doping. Further doping continues to increase the carrier density, but at a lower rate: 0.9×10^{13} cm^{-2} over the next 4 min of doping [Fig. 3(c)]. QFMLG presents similar results: 1.2×10^{13} cm^{-2} and 0.6×10^{13} cm^{-2} increases for the first and second doping steps, respectively. Besides doping graphene, the introduction of dopants in the lattice also induces a broadening of the π band after each doping step. We note, however, that this broadening is more pronounced for EMLG than for QFMLG. As demonstrated in Ref. [23] and confirmed by STM in the present work for surfaces annealed to 1000 K (not shown), the method used here for doping does not introduce any defects in the graphene lattice other than substitutional N dopants. Therefore, the band broadening cannot stem from a defective lattice.

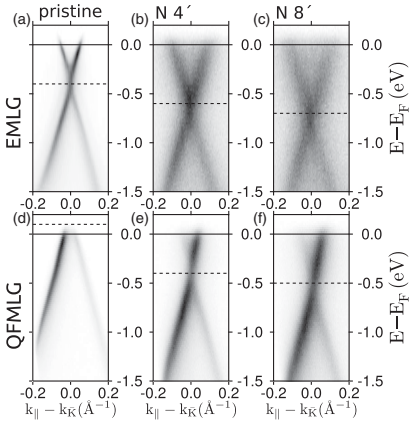

FIG. 3. ARPES spectra of the EMLG (a)–(c) and QFMLG (d)–(f) valence measured around the $\bar{K}$ point in the $\bar{\Gamma}\bar{K}$ direction of the graphene Brillouin zone with a HeI$_\alpha$ radiation for (a) and (d) pristine graphene, (b) and (e) after 4 min, (c) and (f) after 8 min doping. The Fermi and Dirac energies are represented by dashed and solid lines, respectively. In panels (d)–(f) and (a)–(c) the UV lamp is installed in and out of the scattering plane, respectively.

To better understand the origin of this broadening, we simulated the effects of N doping on the band structure of graphene. We performed total energy DFT [26] simulations on a (12×12) supercell of freestanding graphene containing three randomly distributed N substitutional dopants in the lattice. Four different dopant configurations have been included, and one example is given in Fig. 4(c). After relaxing the geometric structure, the band structure of the supercell is projected onto the first Brillouin zone for a direct comparison with the experimental data [27]. The results are shown in Fig. 4. Each of the four dopant configurations yields a slightly modified band structure with a band gap smaller than 0.1 eV and a slightly different downward energy shift of about 0.2 eV with respect to the pristine graphene. Superimposing them results in an effective broadening of the π band of graphene, without opening a sizable band gap. We therefore attribute the band broadening observed in the experimental ARPES data shown in Fig. 3 to the random N substitution in the graphene lattice.

From our combined study, an understanding of how the various N species contribute to the doping of graphene can be reached: For the same sputtering conditions, XPS reveals that the total amount of N incorporated in the graphene lattice (N_{gr}) of QFMLG is only half of that of EMLG, while ARPES shows comparable increases of carrier densities for the two samples. This indicates that N atoms substituting hydrogen at the interface of QFMLG (N_{int}) also contribute to the doping. This is consistent with the strong overlap of vdW radii between graphene and N_{int} that is observed by NIXSW for QFMLG. In contrast to EMLG, where N_{gr} contains multiple components but no N exists in the BL, the additional doping induced by N_{int} in QFMLG allows the same

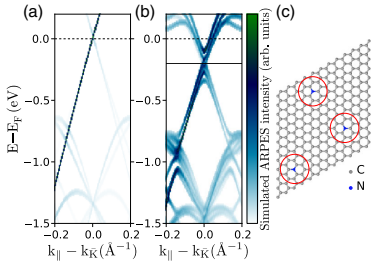

FIG. 4. (a) Simulated ARPES spectrum of a freestanding graphene layer, relaxed in a 12×12 supercell. (b) Superimposition of four simulated ARPES spectra of differently N-doped freestanding graphene supercells. (c) Sketch of one of the N-doped supercells used in (b). The N atoms are highlighted by red circles.

number of charge carriers to be generated, albeit with fewer substitutional dopants in graphene that are, moreover, of a single type only, both of which in turn reduce the π-band broadening of QFMLG in ARPES.

To conclude, we find clear evidence that the support has multiple influences on the doping of a graphene layer. It affects the quantity as well as the variety of dopants created in the honeycomb lattice. Furthermore, we show that the support can host foreign species that make an additional contribution to the doping of graphene.

F. C. B. acknowledges financial support from the Initiative and Networking Fund of the Helmholtz Association, Postdoc Programme VH-PD-025. Support by the German Research Foundation (DFG) in the framework of the Priority Program 1459 Graphene, project Sta315/8-2 is gratefully acknowledged. This work has been supported by the grant agency of the Czech republic, Grant No. 15-07172S. Access to computing and storage facilities owned by parties and projects contributing to the Czech National Grid Infrastructure MetaCentrum, provided under the program "Projects of Large Infrastructure for Research, Development, and Innovations" (LM2010005), is greatly appreciated. The authors would like to thank D. McCue for his excellent technical support at the I09 beam line.

*f.bocquet@fz-juelich.de

[1] A. K. Geim, Graphene: Status and prospects, Science **324**, 1530 (2009).

[2] A. H. Castro Neto, F. Guinea, N. M. R. Peres, K. S. Novoselov, and A. K. Geim, The electronic properties of graphene, Rev. Mod. Phys. **81**, 109 (2009).

[3] Q. Tang, Z. Zhou, and Z. Chen, Graphene-related nanomaterials: tuning properties by functionalization, Nanoscale **5**, 4541 (2013).

[4] L. S. Panchakarla, K. S. Subrahmanyam, S. K. Saha, A. Govindaraj, H. R. Krishnamurthy, U. V. Waghmare, and C. N. R. Rao, Synthesis, structure, and properties of boron- and nitrogen-doped graphene, Adv. Mater. **21**, 4726 (2009).

[5] F. Karlický, K. Kumara Ramanatha Datta, M. Otyepka, and R. Zbořil, Halogenated graphenes: Rapidly growing family of graphene derivatives, ACS Nano **7**, 6434 (2013).

[6] H. Wang, T. Maiyalagan, and X. Wang, Review on recent progress in nitrogen-doped graphene: Synthesis, characterization, and its potential applications, ACS Catal. **2**, 781 (2012).

[7] A. L. M. Reddy, A. Srivastava, S. R. Gowda, H. Gullapalli, M. Dubey, and P. M. Ajayan, Synthesis of nitrogen-doped graphene films for lithium battery application, ACS Nano **4**, 6337 (2010).

[8] H. M. Jeong, J. W. Lee, W. H. Shin, Y. J. Choi, H. J. Shin, J. K. Kang, and J. W. Choi, Nitrogen-doped graphene for high-performance ultracapacitors and the importance of nitrogen-doped sites at basal planes, Nano Lett. **11**, 2472 (2011).

[9] M. D. Stoller, S. Park, Y. Zhu, J. An, and R. S. Ruoff, Graphene-based ultracapacitors, Nano Lett. **8**, 3498 (2008).

[10] B. Xia, Y. Yan, X. Wang, and X. W. Lou, Recent progress on graphene-based hybrid electrocatalysts, Mater. Horiz. **1**, 379 (2014).

[11] D. Wei, Y. Liu, Y. Wang, H. Zhang, L. Huang, and G. Yu, Synthesis of N-doped graphene by chemical vapor deposition and its electrical properties, Nano Lett. **9**, 1752 (2009).

[12] B. Guo, Q. Liu, E. Chen, H. Zhu, L. Fang, and J.-R. Gong, Controllable N-doping of graphene, Nano Lett. **10**, 4975 (2010).

[13] D. Geng, S. Yang, Y. Zhang, J. Yang, J. Liu, R. Li, T.-K. Sham, X. Sun, S. Ye, and S. Knights, Nitrogen doping effects on the structure of graphene, Appl. Surf. Sci. **257**, 9193 (2011).

[14] D. Y. Usachov, A. V. Fedorov, O. Y. Vilkov, B. V. Senkovskiy, V. K. Adamchuk, B. V. Andryushechkin, and D. V. Vyalikh, Synthesis and electronic structure of nitrogen-doped graphene, Phys. Solid State **55**, 1325 (2013).

[15] C. Riedl, C. Coletti, and U. Starke, Structural and electronic properties of epitaxial graphene on SiC(0001): A review of growth, characterization, transfer doping and hydrogen intercalation, J. Phys. D **43**, 374009 (2010).

[16] More details of the experiments and the end-station can be found in Ref. [24].

[17] D. P. Woodruff, Surface structure determination using x-ray standing waves, Rep. Prog. Phys. **68**, 743 (2005).

[18] D. P. Woodruff, Non-dipole effects in high-energy photoelectron emission; identification and quantification using x-ray standing waves, Nucl. Instrum. Methods Phys. Res., Sect. A **547**, 187 (2005).

[19] See Refs. [20,21,24]. As an example, the measured positions $z_{C_{BL}}$ of the C atoms in the buffer layer relative to the topmost Si atoms are 2.30 ± 0.02 Å and 2.37 ± 0.02 Å for the BL and EMLG samples, respectively, compared to predicted positions of 2.32 Å and 2.36 Å [20].

[20] L. Nemec, V. Blum, P. Rinke, and M. Scheffler, Thermodynamic Equilibrium Conditions of Graphene Films on SiC, Phys. Rev. Lett. **111**, 065502 (2013).

[21] J. D. Emery, B. Detlefs, H. J. Karmel, L. O. Nyakiti, D. K. Gaskill, M. C. Hersam, J. Zegenhagen, and M. J. Bedzyk, Chemically Resolved Interface Structure of Epitaxial Graphene on SiC(0001), Phys. Rev. Lett. **111**, 215501 (2013).

[22] M. B. Wijesundara, C. R. Stoldt, C. Carraro, R. T. Howe, and R. Maboudian, Nitrogen doping of polycrystalline 3C-SiC films grown by single-source chemical vapor deposition, Thin Solid Films **419**, 69 (2002).

[23] M. Telychko, P. Mutombo, M. Ondrcáček, P. Hapala, F. C. Bocquet, J. Kolorenč, M. Vondráček, P. Jelínek, and M. Švec, Achieving high-quality single-atom nitrogen doping of graphene/SiC(0001) by ion implantation and subsequent thermal stabilization, ACS Nano **8**, 7318 (2014).

[24] J. Sforzini, L. Nemec, T. Denig, B. Stadtmüller, T.-L. Lee, C. Kumpf, S. Soubatch, U. Starke, P. Rinke, V. Blum, F. C. Bocquet, and F. S. Tautz, Approaching Truly Freestanding Graphene: The Structure of Hydrogen-Intercalated Graphene on 6*H*-SiC(0001), Phys. Rev. Lett. **114**, 106804 (2015).

[25] I. Gierz, C. Riedl, U. Starke, C. R. Ast, and K. Kern, Atomic Hole Doping of Graphene, Nano Lett. **8**, 4603 (2008).

[26] J. P. Lewis, P. Jelínek, J. Ortega, A. A. Demkov, D. G. Trabada, B. Haycock, H. Wang, G. Adams, J. K. Tomfohr,

E. Abad, H. Wang, and D. A. Drabold, Advances and applications in the FIREBALL *ab initio* tight-binding molecular-dynamics formalism, Phys. Status Solidi (b) **248**, 1989 (2011).

[27] See the Supplemental Material of M. Švec, P. Hapala, M. Ondráček, P. Merino, M. Blanco-Rey, P. Mutombo, M. Vondráček, Y. Polyak, V. Cháb, J. A. Martín Gago, and P. Jelínek, Silicene versus two-dimensional ordered silicide: Atomic and electronic structure of Si-$(\sqrt{19} \times \sqrt{19})R23.4°$/Pt(111), Phys. Rev. B **89**, 201412(R) (2014).

7 Boron Doping of Graphene

7.1 Introduction

In the previous chapter, details of the n-type doping of graphene have been presented. By substituting heteroatoms into the graphene lattice with less valence electrons than carbon, p-type doping is achieved. Also, p-type doped graphene, for example through boron substitution, gives rise to useful applications [13]. However, during the last years the boron doping of graphene has not received as much consideration as the nitrogen doping, mostly because of the difficult synthesis of boron-doped graphene [88].

Recently, Telychko *et al.* reported a simple method to prepare high-quality boron-doped graphene on SiC [71]. After the bare 6H-SiC(0001) is cleaned, boron atoms are deposited on the surface and graphene growth is achieved by thermal annealing. The authors carried out extensive investigation using the STM technique, demonstrating that the boron dopants are homogeneously distributed in the graphene lattice. However, before using boron-doped graphene obtained with this method in electronic applications, knowledge regarding the chemical environment of the dopants is necessary. The experimental results reported in: *Trasformation of metallic boron into substitutional dopants in graphene on 6H-SiC(0001)* contributes to this knowledge.

The growth of B-doped EMLG on 6H-SiC(0001) is followed by XPS and NEXAFS in order to investigate the mechanism of boron incorporation into the graphene lattice. An important question is whether they also affect the interface and substrate. The observed two distinct boron chemical states suggest that a fraction of the boron atoms diffuse into the SiC substrate upon annealing, while the remaining part is successfully incorporated into the carbon lattice. However, as no chemical shift is detected between the BL and EMLG surfaces, the dopants are incorporated into both lattices with the same chemical bonding. The NEXAFS experiments, supported by

DFT calculations, demonstrate that the dopants effectively participate in the valence electronic states of graphene.

7.2 Reprint of Physical Review B 93, 041302(R) (2016)

The following paper with the title *Trasformation of metallic boron into substitutional dopants in graphene on 6H-SiC(0001)* [89] Copyright 2016 by the American Physical Society contains the following contributions from the authors:

The STM image has been acquired by M. Telychko, M. Švec and P. Jelínek.

The DFT calculations of the graphene structure and adsorption spectra have been performed by O. Krecjčí and P. Jelínek.

The experiments have been carried out at the Material Science beamline by J. Sforzini, M. Telychko, M. Švec and F. C. Bocquet with the support of M. Vondráček.

The experimental data have been analyzed by J. Sforzini with the support of F. C. Bocquet and F. S. Tautz.

The interpretation of the results has been developed in discussion between J. Sforzini, F. C. Bocquet, M. Švec and F. S. Tautz.

The paper has been written by J. Sforzini, F. C. Bocquet and F. S. Tautz.

RAPID COMMUNICATIONS

PHYSICAL REVIEW B **93**, 041302(R) (2016)

Transformation of metallic boron into substitutional dopants in graphene on 6*H*-SiC(0001)

J. Sforzini,[1,2] M. Telychko,[3,4] O. Krejčí,[3,4] M. Vondráček,[5] M. Švec,[3] F. C. Bocquet,[1,2,*] and F. S. Tautz[1,2]

[1]*Peter Grünberg Institut (PGI-3), Forschungszentrum Jülich, 52425 Jülich, Germany*

[2]*Jülich Aachen Research Alliance (JARA), Fundamentals of Future Information Technology, 52425 Jülich, Germany*

[3]*Institute of Physics of the Czech Academy of Sciences, Cukrovarnická 10, 16200 Prague, Czech Republic*

[4]*Faculty of Mathematics and Physics, Charles University, V Holešovičkách 2, 18000 Prague, Czech Republic*

[5]*Institute of Physics of the Czech Academy of Sciences, Na Slovance 2, 18221 Prague, Czech Republic*

(Received 5 October 2015; published 19 January 2016)

We investigate the development of the local bonding and chemical state of boron atoms during the growth of B-doped graphene on 6*H*-SiC(0001). Photoemission experiments reveal the presence of two chemical states, namely, boron in the uppermost SiC bilayers and boron substituted in both the graphene and buffer layer lattices. We demonstrate the participation of the dopant in the π electron system of graphene by the presence of the π^* resonance in the near edge x-ray adsorption fine structure (NEXAFS) recorded at the B *K*-edge. The experimental findings are supported by NEXAFS simulations.

DOI: 10.1103/PhysRevB.93.041302

In recent years, graphene has attracted a considerable interest because its physical properties make it suitable for, among others, spintronic devices [1] and transistors [2]. It is well known that covalent and noncovalent modifications of graphene can lead to an enhancement of its magnetic and electrical properties and, consequently, to an improvement of graphene-based devices [3]. For example, substitutional doping, i.e., the replacement of a C atom by a heteroatom in the graphene lattice, is one way to tune the intrinsic properties of graphene. Doped graphene can be used in supercapacitors [4], batteries [5], electrocatalysts [6], and as support for alternative energy devices [7]. While *n*-doped graphene, mostly made through substitutional N doping [8], is extensively studied, *p*-doped graphene, e.g., with B, has been less explored experimentally [9].

In our previous work [10] we demonstrated by scanning tunneling microscopy (STM) that, using a suitable doping procedure, the B dopants are homogeneously distributed in the graphene layer. However, STM experiments do not provide any information on their chemical states in terms of local bonding, their activation, and whether the doping procedure itself influences the substrate underneath the graphene layer. In this Rapid Communication, we present a detailed spectroscopic study of the growth of B-doped graphene on 6*H*-SiC(0001) obtained by depositing B on SiC prior to graphene formation. In contrast to other methods already proposed [11–15], in which either exfoliated graphene or chemical vapor deposition is employed, this preparation ensures a simple routine free of any precursors to achieve high-quality B-doped graphene. We find that the B atoms are incorporated in an identical chemical environment into the graphene layer as well as into the buffer layer, exhibiting the same local structure in both lattices. Moreover, the dopants become part of the π system of graphene and are thus activated. Our experimental results are supported by theoretical calculations. We also show that part of the B diffuses into the SiC bulk.

The experiments were carried out at the Materials Science Beamline at the Elettra Synchrotron. The Si-rich (3×3) surface reconstruction of SiC was prepared by 30 min of annealing at 900 °C under a flux of Si atoms until a sharp and intense low electron energy diffraction (LEED) pattern was obtained. The doping was achieved by depositing B for 1 min from an *e*-beam evaporator keeping the substrate at 900 °C. The B-doped graphene layer was then prepared from the (3×3) reconstruction by annealing slowly for approximately 10 min in 50 °C steps up to 1150 °C. The growth was monitored by LEED, x-ray photoelectron spectroscopy (XPS), and near edge x-ray adsorption fine structure (NEXAFS). The XPS and NEXAFS spectra were recorded with a Specs Phoibos 150 hemispherical electron energy analyzer. The angle between the beamline axis and the analyzer is 60°. We used the following measurement geometries: a grazing incidence geometry (GI), in which the angle between the incident x-ray beam and the surface normal is 60° for XPS and 80° for NEXAFS, and a normal incidence geometry (NI) for NEXAFS only. The XPS spectra were recorded with photon energies of 400, 250 and 150 eV for C 1*s*, B 1*s*, and Si 2*p*, respectively. The binding energies (BEs) were calibrated by measuring the Fermi edge on a tantalum foil. The NEXAFS spectra were acquired at the C and B *K*-edges using KLL Auger yields. For B, the NEXAFS data were normalized to the intensity of the photon flux (measured by a high transmission gold mesh) and subtracted by the background (clean sample). For C, the intensity normalization was not possible because of the mesh contamination and only the background subtraction was applied. STM images were acquired in ultrahigh vacuum and at room temperature using a tungsten tip. In order to confirm the interpretation of the experimental NEXAFS spectra, simulations were performed with the transition potential method [16,17] built within the GPAW code [18,19] and with the spin-polarized general-gradient approximation (GGA) exchange-correlation functional of Perdew, Burke, and Ernzerhof (PBE) [20]. The simulated spectra were broadened by a Lorentzian and a Gaussian of full width at half maximum

*f.bocquet@fz-juelich.de

RAPID COMMUNICATIONS

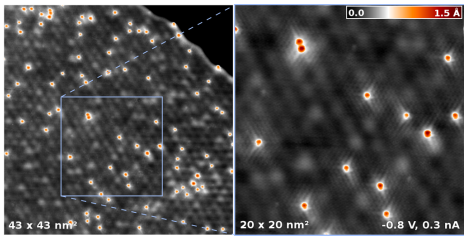

FIG. 1. STM topography images of B-doped bilayer graphene obtained with a bias voltage of −0.8 V and with a tunneling current of 0.3 nA.

(FWHM) 0.1 and 0.5 eV, respectively. The Gaussian FWHM was linearly increased from 0.5 to 10 eV for photon energies from 187 to 207 eV. The structure of freestanding B-doped graphene was optimized with density functional theory (DFT) via the FIREBALL DFT code [21,22].

Figure 1 shows STM images of the doped graphene layer prepared using the method described above. The images are recorded in a bilayer region for better visualization of the B dopants, but we have checked that B atoms show the same incorporation behavior also in single layer graphene. The B atoms, seen as red-orange dots in the image, are present in the graphene layer with a concentration of $(0.13 \pm 0.03)\%$ and are homogeneously distributed. In order to study whether the B atoms are incorporated into the graphene lattice and to find out if the doping also affects the substrate, we turn to photoemission experiments and take advantage of its chemical sensitivity to follow the mechanism of the incorporation of B into the graphene lattice.

Figure 2 shows the XPS spectra of C 1*s* [Fig. 2(a)] and B 1*s* [Fig. 2(c)] core levels at each annealing step during graphene growth, accompanied by the corresponding LEED patterns [Fig. 2(b)]. For the clean Si-rich (3×3) reconstruction a single C 1*s* component at a BE of 282.7 eV is observed. It corresponds to C in the bulk of SiC (C_{SiC}). After depositing the B atoms, a peak at 187.5 eV is detected in the B 1*s* spectra. The annealing step at 950 °C does not affect this peak. Since its BE is found to be the same as the one reported for metallic B [23] and since LEED still presents a sharp (3×3) pattern, we assign this peak to unreacted B present at the surface ($B_{(3\times3)}$). We note in passing that due to previous preparations, a small quantity of $B_{(3\times3)}$ is detectable on the clean (3×3) reconstruction.

After annealing at 1000 °C, a mixture of the Si-rich $(\sqrt{3}\times\sqrt{3})R30^\circ$ and the C-rich $(6\sqrt{3}\times6\sqrt{3})R30^\circ$ (the so-called buffer layer, BL) reconstructions is observed. The distinct band bendings of the two new reconstructions, simultaneously present at this annealing temperature only, broaden the C_{SiC} peak and shift it towards higher BE [24], since now two distinct signals contribute to it: bulk C below the Si-terminated $(\sqrt{3}\times\sqrt{3})R30^\circ$ at 283.2 eV, present only at this annealing step, and second, bulk C below the C-terminated $(6\sqrt{3}\times6\sqrt{3})R30^\circ$ at 284 eV, detected also after annealing to higher temperatures. The formation of the BL, a carbon layer covalently bonded to the topmost Si atoms, stemming from the depletion of Si atoms at high temperature [25] and present only on parts of the surface, produces the peak at 285.3 eV, labeled C_{BL}.

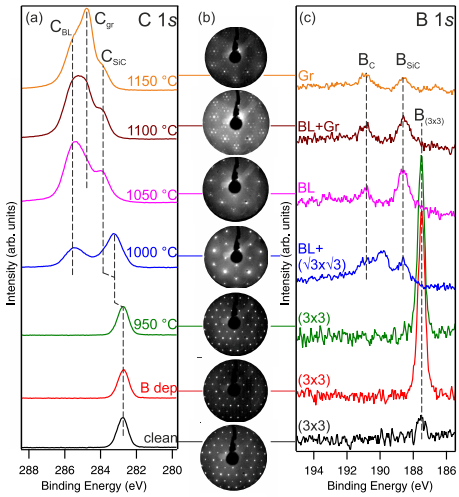

FIG. 2. The XPS spectra of (a) C 1*s* and of (c) B 1*s* measured with a photon energy of 400 and 250 eV, respectively, are shown for each annealing temperature. The corresponding LEED images are displayed in (b).

At the same annealing step, the B 1*s* spectrum clearly shows a chemical change, resulting in the appearance of several features. We attribute the central peak at 189.8 eV to an intermediate state related to the $(\sqrt{3}\times\sqrt{3})R30^\circ$ reconstruction, as it appears only at this annealing temperature. The peaks at 188.6 (B_{SiC}) and 190.8 eV (B_C), observed until the final step of graphene formation, must be related to the growth of the C-rich $(6\sqrt{3}\times6\sqrt{3})R30^\circ$ reconstruction, as no band bending induced shift of these peaks is observed between 1000 and 1150 °C. The peak at lower BE, B_{SiC}, detected also in spectra of SiC-B composite powders [26], shows that part of the deposited B in the C-rich region diffuses to the SiC bulk. Our results suggest that this diffusion only occurs at temperatures high enough for the BL to form. The peak at higher BE, B_C, indicates the participation of B in the formation of the BL sp^2/sp^3 lattice.

At higher annealing temperatures (from 1050 to 1150 °C) the BL, in which part of the B is incorporated, transforms into epitaxial graphene, yielding a new component, C_{gr}, at 284.7 eV in the C 1*s* core level spectra [Fig. 2(a)]. This proceeds as a new BL grows underneath. As this process does not affect the B 1*s* chemical environment, no shift of either B_{SiC} or B_C is observed [Fig. 2(c)]. The B_{SiC} intensity decreases with the annealing temperature, which can be explained by a further diffusion of B into the SiC bulk and/or by an attenuation of the signal due to the carbon layers (BL and graphene). In contrast, the B_C intensity is constant, suggesting that the B atoms in the graphene and BL lattices are thermally stable.

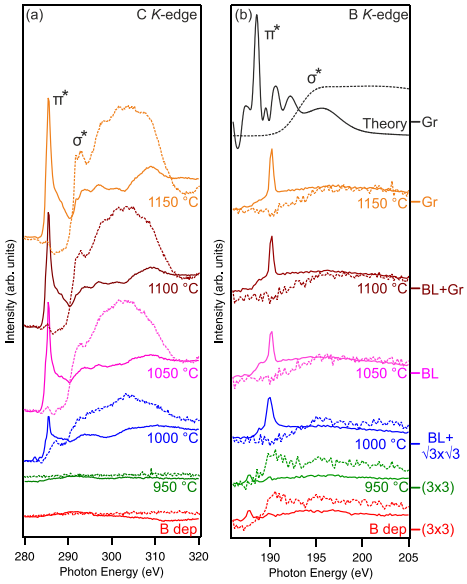

FIG. 3. The NEXAFS difference spectra measured in the GI (continuous line) and the NI geometries (dotted line) of (a) C K-edge and (b) B K-edge are shown for each annealing temperature. The corresponding spectra of the (3×3) reconstruction have been subtracted. The top black curves in (b) present the calculated B K-edge NEXAFS spectra of B-doped freestanding graphene.

Unlike in N-doped graphene [27], there is only one local bonding configuration between the dopant and the host lattice, as evidenced by the single peak B_C at 190.8 eV. Moreover, as no BE shift is observed for B_C between 1050 and 1150 °C, it implies that B has the same chemical environment in the BL and in graphene.

In order to determine this chemical environment, we have carried out NEXAFS experiments, which allow us to distinguish between the sp^2 and sp^3 hybridizations of B. Only in the case of sp^2 hybridization we expect a directionally dependent π^* resonance in our spectra. Figures 3(a) and 3(b) show C K- and B K-edge spectra in grazing (continuous lines) and normal incidence (dotted lines), respectively, from which the corresponding spectra of the clean (3×3) reconstruction have been subtracted. In the B K-edge spectrum no peak is detected for the clean sample in either geometries (not shown). As the (3×3) reconstruction is stable up to 950 °C, no features are detected in the C K-edge difference spectra. However, in the B K-edge difference spectra, a small peak appears in both GI at $h\nu = 187.7$ eV and NI at $h\nu = 190.8$ eV. This peak is related to metallic B on the Si-rich (3×3) reconstruction.

As the C-rich phase starts to evolve above the annealing temperature of 1000 °C, both peaks disappear in the B K-edge spectra, while a new one is observed at $h\nu = 190.1$ eV in GI only. In the corresponding C K-edge spectra the transition from the C 1s initial state to the p_z orbitals (π^* resonance) is detected at $h\nu = 285.5$ eV. As expected, this resonance is quenched in the NI geometry [28], but the transition from the C 1s to the p_{xy} orbitals (σ^* resonance) is visible around $h\nu = 292$ eV in NI [29]. The simultaneous appearance of the carbon π^* transition, accompanied by the formation of B_C and C_{BL} in the XPS spectra of Fig. 2, demonstrates that the peak at $h\nu = 190.1$ eV in the B K-edge spectra is a transition from the B 1s core level to the π system of graphene and the BL. This shows that at least some of the B atoms are indeed incorporated into the host lattices and participate in their π systems. This is confirmed by the expected disappearance of this peak in NI.

In order to support these results, the GI and NI spectra were simulated for B-doped freestanding graphene [Fig. 3(b), top curves]. The behavior of the calculated π^* resonance reproduces our experimental results. According to Ljungberg *et al.* [17], the precision of the Δ Kohn-Sham (ΔKS) approach is within 1 eV. In our case the experimental peaks are shifted by about 1.6 eV towards higher photon energies compared to the calculated ones. This difference can be caused by the effect of the SiC substrate (the calculations being performed on freestanding graphene), which shifts the core levels to higher BE and therefore the corresponding NEXAFS transitions to a higher photon energy.

In summary, we have investigated the chemical state of boron, deposited on the (3×3) reconstruction, during the growth of graphene on 6H-SiC(0001). STM experiments show that the graphene layer is homogeneously decorated by single B atoms. The presence of the π^* transition in the B NEXAFS spectra proves that the B atoms dope the graphene layer by contributing to its π system. Moreover, B is found in a single chemical environment in both the buffer layer and graphene lattices. XPS measurements reveal also that a part of the B atoms diffuse into the upper SiC bilayers. Therefore, we conclude that this preparation is a valid method to obtain high quality B-doped graphene.

F.C.B. acknowledges financial support from the Initiative and Networking Fund of the Helmholtz Association, Postdoc Programme VH-PD-025. This work has been supported by grant agency of the Czech republic, Grant No. 15-07172S. Access to computing and storage facilities owned by parties and projects contributing to the Czech National Grid Infrastructure MetaCentrum, provided under the program "Projects of Large Infrastructure for Research, Development, and Innovations" (LM2010005), is greatly appreciated.

[1] W. Han, R. K. Kawakami, M. Gmitra, and J. Fabian, Graphene spintronics, Nat. Nanotechnol. **9**, 794 (2014).

[2] D. Logoteta, G. Fiori, and G. Iannaccone, Graphene-based lateral heterostructure transistors exhibit better intrinsic performance than graphene-based vertical transistors as post-CMOS devices, Sci. Rep. **4**, 6607 (2014).

[3] D. Kepaptsoglou, T. P. Hardcastle, C. R. Seabourne, U. Bangert, R. Zan, J. A. Amani, H. Hofsäss, R. J. Nicholls, R. M. D.

Brydson, A. J. Scott, and Q. M. Ramasse, Electronic structure modification of ion implanted graphene: The spectroscopic signatures of *p*- and *n*-type doping, ACS Nano **9**, 11398 (2015).

[4] K. Gopalakrishnan, A. Govindaraj, and C. N. R. Rao, Extraordinary supercapacitor performance of heavily nitrogenated graphene oxide obtained by microwave synthesis, J. Mater. Chem. A **1**, 7563 (2013).

[5] Z.-S. Wu, W. Ren, L. Xu, F. Li, and H.-M. Cheng, Doped graphene sheets as anode materials with superhigh rate and large capacity for lithium ion batteries, ACS Nano **5**, 5463 (2011).

[6] C. Zhu and S. Dong, Recent progress in graphene-based nanomaterials as advanced electrocatalysts towards oxygen reduction reaction, Nanoscale **5**, 1753 (2013).

[7] U. Maitra, U. Gupta, M. De, R. Datta, A. Govindaraj, and C. N. R. Rao, Highly effective visible-light-induced H(2) generation by single-layer 1T-MoS(2) and a nanocomposite of few-layer 2H-MoS(2) with heavily nitrogenated graphene, Angew. Chem., Int. Ed. **52**, 13057 (2013).

[8] H. Wang, T. Maiyalagan, and X. Wang, Review on recent progress in nitrogen-doped graphene: Synthesis, characterization, and its potential applications, ACS Catal. **2**, 781 (2012).

[9] D.-A. Yeom, W. Jeon, N. D. K. Tu, S. Y. Yeo, S.-S. Lee, B. J. Sung, H. Chang, J. A. Lim, and H. Kim, High-concentration boron doping of graphene nanoplatelets by simple thermal annealing and their supercapacitive properties, Sci. Rep. **5**, 9817 (2015).

[10] M. Telychko, P. Mutombo, P. Merino, P. Hapala, M. Ondráček, F. C. Bocquet, J. Sforzini, O. Stetsovych, M. Vondráček, P. Jelínek, and M. Švec, Electronic and chemical properties of donor, acceptor centers in graphene, ACS Nano **9**, 9180 (2015).

[11] W. Norimatsu, K. Hirata, Y. Yamamoto, S. Arai, and M. Kusunoki, Epitaxial growth of boron-doped graphene by thermal decomposition of B4C, J. Phys.: Condens. Matter **24**, 314207 (2012).

[12] Z.-H. Sheng, H.-L. Gao, W.-J. Bao, F.-B. Wang, and X.-H. Xia, Synthesis of boron doped graphene for oxygen reduction reaction in fuel cells, J. Mater. Chem. **22**, 390 (2012).

[13] Y. A. Kim, K. Fujisawa, H. Muramatsu, T. Hayashi, M. Endo, T. Fujimori, K. Kaneko, M. Terrones, J. Behrends, A. Eckmann, C. Casiraghi, K. S. Novoselov, R. Saito, and M. S. Dresselhaus, Raman spectroscopy of boron-doped single-layer graphene, ACS Nano **6**, 6293 (2012).

[14] W. Zhao, J. Gebhardt, K. Gotterbarm, O. Höfert, C. Gleichweit, C. Papp, A. Görling, and H.-P. Steinrück, Gold intercalation of boron-doped graphene on Ni(111): XPS and DFT study, J. Phys.: Condens. Matter **25**, 445002 (2013).

[15] Y.-B. Tang, L.-C. Yin, Y. Yang, X.-H. Bo, Y.-L. Cao, H.-E. Wang, W.-J. Zhang, I. Bello, S.-T. Lee, H.-M. Cheng, and C.-S. Lee, Tunable band gaps and *p*-type transport properties of boron-doped graphenes by controllable ion doping using reactive microwave plasma, ACS Nano **6**, 1970 (2012).

[16] L. Triguero, L. G. M. Pettersson, and H. Ågren, Calculations of near-edge x-ray-absorption spectra of gas-phase and chemisorbed molecules by means of density-functional and transition-potential theory, Phys. Rev. B **58**, 8097 (1998).

[17] M. P. Ljungberg, J. J. Mortensen, and L. G. M. Pettersson, An implementation of core level spectroscopies in a real space projector augmented wave density functional theory code, J. Electron Spectrosc. Relat. Phenom. **184**, 427 (2011).

[18] J. J. Mortensen, L. B. Hansen, and K. W. Jacobsen, Real-space grid implementation of the projector augmented wave method, Phys. Rev. B **71**, 035109 (2005).

[19] J. Enkovaara, C. Rostgaard, J. J. Mortensen, J. Chen, M. Duak, L. Ferrighi, J. Gavnholt, C. Glinsvad, V. Haikola, H. A. Hansen, H. H. Kristoffersen, M. Kuisma, A. H. Larsen, L. Lehtovaara, M. Ljungberg, O. Lopez-Acevedo, P. G. Moses, J. Ojanen, T. Olsen, V. Petzold, N. A. Romero, J. Stausholm-Møller, M. Strange, G. A. Tritsaris, M. Vanin, M. Walter, B. Hammer, H. Häkkinen, G. K. H. Madsen, R. M. Nieminen, J. K. Nørskov, M. Puska, T. T. Rantala, J. Schiøtz, K. S. Thygesen, and K. W. Jacobsen, Electronic structure calculations with GPAW: A real-space implementation of the projector augmented-wave method, J. Phys.: Condens. Matter **22**, 253202 (2010).

[20] J. P. Perdew, K. Burke, and M. Ernzerhof, Generalized Gradient Approximation Made Simple, Phys. Rev. Lett. **77**, 3865 (1996).

[21] P. Jelínek, H. Wang, J. P. Lewis, O. F. Sankey, and J. Ortega, Multicenter approach to the exchange-correlation interactions in *ab initio* tight-binding methods, Phys. Rev. B **71**, 235101 (2005).

[22] J. P. Lewis, P. Jelínek, J. Ortega, A. A. Demkov, D. G. Trabada, B. Haycock, H. Wang, G. Adams, J. K. Tomfohr, E. Abad, H. Wang, and D. A. Drabold, Advances and applications in the FIREBALL *ab initio* tight-binding molecular-dynamics formalism, Phys. Status Solidi B **248**, 1989 (2011).

[23] W. E. Moddeman, A. R. Burke, W. C. Bowling, and D. S. Foose, Surface oxides of boron and $B_{12}O_2$ as determined by XPS, Surf. Interface Anal. **14**, 224 (1989).

[24] W. Chen, S. Chen, Z. H. Ni, H. Huang, D. C. Qi, X. Y. Gao, Z. X. Shen, and A. T. S. Wee, Band-bending at the graphene-SiC interfaces: Effect of the substrate, Jpn. J. Appl. Phys. **49**, 01AH05 (2010).

[25] C. Riedl, C. Coletti, and U. Starke, Structural and electronic properties of epitaxial graphene on SiC(0001): A review of growth, characterization, transfer doping and hydrogen intercalation, J. Phys. D: Appl. Phys. **43**, 374009 (2010).

[26] L. Chen, T. Goto, T. Hirai, and T. Amano, State of boron in chemical vapour-deposited SiC-B composite powders, J. Mater. Sci. Lett. **9**, 997 (1990).

[27] M. Telychko, P. Mutombo, M. Ondráček, P. Hapala, F. C. Bocquet, J. Kolorenč, M. Vondráček, P. Jelínek, and M. Švec, Achieving high-quality single-atom nitrogen doping of graphene/SiC(0001) by ion implantation and subsequent thermal stabilization, ACS Nano **8**, 7318 (2014).

[28] J. Stöhr and R. Jaeger, Absorption-edge resonances, core-hole screening, and orientation of chemisorbed molecules: CO, NO, and N_2 on Ni(100), Phys. Rev. B **26**, 4111 (1982).

[29] D. Pacilé, M. Papagno, A. Fraile Rodríguez, M. Grioni, L. Papagno, Ç. Ö. Girit, J. C. Meyer, G. E. Begtrup, and A. Zettl, Near-Edge X-Ray Absorption Fine-Structure Investigation of Graphene, Phys. Rev. Lett. **101**, 066806 (2008).

8 Pd- and Pt-Phthalocyanine

8.1 Introduction

Among organic compounds, metal-phthalocyanine molecules have extensively been investigated during the last years because of their extended aromaticity and flexibility in forming 2D layers [16]. Materials with added functionality beyond simple switching, such as chemical recognition, piezoelectricity, and hysteresis can be realized and employed in, e.g., organic light emitting diodes, field effect transistors and solar cells [14, 90–92].

For the use of Pc layers in electronic and optoelectronic devices, it is important to study and control the interaction between the layers and the metal on which they are absorbed. In general, the device performance is related on the nature of the interaction, i.e. chemisorptive or physisorptive, at the interface and/or on specific contributions from, i.e. central metal or π electronic system. Thus, the presence and behavior of the charge transfer between the molecules and the substrate must be explored.

For this particular class of molecules two situations are feasible in the presence of an interaction with the substrate. Since the LUMO of a Pc molecule is doubly degenerate, as described in Sec. 3.2, both of the LUMO levels or only one level can be involved in the charge transfer. This can easily be investigated using, for example, the orbital tomography approach [93, 94]. However, this method is not always available and does not perform well when the molecules are adsorbed on a surface of (111) orientation due to the presence of many symmetry-related domains.

A reasonable alternative is to study, using HREELS, the molecular symmetry reduction upon adsorption as it implies the activation of non-active IR vibrational modes through i.e. degeneracy lifting. This new approach based on the analysis of the molecule/substrate complex symmetry is presented in: *Adsorption-induced*

symmetry reduction of metal-phthalocyanine studied by vibrational spectroscopy and summarized in the following.

The symmetry and vibrational properties of PtPc and PdPc layers on Ag(111) are investigated using HREELS. Our results show that both molecules adsorb with their molecular plane parallel to the surface, and that there is an interaction with the substrate. With the help of the surface selection rule and group theory, the symmetry of the molecule/substrate complex is identified by analyzing the experimentally observed activated dipole scattering modes. As these modes belong to the two-fold symmetry and are coupled with the charge transfer, an unequal occupancy of the LUMO is demonstrated.

8.2 Reprint of Physical Review B 96, 165410 (2017)

The following paper with the title *Adsorption-induced symmetry reduction of metal-phthalocyanine studied by vibrational spectroscopy* contains the following contributions from the authors:

The research has been conceived and designed by J. Sforzini, F. C. Bocquet, and F. S. Tautz.

The experiments have been carried out by J. Sforzini in the HREELS laboratory.

The theoretical calculations have been performed by J. Sforzini.

The data have been analyzed by J. Sforzini with the support of F. C. Bocquet and F. S. Tautz.

The interpretation of the results has been developed in discussions between J. Sforzini, F. C. Bocquet and F. S. Tautz.

The paper has been written by J. Sforzini, F. C. Bocquet and F. S. Tautz.

PHYSICAL REVIEW B **96**, 165410 (2017)

Adsorption-induced symmetry reduction of metal-phthalocyanines studied by vibrational spectroscopy

J. Sforzini, F. C. Bocquet,* and F. S. Tautz
Peter Grünberg Institut (PGI-3), Forschungszentrum Jülich, 52425 Jülich, Germany
and Jülich Aachen Research Alliance (JARA), Fundamentals of Future Information Technology, 52425 Jülich, Germany
(Received 25 September 2016; revised manuscript received 14 August 2017; published 5 October 2017)

We investigate the vibrational properties of Pt- and Pd-phthalocyanine (PtPc and PdPc) molecules on Ag(111) with high-resolution electron energy loss spectroscopy (HREELS). In the monolayer regime, both molecules exhibit long-range order. The vibrational spectra prove a flat adsorption geometry. The redshift of specific vibrational modes suggests a moderate interaction of the molecules with the substrate. The presence of asymmetric vibrational peaks indicates an interfacial dynamical charge transfer (IDCT). The molecular orbital that is involved in IDCT is the former E_g lowest unoccupied molecular orbital (LUMO) of the molecules that becomes partially occupied upon adsorption. A group-theoretical analysis of the IDCT modes, based on calculated vibrational frequencies and line shape fits, provides proof for the reduction of the symmetry of the molecule-substrate complex from fourfold D_{4h} to $C_{2v}(\sigma_v)$, $C_s(\sigma_v)$, or C_2 and the ensuing lifting of the degeneracy of the former LUMO of the molecule. The vibration-based analysis of orbital degeneracies, as carried out here for PtPc/Ag(111) and PdPc/Ag(111), is particularly useful whenever the presence of multiple molecular in-plane orientations at the interface makes the analysis of orbital degeneracies with angle-resolved photoemission spectroscopy difficult.

DOI: 10.1103/PhysRevB.96.165410

I. INTRODUCTION

Organic molecules with π-conjugated electron systems have been intensively studied in recent years. Apart from a fundamental interest in their electronic properties, this activity is motivated by the wide range of possible applications in the fields of optoelectronics [1,2] and spintronics [3]. Among these molecules, metal-phthalocyanines (MPc), i.e., tetrabenzoporphyrazine macrocycles with a metal atom in their center, play an important role, because of their planar geometry, their thermal stability, their suitability for organic molecular beam epitaxy, and their chemical versatility that its brought about by very diverse central metal atoms [4]. In fact, MPc molecules have been employed in organic light-emitting diodes [5], field effect transistors [6,7], and solar cells [8].

The interaction of MPc with metal surfaces is interesting both from a fundamental point of view, in particular regarding the balance between the contributions of the central metal atom and the π-electron system, and for applications, in which such interfaces are the primary functional elements. For MPc with almost filled d shells, the molecule-substrate interaction is dominated by the chemisorptive or physisorptive interaction of the macrocycle with the metal surface [4]. If there is a chemisorptive contribution to this bond, this often leads to charge transfer from the metal into the lowest unoccupied molecular orbital (LUMO) of the molecule [4]. This is also true in the case of PtPc and PdPc on Ag(111), as we show in this paper.

An interesting issue in relation to the molecule-substrate interaction in general and the charge transfer in particular is the symmetry of adsorbed MPc molecules. Except for a few cases, e.g., SnPc [9], the central metal fits into the inner cavity and the corresponding isolated MPc belongs to the D_{4h} point group [4]. Because of the presence of the surface, the symmetry of the molecule is lowered to C_{4v}. However, a further molecular symmetry reduction to a twofold symmetry is often observed in scanning tunneling microscopy (STM) [9–14].

The symmetry reduction of MPc molecules from fourfold to twofold symmetry raises an intriguing question regarding the charge transfer into the molecule. The LUMO of isolated MPc is twofold degenerate and belongs to the irreducible representation E_g of the D_{4h} point group. This degeneracy is closely related to cross-conjugation in the central porphyrazine macrocycle of phthalocyanine molecules [4,15]. When charge is transferred into the LUMO, two situations are conceivable: either both orbitals remain degenerate and receive the same amount of charge, or the degeneracy is lifted and charge is transferred preferentially into one of the two. Degeneracy lifting has been invoked in certain cases to explain the symmetry reduction of MPc molecules [11,14,16], while in other cases equal filling of both E_g orbitals was conjectured [17], or the symmetry reduction was assigned to structural effects [10,13,18].

At first glance, STM seems to be the method of choice for symmetry analysis of molecular adsorbates, because any symmetry breaking should become immediately obvious in the image. However, in STM purely electronic as well as purely geometric effects can both lead to a symmetry reduction in the image, and there are only a few cases in which the origin of the broken symmetry can be determined on basis of STM alone (e.g., Ref. [16]). Of course, in most cases geometric and electronic effects will be coupled to each other, because a geometric distortion of the molecule by the influence of the external environment will also break the electronic symmetry within the molecule, and vice versa an electronic symmetry reduction will generally lead to a structural distortion (Jahn-Teller effect [16,19,20]). Yet, it is still an important question

*f.bocquet@fz-juelich.de

to ask which is the dominant of the two effects. For example, a strong geometric distortion may lead to a negligible symmetry breaking of electronic states.

For this reason, additional experimental methods have been employed to settle the issue of a possible lifting of the degeneracy. These include core level spectroscopy [14], near-edge x-ray absorption spectroscopy (NEXAFS) [21], or density functional theory (DFT) [14]. Recently, also photoemission tomography [22,23] has been applied to this problem: In the case of FePc/Ag(111) no splitting of the LUMO was found [17], while for CuPc/Ag(110) a clear splitting was observed [24]. Photoemission tomography has the unique advantage that if a degeneracy lifting takes place, the actual orientation of the filled orbital can be determined [24]. However, this orientational sensitivity can also be a drawback, if many molecules with many different orientations are present at the surface. In this case, photoemission tomography results become difficult to analyze [17].

Here we present an approach that does not suffer from the presence of multiple orientations, because only the internal symmetry of the molecule-surface complex matters. Yet at the same time, if applicable, it leads to unambiguous results regarding electronic symmetry breaking, i.e., degeneracy lifting. This approach is based on vibrational spectroscopy. Specifically, we employ high-resolution electron energy loss spectroscopy (HREELS) which in its dipole scattering mechanism is sensitive to infrared (IR) active vibrational modes [25]. Due to the surface selection rule, only totally symmetric modes of the molecule-surface complex are IR active [25]. Any reduction of the molecular point group upon adsorption may imply that formerly inactive modes can become IR active. Because, as mentioned above, the symmetry reduction can be effected both by geometric and electronic effects, also the corresponding IR activation can have these two distinct origins. However, if additionally the line shape of an activated mode is taken into account, it is (under favorable conditions) possible to unambiguously link the activation of certain vibrational modes to an electronic symmetry breaking. More specifically, we argue here for the example of MPc molecules that if a mode that indicates a particular symmetry reduction has a Fano line shape, this proves an electronic contribution (i.e., degeneracy lifting) to this symmetry reduction, because the Fano line shape indicates an interfacial dynamical charge transfer (IDCT), and for an IDCT to be observable in a MPc molecule, there must exist an imbalance in the occupation of the two E_g LUMOs. Hence, their degeneracy must be broken.

II. EXPERIMENTAL DETAILS

The experiments were performed in an ultrahigh vacuum (UHV) system consisting of a preparation and an analysis chamber equipped with low energy electron diffraction (LEED) and HREELS. The pressures in the chambers were 4×10^{-9} and 4×10^{-10} mbar, respectively. The Ag(111) crystal surface was prepared by Ar^+ sputtering at 1 keV followed by annealing to 730 K until a sharp LEED pattern was observed. Thin films of PdPc and PtPc were prepared in UHV by depositing the molecules, evaporated from a homemade Knudsen cell, on the crystal kept at room temperature. The sublimation temperatures were 770 K and 670 K for PdPc and PtPc, respectively. A multilayer phase, which does not exhibit a LEED pattern, is prepared by sublimating PtPc more than ten times longer than the sublimation time necessary to obtain the ordered monolayer phase. The pressure in the preparation chamber did not exceed 1×10^{-8} mbar during sublimation.

After the layer was prepared, its long-range order was checked by LEED. Vibrational features were recorded in HREELS with a primary electron beam energy of 6.3 eV in both specular and off-specular geometries. The incoming beam is directed to the sample with an angle of 45° with respect to surface normal. In the specular (off-specular) geometry the electrons are detected at an angle of 45° (60°) with respect to the surface normal. The energy resolution, estimated from the full width at half maximum (FWHM) of the elastic peak, is in the range of 16–22 cm^{-1} (2–2.7 meV). In order to interpret the complex vibrational spectra, we performed theoretical calculations of isolated PtPc and PdPc molecules using GAUSSIAN [26]. The DFT calculations of their electronic structure and of their vibrational eigenfrequencies were carried out using the LanL2DZ basis set and the B3LYP functional. The calculated vibration energies were compressed by a factor of 0.9456 [27,28].

III. PLATINUM-PHTHALOCYANINE ON Ag(111)

A. Long-range order

PtPc molecules form ordered two-dimensional structures on the Ag(111) surface. Like for most of the MPc molecules, two diffuse rings are detected at room temperature in LEED at low coverage after annealing a thick layer up to 730 K (see Ref. [29]). This two-dimensional disordered phase has already been observed in the case of, for example, CuPc on Ag(111) and Au(111) [24,30,31]. Stadler *et al.* interpreted the presence of this two-dimensional gas phase at low coverage as the result of an intermolecular repulsion [32]. As the density of the PtPc molecules on the surface increases, diffraction spots are detected in LEED at room temperature (ordered phase). According to high-resolution structural measurements for CuPc, the unit cell formed by the CuPc molecules decreases continuously in size as the coverage is increased. Our LEED measurements indicate a similar behavior for PtPc on Ag(111).

B. Vibrational properties of the multilayer and mode assignment

PtPc has $3N - 6 = 165$ distinct vibrational modes ($N = 57$ is the number of atoms in the molecule). Its point group is D_{4h} and its vibrational representation is $\Gamma = 14A_{1g} + 13A_{2g} + 14B_{1g} + 14B_{2g} + 26E_g + 56E_u + 8A_{2u} + 6A_{1u} + 7B_{1u} + 7B_{2u}$. Modes transforming according to the irreducible representations A_{2u} and E_u are IR-active modes; i.e., the motion of the atoms produces a dynamic dipole moment $\vec{\mu}_{dyn}$. Depending on the direction of $\vec{\mu}_{dyn}$, the IR-active modes can be classified as in-plane modes, in which $\vec{\mu}_{dyn}$ lies in the molecular xy plane [$E_u(x,y)$ modes], and as out-of-plane modes, in which $\vec{\mu}_{dyn}$ is oriented perpendicular to the molecular plane along the z direction [$A_{2u}(z)$ modes]. The modes belonging to the A_{1g}, E_g, B_{1g}, and B_{2g} irreducible representations are Raman (R) active modes; i.e., the atomic vibration induces a change of the molecular polarizability.

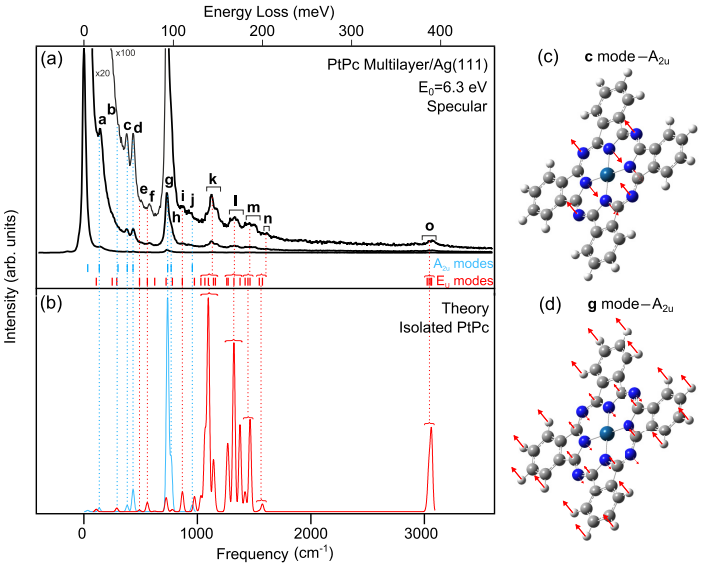

FIG. 1. (a) The experimental specular HREELS spectrum of the PtPc multilayer on Ag(111) and (b) the calculated spectrum of the isolated molecule are shown. The calculated vibrational frequencies of the out-of-plane A_{2u} and in-plane E_u IR-active modes are displayed in blue and red, respectively. The atomic displacements of the **c** mode and **g** mode are shown in (c) and (d), respectively.

We refer the reader to Ref. [33] for an introduction to symmetry-based selection rules.

In this work we are interested in IR-active modes, because HREELS is sensitive to the dynamic dipole moment $\vec{\mu}_{\mathrm{dyn}}$. According to the surface selection rule [25], modes for which $\vec{\mu}_{\mathrm{dyn}}$ is oriented perpendicular to the surface are excited in the dipole scattering mechanism (specular geometry), whereas modes having a dynamic dipole oriented parallel to the surface are suppressed, because the $\vec{\mu}^{*}_{\mathrm{dyn}}$ produced by the image charges in the substrate is antiparallel to $\vec{\mu}_{\mathrm{dyn}}$, leading to a cancellation of the two. In the language of group theory, the surface selection rule states that only totally symmetric modes (A_1, A', and A representations) of the molecule-substrate complex may be visible in HREELS. In contrast, all modes can be excited in the impact scattering regime (off-specular geometry). The appearance and/or disappearance of specific modes in the HREELS spectrum, depending on the measurement geometry, gives important information on the symmetry of the molecule-substrate complex. Therefore, an accurate assignment of the vibrational features is necessary.

The assignment is carried out by comparing the experimental peaks in the spectrum of a multilayer with calculated frequencies of the isolated PtPc molecule. In the multilayer, the effect of the substrate is reduced and thus the spectral properties are expected to be similar to the isolated molecule. Figure 1(a) shows the experimental spectrum of a PtPc multilayer on Ag(111), acquired in specular geometry, in comparison with the calculated spectrum of the isolated PtPc molecule [Fig. 1(b)]. The calculated spectrum contains a Gaussian broadening of 20 cm^{-1}, similar to the experimentally observed one, and is composed of A_{2u} (blue lines) and E_u (red lines) modes only, because these are the sole IR-active vibrations. We note that all experimental features can be identified in good agreement with theory. A simplified description of the modes is given in Table I (see Ref. [29] for details). The spectrum is dominated by the A_{2u} modes, with dynamic dipole moments perpendicular to the molecular plane, such as the strongest vibrations **a** at 145 cm^{-1} (out-of-plane bending of the whole molecule except Pt) and **g** at 730 cm^{-1} [out-of-plane bending of the central ring of alternating C and N atoms around the metal porphyrazin macrocycle together with the H atoms; Fig. 1(d)]. Compared to theory, the experimental E_u mode intensities appear reduced, suggesting a predominantly flat adsorption orientation of the molecules in the multilayer. However, the intensity ratio of the in-plane modes (E_u) and out-of-plane modes (A_{2u}) is conserved in the off-specular spectrum (not shown). This can be caused by a residual contribution of the dipole scattering in the off-specular geometry due to, e.g., surface roughness.

C. Vibrational properties of the ordered monolayer phase and molecular symmetry reduction

The vibrational properties of the ordered monolayer phase are discussed in comparison with those of the multilayer and calculated frequencies. Experimental modes are assigned to

TABLE I. List of the experimental vibrational modes present in the PtPc multilayer and ordered monolayer phase specular spectra on Ag(111) accompanied by their irreducible representation and description. The calculated frequencies are compressed by a factor of 0.9456. The abbreviations are as follows: OP = out of plane, IP = in plane, bend = bending mode, deform = deformation mode, sciss = scissoring mode, stretch = stretching mode, rock = rocking mode. All values are given in cm^{-1}.

Modes	Multilayer	Ordered monolayer	DFT	Irreducible representation	Description	
a	145	145	136	A_{2u}	OP bend:	Molecule
R1		255				
b	310		301	A_{2u}	OP bend:	Molecule
c	380	350	382	A_{2u}	OP bend:	N atoms
d	430	430	434	A_{2u}	OP bend:	N + C atoms
e	505		490	E_u	IP sciss:	N + C atoms
R2		565				
f	575		574	E_u	IP deform:	Molecule
R3		655				
g	730	715	738	A_{2u}	OP bend:	Main ring
h	765	765	770	A_{2u}	OP bend:	N atoms + Phenyl groups
i	880		869	E_u	IP deform:	Molecule
j	925		956	A_{2u}	OP bend:	Phenyl groups
k	1075–1200		1031–1159	E_u	IP deform/stretch:	Molecule
F1		1075–1200				
l	1285–1375		1260–1323	E_u	IP rock/stretch:	N atoms + Phenyl groups
F2		1285–1375				
m	1410–1530		1376–1465	E_u	IP stretch:	Main ring
F3		1410–1530				
n	1585–1640		1546–1574	E_u	IP stretch:	Phenyl groups
o	3010–3030		3025–3064	E_u	IP stretch:	H atoms

calculated ones within 50 cm^{-1} of their centroids, a range that corresponds to the typical experimental width of isolated peaks (see semitransparent blue boxes in Fig. 2 and Fig. 4). Figure 2(a) shows specular HREELS spectra of the ordered monolayer phase and the multilayer. In the ordered monolayer, most of the E_u in-plane modes are absent, especially between 1000 and 1600 cm^{-1}. But in this range three asymmetric peaks (**F1**, **F2**, and **F3**) are detected. Their origin will be discussed later. The absence of the in-plane vibrations indicates that the surface selection rule strongly attenuates the in-plane E_u modes in comparison to the out-of-plane A_{2u} modes. We conclude that the molecules in the monolayer are oriented strictly parallel to the Ag surface. Note that the A_{2u} peaks **b** and **j**, of very weak intensity in the multilayer (Fig. 1), are not detectable in the ordered monolayer phase [Fig. 2(a)] in agreement with results on other phthalocyanines [34–36].

1. Out-of-plane A_{2u} modes

Like in the multilayer, all of the out-of-plane A_{2u} modes are detected in the spectrum of the ordered monolayer phase (except **b** and **j**). However, in the latter the **c** and **g** modes are shifted to lower wave numbers. The shift of the **c** mode ($\simeq$ 30 cm^{-1}) is larger than that of the **g** mode ($\simeq$ 15 cm^{-1}). The **c** mode is associated with the out-of-plane bending of the aza bridge N atoms against the pyrrole N atoms [Fig. 1(c)], while in the **g** mode all N atoms move in phase against the C atoms in the porphyrazin macrocycle and the H atoms in the phenyl groups [Fig. 1(d)]. We assign the sizable shifts of these two modes to the molecule-substrate interaction. In contrast to FePc and CoPc on Ag(111) [37,38], for which the central metal forms a covalent bond with the substrate, the molecule-substrate interaction in PtPc takes place through the porphyrazin macrocycle, because neither the **c** nor the **g** modes, which are the ones that are most strongly influenced by the substrate, involve the central metal atom, unlike the **a** mode for example, which involves the metal atom but does not show an appreciable shift. This observation is in agreement with the general trend of a reduced metal participation in the molecule-substrate bond as the number of d-electrons increases [4]. The observation that the shift of **c** is larger than that of **g**, in conjunction with the fact that the **c** mode displacement is due to the N atoms only while in the **g** mode the displacements of N atoms are relatively small, suggests that most of the interaction between the molecule and the Ag substrate occurs via the N atoms.

2. Raman modes

Another noteworthy difference between the vibrational properties of the ordered monolayer phase and the multilayer is the appearance of new modes labeled **R1**, **R2**, and **R3** in Fig. 2(a). Employing a range of 50 cm^{-1} around their centroids, the **R1** peak at 255 cm^{-1} can be interpreted either as a E_u, A_{1g} or as a E_g mode, while the **R2** peak at 565 cm^{-1} may be attributed to either a E_u or a A_{1g} mode. Finally, the **R3** peak at 655 cm^{-1} can either be ascribed to a A_{1g} or a B_{2g} mode. The possible assignments are summarized in Table III. Ruling out the E_u modes, because as in-plane IR modes they should be screened by the metal surface, only modes having an A_{1g}, E_g, or B_{2g} irreducible representation in the D_{4h} point group remain as possible assignments. However, they are R-active modes and as such not expected to contribute to the spectrum of an isolated

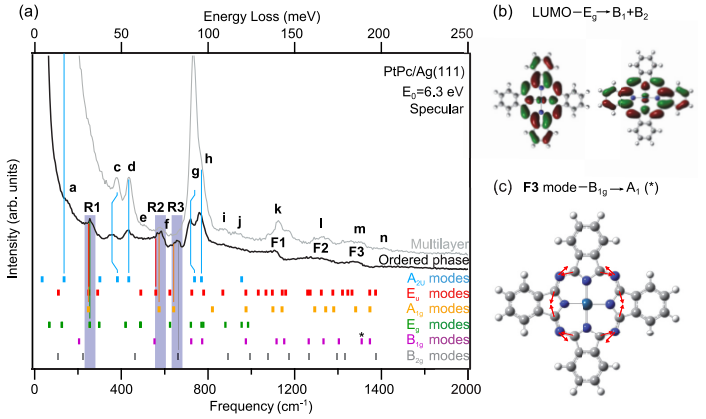

FIG. 2. (a) The comparison of the specular HREELS spectra of the PtPc ordered monolayer phase and multilayer on Ag(111). The simulated vibrational modes of the isolated molecule are indicated as thick colored vertical bars. The energy ranges used for assignment around the centroids of **R1**, **R2**, and **R3** are depicted as semitransparent blue boxes, and possible assignments are indicated by thin vertical bars. Note that the vibrational properties of the ordered monolayer phase do not change with the coverage. (b) The calculated charge density of the two degenerate LUMOs of isolated PtPc. (c) Sketch of the Raman mode belonging to the B_{1g} irreducible representation at 1509 cm^{-1} [marked with * in panel (a)] that is used to fit the Fano peak **F3** at approximately 1500 cm^{-1} (see text).

molecule. But they can be activated if the molecular symmetry is reduced. Thus, a symmetry reduction of the molecule in contact with the surface must be considered.

When a PtPc molecule adsorbs with its plane parallel to the surface, its molecular symmetry is reduced from the original D_{4h} point group. Specifically, at least the in-surface-plane (x,y) mirror symmetry is broken. A PtPc molecule lacking its (x,y)-plane symmetry belongs to the C_{4v} point group. However, further symmetry reductions are possible, e.g., to the C_{2v} point group, if the fourfold symmetry of the molecule is broken. With the help of so-called correlation tables it is possible to deduce how the modes (irreducible representations) of the isolated molecule (D_{4h}) relate to the ones of the molecule-substrate system of reduced symmetry (C_{4v} or lower) [25]. An adaptation of the correlation tables of the D_{4h} point group from Ref. [25], considering the observed **R** modes (and the **F** modes, introduced in the next section), is given in Table II.

In principle, there is a chance that the observation of the R modes allows us to deduce the symmetry of the molecule-substrate complex. For example, a B_{2g} mode would become activated for HREELS dipole scattering only if the D_{4h} symmetry was reduced to $C_{2v}(\sigma_d)$, $C_s(\sigma_d)$, or C_2 upon adsorption (Table II). Hence, we must look for a single reduced point group in which the vibrational modes of the free molecule which we assign to **R1**, **R2**, and **R3** each map onto a

TABLE II. Correlation table of the D_{4h} point group limited to the possible modes assignment of the **R** and **F** modes [25,33,39]. The notations x, y, and z denote linear functions which transform according to the given irreducible representations. The other irreducible representations are not IR active.

D_{4h}	C_{4v}	$C_{2v}(\sigma_v)$	$C_s(\sigma_v = m_x)$	$C_s(\sigma_v = m_y)$	C_4	C_2
A_{1g}	$A_1(z)$	$A_1(z)$	$A'(z)$	$A'(z)$	$A(z)$	$A(z)$
B_{1g}	B_1	$A_1(z)$	$A'(z)$	$A'(z)$	B	$A(z)$
B_{2g}	B_2	A_2	$A''(x)$	$A''(y)$	B	$A(z)$
E_g	$E(x,y)$	$B_1(x) + B_2(y)$	$A''(x) + A'(y)$	$A'(x) + A''(y)$	$E(x+iy) + E(x-iy)$	$B(x) + B(y)$
$E_u(x,y)$	$E(x,y)$	$B_1(x) + B_2(y)$	$A''(x) + A'(y)$	$A'(x) + A''(y)$	$E(x+iy) + E(x-iy)$	$B(x) + B(y)$

D_{4h}	$C_{2v}(\sigma_d)$	$C_s(\sigma_d = m_d)$	$C_s(\sigma_d = m_{d'})$
A_{1g}	$A_1(z)$	$A'(z)$	$A'(z)$
B_{1g}	A_2	$A''(x-y)$	$A''(x+y)$
B_{2g}	$A_1(z)$	$A'(z)$	$A'(z)$
E_g	$B_1(x+y) + B_2(x-y)$	$A'(x+y) + A''(x-y)$	$A''(x+y) + A'(x-y)$
$E_u(x,y)$	$B_1(x+y) + B_2(x-y)$	$A'(x+y) + A''(x-y)$	$A''(x+y) + A'(x-y)$

TABLE III. Possible assignments of the **R** and **F** modes observed in the ordered monolayer phase of PtPc on Ag(111). The **F** mode assignments are based on the fit results presented in the Supplemental Material [29].

Mode	Symmetry
R1	$A_{1g}/E_u(x,y)/E_g$
R2	$A_{1g}/E_u(x,y)$
R3	A_{1g}/B_{2g}
F1	$A_{1g}/E_u(x,y)/B_{1g}$
F3	B_{1g}

totally symmetric representation (A_1, A', or A; see Ref. [39]). However, since it is a possibility that **R1**, **R2**, and **R3** could all originate from A_{1g} modes (see Table III), all three would in this case be visible in dipole scattering HREELS irrespective of the symmetry of the molecule-substrate complex (C_{4v}, C_{2v}, C_4, C_s, or C_2). Hence, it is not possible to conclude on the basis of **R1**, **R2**, and **R3** alone whether PtPc preserves its fourfold symmetry upon adsorption (C_{4v}) or lowers its symmetry (C_{2v}, C_4, C_s, or C_2).

3. Asymmetric peaks

In order to see whether the symmetry of the PtPc molecule on the Ag surface can be identified, we now turn to the analysis of the **F** modes. Between 1000 and 1600 cm^{-1}, where the E_u modes are excited in the multilayer spectrum [Fig. 1(a)], three asymmetric features, labeled **F1**, **F2**, and **F3** in Fig. 2(a), are visible in the spectrum of the ordered monolayer. Asymmetric line shapes of Fano type are well known for molecular and atomic adsorbates on metallic surfaces in the presence of an IDCT [34,35,40–45]. Since we are going to employ both IDCT selection rules and line shape analysis in our argument, we briefly sketch out their theoretical basis.

A prerequisite for the occurrence of IDCT is an electron-vibron coupling that breaks the Born-Oppenheimer approximation according to which electronic degrees of freedom are decoupled from vibrational degrees of freedom, obeying their own separate electronic Schrödinger equation. While in the vibrational Schrödinger equation the energy eigenvalues of the electronic Schrödinger equation always serve as potential energy terms for the nuclear degrees of freedom, in the Born-Oppenheimer approximation the dependence of the electronic Schrödinger equation on nuclear coordinates is usually taken as being merely parametric.

In contrast, the explanation of IDCT requires the presence of a term in the Hamiltonian of the electron system that makes its dependence on vibrational coordinates explicit. In linear Taylor expansion, this electron-vibron coupling term has the form

$$E(\{Q_{\alpha 0}+\Delta Q_\alpha\}) = E_0 + \sum_\alpha \left(\frac{\partial E(\{Q_\alpha\})}{\partial Q_\alpha}\right)_0 \Delta Q_\alpha + \cdots . \tag{1}$$

Here $E_0 = E(\{Q_{\alpha 0}\})$. In the following we set $Q_{\alpha 0} = 0$ and thus $\Delta Q_\alpha = Q_\alpha$. Moreover, we focus on a single normal vibrational mode Q_α. Then the relevant coupling term in the Hamiltonian becomes

$$\hat{H}_\alpha^{\mathrm{el-vib}} = \sqrt{\frac{\hbar}{2\omega_\alpha}}\frac{\partial E(\{Q_\alpha\})}{\partial Q_\alpha}(b_\alpha + b_\alpha^\dagger), \tag{2}$$

where we have inserted the second quantized expression for the vibrational mode Q_α [39], and where b_α ($b_\alpha^\dagger$) is the annihilation (creation) operator of a vibrational quantum of mode α.

To see whether the coupling term in Eq. (2) is allowed by symmetry we calculate its matrix element and analyze under which conditions it may be nonvanishing [39]. In calculating the matrix element we use wave functions $\Psi = |\psi\rangle|n_\alpha\rangle$ that consist of an electronic part $|\psi\rangle$ and a vibrational part $|n_\alpha\rangle$, where n_α designates the occupancy of vibrational mode Q_α. The matrix element then reads

$$M_\alpha = |\langle\Psi_f|\hat{H}_\alpha^{\mathrm{el-vib}}|\Psi_i\rangle|^2, \tag{3}$$

where the indices denote initial and final states. Inserting the wave functions in M_α one finds

$$M_\alpha \propto \sqrt{\frac{\hbar}{2\omega_\alpha}}s_\alpha\left|\langle\psi_f|\frac{\partial E(\{Q_\alpha\})}{\partial Q_\alpha}|\psi_i\rangle\right|^2 \tag{4}$$

for processes involving a single vibrational quantum, where $s_\alpha = n_\alpha$ ($s_\alpha = n_\alpha + 1$) for the absorption (emission) of a vibrational quantum. Only if the right-hand side of Eq. (4) transforms totally symmetric under all symmetry operations of the system's Hamiltonian can M_α have a nonvanishing value.

Let us denote the totally symmetric irreducible representation of the point group G of the Hamiltonian as Γ_{ts} (depending on the particular G under investigation, this may be A_1, A_{1g}, A_g, A_1', A', or A; see Ref. [39]). Clearly, the energy E in Eq. (4) has to have the full symmetry of the Hamiltonian, i.e., must transform according to Γ_{ts}. The vibrational mode Q_α, being an eigenstate of the vibrational Hamiltonian, transforms as the irreducible representation Γ_α of G. The same is thus true of the partial derivative $\partial E(\{Q_\alpha\})/\partial Q_\alpha$. As eigenstates of the electronic Hamiltonian the wave functions ψ_i and ψ_f transform according to Γ_i and Γ_f, respectively, both of which are irreducible representations of G, too. Hence, the matrix element M_α transforms according to the direct product representation $\Gamma_{M_\alpha} = \Gamma_f \otimes \Gamma_\alpha \otimes \Gamma_i$. As a rule, Γ_{M_α} is reducible, and only if the reduction of Γ_{M_α} contains Γ_{ts} can M_α be nonzero. The condition for $M_\alpha \neq 0$ thus is

$$\Gamma_f \otimes \Gamma_\alpha \otimes \Gamma_i \supseteq \Gamma_{ts}. \tag{5}$$

According to a well-known theorem of group theory this can only happen if the reduction of the direct product of any pair of irreducible representations on the left of Eq. (5) contains the third [46]. For instance,

$$\Gamma_f \otimes \Gamma_i \supseteq \Gamma_\alpha \tag{6}$$

must hold. At this stage we deploy additional information regarding the vibrational mode Q_α. Since we excite this mode via dipole scattering in electron energy loss spectroscopy, the surface selection rule applies. Thus $\Gamma_\alpha = \Gamma_{ts}$, i.e., the vibration must be totally symmetric. As an immediate consequence, $\Gamma_f \supseteq \Gamma_i$ follows from Eq. (6) because of the above mentioned theorem, which means $\Gamma_f = \Gamma_i$, since Γ_f and Γ_i are irreducible. In other words, initial and final states ψ_i and ψ_f of the electron involved in the coupling may transform according to

an arbitrary irreducible representation, provided they are the same. Obviously, this condition is trivially fulfilled if $\psi_i = \psi_f$. While in an electron-vibron scattering process, occurring with an electron of the material, ψ_i and ψ_f cannot be equal, since this would contradict the conservation of energy $E_i = E_f + \omega_\alpha$ for vibron emission or $E_f = E_i + \omega_\alpha$ for vibron absorption (note that we set $\hbar = 1$ from now on), in the present case, where the energy for the excitation of the vibron is provided completely by the probing electron, $\psi_i = \psi_f$ is in fact necessarily fulfilled for reasons of energy conservation (disregarding an accidental degeneracy between electronic states ψ_i and ψ_f). We can thus conclude that for totally symmetric vibrations taking part in IDCT the matrix element M_α in Eq. (4) is symmetry-allowed for electronic levels that transform according to an arbitrary irreducible representation.

In addition to the participation of a totally symmetric vibrational mode, a further prerequisite of IDCT is the partial filling of the orbital with energy E_i that couples to the molecular vibration in question. Then, as the vibration is excited, the associated distortion of the molecule along the vibrational coordinate modulates the orbital energy periodically, leading to the excitations of electron hole pairs and oscillatory charge flow between the molecule and the substrate that is effectively pumped by the vibration.

We now turn to the line shape of modes taking part in interfacial dynamical charge transfer. The line shape of the vibration as measured in electron energy loss spectroscopy follows from the loss function $-\mathrm{Im}\,\epsilon^{-1}$, where ϵ is the dielectric response function. Since ϵ is given by $\epsilon(\omega) = \epsilon_\infty + 4\pi\chi(\omega)$ (ϵ_∞ is the background dielectric constant), one must calculate the generalized susceptibility $\chi(\omega) = \delta\hat{n}/E_{\mathrm{ext}}$ that determines the dynamic charge transfer response $\delta\hat{n}$ to the electric field E_{ext} of the dipole-scattered probing electron. Based on the linear expansion in Eq. (1), $\chi(\omega)$ is given by [42]

$$\chi(\omega) = \frac{\rho(E_F)(ed)^2 N\omega_{CT}^2}{\omega_{CT}^2(1-\lambda_\alpha D_\alpha) - \omega^2 - i\omega\gamma_{CT}}. \tag{7}$$

e is the elementary charge, ω_{CT} is the eigenfrequency of the charge transfer oscillation (equivalent to the excitation of electron hole pairs by the modulation of the orbital energy E_i), γ_{CT} its damping, d the length scale of the dynamical dipole, N the dipole density, $\lambda_\alpha = 2g_\alpha^2\rho(E_F)/\omega_\alpha$ [where $g_\alpha \equiv \frac{1}{\sqrt{2}}\frac{\partial E_i}{\partial Q_\alpha}$ and $\rho(E_F)$ is the density of states at the Fermi level] the dimensionless electron-vibron coupling parameter, $D_\alpha = \omega_\alpha^2/(\omega_\alpha^2 - \omega^2 - i\omega\gamma_\alpha)$, and γ_α and ω_α are the damping and the eigenfrequency of the vibrational mode in the absence of coupling to electron-hole pairs, respectively. With Eq. (7), one can calculate the line shapes of vibrations that are subject to IDCT. This line shape turns out to be of Fano type [42].

We now show that the approach of Ref. [42] that leads to Eq. (7) is equivalent to the one adopted by Langreth [47]. To this end we analyze the vibrational line shape from a slightly different but fully equivalent point of view, focusing on the electronic dynamical dipole moment $\mu_\alpha^{el} = \partial P/\partial Q_\alpha$ of vibration Q_α. Specifically, we calculate the line shape of the vibration from the response of the polarization $P = Ned\delta\hat{n}$ [42] to the modulation of the electronic level energy E_i. This can be derived directly from Eq. (7), yielding

$$\frac{\partial P}{\partial E_i} = -\frac{\omega_\alpha\left(\mu_\alpha^{el}\right)^2}{\omega_\alpha^2(1-\lambda_\alpha D_{CT}) - \omega^2 - i\omega\gamma_\alpha}, \tag{8}$$

where μ_α is the dynamical dipole moment of the vibration Q_α with frequency ω_α and damping γ_α and $D_{CT} = \omega_{CT}^2/(\omega_{CT}^2 - \omega^2 - i\omega\gamma_{CT})$. In the limit $\omega \ll \omega_{CT}$ and under the assumption that the electron-hole pair continuum that damps the vibration can be modeled by a single damped harmonic oscillator, whose frequency ω_{CT} and damping γ_{CT} are related by $\omega_{CT} = \gamma_{CT}/2$ (aperiodic limit), this becomes

$$\frac{\partial P}{\partial E_i} = -\frac{\omega_\alpha\left(\mu_\alpha^{el}\right)^2}{\bar{\omega}_\alpha^2 - \omega^2 - i\omega\bar{\gamma}_\alpha} \tag{9}$$

with $\bar{\omega}_\alpha^2 = \omega_\alpha^2(1-\lambda_\alpha)$ and $\bar{\gamma}_\alpha = \gamma_\alpha(1+\beta_\alpha)$. λ_α is the dimensionless electron-vibron coupling parameter introduced above and $\beta_\alpha = 8g_\alpha^2\omega_\alpha\rho(E_F)/\gamma_\alpha\gamma_{CT}$. Finally, if the position of the electronic level E_i is approximately $\gamma_{CT}/2$ above the Fermi level E_F ($\gamma_{CT} \sim [\pi\rho(E_F)]^{-1}$) [47], β_α becomes

$$\beta_\alpha = \frac{8\pi g_\alpha^2\omega_\alpha\rho(E_F)^2}{\gamma_\alpha} = \lambda_\alpha\frac{\omega_\alpha^2}{\gamma_\alpha}4\pi\rho(E_F). \tag{10}$$

As expected, the coupling of the vibration Q_α to the electron-hole pair continuum leads to a renormalization of the vibrational frequency $\omega_\alpha \to \bar{\omega}_\alpha$ and an increase of its damping $\gamma_\alpha \to \bar{\gamma}_\alpha$. However, as Langreth has pointed out [47], this is not its only effect. The very same mechanism that leads to the renormalization of ω_α and γ_α will also lead to a complex dynamical dipole moment μ_α^{el} in Eq. (9) that changes the line shape of the vibration from a symmetric Lorentzian to an asymmetric Fano line shape.

From the equation for μ_α^{el} (Ref. [42])

$$\mu_\alpha^{el} = Ned\frac{\partial\hat{n}}{\partial Q_\alpha} = -\frac{\sqrt{2}g_\alpha Ned\rho(E_F)\omega_{CT}^2}{\omega_{CT}^2 - \omega^2 - i\omega\gamma_{CT}} \tag{11}$$

we obtain in the limit $\omega \ll \omega_{CT}$ the expressions

$$\mathrm{Re}\,\mu_\alpha^{el} = -\sqrt{2}g_\alpha Ned\rho(E_F) \tag{12}$$

and

$$\mathrm{Im}\,\mu_\alpha^{el} = -\sqrt{2}g_\alpha Ned\rho(E_F)\omega\gamma_{CT}/\omega_{CT}^2 \tag{13}$$

for the real and imaginary parts of the dynamical dipole moment. If the electron-hole pair continuum that damps the vibration is modeled by a single damped harmonic oscillator in the aperiodic limit, as in the derivation of Eq. (9), one finds

$$\mathrm{Im}\,\mu_\alpha^{el} = -4\pi\sqrt{2}g_\alpha Ned\rho(E_F)^2\omega, \tag{14}$$

which with Eq. (12) yields

$$\frac{\mathrm{Im}\,\mu_\alpha^{el}}{\mathrm{Re}\,\mu_\alpha^{el}} = 4\pi\rho(E_F)\omega. \tag{15}$$

Equations (12)–(15) are analogous to the corresponding ones derived by Langreth [47].

If, as in the derivation of Eq. (10), we again assume that the position of the electronic level E_i is approximately $\gamma_{CT}/2$ above the Fermi level E_F ($\gamma_{CT} \sim [\pi\rho(E_F)]^{-1}$), a particularly intuitive argument for the emergence of the imaginary part

of the dynamical dipole moment becomes apparent. From Eq. (15) we find

$$\frac{\mathrm{Im}\,\mu_\alpha^{\mathrm{el}}}{\mathrm{Re}\,\mu_\alpha^{\mathrm{el}}} = \frac{4\omega}{\gamma_{\mathrm{CT}}}, \tag{16}$$

which at $\omega = \omega_\alpha$ becomes

$$\frac{\mathrm{Im}\,\mu_\alpha^{\mathrm{el}}}{\mathrm{Re}\,\mu_\alpha^{\mathrm{el}}} = 2\pi\frac{\tau_{\mathrm{CT}}}{T_\alpha}. \tag{17}$$

If the lifetime $\tau_{\mathrm{CT}} \equiv 4/\gamma_{\mathrm{CT}}$ of the electronic level and therefore also of the electron-hole pair excitations is much shorter than the period T_α of a vibrational oscillation (i.e., $\tau_{\mathrm{CT}} \ll T_\alpha$), the electrons can follow the vibration adiabatically. According to Eq. (17), in this limit $\mathrm{Im}\,\mu_\alpha^{\mathrm{el}}$ is indeed negligible and μ_α^{el} is in phase with the vibration Q_α and accordingly also with $\mu_\alpha^{\mathrm{ion}}$, the intrinsic dynamical dipole moment resulting from the motion of the ion cores. If, on the other hand, $\tau_{\mathrm{CT}} \gtrsim T_\alpha$, i.e., the lifetime of electron-hole pair excitations involving E_i is comparable to or larger as the vibration period, $\mathrm{Im}\,\mu_\alpha^{\mathrm{el}}$ becomes appreciable and μ_α^{el}, which is driven by the vibration at ω_α, lags behind $\mu_\alpha^{\mathrm{ion}}$ in phase. This is the source of the additional vibrational damping beyond γ_α in Eq. (9) *and* leads to the nontrivial Fano line shape. Note that it is the lifetime of the electronic level, rather than the resonance frequency ω_{CT} of the charge transfer oscillation, that defines the relevant time scale in Eq. (17).

Equation (9) can be used to calculate the line shape as $L(\omega) = -\mathrm{Im}\,[\partial P(\omega)/\partial E_i]$. Instead of using only the electronic dynamical dipole μ_α^{el} arising from the modulation of the electronic level (giving rise in turn to electron hole pair excitations), we employ $\mu_\alpha = \mu_\alpha^{\mathrm{ion}} + \mu_\alpha^{\mathrm{el}}$; i.e., we add the intrinsic dynamical dipole moment of the vibration that arises from the motion of the ion cores and for which $\mu_\alpha^{\mathrm{ion}} = \mathrm{Re}\,\mu_\alpha^{\mathrm{ion}}$. Then $\mu_\alpha = \mathrm{Re}\,\mu_\alpha(1 + i\omega\tau)$ with

$$\tau = \frac{\tau_{\mathrm{CT}}}{1 + \mathrm{Re}\,\mu_\alpha^{\mathrm{ion}}/\mathrm{Re}\,\mu_\alpha^{\mathrm{el}}} \tag{18}$$

and we find [47–49]

$$L(\omega) = c\bar{\omega}_\alpha\omega\bar{\gamma}_\alpha\frac{\left[1 - \left(\omega^2 - \bar{\omega}_\alpha^2\right)\tau/\bar{\gamma}_\alpha\right]^2}{\left(\omega^2 - \bar{\omega}_\alpha^2\right)^2 + \omega^2\bar{\gamma}_\alpha^2} - c\bar{\omega}_\alpha\omega\frac{\tau^2}{\bar{\gamma}_\alpha}, \tag{19}$$

where $c = (\mathrm{Re}\,\mu_\alpha)^2/\sqrt{1-\lambda_\alpha}$ is a constant. The small and linearly varying term in Eq. (19) is usually ignored, as it is canceled by an equal term of opposite sign that arises from the electronic polarizability [47].

We have used the first term in Eq. (19) to fit the **F** modes observed in our data. In the process we have treated τ and $\bar{\gamma}_\alpha$ as fit parameters, while DFT-calculated vibrational frequencies were used as input parameters for $\bar{\omega}_\alpha$. Note that it would be more correct to use the calculated frequencies as input for the unrenormalized ω_α. However, since typically $\lambda_\alpha \simeq 0.1$ (Ref. [42]), the renormalization is approximately 5% and thus the incurred error is small. In some cases we have found negative τ as the result of the fitting. According to Eq. (18) the sign of τ is determined by the relative phases of $\mu_\alpha^{\mathrm{ion}}$, $\mathrm{Re}\,\mu_\alpha^{\mathrm{el}}$, and $\mathrm{Im}\,\mu_\alpha^{\mathrm{el}}$ as rotating vectors in a polar diagram.

We now turn to our data in Fig. 3. In order to identify which vibrational modes are involved in the IDCT that produces **F1**, **F2,** and **F3**, Eq. (19) is used to fit these features, using values

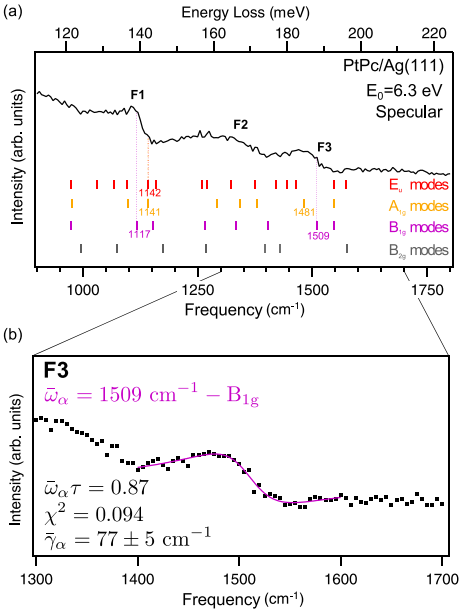

FIG. 3. (a) Zoom of the specular HREELS spectrum of the ordered monolayer phase spectrum of PtPc on Ag(111) showing the asymmetric peaks **F1**, **F2**, and **F3** together with the calculated vibrational modes (vertical bars). Each peak has been fitted using all the calculated vibrations marked in panel (a), and all the $\bar{\omega}_\alpha$ values which give reasonable fits of **F1**, **F2**, and **F3** are shown with dotted lines. (b) Best fit of **F3** using $\bar{\omega}_\alpha = 1509\ \mathrm{cm}^{-1} - B_{1g}$.

of $\bar{\omega}_\alpha$ that are determined by DFT calculations of an isolated molecule. All the calculated $\bar{\omega}_\alpha$ frequencies in the range from 900 to 1800 cm^{-1} have been tested [Fig. 3(a)]. The fits can be found in the Supplemental Material [29]. For a given Fano peak, the best fits are selected first on the basis of the smallest χ^2 value(s) within all possible α modes, and second the value of $\bar{\gamma}_\alpha$ must be below 100 cm^{-1} [50]. The few modes that yield reasonable fits for **F1** are summarized in Table III. Because **F1** may possibly be assigned to a mode with an A_{1g} irreducible representation in the D_{4h} point group that maps onto a mode belonging to a totally symmetric irreducible representation in any subgroup of D_{4h}, it is not possible to identify the symmetry of the molecule-substrate complex by considering this mode. As clearly seen in Fig. 3(a), **F2** appears much broader than **F1** and **F3**. This is confirmed by the fits that show $\bar{\gamma}_\alpha$ values always larger than 125 cm^{-1} [29]. This is an indication that several vibrational modes contribute to **F2**, and therefore renders an accurate assignment of this mode impossible.

We now turn to **F3** at about 1500 cm^{-1}. Using calculated frequencies in the fit, by far the best fit is achieved with the B_{1g} mode at $\bar{\omega}_\alpha = 1509\ \mathrm{cm}^{-1}$; see Fig. 3(b). The fitted value of $\bar{\gamma}_\alpha$ ($77 \pm 5\ \mathrm{cm}^{-1}$) compares well to the results for ZnPc/Ag(110) (60 cm^{-1}) [34]. We stress again that $\bar{\omega}_\alpha$ is not a fitting

parameter. If a strong renormalization $\omega_\alpha \rightarrow \tilde{\omega}_\alpha$ is expected, then also the A_{1g} mode at 1546 cm^{-1} could be a candidate and the assignment remains ambiguous. However, on the basis of the overall agreement between DFT calculation and experimental frequencies as documented in Table I we believe that the correct assignment is the B_{1g} mode at 1509 cm^{-1}. According to the correlation table in Table II, the B_{1g} mode maps to a totally symmetric A_1 mode for the $C_{2v}(\sigma_v)$ subgroup, to the totally symmetric A' for the $C_s(\sigma_v)$ subgroup, or to the totally symmetric A mode for the C_2 subgroup. Hence, the symmetry of the molecule substrate complex must be $C_{2v}(\sigma_v)$, $C_s(\sigma_v)$, or C_2.

However, the mere appearance of the B_{1g} mode in the spectrum does not yet clarify the origin of the symmetry reduction $D_{4h} \rightarrow C_{2v}(\sigma_v)$, $C_s(\sigma_v)$, or C_2. In principle, it is possible that because of a geometric distortion of the molecule μ_α^{ion} is tilted out of the surface plane and acquires a perpendicular component. But in this case μ_α would necessarily remain real, and we would observe a conventional, symmetric line shape for **F3**. This is evidently not the case. Its Fano line shape shows that μ_α of **F3** is complex. Hence, there must be a phase-shifted electronic contribution μ_α^{el} to its overall dynamical dipole moment μ_α.

We have already mentioned above that for PtPc/Ag(111) the LUMO is the most likely partner in IDCT, because it becomes filled upon adsorption and straddles the Fermi energy. Note that the reduction of the point group of the molecule-substrate complex from D_{4h} implies a lifting of the degeneracy of the LUMO. For example, in the case of the $C_{2v}(\sigma_v)$ point group the two degenerate orbitals of the E_g representation map to two nondegenerate orbitals with a B_1 and B_2 irreducible representation. Moreover, a comparison of the elongation pattern of **F3**, which predominantly involves the stretching of the C-N bonds in the porphyrazine macrocycle [Fig. 2(c)], with the lobular structure of the LUMO [Fig. 2(b)] shows that the ionic motion of **F3** should indeed couple well to the LUMO. Specifically, the stretching of the C-N bonds modulates the electron density along these bonds. Since the LUMO has bonding character with respect to them, the modulation of the electron density will have a strong impact on the energy of the LUMO. We note that it is the charge density along critical bonds, i.e., the square of the wave function irrespective of its phase, that determines the coupling to the orbital in question. In fact, this is the underlying physical reason why in IDCT orbitals transforming to any arbitrary one-dimensional representation may couple to any totally symmetric vibrational mode, as we have shown above on the basis of a general group-theory argument: Irrespective of the representation, the square of the wave function is totally symmetric. For this reason, the B_1 and B_2 orbitals of Fig. 2(b) may in fact couple to the **F3** mode in Fig. 2(c). Comparing Figs. 2(b) and 2(c) moreover shows that exciting **F3** with positive amplitude has the same effect on the B_1-LUMO as exciting **F3** with negative amplitude has on the B_2-LUMO. Hence, if B_1 and B_2 were still degenerate, dynamic filling and depletion of the two would be 180° out of phase (assuming that the phase lag relative to the ionic movement is the same for both LUMOs, which is expected to be a good approximation, in spite of the observed symmetry breaking; see below). In other words, in one half of the vibrational oscillation cycle the B_1-LUMO would be filled, while the B_2-LUMO would be depleted, and vice versa in the other half. Overall, no μ_α^{el} would prevail (small differences between the IDCT in the B_1- and B_2-LUMOs notwithstanding).

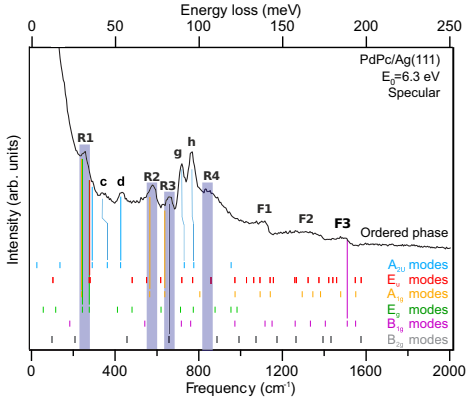

FIG. 4. Specular HREELS spectra of the PdPc ordered monolayer phase on Ag(111). The simulated vibrational modes of the isolated molecule are shown as thick colored vertical bars. The energy ranges used for assignment around the centroids of **R1** to **R4** are depicted as semitransparent blue boxes, and possible assignments are indicated by thin vertical bars (see text).

However, in the experimental spectrum a substantial μ_α^{el} is observed, as argued above. This can mean two things. Either the two LUMOs are still degenerate and their dynamic couplings to the **F3** vibration are different, or the LUMO levels B_1 and B_2 are indeed split. We consider it unlikely that the static level positions of the LUMOs are not affected by symmetry breaking, while their dynamic couplings to **F3** are. Therefore, we conclude that the B_1- and B_2-LUMO levels must be split; i.e., the degeneracy of the PtPc LUMO is lost upon adsorption on Ag(111). One may speculate that this LUMO splitting proceeds via a geometric distortion that is induced by the environment [the Ag(111) surface], enhanced by a Jahn-Teller-like internal stabilization of this external geometric distortion via the splitting of the electronic LUMO state [16,19,20].

IV. PALLADIUM-PHTHALOCYANINE ON Ag(111)

PdPc molecules adsorbed on Ag(111) show similar long-range order to that of PtPc/Ag(111). A two-dimensional gas phase is found after annealing the thick layer up to 730 K and an ordered phase is detected in LEED for lower annealing temperatures, that is at higher coverages.

In Fig. 4 the specular HREELS spectrum of the PdPc ordered monolayer phase is shown together with the simulated results for the isolated molecule. The assignment of the experimental vibrational frequencies can be found in the Supplemental Material [29]. As in the case of PtPc, the in-plane E_u modes are absent and only the dipole scattering allowed out-of-plane A_{2u} modes of the isolated molecule are present.

TABLE IV. Possible assignments of the **R** and **F** modes observed in the ordered monolayer phase of PdPc on Ag(111). The **F** mode assignments are based on the fit results.

Mode	Symmetry
R1	$A_{1g}/E_g/E_u(x,y)$
R2	A_{1g}
R3	A_{1g}/B_{2g}
F1	$A_{1g}/E_u(x,y)/B_{1g}$
F3	B_{1g}

This indicates an essentially flat adsorption geometry. The **c**, **g**, and **h** modes are shifted to lower frequencies by approximately 37, 18, and 5 cm^{-1} with respect to theory, respectively. The larger shift of the **c** mode for PdPc (37 cm^{-1}) than for PtPc (32 cm^{-1}) suggests a marginally stronger interaction of PdPc with the Ag(111) substrate.

The presence of R modes in Fig. 4 suggests a reduction of the molecular symmetry upon adsorption. In addition to the **R1**, **R2**, and **R3** peaks that are also observed for PtPc/Ag(111), the PdPc spectrum shows a peak at 850 cm^{-1}, labeled **R4**. Due to the large width of **R4**, an assignment is not possible. Likely, several components participate in it. Possible assignments of **R1**, **R2**, and **R3** are listed in Table IV using a range of 50 cm^{-1} around their centroid. Since there is the possibility to assign the **R1**, **R2**, and **R3** peaks to modes with a A_{1g} irreducible representation, they would then be detectable in HREELS in specular geometry irrespective of the point group of the molecule-substrate complex (C_{4v}, C_{2v}, C_s, C_4, or C_2); cf. Table II.

Three asymmetric peaks (**F1**, **F2**, and **F3**) are observed between 1000 and 1600 cm^{-1}, which indicates that several vibrational modes are involved in an IDCT. Using Eq. (19), we single out vibrational frequencies given by DFT calculations for isolated PdPc ($\bar{\omega}_\alpha$) that yield the best fit of the experimental data as explained in Sec. III C 3. As in the case of PtPc, several modes yield a reasonable fit for **F1**. Due to the large $\bar{\gamma}_\alpha$ value of **F2**, a clear assignment is not possible. **F3** can be fitted only with $\bar{\omega}_\alpha = 1506\ cm^{-1}$, a mode which belongs to the B_{1g} irreducible representation of the D_{4h} point group (see Fig. 5), and a B_{1g} mode can only be detected in HREELS in the specular direction if the fourfold molecular symmetry is reduced to $C_{2v}(\sigma_v)$, $C_s(\sigma_v)$, or C_2 (see Table II). As in the case of PtPc, this demonstrates that a preferential charge transfer occurs in one of the two LUMOs. Thus, the Ag(111) substrate lifts the degeneracy of the LUMO also in the case of PdPc.

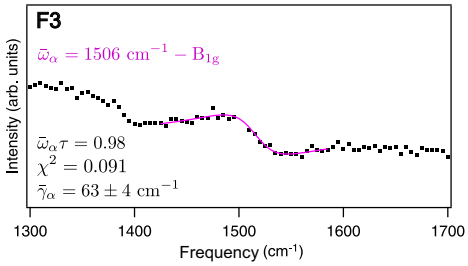

FIG. 5. Best fit of **F3** using $\bar{\omega}_\alpha = 1506\ cm^{-1} - B_{1g}$, for the ordered monolayer PdPc phase on Ag(111).

V. SUMMARY AND CONCLUSION

In conclusion, the vibrational properties of Pt- and Pd-phthalocyanine molecules on the Ag(111) surface show that both molecules adsorb with their molecular plane parallel to the surface in the ordered monolayer phase. The redshift of some of the out-of-plane modes reflects a moderate interaction between the meso-tetraazaporphin (porphyrazin) macrocycle of the molecule and the Ag substrate. The presence of Raman vibrational modes proves the lowering of the molecular symmetry from the D_{4h} group of the isolated molecule upon adsorption on Ag(111). The asymmetrical line shape of some of the molecular vibrational modes further demonstrates that charge transfer to the molecule is involved in the symmetry reduction to at least $C_{2v}(\sigma_v)$ or lower. Therefore, this study shows that HREELS is a valuable tool to determine the origin of the molecular degeneracy lifting upon adsorption on a metal surface.

ACKNOWLEDGMENTS

F.C.B. acknowledges financial support from the Initiative and Networking Fund of the Helmholtz Association, Postdoc Programme VH-PD-025. J.S. thanks Prof. Dr. P. Jakob, Philipps Universität Marburg, and Dr. P. Amsalem, Humboldt Universität Berlin, for fruitful discussions.

[1] R. H. Friend, R. W. Gymer, A. B. Holmes, J. H. Burroughes, R. N. Marks, C. Taliani, D. D. C. Bradley, D. A. Dos Santos, J. L. Brédas, M. Lögdlund, and W. R. Salaneck, Electroluminescence in conjugated polymers, Nature (London) **397**, 121 (1999).

[2] P. W. M. Blom, V. D. Mihailetchi, L. J. A. Koster, and D. E. Markov, Device physics of polymer: Fullerene bulk heterojunction solar cells, Adv. Mater. **19**, 1551 (2007).

[3] S. Sanvito, Molecular spintronics, Chem. Soc. Rev. **40**, 3336 (2011).

[4] J. M. Gottfried, Surface chemistry of porphyrins and phthalocyanines, Surf. Sci. Rep. **70**, 259 (2015).

[5] J. Blochwitz, M. Pfeiffer, T. Fritz, and K. Leo, Low voltage organic light emitting diodes featuring doped phthalocyanine as hole transport material, Appl. Phys. Lett. **73**, 729 (1998).

[6] B. Crone, A. Dodabalapur, Y.-Y. Lin, R. W. Filas, Z. Bao, A. LaDuca, R. Sarpeshkar, H. E. Katz, and W. Li, Large-scale complementary integrated circuits based on organic transistors, Nature (London) **403**, 521 (2000).

[7] G. Horowitz, Organic field-effect transistors, Adv. Mater. **10**, 365 (1998).

[8] J. C. Conboy, E. J. C. Olson, D. M. Adams, J. Kerimo, A. Zaban, B. A. Gregg, and P. F. Barbara, Impact of solvent vapor

annealing on the morphology and photophysics of molecular semiconductor thin films, J. Phys. Chem. B **102**, 4516 (1998).

[9] Y. Wang, J. Kröger, R. Berndt, and W. Hofer, Structural and electronic properties of ultrathin tin-phthalocyanine films on Ag(111) at the single-molecule level, Angew. Chem. Int. Ed. **48**, 1261 (2009).

[10] S.-H. Chang, S. Kuck, J. Brede, L. Lichtenstein, G. Hoffmann, and R. Wiesendanger, Symmetry reduction of metal phthalocyanines on metals, Phys. Rev. B **78**, 233409 (2008).

[11] H. Karacuban, M. Lange, J. Schaffert, O Weingart, Th. Wagner, and R. Möller, Substrate-induced symmetry reduction of CuPc on Cu(111): An LT-STM study, Surf. Sci. **603**, L39 (2009).

[12] Y. Wang, X. Ge, C. Manzano, J. Kröger, R. Berndt, W. A. Hofer, H. Tang, and J. Cerda, Supramolecular patterns controlled by electron interference and direct intermolecular interactions, J. Am. Chem. Soc. **131**, 10400 (2009).

[13] R. Cuadrado, J. I. Cerdá, Y. Wang, G. Xin, R. Berndt, and H. Tang, CoPc adsorption on Cu(111): Origin of the C4 to C2 symmetry reduction, J. Chem. Phys. **133**, 154701 (2010).

[14] O. Snezhkova, J. Lüder, A. Wiengarten, S. R. Burema, F. Bischoff, Y. He, J. Rusz, J. Knudsen, M.-L. Bocquet, K. Seufert, J. V. Barth, W. Auwärter, B. Brena, and J. Schnadt, Nature of the bias-dependent symmetry reduction of iron phthalocyanine on Cu(111), Phys. Rev. B **92**, 075428 (2015).

[15] N. F. Phelan and M. Orchin, Cross conjugation, J. Chem. Educ. **45**, 633 (1968).

[16] C. Uhlmann, I. Swart, and J. Repp, Controlling the orbital sequence in individual Cu-phthalocyanine molecules, Nano Lett. **13**, 777 (2013).

[17] V. Feyer, M. Graus, P. Nigge, M. Wießner, R. G. Acres, C. Wiemann, C. M. Schneider, A. Schöll, and F. Reinert, Adsorption geometry and electronic structure of iron phthalocyanine on Ag surfaces: A LEED and photoelectron momentum mapping study, Surf. Sci. **621**, 64 (2014).

[18] T. Niu, M. Zhou, J. Zhang, Y. Feng, and W. Chen, Dipole orientation dependent symmetry reduction of chloroaluminum phthalocyanine on Cu(111), J. Phys. Chem. C **117**, 1013 (2013).

[19] H. A. Jahn and E. Teller, Stability of polyatomic molecules in degenerate electronic states. I. Orbital degeneracy, Proc. R. Soc. A **161**, 220 (1937).

[20] H. Köpper, D. R. Yarkony, and H. Berentzen, *The Jahn-Taller Effect: Fundamentals and Implications for Physics and Chemistry*, Springer Series in Chemical Physics No. 97 (Springer, Berlin, 2009).

[21] P. Borghetti, A. El-Sayed, E. Goiri, C. Rogero, J. Lobo-Checa, L. Floreano, J. E. Ortega, and D. G. de Oteyza, Spectroscopic fingerprints of work-function-controlled phthalocyanine charging on metal surfaces, ACS Nano **8**, 12786 (2014).

[22] P. Puschnig, S. Berkebile, A. J. Fleming, G. Koller, K. Emtsev, T. Seyller, J. D. Riley, C. Ambrosch-Draxl, F. P. Netzer, and M. G. Ramsey, Reconstruction of molecular orbital densities from photoemission data, Science **326**, 702 (2009).

[23] P. Puschnig, E.-M. Reinisch, T. Ules, G. Koller, S. Soubatch, M. Ostler, L. Romaner, F. S. Tautz, C. Ambrosch-Draxl, and M. G. Ramsey, Orbital tomography: Deconvoluting photoemission spectra of organic molecules, Phys. Rev. B **84**, 235427 (2011).

[24] K. Schönauer, S. Weiss, V. Feyer, D. Lüftner, B. Stadtmüller, D. Schwarz, T. Sueyoshi, C. Kumpf, P. Puschnig, M. G. Ramsey, F. S. Tautz, and S. Soubatch, Charge transfer and symmetry reduction at the CuPc/Ag(110) interface studied by photoemission tomography, Phys. Rev. B **94**, 205144 (2016).

[25] H. Ibach and D. L. Mills, *Electron Energy Loss Spectroscopy and Surface Vibrations* (Academic Press, New York, 1982).

[26] M. J. Frisch, G. W. Trucks, H. B. Schlegel, G. E. Scuseria, M. A. Robb, J. R. Cheeseman, G. Scalmani, V. Barone, B. Mennucci, G. A. Petersson, H. Nakatsuji, M. Caricato, X. Li, H. P. Hratchian, A. F. Izmaylov, J. Bloino, G. Zheng, J. L. Sonnenberg, M. Hada, M. Ehara, K. Toyota, R. Fukuda, J. Hasegawa, M. Ishida, T. Nakajima, Y. Honda, O. Kitao, H. Nakai, T. Vreven, J. A. Montgomery, Jr., J. E. Peralta, F. Ogliaro, M. Bearpark, J. J. Heyd, E. Brothers, K. N. Kudin, V. N. Staroverov, R. Kobayashi, J. Normand, K. Raghavachari, A. Rendell, J. C. Burant, S. S. Iyengar, J. Tomasi, M. Cossi, N. Rega, J. M. Millam, M. Klene, J. E. Knox, J. B. Cross, V. Bakken, C. Adamo, J. Jaramillo, R. Gomperts, R. E. Stratmann, O. Yazyev, A. J. Austin, R. Cammi, C. Pomelli, J. W. Ochterski, R. L. Martin, K. Morokuma, V. G. Zakrzewski, G. A. Voth, P. Salvador, J. J. Dannenberg, S. Dapprich, A. D. Daniels, Ó. Farkas, J. B. Foresman, J. V. Ortiz, J. Cioslowski, and D. J. Fox, *Gaussian09 Revision D.01* (Gaussian Inc., Wallingford, CT, 2009).

[27] Z. Liu, X. Zhang, Y. Zhang, and J. Jiang, Theoretical investigation of the molecular, electronic structures and vibrational spectra of a series of first transition metal phthalocyanines, Spectrochim. Acta. **67A**, 1232 (2007).

[28] V. G. Maslov, Interpretation of the electronic spectra of phthalocyanines with transition metals from quantum-chemical calculations by the density functional method, Opt. Spectrosc. **101**, 853 (2006).

[29] See Supplemental Material at http://link.aps.org/supplemental/10.1103/PhysRevB.96.165410 for the LEED patterns, a detailed description of the A_{2u} modes, all fits and a list of vibrational modes for PdPc on Ag(111).

[30] I. Kröger, B. Stadtmüller, C. Stadler, J. Ziroff, M. Kochler, A. Stahl, F. Pollinger, T.-L. Lee, J. Zegenhagen, F. Reinert, and C. Kumpf, Submonolayer growth of copper-phthalocyanine on Ag(111), New J. Phys. **12**, 083038 (2010).

[31] B. Stadtmüller, I. Kröger, F. Reinert, and C. Kumpf, Submonolayer growth of CuPc on noble metal surfaces, Phys. Rev. B **83**, 085416 (2011).

[32] C. Stadler, S. Hansen, I. Kröger, C. Kumpf, and E. Umbach, Tuning intermolecular interaction in long-range-ordered submonolayer organic films, Nat. Phys. **5**, 153 (2009).

[33] R. L. Carter, *Molecular Symmetry and Group Theory* (John Wiley & Sons, Inc., 1998).

[34] P. Amsalem, L. Giovanelli, J.-M. Themlin, and T. Angot, Electronic and vibrational properties at the ZnPc/Ag(110) interface, Phys. Rev. B **79**, 235426 (2009).

[35] W. Dou, Y. Tang, C. S. Lee, S. N. Bao, and S. T. Lee, Investigation on the orderly growth of thick zinc phthalocyanine films on Ag(100) surface, J. Chem. Phys. **133**, 144704 (2010).

[36] W. Dou, S. Huang, R. Q. Zhang, and C. S. Lee, Molecule substrate interaction channels of metal-phthalocyanines on graphene on Ni(111) surface, J. Chem. Phys. **134**, 094705 (2011).

[37] N. Ohta, R. Arafune, N. Tsukahara, N. Takagi, and M. Kawai, Adsorbed states of iron(II) phthalocyanine on Ag(111) studied

by high-resolution electron energy loss spectroscopy, Surf. Interface Anal. **46**, 1253 (2014).

[38] J. D. Baran and J. A. Larsson, Theoretical insights into adsorption of cobalt phthalocyanine on Ag(111): A combination of chemical and van der Waals bonding, J. Phys. Chem. C **117**, 23887 (2013).

[39] R. C. Powell, *Symmetry, Group Theory, and the Physical Properties of Crystals*, Lecture Notes in Physics, No. 824 (Springer, New York, 2010).

[40] Y. J. Chabal, Electronic Damping of Hydrogen Vibration on the W(100) Surface, Phys. Rev. Lett. **55**, 845 (1985).

[41] J. Kröger, S. Lehwald, and H. Ibach, EELS study of the clean and hydrogen-covered Mo(110) surface, Phys. Rev. B **55**, 10895 (1997).

[42] F. S. Tautz, M. Eremtchenko, J. A. Schaefer, M. Sokolowski, V. Shklover, and E. Umbach, Strong electron-phonon coupling at a metal/organic interface: PTCDA/Ag(111), Phys. Rev. B **65**, 125405 (2002).

[43] I. Kröger, Adsorption of phthalocyanines on noble metal surfaces, Ph.D. thesis, Universität Würzburg, Germany, 2010.

[44] C. R. Braatz, G. Öhl, and P. Jakob, Vibrational properties of the compressed and the relaxed 1,4,5,8-naphthalene-tetracarboxylic dianhydride monolayer on Ag(111), J. Chem. Phys. **136**, 134706 (2012).

[45] P. Rosenow, P. Jakob, and R. Tonner, Electron-vibron coupling at metal-organic interfaces from theory and experiment, J. Phys. Chem. Lett. **7**, 1422 (2016).

[46] F. A. Cotton, *Chemical Applications of Group Theory*, 3rd ed. (John Wiley & Sons, Inc., 1990).

[47] D. C. Langreth, Energy Transfer at Surfaces: Asymmetric Line Shapes and the Electron-Hole-Pair Mechanism, Phys. Rev. Lett. **54**, 126 (1985).

[48] Ž. Crljen and D. C. Langreth, Asymmetric line shapes and the electron-hole pair mechanism for adsorbed molecules on surfaces, Phys. Rev. B **35**, 4224 (1987).

[49] J. Kröger, Electron-phonon coupling at metal surfaces, Rep. Prog. Phys. **69**, 899 (2006).

[50] $\tilde{\gamma}_\alpha = 60$ cm^{-1} has been reported for a similar (ZnPc) molecule on Ag(110) in Ref. [34]. Therefore, we expect $\tilde{\gamma}_\alpha$ values for PtPc and PdPc on Ag(111) to be close to 60 cm^{-1}.

Adsorption-induced symmetry reduction of metal-phthalocyanine studied by vibrational spectroscopy –Supplemental Material–

J. Sforzini,[1,2] F. C. Bocquet,[1,2,*] and F. S. Tautz[1,2]

[1] *Peter Grünberg Institut (PGI-3), Forschungszentrum Jülich, 52425 Jülich, Germany*
[2] *Jülich Aachen Research Alliance (JARA), Fundamentals of Future Information Technology, 52425 Jülich, Germany*

(Dated: September 20, 2017)

A. LEED

Fig. 2(a) shows LEED images of PtPc on Ag(111) detected at different coverages (annealing temperatures). At low coverage, two diffuse rings are observed. Increasing the coverage, a LEED pattern is detected. Fig. 2(b) shows the LEED pattern of the ordered monolayer phase of PdPc on Ag(111).

B. A_{2u} modes

The vibrational spectrum of the multilayer and ordered monolayer phase of PtPc on Ag(111) is dominated by the out-of-plane vibrational modes which belong to the A_{2u} representation. All A_{2u} modes are depicted in Fig. 3.

C. Asymmetric peaks

In the vibrational spectrum of the ordered monolayer phase of PtPc on Ag(111), three asymmetric peaks, namely **F1**, **F2** and **F3**, are observed between 1000 cm^{-1} and 1600 cm^{-1} (Fig. 1). These peaks are fitted using a generalization of the Fano equation and using the calculated frequencies ($\bar{\omega}_\alpha$).

The **F1** asymmetric peak lies at about 1000 cm^{-1}. In Fig. 4, all fits produced using the calculated $\bar{\omega}_\alpha$ values in the range 1050-1190 cm^{-1} are shown. A good fit is obtained for $\bar{\omega}_\alpha = 1117$ cm$^{-1} - B_{1g}$, $\bar{\omega}_\alpha = 1141$ cm$^{-1} - A_{1g}$ and $\bar{\omega}_\alpha = 1142$ cm$^{-1} - E_u$.

For **F2** (Fig. 5), no $\bar{\omega}_\alpha$ value yields a χ^2 that is significantly smaller than the others. Further, the width $\bar{\gamma}_\alpha$ is much larger than for **F1** and **F3** in all cases. This indicates that several vibrational modes contribute to this mode, and an accurate assignment is not possible.

The **F3** asymmetric peak lies at about 1500 cm^{-1}. Fig. 6 shows the fits obtained with the $\bar{\omega}_\alpha$ values which lie in the range 1450-1586 cm^{-1}. A good fit is obtained only for $\bar{\omega}_\alpha = 1509$ cm$^{-1} - B_{1g}$.

D. PdPc

In Tab. I, the assignments and irreducible representations of the experimental vibrational modes in the spectrum of a ordered PdPc monolayer phase on Ag(111) are listed together with the theory.

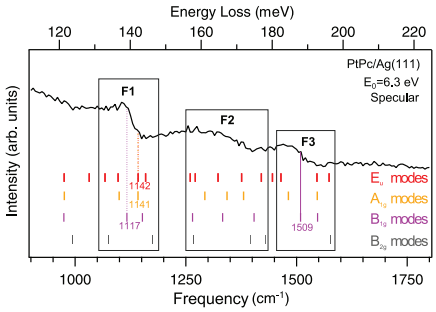

Figure 1: Zoom of the monolayer spectrum of PtPc on Ag(111) showing the asymmetric peaks **F1**, **F2** and **F3** together with the calculated vibrational modes (bars). Each peak has been fitted using all the calculated vibrations. All the fits of **F1**, **F2** and **F3** using the $\bar{\omega}_\alpha$ values located inside the surrounding box of each peak are presented in Fig 4, 5, 5 and 6. All the $\bar{\omega}_\alpha$ values which yield reasonable fits of **F1** are marked with dotted lines. The only good fit of **F3** is marked with a solid line.

2

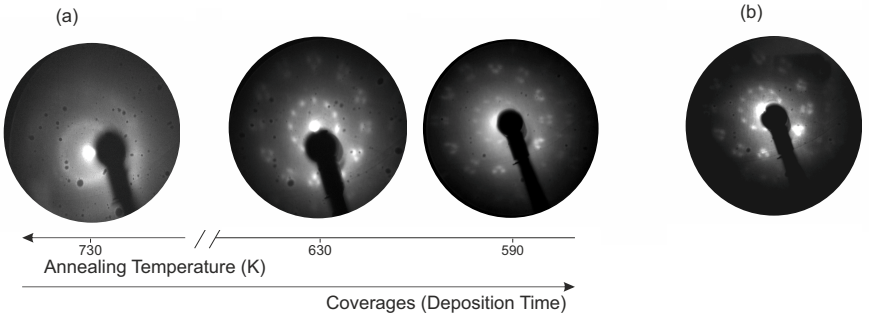

Figure 2: (a) The LEED images of PtPc on Ag(111) are obtained by annealing a thick layer of PtPc to the corresponding annealing temperatures. The images are acquired with a primary beam energy of 16 eV. (b) The LEED pattern, acquired with a primary beam energy of 20 eV, of the PdPc ordered phase on Ag(111).

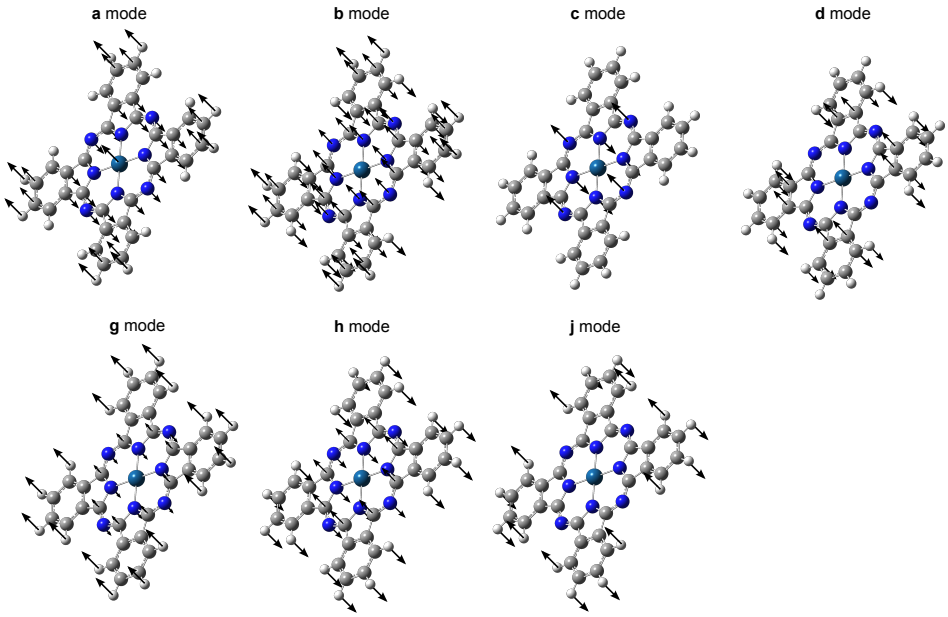

Figure 3: Detailed description of the out-of-plane A_{2u} modes observed in the spectra of PtPc and PdPc on Ag(111).

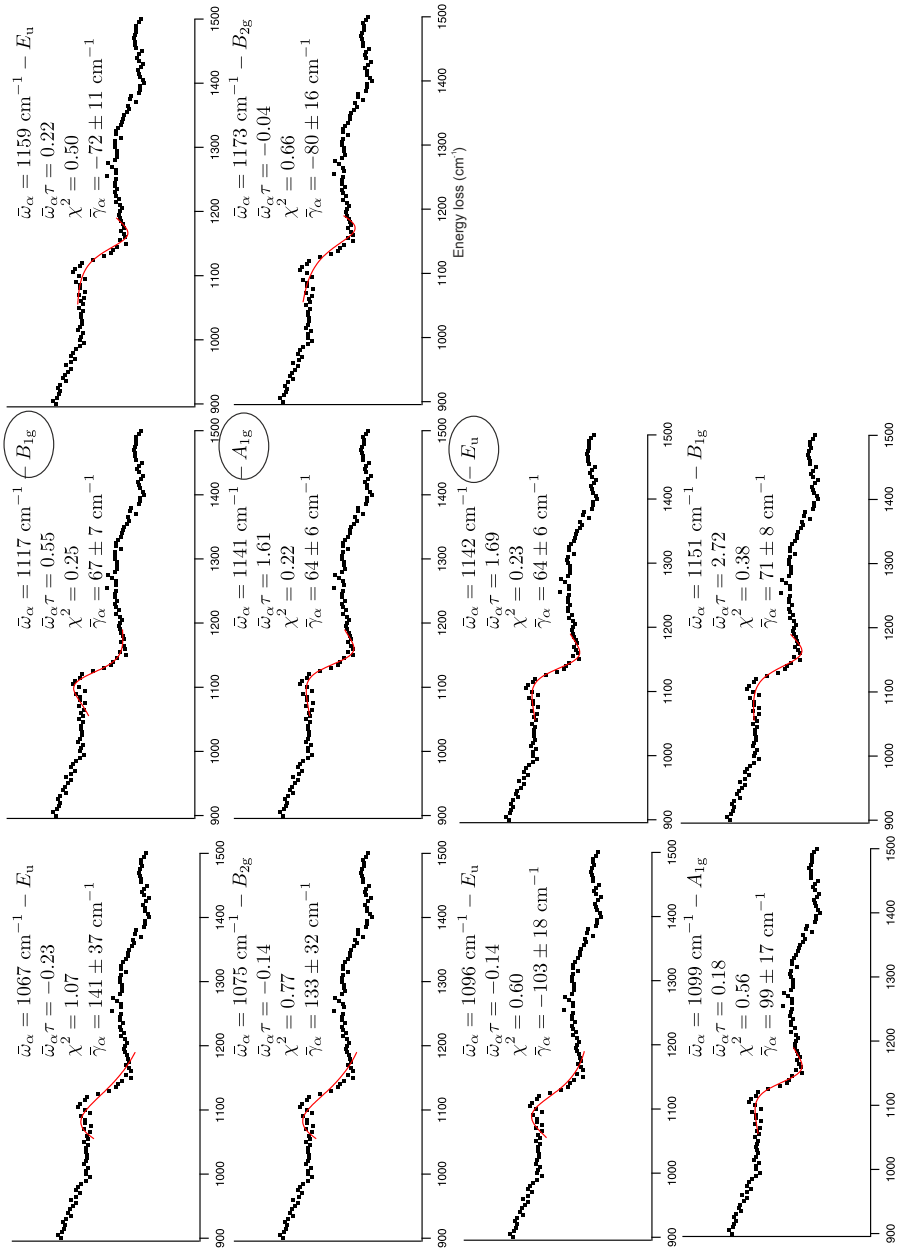

Figure 4: Fits of the asymmetric peak **F1** of the PtPc ordered monolayer phase using all the calculated $\bar{\omega}_\alpha$ situated in a range around **F1** defined in Fig. 1 together with their corresponding irreducible representations. The irreducible representations related to $\bar{\omega}_\alpha$ which give a reasonable fit are marked with a circle.

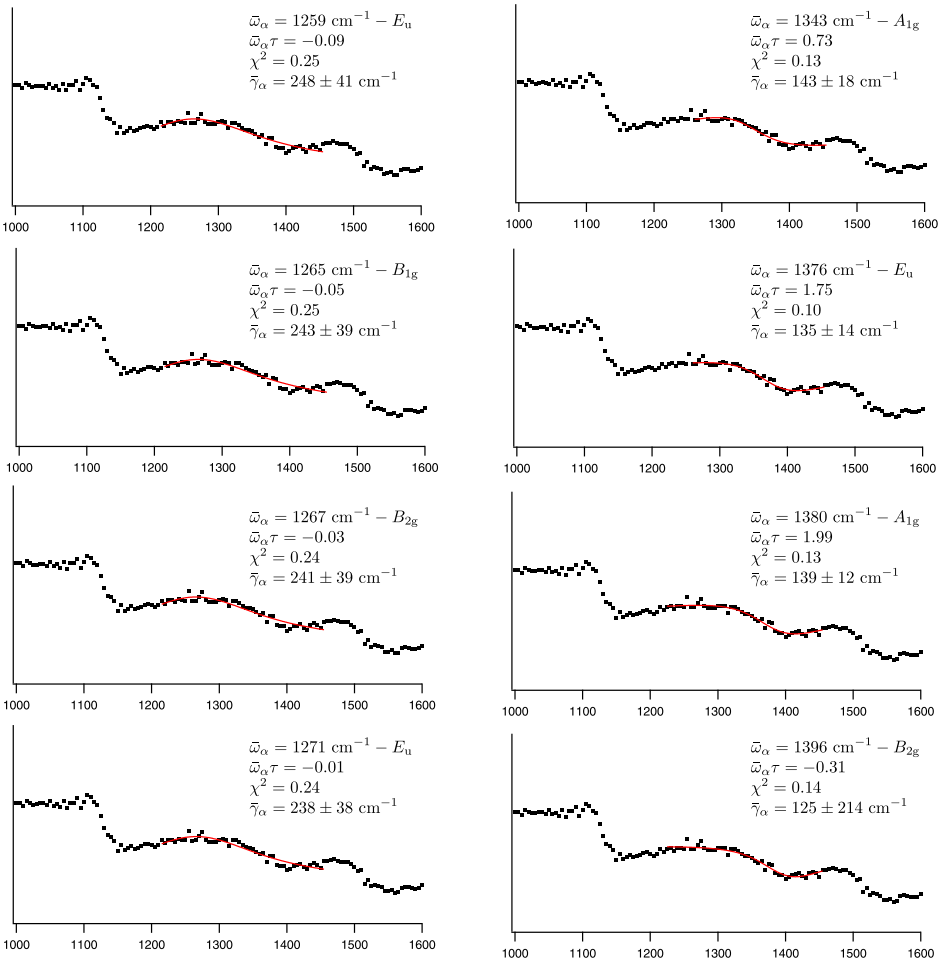

Figure 5: Fits of the asymmetric peak **F2** of the PtPc ordered monolayer phase using all the calculated $\bar{\omega}_\alpha$ situated in a range around **F2** defined in Fig. 1 together with their corresponding irreducible representations. The irreducible representations related to $\bar{\omega}_\alpha$ which give a reasonable fit are marked with a circle.

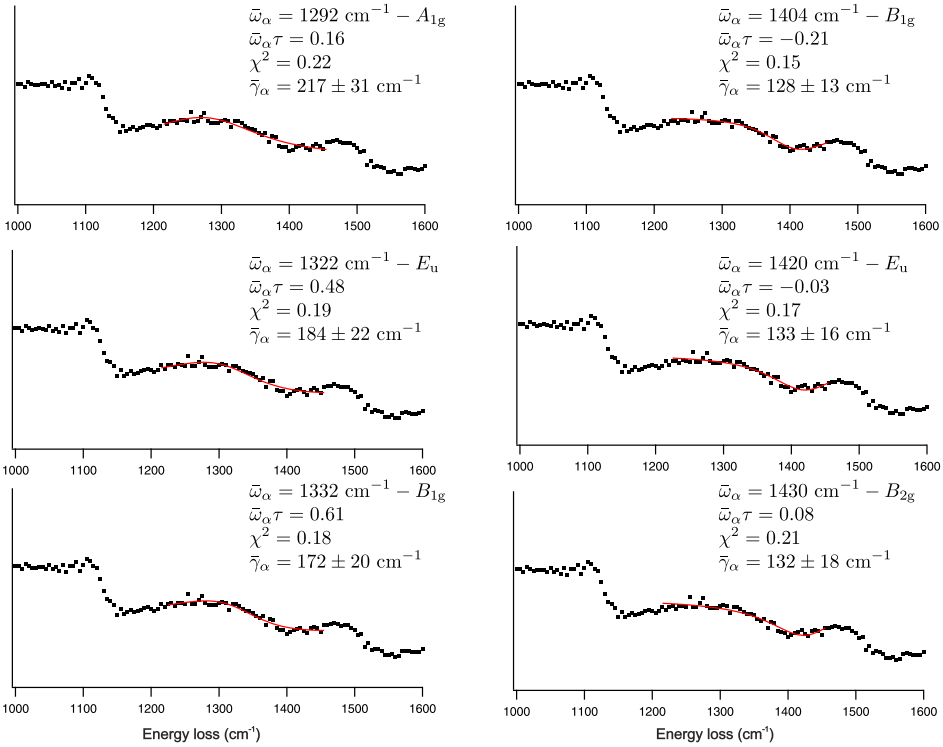

Figure 5 (Continued).

Modes	Ordered monolayer	DFT	Irreducible representation	Description
R1	256	-	-	-
c	345	382	A_{2u}	OP bend: N atoms
d	430	434	A_{2u}	OP bend: N + C atoms
R2	578	-	-	-
R3	662	-	-	-
g	720	738	A_{2u}	OP bend: Main ring
h	765	770	A_{2u}	OP bend: N atoms + Phenyl groups
R4	844	-	-	-
F1	$1075 - 1200$	-	-	-
F2	$1285 - 1435$	-	-	-
F3	$1450 - 1560$	1506	B_{1g}	IP stretch: C-N bond

Table I: List of the experimental vibrational frequencies present in the specular spectra of the PdPc multilayer and ordered monolayer phases on Ag(111) accompanied by their description and symmetries. The calculated frequencies are compressed by a factor 0.9456. The acronyms stand for: OP=out-of-plane, IP=in-plane; bend=bending mode, deform=deformation mode. All values are given in cm^{-1}.

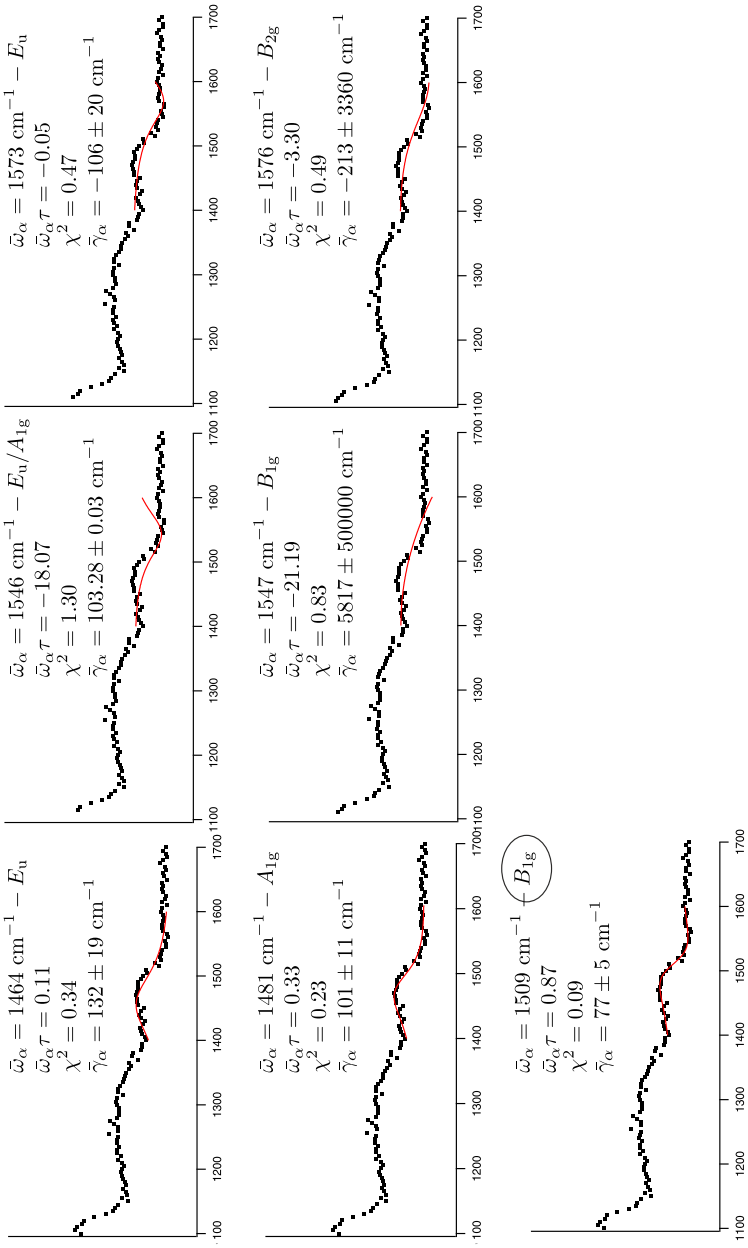

Figure 6: Fits of the asymmetric peak **F3** of the PtPc ordered monolayer phase using all the calculated $\bar{\omega}_\alpha$ situated in a range around **F3** defined in Fig. 1 together with their corresponding irreducible representations. The irreducible representations related to $\bar{\omega}_\alpha$ which give a reasonable fit are marked with a circle.

8.4 Interaction with Molecular Hydrogen

8.4.1 Introduction

In addition to electronics applications, metal-organic frameworks compounds have been studied as possible surfaces for hydrogen storage. Their versatility in forming three-dimensional networks ensures flexible composition with consequent possibility of tailoring the properties. Interest in them has rapidly grown in the last years due to the linear increase of the hydrogen gravimetric uptake with surface area [95, 96]. The area that can be obtained in this metal-organic materials depends mostly on the nature of the organic linkers.

However, high hydrogen storage capacities are reached only at low temperature because of the weak interaction between the hydrogen molecule and those surfaces [40]. Only in the vicinity of the metals the interaction between the surface and the hydrogen is important [97]. Also, in some cases, the metal atoms are not uniformly distributed on the surface, but they cluster due to inefficient catalysis or synthesis.

A reasonable alternative is to form such organic systems, similar to graphene, where there is the possibility to form two-dimensional materials allowing a better metal exposure, highly ordered structures and larger surface area. In this context, the interaction of PtPc and PdPc layers with molecular hydrogen is investigated.

8.4.2 Experimental Results

In order to evaluate if PtPc and PdPc molecules interact with molecular hydrogen, we expose the organic layers to molecular hydrogen/deuterium at room temperature, and perform the HREELS experiments as for the clean sample (see Sec. 8.2). The vibrational properties of the molecules do not change after the exposure. No additional peaks related to the presence of hydrogen appear in the spectra in both specular and off-specular geometry. However, the presence of hydrogen/deuterium in the two-dimensional structures is confirmed by Temperature Programmed Desorption (TPD) experiments. Fig. 8.1 shows the QMS intensities recorded as a function of the annealing temperature for different samples and exposure. A peak appears around 380 K when annealing the multilayer and the monolayer previously exposed

to deuterium for 20 minutes. Since annealing the bare crystal after a deuterium exposure or annealing a clean multilayer produce no signal, the previous peak must be related to the presence of hydrogen at the interface.

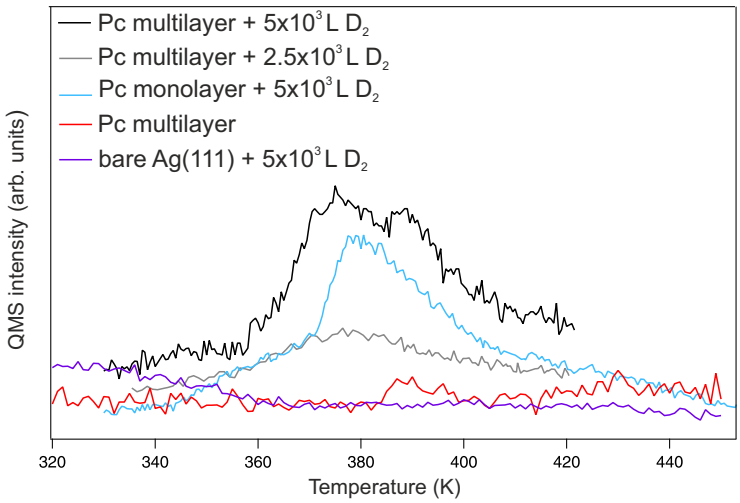

Figure 8.1: TPD spectra of PtPc showing the signal of 4 a.m.u. recorded with the QMS at heating rate of 1 Ks^{-1} after the D_2 exposure.

8.4.3 Summary and Conclusion

We have exposed the organic layers, prepared at different coverages, to H_2/D_2. The presence of H_2 at the interface is demonstrated by the appearance of a desorption peak in the TPD spectra. However no additional peaks are visible at room temperature in the HREELS spectra. Either the spectrometer sensitivity is too low or the modes related to the hydrogen/deuterium molecule are not IR active. Therefore, more systematic experiments are needed on the layers, at low temperature and with a new spectrometer, which is described in the next section.

9 Testing a New HREELS Set-Up

9.1 Introduction

The results presented in the previous chapter show that HREELS is a very powerful technique to study surface excitations, e.g., molecular vibrations, excited by the dipole scattering. If one wants to investigate features excited by the impact scattering, limitations may arise when a conventional spectrometer is used. In the impact scattering regime the electrons are inelastically scattered via the short range interactions not in a narrow lobe as for the dipole scattering regime, but in a broad angular distribution and with much lower intensity. Consequently, long acquisition times are usually required in order to have a reasonable intensity, and the rotation of the sample around the scattering chamber is needed to detect off-specular electrons due to the low acceptance angle of the conventional detector.

An example for such experiments is the measurement of energy dispersion curves. In order to measure phonons as a function of momentum, multiple one-dimensional spectra of the reflected intensity vs energy are normally measured at different angles in the conventional set-up to map a large part of the Brillouin zone of solids. In this context, the use of a two-dimensional hemispherical analyzer permits to simultaneously collect the scattered electrons in a wide angular range.

As the low-index (111) surface of Cu is thoroughly investigated in terms of phonon dispersion curves (Sec. 3.3), in this chapter the phonon curves of Cu(111) are presented in order to illustrate the advanced features of an HREELS electron gun developed in the PGI-3 institute, Forschungszentrum Jülich, Germany. The design of the transfer lens systems as well as the electron trajectory simulations have been performed by Prof. Dr. H. Ibach (PGI-6), while the following experimental results have been carried out in close collaboration with him. With this new design the reflected beam is collected by a hemispherical analyzer, and the electron intensity

is measured simultaneously as a function of the loss energy and angle. Thus, a two-fold multiplex gain is obtained and a substantial part of the Brillouin zone can be obtained as two-dimensional data (intensity vs energy and momentum) and in one single measurement.

9.2 Experimental Details

The experiments were performed in the ESCA laboratory, PGI-3 institute, Forschungszentrum Jülich, Germany. The description of the experimental chamber is presented in Sec. 3.4.4. The Cu(111) surface was prepared by cycles of Ar^+ sputtering at 800 eV and consequent annealing to 700 K until a sharp LEED pattern was obtained. The $\overline{\Gamma M}$ direction of the Brillouin zone was determined by moving the sample angle until two consecutive $\overline{\Gamma}$ points were found. Surface excitations were measured using a primary beam energy in a range of $20 - 150$ eV.

9.3 Experimental Results

In Fig. 9.1, a representation of the new HREELS spectrometer is provided. It consists of a cathode lens system, a double stage monochromator, and a transfer lenses system. The cathode and monochromator sections are the same as in the

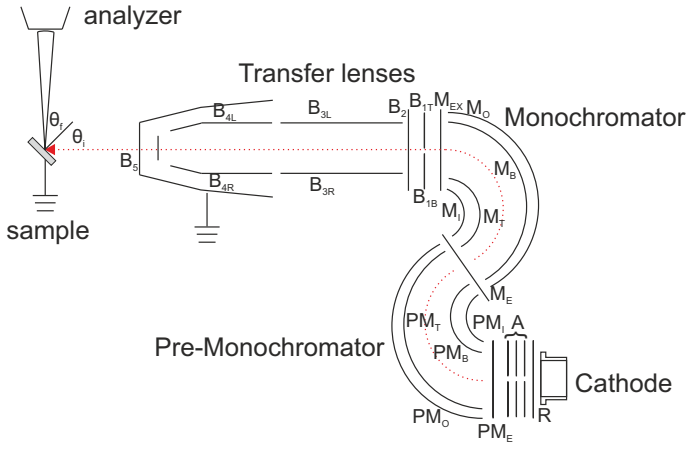

Figure 9.1: Representation of the new HREELS spectrometer coupled with the hemisperical analyzer, present in the ESCA laboratory, Forschungszentrum Jülich, Germany.

conventional spectrometer, and so is their operation. Regarding this, details can be found in Sec. 3.4.3. After the beam exits from the monochromator, it passes through the transfer lenses system, which represents the innovation of this new design. The task of the transfer lenses system is to focus the beam on the sample surface. After modifying the impact energy or the sample position, the optimal focus may be affected. Thus, a fast optimization of the five lenses of the transfer tube may be necessary in order to improve the focus on the sample and to recover the intensity lost. Another important feature of the transfer tube is to guarantee that the area illuminated by the gun matches the area viewed by the analyzer. Also after changing the analyzer settings, an optimization of the transfer lenses adjusts the beam spot according to the analyzer slits.

After passing through the transfer lenses, the beam is directed on the sample surface with an angle θ_i, and the reflected beam is acquired by the analyzer with an angle $\theta_f \pm 15°$ since the analyzer acceptance angle is 30°. As the parallel momentum is conserved while the electron is scattered, the wave vector of the excitation is expressed by

$$|\mathbf{k}_{||}| = k_i \sin(\theta_i) - k_f \sin(\theta_f) = \sqrt{\frac{2m}{\hbar^2}\mathrm{E}_{kin}}(\sin(\theta_i) - \sin(\theta_f)), \tag{9.1}$$

where k_i and are k_f are the wave vectors of the incident and scattered electrons.

In the angular mode of the analyzer the intensity of the scattered electrons are detected as a function of the energy and emission angle. Fig. 9.2 shows the two-dimensional distribution of the electrons reflected from the Cu(111) surface and detected at the analyzer in the specular direction. In order to avoid any damage of the multichannel plate detector, its high voltage is reduced to around 1200 V instead of the typical 1500 V used for measurements. As a consequence, the low intensity electrons are not measured and the resolution of the elastic peak in terms of energy and angle is smaller than the real one. Further, only the elastic peak is detected and inelastic features are not visible.

By tilting the angle of the sample such that the intense specular reflected beam is outside the angle range viewed by the analyzer, the voltage of the detector can be increased to 1500 V, and phonons can be measured. Fig. 9.3 shows the HREELS image acquired with an impact energy of 112 eV in comparison with theory (red lines) [61]. The elastic peak onset is visible at the $\overline{\Gamma}$ point. The main feature is the S_1 branch which detaches from the elastic peak at high wave vector and is found at 13 meV at the $\overline{\mathrm{M}}$ point. Weaker contributions corresponding to the S_2 and S_3

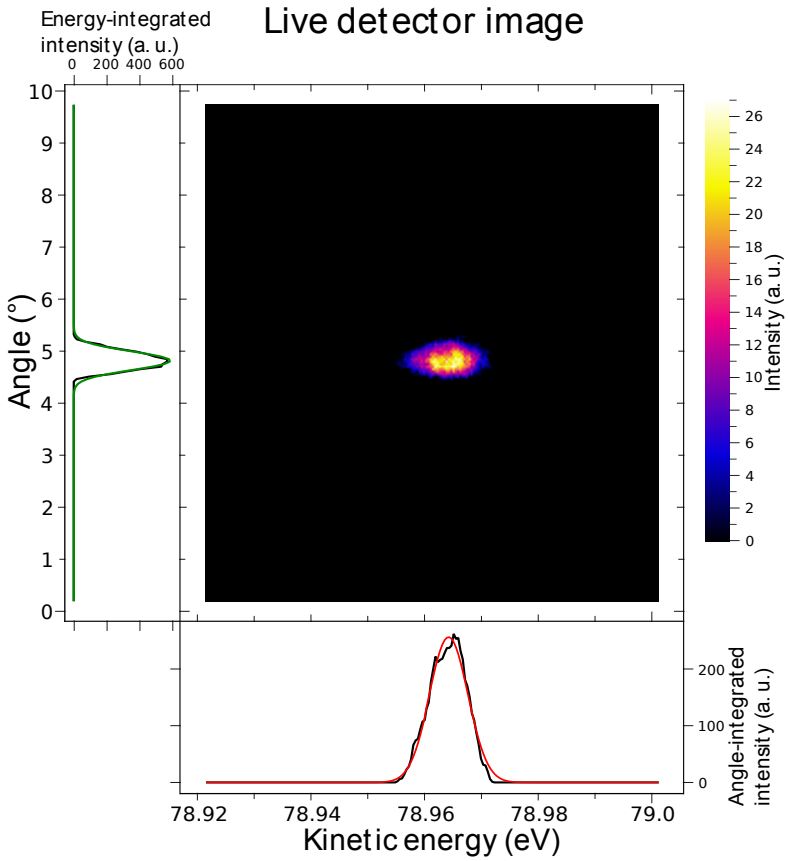

Figure 9.2: Image of the specular electron beam detected at the analyzer using an impact energy equal to 65 eV, an analyzer slit of 600 and 1120 eV as high voltage of the multichannel plate detector. The Gaussian fits of the integrated beam over the energy slides and over the angle slides produce the FWHM of 3.73 meV and 0.44°, respectively.

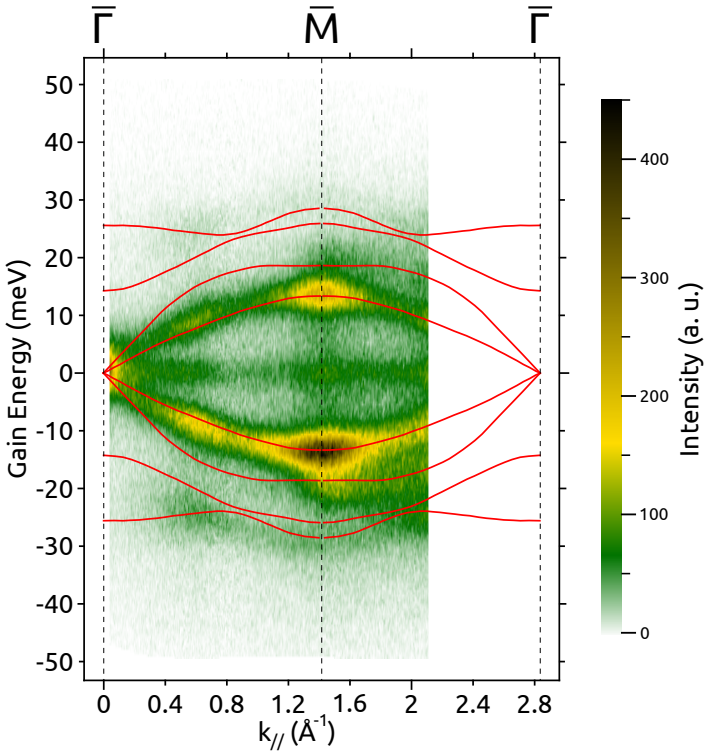

Figure 9.3: Phonon dispersion curves of Cu(111) measured along the $\overline{\Gamma M}$ direction and with a E_{kin} of 112 eV. The red lines represent the theoretical phonons taken from Ref.[62], © IOP Publishing. Reproduced with permission. All rights reserved.

modes are also present. As expected, the intensity of the modes differs for loss and gain due to the difference in the phonon population and to the lowering to a three-fold symmetry of the surface with consequent dissimilar cross sections [64]. In contrast to the conventional HREELS set-up, where numerous measurements were needed to cover the $\overline{\Gamma M}$ direction (see Sec. 3.3), with this new set-up we demonstrate that it is possible to measure losses in a 0-2.1 Å^{-1} wave vector range and in only 7 minutes.

9.4 Summary and Conclusion

The overall performance of the new HREELS coupled with the hemispherical analyzer have been presented by studying the phonon dispersion curves of Cu(111) along the $\overline{\Gamma M}$ direction. In contrast to the traditional set-up, a large part of the

Brillouin zone is measured in one scan producing a two-dimensional image of the intensity as a function of the energy and momentum. The typical three phonon dispersion curves of Cu(111) have been observed in the range from 0 to 2.1 Å^{-1}. This demonstrates that, with this new set-up, the measurement time is significantly improved.

10 Conclusions

In the first part of this dissertation, the coupling of the graphene layer with different supporting materials has been determined in terms of covalent and non-covalent bonding, layer corrugation and doping. This would have been impossible without the introduction of a new parameter, the van der Waals overlap, which estimates the influence of the substrate on the electronic and structural properties of graphene allowing a direct comparison between different systems given the graphene adsorption height (available from NIXSW experiments).
From the structural analysis of H-QFMLG and of EMLG on 6H-SiC(0001), there is the clear evidence that the intercalation process softens the influence of the underlying SiC as the interface in QFMLG comprises predominantly of weak van der Waals interactions. As a consequence, H-QFMLG is much more ideal for device applications than EMLG, as also confirmed by DFT calculations. However, based on our NIXSW results on Ge-QFMLG, the intercalation process is not always convenient. When intercalating one monolayer of Ge between graphene and SiC (leading to n-type graphene), the interaction at the interface as well as the layer buckling significantly increases making EMLG a better choice than n-type Ge-QFMLG. On the other hand, it seems these effects can be reversed by doubling the amount of germanium at the interface (leading to p-type graphene) resulting in a flatter graphene layer. Obviously, this is strongly linked to a different arrangement of the Ge atoms at the interface, whose vertical structure has however experimentally been resolved only for the n-type phase clarifying long-standing uncertainties, and hopefully, being the input for further theoretical studies on the p-type phase.
In spite of this, our results have been further compared to other graphene/substrate systems for which the graphene adsorption height had been measured and/or calculated. One of the main conclusions is that H-QFMLG/SiC, having the largest adsorption distance, in other words a vanishing van der Waals overlap, is the weakest interacting system suggesting that the adsorption distance is a valid parameter to determine the ideality of graphene.

Whereas hydrogen-intercalated SiC is a weaker interacting support for graphene

compared to BL-terminated SiC, this is not the case for its corresponding nitrogen-doped structure. To the best of our knowledge, we have been the first to investigate the doping process of graphene taking into consideration the substrate (and interface) contribution. From the comparative NIXSW and ARPES studies on nitrogen-doped H-QFMLG and EMLG, both on SiC(0001), there is the clear evidence that the support has multiple influences on the doping of graphene. Specifically, the concentration of dopants substituted into the layer as well as their configuration and thus the graphene effective doping are strictly linked to the type of interface.
In the case of doped H-QFMLG, the graphene n-type carrier increase has only partially been attributed to dopants substituted into the graphene layer. A significant contribution comes from nitrogen replacing hydrogen at the interface, leading to the surprising outcome that atoms confined underneath the graphene layer (outside the lattice) can inject charge carriers ('proximity doping'). Indeed, in terms of layer/substrate interactions, the van der Waals overlap necessarily increases accompanied by a buckling of the layer with consequent reduction of the freestanding character of graphene in H-QFMLG. On the contrary, the BL structure in EMLG remains structurally intact and inert under nitrogen doping, preventing any degradation of the graphene layer and allowing a multicomponent substitution of all the dopants into the layer.
Because of this surprising BL inactive behavior, EMLG and thus BL have been further doped with boron and investigated using XPS and NEXAFS, revealing the presence of dopants in one bonding configuration and in both lattices (graphene and BL). This different behavior can be attributed to the dopant nature in relation to the bonding configuration, and to the synthesis in relation to the BL activity/inactivity. Independent of synthesis, dopant nature and interface type was the systematic detection of dopants (N and B) in the SiC substrate. This additionally points out that any contribution from the substrate (and interface) has to be taken into account as our findings have revealed that doping of graphene is hence a matter of substrate choice.

In the second part of this dissertation, a new approach based on HREELS has been presented which permits unambiguously to assess the symmetry reduction of phthalocyanine molecules, which have a doubly degenerate LUMO, upon adsorption via degeneracy lifting. When considering the vibrational properties of PtPc and PdPc on Ag(111), a large amount of information about the charge transfer at the interface and molecular symmetry can be obtained. Certainly, a possible interaction between the molecules and the substrate can be visible in the shift of some of the molecular vibrational peaks with respect to the isolated molecule, as indeed

observed for both molecules. However, only because of the presence of a Fano-type line shape (asymmetric vibrational peak), it has been possible to correlate a molecular symmetry reduction (of both molecules) to two-fold with an unequal occupancy of the LUMO. Specifically, given the charge transfer induced-Fano peak, its assignment to a vibrational mode, which is IR non-active in the isolated Pc four-fold symmetry group but becomes IR active in the two-fold symmetry group, demonstrates that the molecule/substrate complex assumes a two-fold symmetry accompanied by a LUMO electronic splitting. Therefore, exploiting the activation of modes associated with Fano-line shape can allow the HREELS technique to study the symmetry of molecules/substrate complex systems in, effectively, a very simple way.

Altogether, the present thesis provides insights into the interactions at the interface in graphene/substrate and phthalocyanine/metal systems obtained with alternative and new approaches. Even though these results advance the research in carbon-based 2D materials, the unexpected findings related to, for example, doped graphene show that further advancement in the main theme of this work −the influence of the substrate− will be critical as we move forward in technology.

11 Appendix A

In Sec. 3.4.3 the DFT of the electronic structure and vibrational frequencies of the isolated PdPc and PtPc are given. Here, the list of the calculated vibrational frequencies is presented. A sketch of the molecule is shown in Fig. 11.1 illustrating the acronyms used to describe the movement of the atoms or group of atoms in each mode.

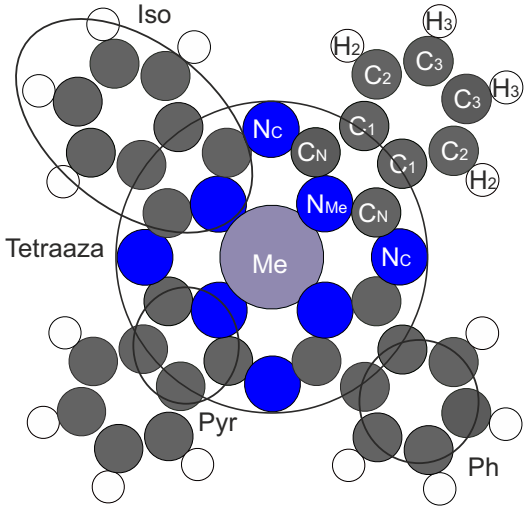

Figure 11.1: Illustration of the metal-phthalocyanine molecule. The acronyms stand for: Ph=Phenyl group, Pyr=Pyrrole group, Tetraaza=Tetraazaporphyrin ring, Iso=Isoindole group.

Table 11.1: Vibrational modes of PtPc calculated using using LanL2DZ basis set and B3LYP functional accompanied by their assignments and symmetries. The frequencies are compressed by f=0.9456 to match the experimental ones. The acronyms of the molecule refers to the labels defined in Fig. 11.1 and OOP=out-of-plane, IP=in-plane, bend=bending mode, sciss=scissoring mode, breath=breathing mode, stret=stretching mode, def=deformation mode and rock=rocking mode.

Mode	DFT*f (cm^{-1})	DFT*f (meV)	Assignment	Symm
1	21.931	2.741	OOP bend: Ph	B_{2U}
2	34.473	4.309	OOP bend: Me+N+C_N vs Ph	A_{2U}
3	56.524	7.066	OOP bend: Ph+Pyr+N_C	B_{1U}
4	67.615	8.452	OOP bend: Ph+Pyr+N_C	E_G
5	67.615	8.452	OOP bend: Iso+ N_C	E_G
6	107.028	13.379	IP sciss: Iso+ N_C	B_{2G}
7	109.931	13.741	IP sciss: Ph	E_U
8	109.931	13.741	IP sciss: Ph	E_U
9	118.803	14.850	OOP def: Ph	A_{1U}
10	125.441	15.680	OOP def: Ph	E_G
11	125.441	15.680	OOP def: Ph	E_G
12	135.734	16.967	OOP bend: C_3+H_3 vs N_C+C_N+C_1	A_{2U}
13	148.748	18.593	OOP def: Iso	B_{2U}
14	202.745	25.343	IP sciss: Mol	A_{2G}
15	204.506	25.563	IP breath: Mol	B_{1G}
16	216.543	27.068	OOP def: Ph+N_C+C_N	B_{1U}
17	220.735	27.592	IP sciss: Tetraaza	B_{2G}
18	249.861	31.233	IP breath: Mol	E_U
19	249.861	31.233	IP breath: Mol	E_U
20	254.297	31.787	IP breath: Mol	A_{1G}
21	255.036	31.880	OOP def: Mol	E_G
22	255.036	31.880	OOP def: Mol	E_G
23	290.765	36.346	IP stret: Iso+N_C	E_U
24	290.765	36.346	IP stret: Iso+N_C	E_U
25	297.474	37.184	OOP bend: N_{Me}+C_3+H_3 vs N_C+C_2+H_2	E_G
26	297.474	37.184	OOP bend: N_{Me}+C_3+H_3 vs N_C+C_2+H_2	E_G

27	300.891	37.611	OOP bend: Me+$C_{1,2}$+H_2 vs N+$C_{N,3}$+H_3	A_{2U}
28	336.958	42.120	OOP def: Mol	B_{2U}
29	382.323	47.790	OOP bend: N_C vs N_{Me}	A_{2U}
30	419.960	52.495	OOP bend: H_2+C_2 vs $C_{1,3}$+H_3	E_G
31	419.960	52.495	OOP bend: H_2+C_2 vs $C_{1,3}$+H_3	E_G
32	423.577	52.947	OOP def: Iso	A_{1U}
33	430.400	53.800	OOP bend: Ph+N_{Me}	B_{2U}
34	434.490	54.311	OOP bend: N+C_2+H_2 vs C_1	A_{2U}
35	462.780	57.848	IP sciss: Mol	B_{2G}
36	487.809	60.976	OOP def: Iso+N_C	E_G
37	487.809	60.976	OOP def: Iso+N_C	E_G
38	489.929	61.241	IP sciss: Iso+N_C	E_U
39	489.929	61.241	IP sciss: Iso+N_C	E_U
40	511.310	63.914	OOP def: Ph+N_C	B_{1U}
41	552.855	69.107	IP breath: Mol	B_{1G}
42	559.305	69.913	IP defn: Mol	E_U
43	559.305	69.913	IP def: Mol	E_U
44	560.437	70.055	IP def: Iso+N_C	A_{2G}
45	574.215	71.777	IP breath: Mol	A_{1G}
46	607.887	75.986	IP sciss: Tetraaza	A_{2G}
47	608.068	76.008	OOP def: Iso	A_{1U}
48	623.975	77.997	IP def: Mol	E_U
49	623.975	77.997	IP def: Mol	E_U
50	624.869	78.109	OOP def: Iso+N_C	E_G
51	624.869	78.109	OOP def: Iso+N_C	E_G
52	641.839	80.230	IP sciss: Ph+N_C	A_{1G}
53	662.779	82.847	IP def: Ph	B_{2G}
54	669.276	83.659	OOP def: Iso+ N_C	B_{1U}
55	688.139	86.017	OOP bend: H+N_C vs N_{Me}	B_{2U}
56	721.058	90.132	OOP bend: H+N_C vs N_{Me}	E_G
57	721.058	90.132	OOP bend: H+N_C vs N_{Me}	E_G
58	722.319	90.290	IP stret: Pyr	B_{1G}
59	725.492	90.686	IP sciss: Tetraaza	E_U

60	725.492	90.686	IP sciss: Tetraaza	E_U
61	738.449	92.306	OOP bend: N vs $H_{2,3}$+C_N	A_{2U}
62	768.344	96.043	OOP bend: H	B_{2U}
63	770.113	96.264	OOP bend: H+C_1 vs C_N	E_G
64	770.113	96.264	OOP bend: H+C_1 vs C_N	E_G
65	771.713	96.464	OOP def: Ph+C_N	A_{1U}
66	773.475	96.684	IP def: Ph+Tetraaza	B_{1G}
67	776.219	97.027	OOP def: H_2+$C_{1,N}$	B_{1U}
68	778.500	97.313	OOP def: Mol	E_G
69	778.500	97.313	OOP def: Mol	E_G
70	779.907	97.488	IP def: Mol	E_U
71	779.907	97.488	IP def: Mol	E_U
72	783.448	97.931	OOP bend: N+H+C_1 vs $C_{N,2,3}$	A_{2U}
73	820.441	102.555	IP breath: Mol	A_{1G}
74	828.314	103.539	IP def: Mol	A_{2G}
75	868.749	108.594	IP def: Ph+Tetraaza	E_U
76	868.749	108.594	IP def: Ph+Tetraaza	E_U
77	879.957	109.995	OOP bend: H	A_{1U}
78	880.384	110.048	OOP bend: H	B_{1U}
79	880.488	110.061	OOP bend: H	E_G
80	880.488	110.061	OOP bend: H	E_G
81	890.594	111.324	IP def: Mol	B_{2G}
82	954.885	119.361	OOP bend: H	B_{2U}
83	955.415	119.427	OOP bend: H	E_G
84	955.415	119.427	OOP bend: H	E_G
85	956.000	119.500	OOP bend: C_2+H_2 vs C_3+H_3	A_{2U}
86	974.612	121.827	IP breath: Ph	B_{1G}
87	975.040	121.880	IP breath: Ph	E_U
88	975.040	121.880	IP breath: Ph	E_U
89	975.466	121.933	IP breath: Ph	A_{1G}
90	984.226	123.028	OOP bend: H	A_{1U}
91	984.466	123.058	OOP bend: H	E_G
92	984.466	123.058	OOP bend: H	E_G
93	984.696	123.087	OOP bend: H	B_{1U}

94	995.026	124.378	IP def: Mol	B_{2G}
95	1031.647	128.956	IP def: Mol	E_U
96	1031.647	128.956	IP def: Mol	E_U
97	1058.858	132.357	IP def: Ph	A_{2G}
98	1067.534	133.442	IP stret: Pyr	E_U
99	1067.534	133.442	IP stre: Pyr	E_U
100	1073.030	134.129	IP stret: Pyr	A_{2G}
101	1075.100	134.387	IP stret: Pyr	B_{2G}
102	1096.961	137.120	IP def: Iso	E_U
103	1096.961	137.120	IP def: Iso	E_U
104	1099.343	137.418	IP breath: Mol	A_{1G}
105	1116.768	139.596	IP breath: Mol	B_{1G}
106	1141.748	142.718	IP sciss: H	A_{1G}
107	1142.175	142.772	IP sciss: H	E_U
108	1142.175	142.772	IP sciss: H	E_U
109	1151.690	143.961	IP def: Iso	B_{1G}
110	1156.738	144.592	IP def: Iso	A_{2G}
111	1158.911	144.864	IP def: Mol	E_U
112	1158.911	144.864	IP def: Mol	E_U
113	1173.703	146.713	IP stret: H+Pyr	B_{2G}
114	1259.805	157.476	IP rock: H	E_U
115	1259.805	157.476	IP rock: H	E_U
116	1261.699	157.712	IP rock: H	A_{2G}
117	1265.021	158.128	IP stret: Pyr	B_{1G}
118	1267.333	158.417	IP rock: H	B_{2G}
119	1271.389	158.924	IP stret: Pyr	E_U
120	1271.389	158.924	IP stret: Pyr	E_U
121	1292.784	161.598	IP stret: Pyr	A_{1G}
122	1322.590	165.324	IP stret: Ph	E_U
123	1322.590	165.324	IP stret: Ph	E_U
124	1332.857	166.607	IP stret: Ph	B_{1G}
125	1343.098	167.887	IP stret: Ph	A_{1G}
126	1376.045	172.006	IP rock: H	E_U
127	1376.045	172.006	IP rock: H	E_U

128	1380.374	172.547	IP sciss: Iso	A_{1G}
129	1396.441	174.555	IP stret: Tetraaza	B_{2G}
130	1404.042	175.505	IP stret: Ph	B_{1G}
131	1420.601	177.575	IP sciss: H	E_U
132	1420.601	177.575	IP sciss: H	E_U
133	1421.658	177.707	IP sciss: H	A_{2G}
134	1430.193	178.774	IP stret: Pyr	B_{2G}
135	1445.543	180.693	IP stret: Tetraaza	E_U
136	1445.543	180.693	IP stret: Tetraaza	E_U
137	1464.456	183.057	IP stret: N_C+C_N	A_{2G}
138	1464.654	183.082	IP stret: N_C+C_N	E_U
139	1464.654	183.082	IP stret: N_C+C_N	E_U
140	1481.674	185.209	IP stret: N_C+C_N	A_{1G}
141	1509.000	188.625	IP stret: N_C+C_N	B_{1G}
142	1546.008	193.251	IP stret: Ph	E_U
143	1546.008	193.251	IP stret: Ph	E_U
144	1546.937	193.367	IP stret: Ph	A_{1G}
145	1547.616	193.452	IP stret: Ph	B_{1G}
146	1571.216	196.402	IP stret: Ph	A_{2G}
147	1573.535	196.692	IP stret: Ph	E_U
148	1573.535	196.692	IP stret: Ph	E_U
149	1576.070	197.009	IP stret: Ph	B_{2G}
150	3025.196	378.150	IP stret: H	A_{2G}
151	3025.228	378.153	IP stret: H	E_U
152	3025.228	378.153	IP stret: H	E_U
153	3025.241	378.155	IP stret: H	B_{2G}
154	3041.419	380.177	IP stret: H	B_{1G}
155	3041.475	380.184	IP stret: H	E_U
156	3041.475	380.184	IP stret: H	E_U
157	3041.591	380.199	IP stret: H	A_{1G}
158	3057.437	382.180	IP stret: H	A_{2G}
159	3057.559	382.195	IP stret: H	E_U
160	3057.559	382.195	IP stret: H	E_U
161	3057.671	382.209	IP stret: H	B_{2G}

162	3063.884	382.985	IP stret: H	B_{1G}
163	3063.942	382.993	IP stret: H	E_U
164	3063.942	382.993	IP stret: H	E_U
165	3064.181	383.023	IP stret: H	A_{1G}

Table 11.2: Vibrational modes of PdPc calculated using using LanL2DZ basis set and B3LYP functional accompanied by their assignments and symmetries. The frequencies are compressed by f=0.9456 to match the experimental ones. The acronyms of the molecule refers to the labels defined in Fig. 11.1 and OOP=out-of-plane, IP=in-plane, bend=bending mode, sciss=scissoring mode, breath=breathing mode, stret=stretching mode, def=deformation mode and rock=rocking mode.

Mode	DFT*f (cm^{-1})	DFT*f (meV)	Assignment	Symm
1	21.179	2.647	OOP bend: Ph	B_{2U}
2	36.380	4.548	OOP bend: Me+N+C_N vs Ph	A_{2U}
3	55.583	6.948	OOP bend: Ph+Pyr+N_C	B_{1U}
4	66.115	8.264	OOP bend: Ph+Pyr+N_C	E_G
5	66.115	8.264	OOP bend: Ph+Pyr+N_C	E_G
6	105.599	13.200	IP sciss: Iso +N_C	B_{2G}
7	111.977	13.997	IP sciss: Ph	E_U
8	111.977	13.997	IP sciss: Ph	E_U
9	119.045	14.881	OOP def: Ph	A_{1U}
10	124.938	15.617	OOP def: Ph	E_G
11	124.938	15.617	OOP def: Ph	E_G
12	145.814	18.227	OOP bend: C_3+H_3 vs N_C+C_N+C_1	A_{2U}
13	147.673	18.459	OOP def: Iso	B_{2U}
14	191.816	23.977	IP breath: Mol	B_{1G}
15	201.286	25.161	IP sciss: Mol	A_{2G}
16	216.207	27.026	OOP def: Ph+N_C+C_N	B_{1U}
17	216.544	27.068	IP sciss: Tetraaza	B_{2G}
18	248.109	31.014	IP breath: Mol	A_{1G}
19	251.566	31.446	OOP def: Mol	E_G
20	251.566	31.446	OOP def: Mol	E_G
21	284.434	35.554	IP breath: Mol	E_U
22	284.434	35.554	IP breath: Mol	E_U
23	284.434	35.554	OOP def: Mol	E_G
24	284.434	35.554	OOP def: Mol	E_G
25	288.214	36.027	IP def: Tetraaza	E_U
26	288.214	36.027	IP def: Tetraaza	E_U
27	298.536	37.317	OOP bend: Me+$C_{1,2}$+H_2 vs N+$C_{N,3}$+H_3	A_{2U}

28	314.529	39.316	OOP def: Mol	B_{2U}
29	368.524	46.065	OOP bend: N_C vs N_{Me}	A_{2U}
30	417.974	52.247	OOP bend: H_2+C_2 vs $C_{1,3}$+H_3	E_G
31	417.974	52.247	OOP bend: H_2+C_2 vs $C_{1,3}$+H_3	E_G
32	422.900	52.862	OOP bend: Ph+N_{Me}	B_{2U}
33	423.683	52.960	OOP def: Iso	A_{1U}
34	432.816	54.102	OOP bend: N+C_2+H_2 vs C_1	A_{2U}
35	462.206	57.776	IP sciss: Mol	B_{2G}
36	487.061	60.883	OOP def: Iso+N_C	E_G
37	487.061	60.883	OOP def: Iso+N_C	E_G
38	488.002	61.000	IP sciss: Iso+N_C	E_U
39	488.002	61.000	IP sciss: Iso+N_C	E_U
40	509.716	63.715	OOP def: Ph+N_C	B_{1U}
41	547.718	68.465	IP breath: Mol	B_{1G}
42	555.921	69.490	IP def: Mol	E_U
43	555.921	69.490	IP def: Mol	E_U
44	560.312	70.039	IP def: Iso+ N_C	A_{2G}
45	570.352	71.294	IP breath: Mol	A_{1G}
46	602.164	75.271	IP sciss: Tetraaza	A_{2G}
47	608.385	76.048	OOP def: Iso	A_{1U}
48	622.473	77.809	IP def: Mol	E_U
49	622.473	77.809	IP def: Mol	E_U
50	624.616	78.077	OOP def: Iso	E_G
51	624.616	78.077	OOP def: Iso	E_G
52	642.216	80.277	IP sciss: Ph+ N_C	A_{1G}
53	662.130	82.766	IP def: Ph	B_{2G}
54	666.843	83.355	OOP def: Iso+N_C	B_{1U}
55	679.271	84.909	OOP bend: H+N_C vs N_{Me}	B_{2U}
56	716.953	89.619	OOP bend: H+N_C vs N_{Me}	E_G
57	716.953	89.619	OOP bend: H+N_C vs N_{Me}	E_G
58	720.213	90.027	IP sciss: Tetraaza	B_{1G}
59	722.713	90.339	IP def: Mol	E_U
60	722.713	90.339	IP def: Mol	E_U
61	734.444	91.806	OOP bend: N vs H+C_N	A_{2U}

62	764.312	95.539	IP def: Mol	B_{1G}
63	767.486	95.936	OOP bend: H	B_{2U}
64	769.542	96.193	OOP bend: H+C_1 vs C_N	E_G
65	769.542	96.193	OOP bend: H+C_1 vs C_N	E_G
66	771.272	96.409	OOP def: Ph+N_C	A_{1U}
67	774.302	96.788	IP def: Ph+N_C	E_U
68	774.302	96.788	IP def: Ph+N_C	E_U
69	775.269	96.909	OOP def: H_2+$C_{1,N}$	B_{1U}
70	776.908	97.113	OOP def: Mol	E_G
71	776.908	97.113	OOP def: Mol	E_G
72	779.589	97.449	OOP bend: N+H+C_1 vs $C_{N,2,3}$	A_{2U}
73	808.086	101.011	IP breath: Mol	A_{1G}
74	824.713	103.089	IPdef: Mol	A_{2G}
75	863.022	107.878	IP def: Mol	E_U
76	863.022	107.878	IP def: Mol	E_U
77	879.905	109.988	OOP bend: H	A_{1U}
78	880.113	110.014	OOP bend: H	B_{1U}
79	880.397	110.050	OOP bend: H	E_G
80	880.397	110.050	OOP bend: H	E_G
81	887.247	110.906	IP def: Mol	B_{2G}
82	955.191	119.399	OOP bend: H	B_{2U}
83	955.714	119.464	OOP bend: H	E_G
84	955.714	119.464	OOP bend: H	E_G
85	956.288	119.536	OOP bend: C_2+H_2 vs C_3+H_3	A_{2U}
86	973.829	121.729	IP breath: Ph	B_{1G}
87	974.303	121.788	IP breath: Ph	E_U
88	974.303	121.788	IP breath: Ph	E_U
89	974.604	121.826	IP breath: Ph	A_{1G}
90	984.422	123.053	OOP bend: H	A_{1U}
91	984.661	123.083	OOP bend: H	E_G
92	984.661	123.083	OOP bend: H	E_G
93	984.888	123.111	OOP bend: H	B_{1U}
94	994.419	124.302	IP def: Mol	B_{2G}
95	1029.358	128.670	IP def: Mol	E_U

96	1029.358	128.670	IP def: Mol	E_U
97	1057.959	132.245	IP def: Ph	A_{2G}
98	1063.655	132.957	IP stret: Pyr	E_U
99	1063.655	132.957	IP stret: Pyr	E_U
100	1074.650	134.331	IP stret: Pyr	B_{2G}
101	1079.516	134.940	IP stret: Pyr	A_{2G}
102	1092.712	136.589	IP def: Iso	E_U
103	1092.712	136.589	IP def: Iso	E_U
104	1093.592	136.699	IP breath: Mol	A_{1G}
105	1117.050	139.631	IP breath: Mol	B_{1G}
106	1140.883	142.610	IP sciss: H	A_{1G}
107	1141.008	142.626	IP sciss: H	E_U
108	1141.008	142.626	IP sciss: H	E_U
109	1150.335	143.792	IP def: Iso	B_{1G}
110	1155.066	144.383	IP def: Iso	A_{2G}
111	1156.231	144.529	IP def: Mol	E_U
112	1156.231	144.529	IP def: Mol	E_U
113	1173.040	146.630	IP stret: Pyr	B_{2G}
114	1257.924	157.241	IP rock: H	E_U
115	1257.924	157.241	IP rock: H	E_U
116	1259.879	157.485	IP stret: Pyr	B_{1G}
117	1260.292	157.537	IP rock: H	A_{2G}
118	1265.657	158.207	IP rock: H	B_{2G}
119	1266.047	158.256	IP stret: Pyr	E_U
120	1266.047	158.256	IP stret: Pyr	E_U
121	1291.764	161.471	IP stret: Pyr	A_{1G}
122	1320.990	165.124	IP stret: Ph	E_U
123	1320.990	165.124	IP stret: Ph	E_U
124	1331.809	166.476	IP stret: Ph	B_{1G}
125	1343.823	167.978	IP stret: Ph	A_{1G}
126	1372.188	171.524	IP rock: H	E_U
127	1372.188	171.524	IP rock: H	E_U
128	1378.472	172.309	IP sciss: Iso	A_{1G}
129	1391.333	173.917	IP stret: Tetraaza	B_{2G}

130	1402.143	175.268	IP stret: Ph	B_{1G}
131	1419.060	177.383	IP sciss: H	E_U
132	1419.060	177.383	IP sciss: H	E_U
133	1420.972	177.622	IP sciss: H	A_{2G}
134	1428.244	178.531	IP stret: Pyr	B_{2G}
135	1438.051	179.756	IP stret: Tetraaza	E_U
136	1438.051	179.756	IP stret: Tetraaza	E_U
137	1453.682	181.710	IP stret: Tetraaza	A_{2G}
138	1456.448	182.056	IP stret: Tetraaza	E_U
139	1456.448	182.056	IP stret: Tetraaza	E_U
140	1475.564	184.446	IP stret: Tetraaza	A_{1G}
141	1506.753	188.344	IP stret: Tetraaza	B_{1G}
142	1544.659	193.082	IP stret: Ph	E_U
143	1544.659	193.082	IP stret: Ph	E_U
144	1545.759	193.220	IP stret: Ph	A_{1G}
145	1545.853	193.232	IP stret: Ph	B_{1G}
146	1569.975	196.247	IP stret: Ph	A_{2G}
147	1572.264	196.533	IP stret: Ph	E_U
148	1572.264	196.533	IP stret: Ph	E_U
149	1572.264	196.533	IP stret: Ph	B_{2G}
150	3025.362	378.170	IP stret: H	A_{2G}
151	3025.390	378.174	IP stret: H	E_U
152	3025.390	378.174	IP stret: H	E_U
153	3025.408	378.176	IP stret: H	B_{2G}
154	3041.551	380.194	IP stret: H	B_{1G}
155	3041.607	380.201	IP stret: H	E_U
156	3041.607	380.201	IP stret: H	E_U
157	3041.721	380.215	IP stret: H	A_{1G}
158	3057.560	382.195	IP stret: H	A_{2G}
159	3057.682	382.210	IP stret: H	E_U
160	3057.682	382.210	IP stret: H	E_U
161	3057.795	382.224	IP stret: H	B_{2G}
162	3064.018	383.002	IP stret: H	B_{1G}
163	3064.077	383.010	IP stret: H	E_U

164	3064.077	383.010	IP stret: H	E_U
165	3064.319	383.040	IP stret: H	A_{1G}

12 Appendix B

12.1 Calculation of the Reflectivity for 6H-SiC

All NIXSW data reported in this dissertation were analyzed by means of the free and open-source program TORRICELLI, developed by Dr. Giuseppe Mercurio (PGI-3, Forschungszentrum Jülich, Germany) and documented in his PhD thesis [98]. Initially, the software was created with the aim of analyzing data of species adsorbed on crystals with cubic symmetry (Cu(111), Ag(111) and Ag(110)). In our case, the NIXSW data are however related to graphene supported by the 6H-SiC(0001) crystal. In this regard, TORRICELLI has been implemented with additional functionalities in order to fit the experimental reflectivity curve of the hexagonal SiC. Details about the fitting function as well as the calculation of the phase can be found in Ref. [98].

The ideal reflectivity of the sample (and monochromator) for the Bragg case is calculated according to the following expression [99]

$$R = \left|\frac{E_H}{E_0}\right|^2 = \left|\eta \pm \sqrt{(\eta^2 - 1)}\right|^2 \frac{F_H}{F_{\bar{H}}} \tag{12.1}$$

where the parameter η is defined as [100]

$$\eta = \frac{-2\frac{\Delta E}{E}\sin^2(\theta_B) + \Gamma F_0}{\Gamma\sqrt{F_H F_{\bar{H}}}}. \tag{12.2}$$

F_0, F_H and $F_{\bar{H}}$ are the structure factors associated with the forward scattering of the incident beam ((000) reflection), with the Bragg reflection outside the crystal ((hkl) reflection) and with the Bragg back-reflection inside the crystal ($(\bar{h}\bar{k}\bar{l})$ reflection), respectively which will be calculated for SiC in the following. E is the the value of the photon energy which differs by ΔE from the Bragg energy, θ_B is the angle

between the incident x-ray and the scattering plane and Γ is equal to $r_e \frac{\lambda^2}{\pi V}$, being r_e the electron radius, λ the x-ray wavelength in Bragg condition and V the unit cell volume.

12.1.1 Crystal Structure

Silicon carbide (SiC) is a compound semiconductor made out of Si and C atoms. Each silicon atom is surrounded by four carbon atoms (and vice-versa) that are arranged in a tetrahedral geometry (Fig. 12.1(a)). In the hexagonal crystal polytypes, the tetrahedral unit build up bilayers of hexagonal symmetry which stack on top of each other in the direction parallel to the hexagonal c-axis. The bilayers are arranged such that two consecutive bilayers have the same orientation and/or are rotated by 60° with respect to each other. The difference in bilayer stacking does not affect the in-plane lattice parameter **a** (and **b**) which amounts to 3.08 Å for essentially all hexagonal polytypes (Fig. 12.1(b)). On the contrary, the lattice constant **c** depends on the stacking sequence which in turn affects the fundamental bandgap of SiC. The 6H-SiC polytype (Fig. 12.1(b)), used in this work, is composed of two-thirds cubic bonds and one-third hexagonal bonds with a stacking sequence of ABCACB ($\mathbf{c} = 15.12$ Å). The unit cell is composed of 12 atoms (half is Si and the other half is C). Their positions are reported in Tab. 12.1.

Si positions	C positions
(0, 0, 0)	(0, 0, 1/8)
(0, 0, 1/2)	(0, 0, 5/8)
(1/3, 2/3, 1/3)	(1/3, 2/3, 11/24)
(1/3, 2/3, 2/3)	(1/3, 2/3, 19/24)
(2/3, 1/3, 1/6)	(2/3, 1/3, 23/24)
(2/3, 1/3, 5/6)	(2/3, 1/3, 7/24)

Table 12.1: The position of the C atoms and Si atoms in the SiC unit cell given as $\mathbf{r}_n = (x_n, y_n, z_n)$ for a n atom.

12.1.2 Calculation of the Structure Factors

In order to calculate the reflectivity (and phase) of a crystal, the aforementioned structure factors must be determined. With the assumption that the atoms in the

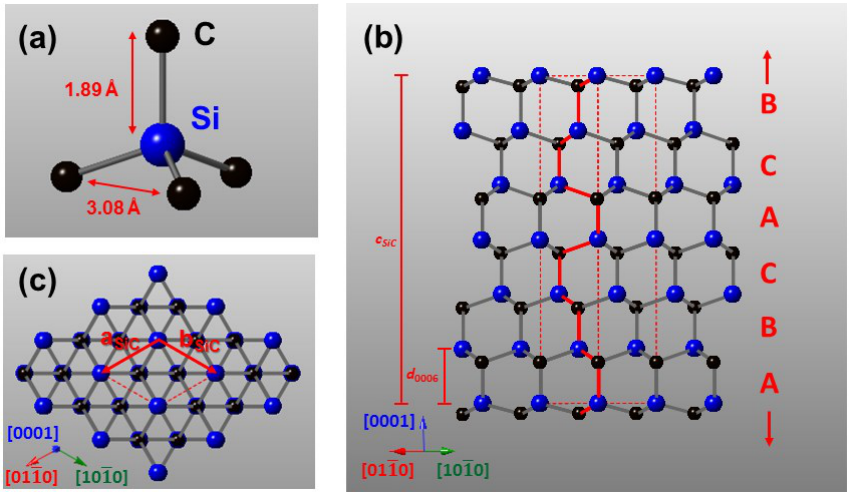

Figure 12.1: (a) SiC tetrahedral geometry; (b) bilayer stacking arrangement for 6H-SiC polytype; (c) lattice vectors and unit cell of SiC. The Fig. is adapted from Ref. [101]

crystal are rigid sphere, the general expression of F_H can be written as

$$F_H = \sum_n f_n \exp(-M_n) \exp(2\pi i \mathbf{H} \cdot \mathbf{r}_n), \tag{12.3}$$

where f_n is the atomic scattering factor, $\exp(-M_n)$ is the Debye-Waller factor and $\mathbf{r}_n = (x_n, y_n, z_n)$ is the position of the n atom in the unit cell with respect to the unit cell vectors **a**, **b** and **c** (reported above in Tab. 12.1 for SiC). The reciprocal vector **H** is defined as $\mathbf{H} = h\mathbf{b}_1 + k\mathbf{b}_2 + l\mathbf{b}_3$, where $\mathbf{b}_1$, $\mathbf{b}_2$ and $\mathbf{b}_3$ are the reciprocal lattice vectors of the unit cell associated with the real space SiC vectors **a**, **b** and **c** (see Fig. 12.1(c)), and h, k and l are the Miller indices. Commonly, for hexagonal crystals a four Miller indexing $(hkil)$ is adopted, e.g. 6H-SiC(0001). The i index originates from the presence of a third in-plane vector located at 120° with respect to **a** and **b**. However, for the derivation of the structure factor, a three Miller indexing (hkl) is adopted.

As the SiC crystal is composed of two atoms, Si and C, F_H can be divided into two

contributions according to the nature of the atom such as

$$F_H = f_{Si}\exp(-M_{Si})\sum_{Si}\exp(2\pi i\mathbf{H}\cdot\mathbf{r}_{Si}) + f_C\exp(-M_C)\sum_{C}\exp(2\pi i\mathbf{H}\cdot\mathbf{r}_C), \quad (12.4)$$

where the indices Si and C run over the Si and C atoms in the unit cell, respectively. In the sections below, 1) the atomic scattering factors (f_{Si} and f_C), 2) Debye-Waller factors ($\exp(-M_{Si})$ and $\exp(-M_C)$) and 3) geometrical factors S ($S_{Si} = \sum_{Si}\exp(2\pi i\mathbf{H}\cdot\mathbf{r}_{Si})$ and $S_C = \sum_C\exp(2\pi i\mathbf{H}\cdot\mathbf{r}_C)$) will be discussed and calculated.

1) Atomic Scattering Factors

The atomic scattering factor describes the interaction between an x-ray beam and the electron cloud of an atom. In practice, it is a measure of the scattering amplitude of a wave by an isolated atom. Its expression can be written as

$$f = f_0 + \Delta f' + i\Delta f'', \quad (12.5)$$

where f_0 is the atomic form factor which is dependent on both angle θ and x-ray energy ($\frac{\sin(\theta)}{\lambda} = \frac{1}{2d_{hkl}}$), while the terms $\Delta f' + i\Delta f''$, called the Hönl corrections, are considered independent of θ and take into account the modification of the atomic scattering factor due to resonance and absorption. The value $f_{0,Si}$ and $f_{0,C}$ as a function of $\frac{\sin(\theta)}{\lambda} = \frac{1}{2d_{hkl}}$, and the values $\Delta f'_{Si} + i\Delta f''_{Si}$ and $\Delta f'_C + i\Delta f''_C$ as a function of the energy are tabulated and interpolated by the program [102, 103].

2) Debye-Waller Factors

Generally, the thermal vibrations of the n atom are included in the atomic scattering factor by replacing f_n by $f_n\exp(-M_n)$ where the exponential is the Debye-Waller factor, defined as

$$M_n = B_n(\frac{\sin\theta}{\lambda})^2, \quad (12.6)$$

with $B_n = 8\pi^2 < \mu_n^2 >$. The fluctuation values $< \mu_n^2 >$ as a function of the temperature for both C and Si are extracted from Fig. 12.2 according to Ref. [104].

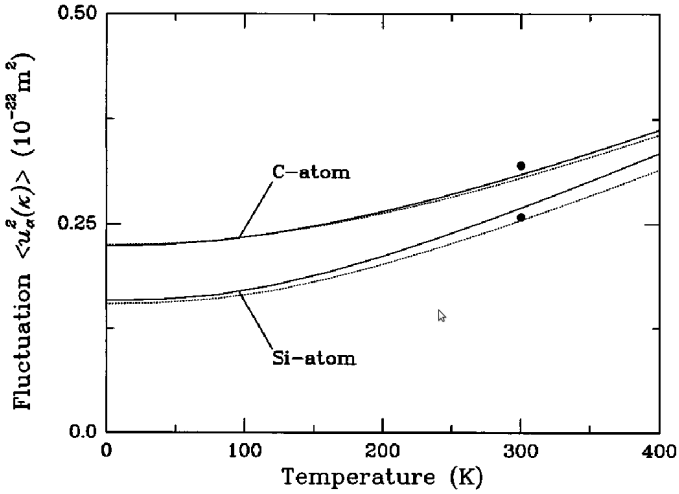

Figure 12.2: Mean-square displacement of C and Si atoms of 3C SiC and of 6H-SiC versus temperature as continuous line and dotted dots respectively taken from Ref. [104] Copyright 1996 by the American Physical Society.

3) Geometrical Factors

The last terms which need to be calculated in order to obtain the structure factors are the geometrical factors S_{Si} and S_C for the (000), (00l) and (00$\bar{l}$) reflections. The general formula of S_{Si} and S_C are

$$S_{Si}(hkl) = \sum_{Si} \exp(2\pi i(hx_{Si} + ky_{Si} + lz_{Si})) \tag{12.7}$$

and

$$S_C(hkl) = \sum_{C} \exp(2\pi i(hx_C + ky_C + lz_C)), \tag{12.8}$$

which, taking into account the atomic positions defined in Tab. 12.1, become

$$\begin{aligned} S_{Si}(hkl) = 1 &+ e^{2\pi i(\frac{1}{2}l)} + e^{2\pi i(\frac{1}{3}h+\frac{2}{3}k+\frac{1}{3}l)} \\ &+ e^{2\pi i(\frac{1}{3}h+\frac{2}{3}k+\frac{2}{3}l)} + e^{2\pi i(\frac{2}{3}h+\frac{1}{3}k+\frac{1}{6}l)} + e^{2\pi i(\frac{2}{3}h+\frac{1}{3}k+\frac{5}{6}l)}, \end{aligned} \tag{12.9}$$

and

$$S_C(hkl) = e^{2\pi i(\frac{1}{8}l)} + e^{2\pi i(\frac{5}{8}l)} + e^{2\pi i(\frac{1}{3}h+\frac{2}{3}k+\frac{11}{24}l)} + e^{2\pi i(\frac{1}{3}h+\frac{2}{3}k+\frac{19}{24}l)} + e^{2\pi i(\frac{2}{3}h+\frac{1}{3}k+\frac{23}{24}l)} + e^{2\pi i(\frac{2}{3}h+\frac{1}{3}k+\frac{7}{24}l)}. \tag{12.10}$$

For the (000) reflection we have $S_{Si}(000) = S_C(000) = 6$.

For the Bragg reflection $(00l)$ and back-reflection $(00\bar{l})$ it would be straightforward to consider the (001) and $(00\bar{1})$ reflections. However, for $l = 1$, Eq. 12.9 becomes

$$S_{Si}(001) = 1 + e^{\pi i} + e^{\frac{2}{3}\pi i} + e^{\frac{4}{3}\pi i} + e^{\frac{1}{3}\pi i} + e^{\frac{5}{3}\pi i}, \tag{12.11}$$

which can be rewritten as

$$S_{Si}(001) = 1 + (-1) + e^{\frac{2}{3}\pi i} + e^{\frac{1}{3}\pi i} \cdot e^{\pi i} + e^{\frac{1}{3}\pi i} + e^{\frac{2}{3}\pi i} \cdot e^{\pi i}. \tag{12.12}$$

As $e^{\pi i} = -1$ and $e^{2\pi i} = +1$, the sum of the terms inside Eq. 12.12 vanishes. Accordingly, with $l = 1$ Eq. 12.10 equals null as well

$$S_C(001) = e^{\frac{1}{4}\pi i} + e^{\frac{5}{4}\pi i} + e^{\frac{11}{12}\pi i} + e^{\frac{19}{12}\pi i} + e^{\frac{23}{12}\pi i} + e^{\frac{7}{12}\pi i} = e^{\frac{1}{4}\pi i} + e^{\frac{1}{4}\pi i} \cdot e^{\pi i} + e^{\frac{11}{12}\pi i} + e^{\frac{7}{12}\pi i} \cdot e^{\pi i} + e^{\frac{11}{12}\pi i} \cdot e^{\pi i} + e^{\frac{7}{12}\pi i} = 0. \tag{12.13}$$

Since a geometrical factor must be $\neq 0$ in order to have a reflection, the (006) and $(00\bar{6})$ reflections of the 6H-SiC(0001) are considered. For $l = 6$ and $l = -6$, Eq. 12.9 and Eq. 12.10 become

$$S_{Si}(006) = 1 + e^{6\pi i} + e^{4\pi i} + e^{8\pi i} + e^{2\pi i} + e^{10\pi i} = 6, \tag{12.14}$$

$$S_C(006) = e^{\frac{3}{2}\pi i} + e^{\frac{15}{2}\pi i} + e^{\frac{11}{2}\pi i} + e^{\frac{19}{2}\pi i} + e^{\frac{23}{2}\pi i} + e^{\frac{7}{2}\pi i} = -6i \tag{12.15}$$

and

$$S_{Si}(00\bar{6}) = 1 + e^{-6\pi i} + e^{-4\pi i} + e^{-8\pi i} + e^{-2\pi i} + e^{-10\pi i} = 6, \tag{12.16}$$

$$S_C(00\bar{6}) = e^{-\frac{3}{2}\pi i} + e^{-\frac{15}{2}\pi i} + e^{-\frac{11}{2}\pi i} + e^{-\frac{19}{2}\pi i} + e^{-\frac{23}{2}\pi i} + e^{-\frac{7}{2}\pi i} = +6i. \qquad (12.17)$$

12.1.3 Summary of the Results

6H-SiC(0001), T=300K	
B_{Si}	0.200
B_C	0.243
$F_0(000)$	$118.983 + 16.906i$
$F_H(006)$	$56.677 - 5.959i$
$F_{\bar{H}}(00\bar{6})$	$55.315 + 38.140i$

Table 12.2: Debey-Waller factors (B_{Si} and B_C) given in Å^2 and related structure factors for the (hkl) reflection given a photon energy of 2464.640 eV and $d_{(006)} = 2.520$ Å.

List of Figures

List of Tables

Bibliography

[1]K. S. Novoselov, A. K. Geim, S. V. Morozov, D. Jiang, Y. Zhang, S. V. Dubonos, I. V. Grigorieva, and A. A. Firsov, "Electric Field Effect in Atomically Thin Carbon Films", Science **306**, 666 (2004).

[2]P. Avouris, Z. Chen, and V. Perebeinos, "Carbon-based electronics", Nature Nanotechnology **2**, 605 (2007).

[3]F. Schwierz, J. Pezoldt, and R. Granzner, "Two-dimensional materials and their prospects in transistor electronics", Nanoscale **7**, 8261 (2015).

[4]M. Burghard, H. Klauk, and K. Kern, "Carbon-Based Field-Effect Transistors for Nanoelectronics", Advance Materials **21**, 2586 (2009).

[5]G. E. Moore, "Cramming more components onto integrated circuits", Proceedings of the IEEE **86**, 82 (1998).

[6]A. Allain, J. Kang, K. Banerjee, and A. Kis, "Electrical contacts to two-dimensional semiconductors", Nature Materials **14**, 1195 (2015).

[7]G. R. Bhimanapati, Z. Lin, V. Meunier, Y. Jung, J. Cha, S. Das, D. Xiao, Y. Son, M. S. Strano, V. R. Cooper, L. Liang, S. G. Louie, E. Ringe, W. Zhou, S. S. Kim, R. R. Naik, B. G. Sumpter, H. Terrones, F. Xia, Y. Wang, J. Zhu, D. Akinwande, N. Alem, J. A. Schuller, R. E. Schaak, M. Terrones, and J. A. Robinson, "Recent Advances in Two-Dimensional Materials beyond Graphene", ACS Nano **9**, 11509. (2015).

[8]D. Akinwande, N. Petrone, and J. Hone, "Two-dimensional flexible nanoelectronics", Nature Communications **5**, 5678 (2014).

[9]W. Norimatsu and M. Kusunoki, "Epitaxial graphene on SiC(0001): advances and perspectives", Physical Chemistry Chemical Physics **16**, 3501 (2014).

[10]K. V. Emtsev, A. A. Zakharov, C. Coletti, S. Forti, and U. Starke, "Ambipolar doping in quasifree epitaxial graphene on SiC(0001) controlled by Ge intercalation", Physical Review B **84**, 125423 (2011).

[11]H. Wang, T. Maiyalagan, and X. Wang, "Review on Recent Progress in Nitrogen-Doped Graphene: Synthesis, Characterization, and Its Potential Applications", ACS Catalysis **2**, 781 (2012).

[12]B. Guo, L. Fang, B. Zhang, and J. R. Gong, "Graphene Doping: A Review", Insciences Journal **1**, 80 (2011).

[13]C. Rao, K. Gopalakrishnan, and A. Govindaraj, "Synthesis, properties and applications of graphene doped with boron, nitrogen and other elements", Nano Today **9**, 324 (2014).

[14]J. Blochwitz, M. Pfeiffer, T. Fritz, and K. Leo, "Low voltage organic light emitting diodes featuring doped phthalocyanine as hole transport material", Applied Physics Letter **73**, 729 (1998).

[15]B. Crone, A. Dodabalapur, Y. Y. Lin, R. W. Filas, Z. Bao, A. La Duca, R. Sarpeshkar, H. E. Katz, and W. Li, "Large-scale complementary integrated circuits based on organic transistors", Nature **403**, 521 (2000).

[16]J. M. Gottfried, "Surface chemistry of porphyrins and phthalocyanines", Surface Science Reports **70**, 259 (2015).

[17]A. Einstein, "Zur Elektrodynamik bewegter Körper", Annalen der Physik **322**, 891 (1905).

[18]S. Hüfner, *Photoelectron Spectroscopy* (Springer Berlin Heidelberg, 1996).

[19]S. D. Kevan, *Angle-Resolved Photoemission: Theory and Current Applications* (Elsevier, 1992).

[20]W. Schattke and M. A. Van Hove, *Solid-State Photoemission and Related Methods: Theory and Experiment* (Wiley-VCH, 2008).

[21]A. C. Thompson, D. T. Attwood, E. M. Gullikson, M. R. Howells, J. B. Kortright, A. I. Robinson, J. Underwood, K. J. Kim, J. Kirz, I. Lindau, P. Pianetta, H. Winick, G. P. Williams, and J. H. Scofield, *X-ray data booklet* (Lawrence Berkeley National Laboratory, 2001).

[22]D. P. Woodruff, "Surface structure determination using x-ray standing waves", Reports on Progress in Physics **68**, 743 (2005).

[23]I. A. Vartanyants and J. Zegenhagen, "Photoelectric scattering from an X-ray interference field ", Solid State Communications **113**, 299 (1999).

[24]M. Trzhaskovskaya, V. Nefedov, and V. Yrzhemsky, "Photoelectron angular distribution parameters for elements Z=1 to Z=54 in the photoelectron energy range 100-5000 eV", Atomic Data and Nuclear Data Tables **77**, 97 (2001).

[25]M. Trzhaskovskaya, V. Nefedov, and V. Yrzhemsky, "Photoelectron angular distribution parameters for elements Z=55 to Z=100 in the photoelectron energy range 100-5000 eV", Atomic Data and Nuclear Data Tables **82**, 257 (2002).

[26]A. Jablonski, F. Salvat, and J. C. Polwell, "NIST Electron Elastic Scattering Cross-Section Database, Version 3.1", National Institute of Standards and Technology, Gaithersburg, Maryland (2003).

[27]J. J. Lee, C. Fisher, D. Woodruff, M. Roper, R. Jones, and B. Cowie, "Non-dipole effects in photoelectron-monitored X-ray standing wave experiments: characterisation and calibration ", Surface Science **494**, 166 (2001).

[28]U. Fano, *Atomic Collisions and Spectra* (Elsevier, 1986).

[29]J. Stöhr, *NEXAFS Spectroscopy* (Springer Berlin Heidelberg, 1992).

[30]F. M. Propst and T. C. Piper, "Electron spectrometry of solid surfaces", Vacuum **17**, 169 (1967).

[31]H. Ibach, *Electron Spectroscopy for Surface Analysis* (Springer Berlin Heidelberg, 1977).

[32]H. Ibach and D. L. Mills, *Electron Energy Loss Spectroscopy and Surface Vibrations* (Academic, New York, 1982).

[33]A. Lucas and J. Vigneron, "Theory of electron energy loss spectroscopy from surfaces of anisotropic materials", Solid State Communications **49**, 327 (1984).

[34]A. Lucas and M. Šunjić, "Fast-electron spectroscopy of collective excitations in solids", Progress in Surface Science **2**, 75 (1972).

[35]W. Ho, R. F. Willis, and E. W. Plummer, "Observation of Nondipole Electron Impact Vibrational Excitations: H on W (100)", Physical Review Letter **40**, 1463 (1978).

[36]S. Y. Tong, C. H. Li, and D. L. Mills, "Inelastic scattering of electrons from adsorbate vibrations: large-angle deflections", Physical Review Letter **44**, 407 (1980).

[37]K. S. Novoselov, Z. Jiang, Y. Zhang, S. V. Morozov, H. L. Stormer, U. Zeitler, J. C. Maan, G. S. Boebinger, P. Kim, and A. K. Geim, "Room-temperature quantum hall effect in graphene", Science **315**, 1379 (2007).

[38]J. Baringhaus, A. Stöhr, S. Forti, S. A. Krasnikov, A. A. Zakharov, U. Starke, and C. Tegenkamp, "Bipolar gating of epitaxial graphene by intercalation of Ge", Applied Physics Letters **104**, 261602 (2014).

[39]P. Avouris and C. Dimitrakopoulos, "Graphene: synthesis and applications", Materials Today **15**, 86 (2012).

[40]A. Züttel, "Materials for hydrogen storage", Materials Today **6**, 24 (2003).

[41]C. W. J. Beenakker, "Colloquium : Andreev reflection and Klein tunneling in graphene", Reviews of Modern Physics **80**, 1337 (2008).

[42]S. Haar, M. El Gemayel, Y. Shin, G. Melinte, M. A. Squillaci, O. Ersen, C. Casiraghi, A. Ciesielski, and P. Samorì, "Enhancing the Liquid-Phase Exfoliation of Graphene in Organic Solvents upon Addition of n-Octylbenzene", Scientific Reports **5**, 16684 (2015).

[43]J. Avila, I. Razado, S. Lorcy, R. Fleurier, E. Pichonat, D. Vignaud, X. Wallart, and M. Asensio, "Exploring electronic structure of one-atom thick polycrystalline graphene films: A nano angle resolved photoemission study", Scientific Reports **3**, 2439 (2013).

[44]C. Enderlein, Y. S. Kim, A. Bostwick, E. Rotenberg, and K. Horn, "The formation of an energy gap in graphene on ruthenium by controlling the interface", New Journal of Physics **12**, 033014 (2010).

[45]S. Forti and U. Starke, "Epitaxial graphene on SiC: from carrier density engineering to quasi-free standing graphene by atomic intercalation", Journal of Physics D: Applied Physics **47**, 094013 (2014).

[46]I. Forbeaux, J.-M. Themlin, and J.-M. Debever, "Heteroepitaxial graphite on $6H-\mathrm{SiC}(0001)$: Interface formation through conduction-band electronic structure", Physical Review B **58**, 16396 (1998).

[47]R. H. Friend, R. W. Gymer, A. B. Holmes, J. H. Burroughes, R. N. Marks, C. Taliani, D. D. C. Bradley, D. A. D. Santos, J. L. Bredas, M. Logdlund, and W. R. Salaneck, "Electroluminescence in conjugated polymers", Nature **397**, 121 (1999).

[48]J. C. Buchholz and G. A. Somorjai, "The surface structures of phthalocyanine monolayers and vaporgrown films: A low energy electron diffraction study", The Journal of Chemical Physics **66**, 573 (1977).

[49]K. Yang, W. D. Xiao, Y. H. Jiang, H. G. Zhang, L. W. Liu, J. H. Mao, H. T. Zhou, S. X. Du, and H.-J. Gao, "Molecule–Substrate Coupling between Metal Phthalocyanines and Epitaxial Graphene Grown on Ru(0001) and Pt(111)", The Journal of Physical Chemistry C **116**, 14052 (2012).

[50]M. Moors, A. Krupski, S. Degen, M. Kralj, C. Becker, and K. Wandelt, "Scanning tunneling microscopy and spectroscopy investigations of copper phthalocyanine adsorbed on $Al_2O_3/Ni_3Al(111)$ ", Applied Surface Science **254**, 4251 (2008).

[51]N. Ishida and D. Fujita, "Adsorption of Co-Phthalocyanine on the Rutile $TiO_2(110)$ Surface: A Scanning Tunneling Microscopy/Spectroscopy Study", The Journal of Physical Chemistry C **116**, 20300 (2012).

[52]C. Stadler, S. Hansen, I. Kröger, C. Kumpf, and E. Umbach, "Tuning intermolecular interaction in long-range-ordered submonolayer organic films", Nature Physics **5**, 153 (2009).

[53]B. Stadtmüller, I. Kröger, F. Reinert, and C. Kumpf, "Submonolayer growth of CuPc on noble metal surfaces", Physical Review B **83**, 085416 (2011).

[54]N. Ohta, R. Arafune, N. Tsukahara, N. Takagi, and M. Kawai, "Adsorbed states of iron(II) phthalocyanine on Ag(111) studied by high-resolution electron energy loss spectroscopy", Surface Interface Analysis **46**, 1253 (2014).

[55]P. Amsalem, L. Giovanelli, J. Themlin, and T. Angot, "Electronic and vibrational properties at the ZnPc/Ag(110) interface", Physical Review B **79**, 235426 (2009).

[56]W. Dou, Y. G. Tang, C. S. Lee, S. N. Bao, and S. T. Lee, "Investigation on the orderly growth of thick zinc phthalocyanine films on Ag(100) surface", The Journal of Chemical Physics **133**, 144704 (2010).

[57]J. Auerhammer, M. Knupfer, H. Peisert, and J. Fink, "The copper phthalocyanine/Au(100) interface studied using high resolution electron energy-loss spectroscopy", Surface Science **506**, 333 (2002).

[58]M. J. Frisch, G. W. Trucks, H. B. Schlegel, G. E. Scuseria, M. A. Robb, J. R. Cheeseman, G. Scalmani, V. Barone, B. Mennucci, G. A. Petersson, H. Nakatsuji, M. Caricato, X. Li, H. P. Hratchian, A. F. Izmaylov, J. Bloino, G. Zheng, J. L. Sonnenberg, M. Hada, M. Ehara, K. Toyota, R. Fukuda, J. Hasegawa, M. Ishida, T. Nakajima, Y. Honda, O. Kitao, H. Nakai, T. Vreven, J. A. J. Montgomery, J. E. Peralta, F. Ogliaro, M. Bearpark, J. J. Heyd, E. Brothers, K. N. Kudin, V. N. Staroverov, R. Kobayashi, J. Normand, K. Raghavachari, A. Rendell, J. C. Burant, S. S. Iyengar, J. Tomasi, M. Cossi, N. Rega, J. M. Millam, M. Klene, J. E. Knox, J. B. Cross, V. Bakken, C. Adamo, J. Jaramillo, R. Gomperts, R. E. Stratmann, O. Yazyev, A. J. Austin, R. Cammi, C. Pomelli, J. W. Ochterski, R. L. Martin, K. Morokuma, V. G. Zakrzewski, G. A. Voth, P. Salvador, J. J. Dannenberg, S. Dapprich, A. D. Daniels, O. Farkas, J. B. Foresman, J. V. Ortiz, J. Cioslowski, and D. J. Fox, *Gaussian09 Revision D.01*, Gaussian Inc. Wallingford CT 2009.

[59]V. G. Maslov, "Interpretation of the electronic spectra of phthalocyanines with transition metals from quantum-chemical calculations by the density functional method", Optics and Spectroscopy **101**, 853 (2006).

[60]W. Kress and F. W. Wette, *Surface Phonons* (Springer-Verlag, 1991).

[61]B. Yan, B. Stadtmüller, N. Haag, S. Jakobs, J. Seidel, D. Jungkenn, S. Mathias, M. Cinchetti, M. Aeschlimann, and C. Felser, "Topological states on the gold surface", Nature Communications **6**, 10167 (2015).

[62]G. Benedek, M. Bernasconi, V. Chis, E. Chulkov, P. M. Echenique, P. Hellsing, and J. P. Toennies, "Theory of surface phonons at metal surfaces: recent advances", Journal of Physics: Condensed Matter **22**, 084020 (2010).

[63]U. Harten, J. P. Toennies, and C. Woll, "Helium time-of-flight spectroscopy of surface-phonon dispersion curves of the noble metals", Faraday Discussion of the Chemical Society **80**, 137 (1985).

[64]B. M. Hall, D. L. Mills, M. H. Mohamed, and L. L. Kesmodel, "Surface lattice dynamics of Cu(111)", Physical Review B **38**, 5856 (1988).

[65]V. Bortolani, F. Nizzoli, G. Santoro, A. Marvin, and J. R. Sandercock, "Brillouin scattering from surface phonons in al-coated semiconductors", Physical Review Letter **43**, 224 (1979).

[66]V. Bortolani, A. Franchini, F. Nizzoli, and G. Santoro, "Explanation of the Anomalous Peak Observed in He-Atom Scattering from Ag(111)", Physical Review Letter **52**, 429 (1984).

[67]M. H. Mohamed, L. L. Kesmodel, B. M. Hall, and D. L. Mills, "Surface phonon dispersion on Cu(111)", Physical Review B Rapid Communication **37**, 2763 (1988).

[68]G. Mercurio, O. Bauer, M. Willenbockel, N. Fairley, W. Reckien, C. H. Schmitz, B. Fiedler, S. Soubatch, T. Bredow, M. Sokolowski, and F. S. Tautz, "Adsorption height determination of nonequivalent C and O species of PTCDA on Ag(110) using x-ray standing waves", Physical Review B **87**, 045421 (2013).

[69] *Torricelli is an XSW data analysis and simulation program written by G. Mercurio; copies can be obtained from s.tautz@fz-juelich.de.*

[70]N. Fairley, *CasaXPS*.

[71]M. Telychko, P. Mutombo, P. Merino, P. Hapala, M. Ondráček, F. C Bocquet, J. Sforzini, O. Stetsovych, M. Vondráček, P. Jelínek, and M. Švec, "Electronic and Chemical Properties of Donor, Acceptor Centers in Graphene", ACS Nano **9**, 9180 (2015).

[72]J. Libra, *KolXPD*.

[73]Wavemetrics Inc., *Igor Pro*.

[74]M. I. Katsnelson, K. S. Novoselov, and A. K. Geim, "Chiral tunnelling and the Klein paradox in graphene", Nature Physics **2**, 620 (2006).

[75]Y. Zhang, Z. Jiang, J. P. Small, M. S. Purewal, Y.-W. Tan, M. Fazlollahi, J. D. Chudow, J. A. Jaszczak, H. L. Stormer, and P. Kim, "Landau-Level Splitting in Graphene in High Magnetic Fields", Physical Review Letter **96**, 136806 (2006).

[76]P. Pasanen, M. Voutilainen, M. Helle, X. Song, and P. J Hakonen, "Graphene for future electronics", Physica Scripta **2012**, 014025 (2012).

[77]C. Riedl, C. Coletti, T. Iwasaki, A. A. Zakharov, and U. Starke, "Quasi-Free-Standing Epitaxial Graphene on SiC Obtained by Hydrogen Intercalation", Physical Review Letter **103**, 246804 (2009).

[78]J. Sforzini, L. Nemec, T. Denig, B. Stadtmüller, T.-L. Lee, C. Kumpf, S. Soubatch, U. Starke, P. Rinke, V. Blum, F. Bocquet, and F. Tautz, "Approaching Truly Freestanding Graphene: The Structure of Hydrogen-Intercalated Graphene on 6H-SiC(0001)", Physical Review Letters **114**, 106804 (2015).

[79]J. Baringhaus, M. Ruan, F. Edler, A. Tejeda, M. Sicot, A. Taleb-Ibrahimi, A.-P. Li, Z. Jiang, E. H Conrad, C. Berger, C. Tegenkamp, and W. A. de Heer, "Exceptional ballistic transport in epitaxial graphene nanoribbons", Nature **506**, 349 (2014).

[80]A. Deretzis and A. La Magna, "Ab Initio Study of Ge Intercalation in Epitaxial Graphene on SiC(0001)", Applied Physics Express **4**, 125101 (2011).

[81]T. P. Kaloni, M. U. Kahaly, Y. C. Cheng, and U. Schwingenschlögl, "Ge-intercalated graphene: the origin of the p-type to n-type transition", Europhysics Letters **99**, 57002 (2012).

[82]H. I. Sirikumara, J. Bohorquez-Ballen, and T. Jayasekera, "Ge cages at the SiC/graphene interface: A first principles calculation", Journal of Crystal Growth **393**, 145 (2014).

[83]I. Yonenaga, "Growth and fundamental properties of SiGe bulk crystals ", Journal of Crystal Growth **275**, 91 (2005).

[84]L. S. Panchakarla, K. S. Subrahmanyam, S. K. Saha, A. Govindaraj, H. R. Krishnamurthy, U. V. Waghmare, and C. N. R. Rao, "Synthesis, Structure, and Properties of Boron- and Nitrogen-Doped Graphene", Advanced Materials **21**, 4726 (2009).

[85]F. Karlický, K. K. R. Datta, M. Otyepka, and R. Zbořil, "Halogenated graphenes: rapidly growing family of graphene derivatives", ACS Nano **7**, 6434 (2013).

[86]M. Telychko, P. Mutombo, M. Ondráček, P. Hapala, F. C. Bocquet, J. Kolorenč, M. Vondráček, P. Jelínek, and M. Švec, "Achieving high-quality single-atom nitrogen doping of graphene/SiC(0001) by ion implantation and subsequent thermal stabilization", ACS Nano **8**, 7318. (2014).

[87]J. Sforzini, P. Hapala, M. Franke, G. van Straaten, A. Stöhr, S. Link, S. Soubatch, P. Jelínek, T.-L. Lee, U. Starke, M. Švec, F. C. Bocquet, and F. S. Tautz, "Structural and Electronic Properties of Nitrogen-Doped Graphene", Physical Review Letter **116**, 126805 (2016).

[88]D.-A. Yeom, W. Jeon, N. D. K. Tu, S. Y. Yeo, S.-S. Lee, B. J. Sung, H. Chang, J. A. Lim, and H. Kim, "High-concentration boron doping of graphene nanoplatelets by simple thermal annealing and their supercapacitive properties", Scientific Reports **5**, 9817 (2015).

[89]J. Sforzini, M. Telychko, O. Krej čí, M. Vondrá ček, M. Švec, F. C. Bocquet, and F. S. Tautz, "Transformation of metallic boron into substitutional dopants in graphene on 6H-SiC(0001)", Physical Review B Rapid Communication **93**, 041302 (2016).

[90]A. Vilan and D. Cahen, "How organic molecules can control electronic devices", Trends in Biotechnology **20**, 22 (2002).

[91]Nature Editorial, "Molecular electronics under the microscope", Nature Chemistry **7**, 181 (2015).

[92]J. C. Conboy, E. J. C. Olson, D. M. Adams, J. Kerimo, A. Zaban, B. A. Gregg, and P. F. Barbara, "Impact of Solvent Vapor Annealing on the Morphology and Photophysics of Molecular Semiconductor Thin Films", Journal of Physical Chemistry B **102**, 4516 (1998).

[93]P. Puschnig, E.-M. Reinisch, T. Ules, G. Koller, S. Soubatch, M. Ostler, L. Romaner, F. S. Tautz, C. Ambrosch-Draxl, and M. G. Ramsey, "Orbital tomography: deconvoluting photoemission spectra of organic molecules", Physical Review B **84**, 235427 (2011).

[94]V. Feyer, M. Graus, P. Nigge, M. Wießner, R. Acres, C. Wiemann, C. Schneider, A. Schöll, and F. Reinert, "Adsorption geometry and electronic structure of iron phthalocyanine on Ag surfaces: A LEED and photoelectron momentum mapping study", Surface Science **621**, 64 (2014).

[95]B. Panella, M. Hirscher, H. Pütter, and U. Müller, "Hydrogen Adsorption in Metal–Organic Frameworks: Cu-MOFs and Zn-MOFs Compared", Advance Functional Materials **16**, 520 (2006).

[96]P. M. Suh, H. J. Park, T. K. Prasad, and D.-W. Lim, "Hydrogen Storage in Metal–Organic Frameworks", Chemical Review **112**, 782 (2012).

[97]L. Klebanoff, *Hydrogen Storage Technology: Materials and Applications* (CRC Press, Taylor and Francis group, 2012).

[98]G. Mercurio, "Study of molecule-metal interfaces by means of the normal incidence X-ray wave technique", PhD thesis (RWTH Aachen University, 2012).

[99]B. W. Batterman and H. Cole, "Dynamical Diffraction of X Rays by Perfect Crystals", Review of Modern Physics **36**, 681 (1964).

[100]D. Woodruff, "Normal incidence X-ray standing wave determination of adsorbate structures", Progress in Surface Science **57**, 1 (1998).

[101]J. D. Emery, "Synchrotron X-ray Studies of Pristine, Intercalated, and Functionalized Epitaxial Graphene on SiC(0001)", PhD thesis (Northwestern University, 2013).

[102]E. N. Maslen, A. G. Fox, and O. M. A., *International Table for Crystallography, Volume C* ((KLUVER ACADEMIC PUBLISHERS, 2006).

[103]B. L. Henke, E. Gullikson, and J. Davis, "X-Ray Interactions: Photoabsorption, Scattering, Transmission, and Reflection at E = 50-30,000 eV, Z =1-92", Atomic Data and Nuclear Data Tables **50**, 181 (1993).

[104]A. Zywietz, K. Karch, and F. Bechstedt, "Influence of polytypism on thermal properties of silicon carbide", Physical Review B **54**, 1791 (1996).

Band / Volume 140
In situ studies of the growth and oxidation of complex metal oxides by pulsed laser deposition
C. Xu (2017), iv, 159 pp
ISBN: 978-3-95806-204-7

Band / Volume 141
Intrinsic and extrinsic spin-orbit torques from first principles
G. Géranton (2017), 122 pp
ISBN: 978-3-95806-213-9

Band / Volume 142
Magnetic Proximity Effects in Nanoparticle Composite Systems and Macrocrystals
G. Wilbs (2017), III, 230 pp
ISBN: 978-3-95806-233-7

Band / Volume 143
Etablierung eines Systems aus Cysteinmutanten der Phosphoglycerat-Kinase für Entfaltungsstudien mit Einzelmolekül-FRET
A. Schöne (2017), 137 pp
ISBN: 978-3-95806-237-5

Band / Volume 144
Structural and electronic characterization of hetero-organic NTCDA-CuPc adsorbate systems on Ag(111)
S. Schröder (2017), vi, 154 pp
ISBN: 978-3-95806-239-9

Band / Volume 145
Tailoring Molecular Magnetism
T. Esat (2017), viii, 163 pp
ISBN: 978-3-95806-240-5

Band / Volume 146
Spin-wave excitations and electron-magnon scattering in elementary ferromagnets from *ab initio* many-body perturbation theory
M. C. T. D. Müller (2017), vi, 174 pp
ISBN: 978-3-95806-242-9

Band / Volume 147
Neutron Scattering
Lectures of the JCNS Laboratory Course held at Forschungszentrum Jülich and at the Heinz-Maier-Leibnitz Zentrum Garching
edited by T. Brückel, S. Förster, G. Roth, and R. Zorn (Eds.) (2017), ca 400 pp
ISBN: 978-3-95806-243-6

Band / Volume 148
Neutron scattering
Experimental Manuals of the JCNS Laboratory Course held at Forschungszentrum Jülich and at the Heinz-Maier-Leibnitz Zentrum Garching
edited by T. Brückel, S. Förster, G. Roth, and R. Zorn (Eds.) (2017), ca 200 pp
ISBN: 978-3-95806-244-3

Band / Volume 149
Kinetic and thermodynamic considerations on the formation of heteromolecular layers on metal surfaces
C. Henneke (2017), vii, 157, XIV pp
ISBN: 978-3-95806-245-0

Band / Volume 150
Spectroscopic characterization of local valence change processes in resistively switching complex oxides
C. Bäumer (2017), x, 206 pp
ISBN: 978-3-95806-246-7

Band / Volume 151
Magnetic structure in relation to the magnetic field induced ferroelectricity in Y-type hexaferrite $Ba_{2-x}Sr_xZn_2Fe_{12}O_{22}$
P. Thakuria (2017), 17, 180 pp
ISBN: 978-3-95806-250-4

Band / Volume 152
Statistical analysis tools for assessing the functional relevance of higher-order correlations in massively parallel spike trains
V. Rostami (2017), x, 176 pp
ISBN: 978-3-95806-251-1

Band / Volume 153
The influence of the substrate on the structure and electronic properties of carbon-based 2D materials
J. Sforzini (2017), XIII, 143 pp
ISBN: 978-3-95806-255-9

Weitere ***Schriften des Verlags im Forschungszentrum Jülich*** unter
http://wwwzb1.fz-juelich.de/verlagextern1/index.asp

Schlüsseltechnologien /
Key Technologies
Band / Volume 153
ISBN 978-3-95806-255-9